UCLA Health

The 9th MR in RT Symposium

CONFERENCE LOCATION
LOS ANGELES, CALIFORNIA

February 6–8, 2023

ORGANIZED BY

UCLA Health
RADIATION ONCOLOGY

The 9th MR in RT Symposium

TABLE *of* CONTENTS

Welcome, Colleagues!

3 Minsong Cao, PhD
Daniel Low, PhD

4 UCLA Planning Committee

5 Scientific Committee and Abstract Reviewers

6 Young Investigator Award Judge Panel

7 Scientific Program (February 6-8)

8 Poster Presentations

9 Satellite Clinical Training Course

10 Sponsors

11 Abstracts

MRIdian® SMART

ABLATIVE DOSES.

TIGHTER MARGINS.

FEWER FRACTIONS.

Stereotactic MRI-Guided Adaptive Radiotherapy (SMART) is the only treatment that integrates diagnostic-quality MR imaging, streamlined on-table adaptive re-planning, and continuous, real-time, soft tissue tracking and automated beam gating. MRIdian SMART allows clinical teams to define tighter treatment margins, deliver ablative doses in five or fewer fractions, while avoiding unwanted dose to OARs, and minimizing toxicities without relying on implanted markers.*

Discover how MRIdian SMART enables teams to treat and prove what others can't. Join others conducting breakthrough research while delivering unmatched clinical results today.

www.viewray.com

VIEWRAY®
VISIBLY BETTER®

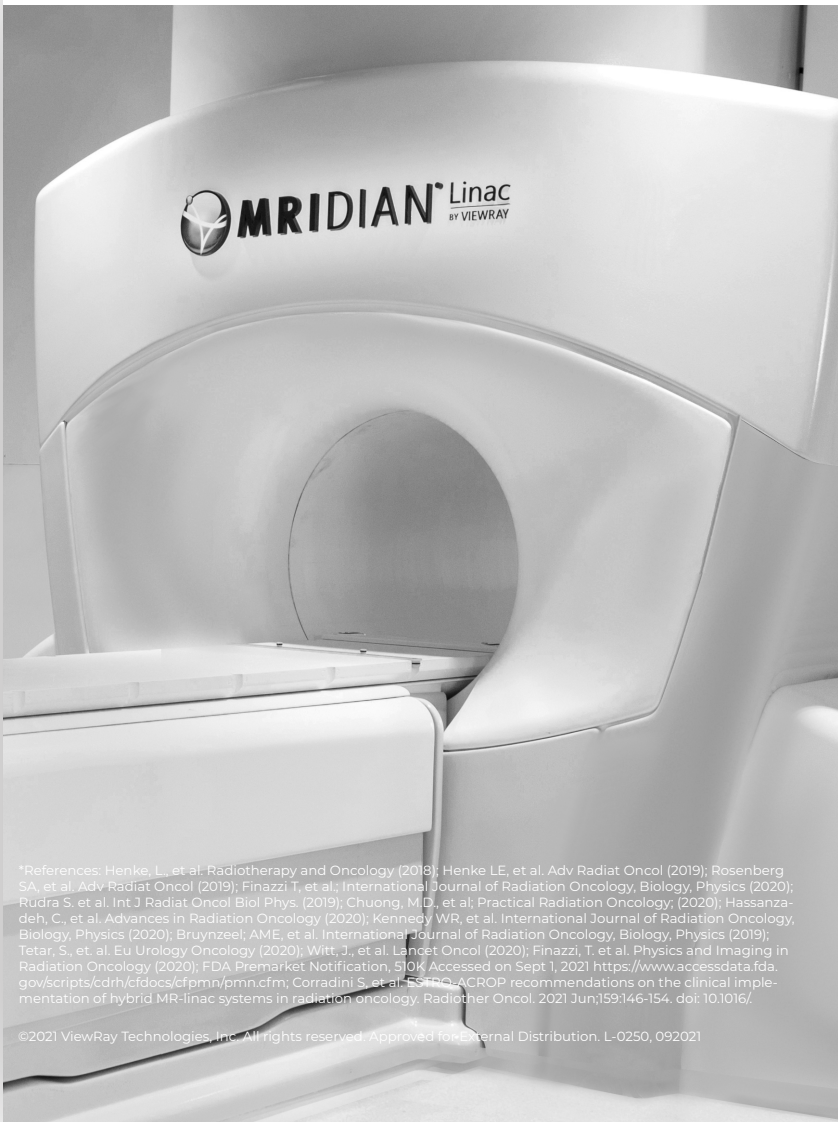

*References: Henke, L., et al. Radiotherapy and Oncology (2018); Henke LE, et al. Adv Radiat Oncol (2019); Rosenberg SA, et al. Adv Radiat Oncol (2019); Finazzi T, et al.; International Journal of Radiation Oncology, Biology, Physics (2020); Rudra S. et al. Int J Radiat Oncol Biol Phys. (2019); Chuong, M.D., et al; Practical Radiation Oncology; (2020); Hassanzadeh, C., et al. Advances in Radiation Oncology (2020); Kennedy WR, et al. International Journal of Radiation Oncology, Biology, Physics (2020); Bruynzeel; AME, et al. International Journal of Radiation Oncology, Biology, Physics (2019); Tetar, S., et. al. Eu Urology Oncology (2020); Witt, J., et al. Lancet Oncol (2020); Finazzi, T. et al. Physics and Imaging in Radiation Oncology (2020); FDA Premarket Notification, 510K Accessed on Sept 1, 2021 https://www.accessdata.fda.gov/scripts/cdrh/cfdocs/cfpmn/pmn.cfm; Corradini S, et al. ESTRO-ACROP recommendations on the clinical implementation of hybrid MR-linac systems in radiation oncology. Radiother Oncol. 2021 Jun;159:146-154. doi: 10.1016/.

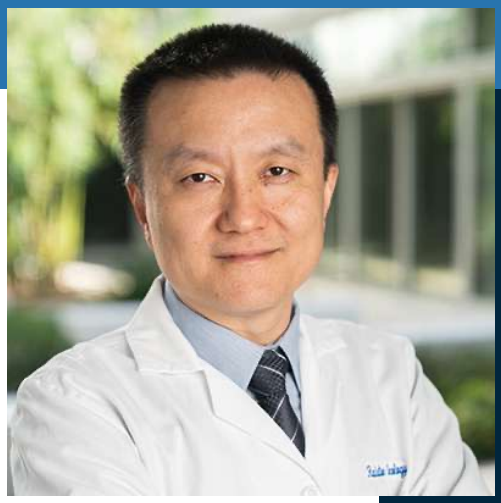

UCLA Health

UCLA Health

Dear Colleagues,

It is our pleasure to welcome you to the 9th MR in RT Symposium, the premier international meeting dedicated to the use of MRI in radiation therapy. This is the 9th in a series of outstanding conferences that have been organized to connect leaders in the development and implementation of the use of MRI for treatment planning, response assessment, and more recently treatment positioning and delivery.

UCLA is proud to serve as the host for this year's conference and we have selected an outstanding venue. Our department has a long history of innovation and developing interdisciplinary work that spans from lab to linac. It is our hope that this conference will serve to continue that trend and provide attendees with opportunities for lively interaction and communication.

This conference brings together some of the world's most renowned researchers and clinicians in the use of MRI for radiation therapy. The conference is intended to be multidisciplinary and collaborative. We have designed the schedule to allow and foster discussion and debate, and we hope that all attendees leave the conference with a deeper understanding of the field and with ideas on how to move the field forward.

We are looking forward to this conference and hope that we all find ideas, people, and moments that provide us with renewed energy, inspiration, and focus.

If you have free time, we hope you will take the opportunity to enjoy our wonderful campus and city.

Sincerely,

Minsong Cao PhD
Daniel Low PhD

Meeting Details

WiFi
Network: LCC_Meeting
Password: LCC2023

Speaker Ready Room (Odyssey)
Monday 7 – 5PM
Tuesday 8 – 5 PM
Wednesday 8-11AM

Please Check In

Then, use the **Speaker Ready Room** to verify and test your PowerPoint

Elekta

Elekta Unity

See the difference

See and treat like never before

With Elekta Unity, we're pushing the boundaries of what's possible, by giving clinicians the power to truly see and treat like never before. Comprehensive Motion Management with True Tracking and Automatic Gating will deliver the next stage of our Elekta Unity vision, combining market-leading diagnostic quality imaging with powerful algorithms and technology to quantify movement and correct for it automatically, as it happens.

Explore the Elekta Unity advantage.

elekta.com

LADMRL230110 Elekta Unity with Comprehensive Motion Management (CMM) is CE marked and pending U.S. FDA 510(k) clearance, with limited global availability.

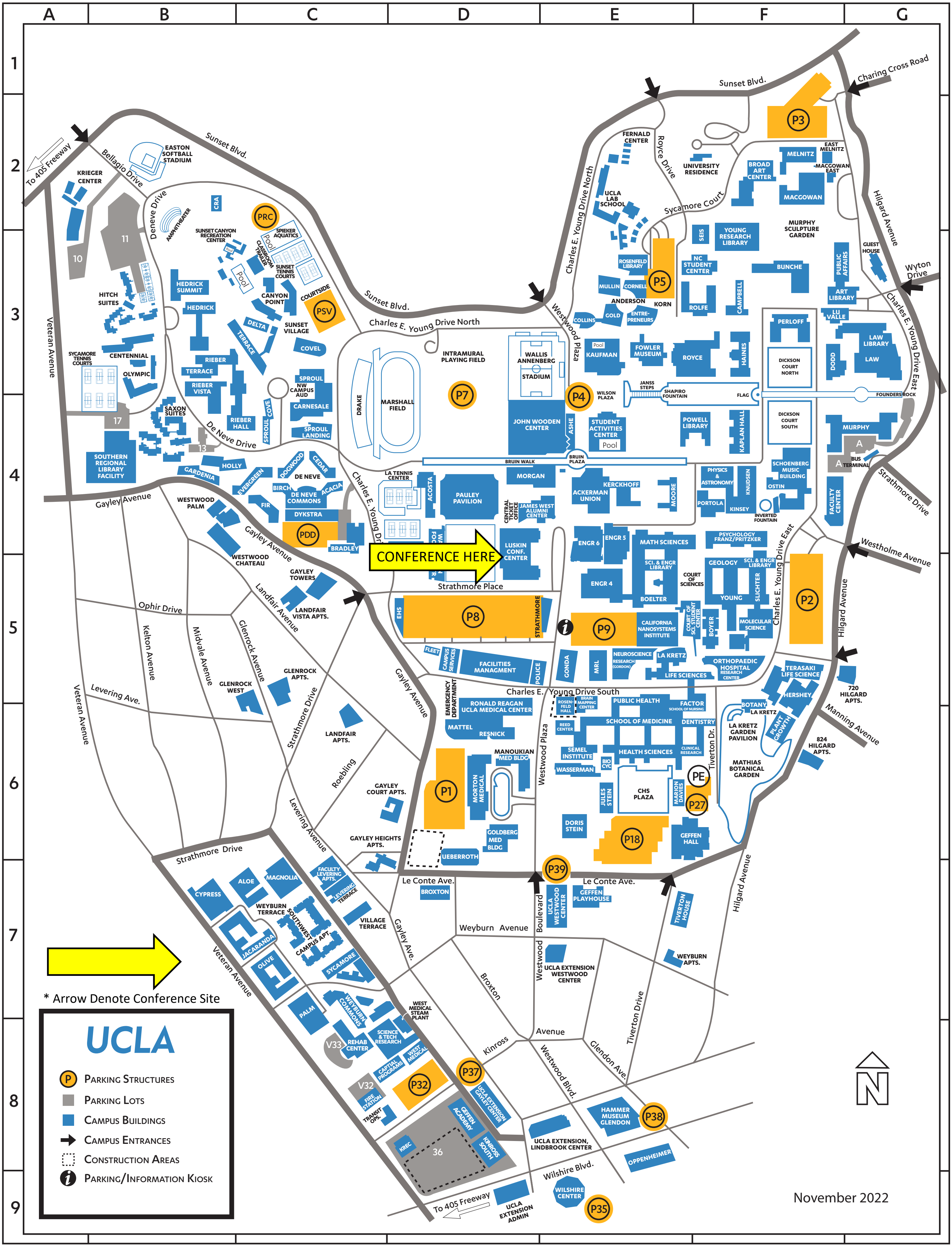
A
B
C
D
E
F
G
1
2
3
4
5
6
7
8
9
CONFERENCE HERE
LUSKIN CONF. CENTER
* Arrow Denote Conference Site
UCLA
Parking Structures
Parking Lots
Campus Buildings
Campus Entrances
Construction Areas
Parking/Information Kiosk
November 2022
Sunset Blvd.
Charing Cross Road
To 405 Freeway
Bellagio Drive
Deneve Drive
De Neve Drive
Veteran Avenue
Gayley Avenue
Ophir Drive
Kelton Avenue
Midvale Avenue
Glenrock Avenue
Levering Ave.
Strathmore Drive
Landfair Avenue
Roebling
Levering Avenue
Gayley Ave.
Strathmore Place
Charles E. Young Drive North
Charles E. Young Drive South
Charles E. Young Drive East
Charles E. Young Dr.
Westwood Plaza
Royce Drive
Sycamore Court
Hilgard Avenue
Wyton Drive
Strathmore Drive
Westholme Avenue
Manning Avenue
Tiverton Dr.
Le Conte Ave.
Weyburn Avenue
Westwood Boulevard
Broxton
Kinross
Avenue
Westwood Blvd.
Glendon Ave.
Tiverton Drive
Wilshire Blvd.
EASTON SOFTBALL STADIUM
KRIEGER CENTER
HITCH SUITES
SYCAMORE TENNIS COURTS
CENTENNIAL
OLYMPIC
SAXON SUITES
SOUTHERN REGIONAL LIBRARY FACILITY
HEDRICK SUMMIT
HEDRICK
RIEBER
TERRACE
RIEBER VISTA
RIEBER HALL
DELTA
SUNSET CANYON RECREATION CENTER
SPIEKER AQUATICS
CANYON POINT
SUNSET VILLAGE
COURTSIDE
COVEL
SPROUL
NW CAMPUS AUD
CARNESALE
SPROUL LANDING
HOLLY
CARDENIA
EVERGREEN
DOGWOOD
CEDAR
DE NEVE
BIRCH
DE NEVE COMMONS
ACACIA
FIR
DYKSTRA
BRADLEY
WESTWOOD PALM
WESTWOOD CHATEAU
GAYLEY TOWERS
LANDFAIR VISTA APTS.
GLENROCK APTS.
GLENROCK WEST
LANDFAIR APTS.
GAYLEY COURT APTS.
GAYLEY HEIGHTS APTS.
MARSHALL FIELD
DRAKE
INTRAMURAL PLAYING FIELD
WALLIS ANNENBERG STADIUM
JOHN WOODEN CENTER
WILSON PLAZA
LA TENNIS CENTER
ACOSTA
PAULEY PAVILION
MORGAN
ACKERMAN UNION
KERCKHOFF
JAMES WEST ALUMNI CENTER
BRUIN WALK
BRUIN PLAZA
STUDENT ACTIVITIES CENTER
Pool
KAUFMAN
FOWLER MUSEUM
ROYCE
HAINES
POWELL LIBRARY
KAPLAN HALL
JANSS STEPS
SHAPIRO FOUNTAIN
FLAG
FOUNDERS ROCK
DICKSON COURT NORTH
DICKSON COURT SOUTH
FERNALD CENTER
UCLA LAB SCHOOL
UNIVERSITY RESIDENCE
ROSENFELD LIBRARY
MULLIN
CORNELL
ANDERSON
KORN
COLLINS
GOLD
ENTREPRENEURS
SEIS
YOUNG RESEARCH LIBRARY
NC STUDENT CENTER
ROLFE
CAMPBELL
BROAD ART CENTER
MELNITZ
EAST MELNITZ
MACGOWAN
MACGOWAN EAST
MURPHY SCULPTURE GARDEN
BUNCHE
PUBLIC AFFAIRS
GUEST HOUSE
ART LIBRARY
LU VALLE
PERLOFF
LAW LIBRARY
LAW
DODD
MURPHY
BUS TERMINAL
SCHOENBERG MUSIC BUILDING
PHYSICS & ASTRONOMY
KNUDSEN
PORTOLA
KINSEY
INVERTED FOUNTAIN
OSTIN
FACULTY CENTER
MOORE
ENGR 6
ENGR 5
ENGR 4
MATH SCIENCES
SCI. & ENGR LIBRARY
BOELTER
COURT OF SCIENCES
PSYCHOLOGY FRANZ/PRITZKER
GEOLOGY
YOUNG
SLICHTER
MOLECULAR SCIENCE
BOYER
CALIFORNIA NANOSYSTEMS INSTITUTE
NEUROSCIENCE RESEARCH
LA KRETZ
LIFE SCIENCES
ORTHOPAEDIC HOSPITAL RESEARCH CENTER
TERASAKI LIFE SCIENCE
HERSHEY
720 HILGARD APTS.
824 HILGARD APTS.
BOTANY
LA KRETZ GARDEN PAVILION
PLANT GROWTH
MATHIAS BOTANICAL GARDEN
FLEET
CAMPUS SERVICES
FACILITIES MANAGMENT
POLICE
GONDA
MRL
STRATHMORE
EHS
EMERGENCY DEPARTMENT
RONALD REAGAN UCLA MEDICAL CENTER
MATTEL
RESNICK
MANOUKIAN MED BLDG
MORTON MEDICAL
GOLDBERG MED BLDG
UEBERROTH
PUBLIC HEALTH
FACTOR
SCHOOL OF MEDICINE
DENTISTRY
REED CENTER
SEMEL INSTITUTE
HEALTH SCIENCES
CLINICAL RESEARCH
BIO CYC
WASSERMAN
JULES STEIN
CHS PLAZA
MARION DAVIES
DORIS STEIN
GEFFEN HALL
BROXTON
GEFFEN PLAYHOUSE
UCLA WESTWOOD CENTER
TIVERTON HOUSE
WEYBURN APTS.
UCLA EXTENSION WESTWOOD CENTER
CYPRESS
ALOE
MAGNOLIA
FACULTY LEVERING APTS.
LEVERING TERRACE
WEYBURN TERRACE
SOUTHWEST CAMPUS APT.
VILLAGE TERRACE
JACARANDA
OLIVE
SYCAMORE
PALM
WEYBURN COMMONS
WEST MEDICAL STEAM PLANT
REHAB CENTER
SCIENCE & TECH RESEARCH
WEST MEDICAL
CAPITAL PROGRAMS
FIRE STATION
TRANSIT OPS.
GEFFEN ACADEMY
UCLA EXTENSION GAYLEY CENTER
KREC
KINROSS SOUTH
UCLA EXTENSION, LINDBROOK CENTER
HAMMER MUSEUM GLENDON
OPPENHEIMER
WILSHIRE CENTER
UCLA EXTENSION ADMIN
P1
P2
P3
P4
P5
P7
P8
P9
P18
P27
P32
P35
P37
P38
P39
PE
PRC
PSV
PDD
V32
V33
10
11
13
17
36
A
N

UCLA PLANNING COMMITTEE

Daniel Low PhD
Professor & Vice Chair of Physics

Minsong Cao PhD
Professor & Associate Vice Chair of Education

Ann Raldow MD MPH
Associate Professor & Vice Chair of Education

Amar Kishan MD
Associate Professor &
Vice Chair of Clinical and Translational Research

Kathy Rose
Educational Programs Administrator

YOUNG INVESTIGATORS AWARD JUDGE PANEL

James Balter
University of Michigan

Nesrin Dogan
University of Miami

Paul Keall
University of Sydney, Australia

Allen Li
Medical College of Wisconsin

Carri Glide-Hurst
University of Wisconsin

Bas Raaymakers
University Medical Center Utrecht (UMC)

Daniel Low
University of California, Los Angeles

Parag Parikh
Henry Ford Health System

SCIENTIFIC COMMITTEE

James Balter
University of Michigan

Minsong Cao
University of California,
Los Angeles

Yue Cao
University of Michigan

Indrin Chetty
Henry Ford Health System

Caroline Chung
MD Anderson Cancer Center

Nesrin Dogan
University of Miami

Jennifer Dolan
Henry Ford Health System

Martin Fast
University Medical Center
Utrecht (UMC)

Clifton David Fuller
MD Anderson Cancer Center

Carri Glide-Hurst
University of Wisconsin

Lauren Henke
Case Western Reserve University

Oliver Jäkel
German Cancer Research Center
(DKFZ), Germany

Paul Keall
University of Sydney, Australia

Amar Kishan
University of California,
Los Angeles

Allen Li
Medical College of Wisconsin

Daniel Low
University of California,
Los Angeles

Tyagi Neelam
Memorial Sloan Kettering
Cancer Center

Tufve Nyholm
Umeå University, Sweden

Uwe Oelfke
The Institute of Cancer Research,
UK

Kyle Padgett
University of Miami

Parag Parikh
Henry Ford Health System

Eric Paulson
Medical College of Wisconsin

Marielle Philippens
University Medical Center Utrecht
(UMC)

Bas Raaymakers
University Medical Center Utrecht
(UMC)

Ann Raldow
University of California,
Los Angeles

Christopher Schultz
Medical College of Wisconsin

Jan-Jakob Sonke
Netherlands Cancer Institute,
The Netherlands

Teo Stanescu
Princess Margaret Cancer Centre,
Canada

Daniela Thorwarth
University of Tübingen, Germany

Uulke van der Heide
Netherlands Cancer Institute,
The Netherlands

Petra van Houdt
Netherlands Cancer Institute,
The Netherlands

Jihong Wang
MD Anderson Cancer Center

Yingli Yang
Shanghai Ruijing Hospital, China

Victoria Yu
Memorial Sloan Kettering
Cancer Center

Tong Zhu
Washington University St. Louis

PHILIPS

Radiation Oncology

Ingenia MR-RT XD

Versatility to fit your planning

MRI has proven itself a key player in radiation therapy imaging – continuing its role as a powerful tool for oncology specialists to confidently address today's challenges across the oncology continuum.

With its superior soft tissue contrast compared to CT, MRI offers excellent visualization of tumor boundaries and proximity to nearby critical structures – a key factor for more confident delineation and improved treatment plans. What's more, MRI's advanced imaging capabilities can inform both target characterization and treatment response, providing you with a 'toolbox' to design personalized treatment options for each patient.

Philips Ingenia MR-RT XD platform:

Meets the need for accuracy with advances in image quality, geometric fidelity, and reproducible patient positioning

Streamlines workflow integration through intuitive tools, intelligent automation, and support to excel

Maximizes value across a variety of therapies and applications **through inherent versatility**

innovation + you

Excellent soft-tissue contrast

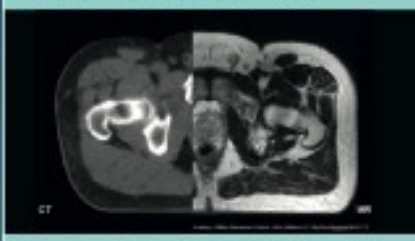

Functional imaging capabilities

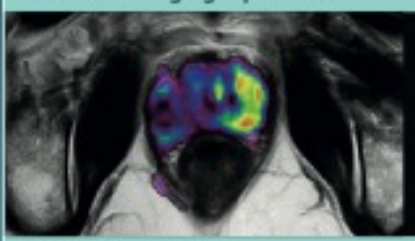

No Ionizing radiation

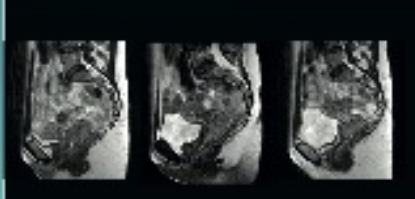


MEYER & RENEE
LUSKIN
CONFERENCE
CENTER

UCLA Health

RADIATION ONCOLOGY

MR IMAGING-GUIDED RADIOTHERAPY

Fellowship

The Department of Radiation Oncology at the David Geffen School of Medicine at UCLA currently seeks applicants at the Clinical Instructor rank for a one-year Magnetic Resonance Imaging-Guided Radiotherapy (MRgRT) Fellowship opportunity under the supervision of Dr. Amar Kishan and Dr. Ann Raldow in the Department of Radiation Oncology at UCLA, Los Angeles, CA. Interested applicants should have a strong interest in advanced MRgRT, research (clinical and physics), and clinical trials.

UCLA Health is the #1 rated Hospital in Los Angeles and #6 in the nation per U.S. News and World Report. The Department of Radiation Oncology offers innovative radiation treatment options across all service lines. The department is equipped with a MRIdian linear accelerator (ViewRay, Inc.) as well as an MRI simulator (Siemens, Inc.). UCLA has established itself as a world leader in the field of MRgRT, having initiated and led multiple clinical trials in the field. The clinical trial portfolio includes the phase III randomized MIRAGE trial, to date the only randomized trial of MRgRT to ever be conducted. Multiple ongoing MRgRT clinical trials run through the Jonsson Comprehensive Cancer Center are complemented by a robust basic science research program with dedicated support from physicists in the Physics & Biology in Medicine program.

The University of California seeks to recruit and retain a diverse workforce as a reflection of our commitment to serve the people of California, to maintain the excellence of the University, and to offer our students richly varied disciplines, perspectives and ways of knowing and learning.

The University of California is an Equal Opportunity/Affirmative Action Employer. All qualified applicants will receive consideration for employment without regard to race, color, religion, sex, sexual orientation, gender identity, national origin, disability, age or protected veteran status. For the complete University of California nondiscrimination and affirmative action policy see: UC Nondiscrimination and Affirmative Action Policy.

APPLY TODAY

SCIENTIFIC AGENDA

Monday, February 6

7:00- 8:00	**Breakfast**
8:15-8:30	**Welcome Session** D. Low, Vice Chair, Department of Radiation Oncology, UCLA M. Cao, Professor and Associate Vice Chair of Education, UCLA M. Steinberg. Chair, Department of Radiation Oncology, UCLA
8:30-9:30	**Invited Session:** MR in RT: Clinical Evidence and Studies **Chairs:** Ann Raldow (UCLA) & Ritchell van Dams (Dana-Farber Brigham Cancer Center) A. Kishan (UCLA): Aggressive Margin Reduction: MRgRT and the MIRAGE Trial P. Parikh (Henry Ford Health System): Lessons Learned with the SMART Trial C. Shultz (Medical College of Wisconsin): High field MR Guided RT using the Unity Platform: Clinical Update from MCW and the MR Linac Consortium
9:30-10:30	**Proffered Abstract Presentation Session: MR in RT Clinical Studies and Applications** **Chairs:** Luca Valle (UCLA) & Jie Deng (University of Texas Southwestern)
	ID 18. P. Keall: ICRU Report on MRI-Guided Radiation Therapy using MRI-Linacs ID 50. V. Koteva: Dosimetric evaluation of plans from automated contours of elective target volumes and organs at risk for head and neck cancer patients for online adaptive MR-Linac treatments ID 51. L. Smith: Dosimetric comparison of MRI-guided vs CT-guided Stereotactic Body Radiotherapy to the Post-Prostatectomy Prostate Bed: A Post-Hoc Analysis of a Phase II Trial ID 52. G. Vlacich: Dosimetric Goals Versus Realities in Initial and Adaptive Plans from an Ongoing Phase II Clinical Trial of Online Adaptive MR-Guided Hypofractionated Radiation with Concurrent Chemotherapy for Locally-Advanced NSCLC ID 80. T. Chiu: Simulation-free adaptive radiosurgery for Malignant Spinal Cord Compression Syndrome using MR-LINAC ID 81. S. Bennett: Examining Gadolinium-Based Nanoparticle Uptake in Brain Metastases as Quantified by T1 Mapping
10:30-11:00	Coffee break
11:00-12:00	**Invited Session: Current Status and Future Trends for MR in RT QA Methods** Chairs: Ali Fatemi (Jackson State University) & Teodor Stanescu (Princess Margaret Cancer Center)
	Lars Olsson (Lund University): QA of MRI-only RT in clinical routine Anthony Doemer (Henry Ford Health System): QA Considerations Across Multiple MR-Linac Platforms Teodor Stanescu (Princess Margaret Cancer Center): Aspects of QA for deeper integration of MR technologies in RT
12:00-13:00	Lunch break

SCIENTIFIC AGENDA

Monday, February 6

13:00- 14:00	**Proffered Abstract Presentation Session: MR Sim and MR Based Planning** **Chairs:** Anthony Doemer (Henry Ford Health System) & Tufve Nyholm (Umeå University)
	ID 2. B. Guevara: Simulated adaptive re-planning during glioblastoma radiotherapy on a combination MRI-Linear accelerator ID 3. C. Jamtheim Gustafsson: Evaluation of using commercial deep learning-based MR image reconstruction for synthetic CT generation in radiation therapy of prostate cancer patients ID 19. A Zerafa: Comparison of 4D-CT and 4D-MRI for volumetric and motion assessment in radiotherapy planning of lung cancer ID 42. E. Kaza: Reduction of DIXON geometric distortions for HDR brachytherapy applicator imaging ID 70. J. Massachi: MRI simulation for breast cancer radiotherapy planning in poorly defined cavities ID 74. V. Yu: Clinical commissioning from bulk density synthetic CT to compressed-sensing-accelerated continuous Hounsfield unit synthetic CT for MR-only treatment planning in prostate: an institutional experience
14:00-15:00	**Invited Session: Panel Discussion on Advances and Future Directions of MR in RT** **Chairs:** James Balter (University of Michigan) & Daniel Low (UCLA) **Panelists:** Paul Keall (University of Sydney), Ann Raldow (UCLA), James Balter (University of Michigan), Daniel Low (UCLA)
15:00-15:30	Coffee break
15:30-17:30	**Young Investigator Award Presentations** **Chairs:** Allen Li (Medical College of Wisconsin) & Paul Keall (University of Sydney)
	ID 34. M Marot: Measurements and Monte Carlo simulations of the response of a Farmer-type ionization chamber for proton beams in the presence of magnetic fields for the determination of kB ID 35. I. Thrussell: Are early radiotherapy changes in quantitative MRI predictive of changes after treatment in soft-tissue sarcomas? ID 37. S. Surla: Output factor measurements for small isocentric and off-axis photon fields at a 0.35 T MR-Linac ID.40. J. Zou: A New Framework for 3D MR Fingerprinting with Efficient Subspace Reconstruction and Posterior Distribution Estimation ID.53. K. Keijnemans: Regularizing breathing during 4D-MRI acquisitions on the MR-linac with visual biofeedback ID.77. N. Warner: MR Imaging of Free Radical Production during Radiation Chemistry Interactions ID 78. J. Chen: Low-field MR Multitasking for an integrated abdominal MRgRT imaging framework ID 79. T. Ma: Treatment delivery gating of MRI-guided stereotactic radiotherapy for prostate cancer: An exploratory analysis of a Phase III Randomized Trial of CT-vs. MR-guided radiotherapy (MIRAGE)
17:30-18:00	Break
18:00-20:00	Reception/Dinner

SCIENTIFIC AGENDA

Tuesday, February 7

7:00-8:00	**Breakfast**
8:30-9:30	**Invited Debate Session: Is a Single Imaging Parameter Sufficient for Prediction of Tumor Outcomes?** **Chairs:** Yue Cao (University of Michigan) & Eric Paulson (Medical College of Wisconsin) **For the proposition:** Daniela Thorwarth (University of Tübingen) **Against the proposition:** Yue Cao (University of Michigan)
9:30-10:30	**Proffered Abstract Presentation Session: Sequence Development and Functional Imaging** **Chairs:** Jihong Wang (MDACC) & Zhaoyang Fan (University of Southern California)
	ID 23. F. Guerreiro: Quantitative MRI associated with patient-reported xerostomia after head and neck radiotherapy ID 43. T Nyholm: PSMA-PET/MRI for classification and delineation of intra-prostatic lesions ID 66: N Tyagi: Diffusion-weighted MRI derived imaging metrics for MR-guided ablative radiotherapy of pancreatic ductal adenocarcinoma ID 67: S. Siddiq: Real-Time MR Signature Matching (MRSIGMA) for Volumetric MRI with less than 300MS Latency on a MR-Linac ID 86: D Lee: R2*-MRI with super-paramagnetic iron oxide nanoparticles (SPION) to auto-contour voxel-wise functional liver parenchyma volume for primary and metastatic liver cancers ID 14: Y Cao: In vivo Microstructure Imaging in Oropharyngeal Squamous Cell Carcinoma
10:30-11:00	Coffee break
11:00-12:00	**Proffered Abstract Presentation Session: MR Linac and QA/QC** **Chairs:** Daniela Thorwarth (University of Tübingen) & Eenas Omari (Medical College of Wisconsin)
	ID7. S Schneider. Commissioning and image distortion analysis of an in-beam MR prototype system for MR-integrated proton therapy ID 8. C. Kensen: Online adaptive MRI-guided radiotherapy for primary tumor and lymph node boosting in rectal cancer ID 13. J Scherman: Dosimetric and geometric impact of on-patient placement of a lightweight receiver coil in a clinical MRI-only radiotherapy workflow for prostate cancer ID 58: S Dorsch. Characterization of MR image quality for simultaneous ion beam scanning in particle therapy ID 64: L Bosma: An error estimator for intra-fraction dose accumulation: introduction and evaluation ID 69: Y Cervantes: Evaluation of the magnetic field effect on scintillator response to megavoltage photon beams.
12:00-13:00	Lunch break
13:00-14:00	**Invited Session: 4D-MRI: Clinical Reality and Future Applications** **Chairs:** Martin Fast (UMC Utrecht) & Yanle Hu (Mayo Clinic)
	J. Scholey (UCSF): Principles of 4D-MRI & applications for MR-sim J. Sonke (NKI-AvL): Clinical application of 4D-MRI for MR-linac R. Otazo (MSKCC): Real-time 4D-MRI: techniques and applications

SCIENTIFIC AGENDA

Tuesday, February 7

14:00-15:00	**Proffered Abstract Presentation Session: MR Based Motion Management** **Chairs:** Kyle Padgett (University of Miami) & John Lewis (Cedars-Sinai)
	ID11. L. Feng: MR Motion Fingerprinting: A Novel Framework for High-Fidelity Real-Time Volumetric MRI with Sub-Second Latency. ID26: E. Omari: Daily 4DMRI motion assessment and the impact on planning target volume for non-gated MRI guided liver stereotactic body radiation therapy ID41. L Liu: Volumetric MRI Reconstruction from Cine Acquisition Using Sparse Priors and Implicit Neural Representation Learning ID60 J Scholey: 4D-MRI reconstruction for radiotherapy treatment planning of liver tumors ID61. N Tyagi: Prospective dose accumulation to assess target coverage gain for locally advanced pancreatic cancer (LAPC) patients undergoing ablative MR-guided adaptive radiotherapy ID57. E Persson: Dosimetric impact of gating and MLC tracking in MR-guided ultra-hypo fractionated prostate radiotherapy
15:00-15:30	Coffee break
15:30-17:30	**Session: Industry Development Update (exhibitor presentations)**
18:00-19:00	**Poster Presentation and Reception**

SCIENTIFIC AGENDA

Wednesday, February 8

7:00-8:00	**Breakfast**
8:30-9:30	**Invited Session: Checking the Beat: Updates on MRI-based Cardiac Applications in Radiation Oncology** **Chairs:** Carri Glide-Hurst (University of Wisconsin) & Geoffrey Hugo (Washington University St. Louis)
	K. Mittauer (Miami Cancer Institute): Management of Cardiac Implantable Electronic Devices for Patients Receiving MR-Guided Radiotherapy: 4-Year Single Institution Experience P. Hu (Shanghai Technology University): Recent advances in Cardiac MRI: Implications for Radiation Therapy J. Verhoeff (UMC Utrecht): Heart-Beat Triggered MRI-guided SBRT for Ventricular Tachycardia: "Always in motion is the future." – Yoda (Star Wars)
9:30-10:30	**Proffered Abstract Presentation Session: Advanced MR Topics in AI and Data Sciences – I** **Chairs:** Nesrin Dogan (University of Miami) & Victoria Yu (MSKCC)
	ID 31. V. Murray: Fast motion-resolved 4D MRI using deep learning reconstruction without explicit data consistency on an MR-Linac system ID 32. B. Oborn: A comprehensive quantification of the dosimetric impact of electron streaming for MRI-guided proton therapy ID 39. Y. Zhang: Promoting the Clinical Application of Deep Learning Auto-segmentation (DLAS) – an Automatic Contour Quality Assurance tool for MRI-guided online adaptive radiotherapy ID 44. L. Vinas: LapGM: A Fast and Accurate Multisequence MR Bias Correction and Normalization Method ID46. J. Jiang: Progressively refined deep joint registration segmentation (ProRSeg) of gastrointestinal organs at risk for MRI dose accumulation ID38. J. Sonke: Radial-RIM: accelerated radial 4D MRI using the recurrent inference machine
10:30-11:00	Coffee break
11:00-12:00	**Proffered Abstract Presentation Session: Advanced MR Topics in AI and data sciences- II** **Chairs:** Tong Zhu (Washington University St. Louis) & James Lamb (UCLA)
	ID47. D. You: Deep-learning based head-and-neck tumor segmentation for fully automated processing of MRI biomarkers ID 4. B. Al-Qaisieh: Deep learning cycleGAN MRI-only synthetic-CT generation for pelvis, brain and head and neck cancers ID 33. M Dassen: Treatment margins for different adaptation strategies in MRI-guided online adaptive radiotherapy for prostate cancer ID 56. B. Eiben: Real-time dose reconstruction with differential target and OAR motion and inter-beam replanning ID 68. C. Bauer: CT-MR-Deformable Image Registration for MR-Guided Radiotherapy using a Biomechanical Skeleton Model ID 82. J. Wei: Optimizing Pre-processing Workflow to Improve Radiomics Robustness for Longitudinal Abdominal MRIs Acquired with Low Field-Strength MR-linac Systems
12:00-12:30	**Young Investigator Award and Closing Remarks**

Comprehensive MRgRT QA Solutions

Zeus MRgRT Motion Management QA Phantom

MICRO+™ Fixed Lasers System

Address the unique challenges magnetic fields present, with custom-designed QA solutions.

Learn more: sunnuclear.com/mrqa

MR Distortion & Image Fusion Head Phantom

Daily QA™- MR array

sunnuclear.com // cirsinc.com

SUN NUCLEAR
A MIRION MEDICAL COMPANY

POSTER PRESENTATIONS

ID 5. A. Amjad: Deep learning-based Auto-Segmentation on Multi-sequence MRI for MR-guided Adaptive Radiation Therapy in Abdomen

ID 6. G. Vlacich: MR-Adaptive Hypofractionated Radiation Therapy for Locally Advanced Non-Small Cell Lung Cancer: Benefits and Challenges Learned from a Prospective Clinical Trial.

ID 9. A. Fatemi: Developing an intelligent solution for accurate MRI-based Stereotactic Radiosurgery

ID10. M. Gach: The Challenge of Model-Based B0 Compensation in 0.35 T MRI-Linac During Gantry Rotation

ID 15. A. Fatemi: MRI Motion Artifact Reduction using 3D Deep Neural Network

ID 16. A. Fatemi: Multicenter MRI and CT Fusion using Unsupervised GAN Deep Learning

ID 17. P. Keall: TOWARDS MRI-GUIDED PROTON THERAPY: THE ULTIMATE CANCER TREATMENT?

ID 21. A Walter: Impact of additional MRI scans on the training of supervised deep learning methods for automatic CTV delineation in head and neck cancers

ID 22. A. Yawson: Pseudo-DECT Generation using 3D U-Net architecture for MRI-only Treatment Planning

ID 25. L Kim: An injectable dosimeter for real-time, in-vivo verification of MR-guided radiation therapy

ID 27. A. Mohamedi: Automated Segmentation of Skeletal Muscle for Sarcopenia Determination in Head and Neck Cancer Patients Using MRI

ID 28. M. Sohlin: Oxygen-enhanced (OE) and intravoxel incoherent motion (IVIM) MRI for detection of radiation therapy induced changes in head and neck cancer

ID 29. J.A. García-Alvarez: A Workflow to Perform MRI-guided Adaptive Radiotherapy for Abdominal SBRT using Deformable Dose Accumulation with Confidence Intervals

ID 36. X Yang: A Feasibility Study on Pseudo-CT from Planning MRI in Single and Multi-fraction Stereotactic Radiosurgery of Brain

ID 45. X.A. Li: MOLAR: Machine learning accelerated On-Line Adaptive Replanning for MRgRT

ID 54. O. G. Valadie: Exploring physiological changes after conformal radiation therapy in orthotopic U251 glioma model as potential biomarkers of response using DCE-MRI

ID 55. B. Meng: Development and clinical implementation of a novel MRI-only planning workflow for prostate cancer external beam radiotherapy

ID 59. A. Feldman: Does Stereotactic Online Adaptive MRgRT Obviate the Need for Rectal Spacer?

ID 62. S. Duong: Developing a 3D printed phantom and analysis software to quantify MRI radiomic features' consistency and variations between institutions and sessions

ID 63. N. Tyagi: Assessment of intrafractional prostate motion in MR-guided online adaptive radiotherapy

ID 65. H. Lee: Initial experience with MR-only workflow validation for accelerator-based stereotactic radiosurgery/radiotherapy of brain tumors

ID 71. D. Erler: Future-Proofing our Radiation Therapy Workforce: Development of an MR-Integrated Radiation Therapy Training Program

ID 72. E. Subashi: 3D-Printed Multi-Contrast Phantom for Quality Assurance of Adaptive Radiotherapy Delivery in a High-Field MR-Linac

ID 73: Z Wen: Study of correlation between patient specific QA gamma index passing rate and IMRT plan complexity for a ViewRay MR-Linac System

ID 75. J Begg: Assessment of differences between treatment using the Australian MRI-linac and standard of care for the MAnTRA clinical trial

ID 76: S. Huh: Clinical Use of an MR-based Motion Map to Determine Patient-specific Volumetric Margins in Proton Therapy for Prostate Cancer

ID 83. Y. Liao: A simulation and phantom study to evaluate the accuracy of T1 measurements and contrast agent concentration conversion for dynamic contrast-enhanced MRI protocol optimization

ID 84. A Sethi: Dosimetric Gains of Plan Adaptation with MR guided RT for Pancreas Patients

ID 87. A. Kirichenko: Radioimmunomodulating Properties of Super-Paramagnetic Iron Oxide Nanoparticles (SPION) in vitro used as Alternative Contrast Agent for MRI-Guided Liver Stereotactic Body Radiotherapy (SBRT)

Bringing the power of MR to RT

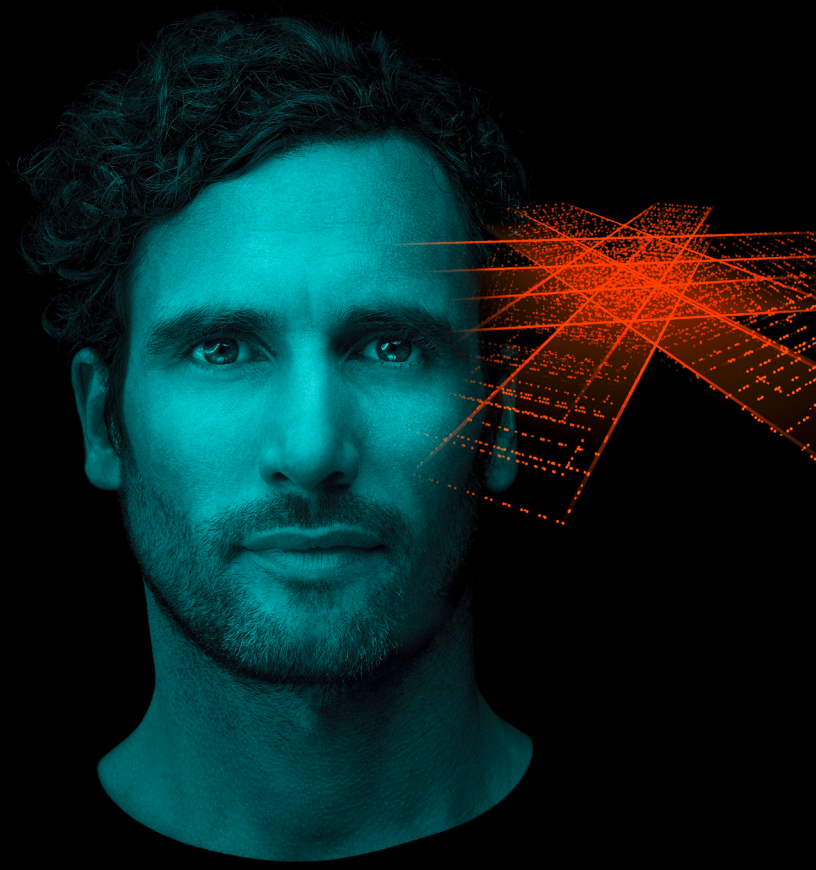

The scientific overlay is not that of the individual pictured and is not from a device of Siemens Healthineers. • 13192 1222

MAGNETOM RT Pro Edition, available for MAGNETOM Sola and MAGNETOM Vida, is dedicated to RT, delivering excellent soft-tissue contrast as well as imaging that can yield information for physicians regarding tumor extent and functional parameters.

Efficiently integrating this additional modality into existing processes can add substantial value to radiation therapy and help advance your institution's clinical capabilities.

siemens-healthineers.com/magnetom-rt-pro-edition

The LAP laser bridge shown in the above picture refers to products of 3rd party manufacturers and thus are in their regulatory responsibility. Please contact the 3rd party manufacturer for further information.

SIEMENS Healthineers

UCLA MRI-GUIDED RADIOTHERAPY (MRgRT) Academy:

Building A Clinical Adaptive Radiotherapy Program

The Department of Radiation Oncology at the University of California, Los Angeles (UCLA) invites you to attend a clinical training course on MRI-guided adaptive radiotherapy (MRgRT) in conjunction with the 9th MR in RT Symposium. This half-day training course brings together clinical experts in the field of MR-guided adaptive radiotherapy to get you prepared for the future radiotherapy paradigm. In this course, the participants will learn the basic physics and technologies of MRI-guided radiotherapy, review the available clinical evidence and promising indications across different cancer sites, gain a deep understanding of the complexity and challenges associated with the clinical implementation of the MRgRT process, and identify staff requirements, training, and safety required to build the clinical adaptive program.

Date: Feb 8 (Wednesday), 2023

Location: UCLA Luskin Conference Center

Sponsored By VIEWRAY VISIBLY BETTER

UCLA MRI-GUIDED RADIOTHERAPY (MRgRT) Academy:

Building A Clinical Adaptative Radiotherapy Program

Wednesday, February 8

Time	Lectures
12:30-1:30PM	Registration (UCLA Luskin Laureate Room)
	Lunch (UCLA Luskin Plateia Restaurant)
1:30 - 1:50	**Overview of MR Linac Technology and Features for Adaptive Radiotherapy** Daniel Low, PhD, FAAPM, FASTRO, Professor and Vice Chair of Medical Physic Research and Innovation, Department of Radiation Oncology, UCLA
1:50 - 2:20	**Clinical Evidence and Indicators of MRI Guided Adaptive Radiotherapy (MRgRT)** Ann Raldow, MD, MPH. Associate Professor and Vice Chair of Education, Department of Radiation Oncology, UCLA
2:20 - 2:40	**Workflow Management and Clinical Implementation of MRgRT** James Lamb, PhD, Associate Professor and Vice Chair of Medical Physics. Department of Radiation Oncology, UCLA
2:40 - 3:00	Break
3:00 - 3:20	**Robust Treatment Planning for MRgRT** Minsong Cao, PhD. Professor and Associate Vice Chair of Education of Medical Physics. Department of Radiation Oncology, UCLA
3:20 - 3:50	**QA/QC and Commissioning Considerations for MRgRT** Kathryn Mittauer, PhD. Assistant Professor. Miami Cancer Institute and Florida International University.
3:50 - 4:10	**Staffing, Training, and Safety Consideration for MRgRT** James Lamb, PhD, Associate Professor and Vice Chair of Medical Physics. Department of Radiation Oncology, UCLA
4:10 - 5:00	**Clinical Case Review and Q&A Discussions** Ann Raldow, MD, MPH. Associate Professor and Vice Chair of Education, Department of Radiation Oncology, UCLA Amar Kishan, MD. Associate Professor and Vice Chair of Clinical and Translational Research Minsong Cao, PhD. Professor and Associate Vice Chair of Education of Medical Physics. Department of Radiation Oncology, UCLA

Sponsored By  VIEWRAY VISIBLY BETTER

THERAPANACEA
Reinventing cancer care through AI

ART-Plan™:
Unlock true MR-only workflow in your clinic through AI

TheraPanacea has released an AI-assisted MR-only workflow that includes automatic annotation and a deep-learning based tool for pseudo-CT generation from MR images to reduce overall treatment costs, clinician's workload, and patient exposure to ionizing radiation.

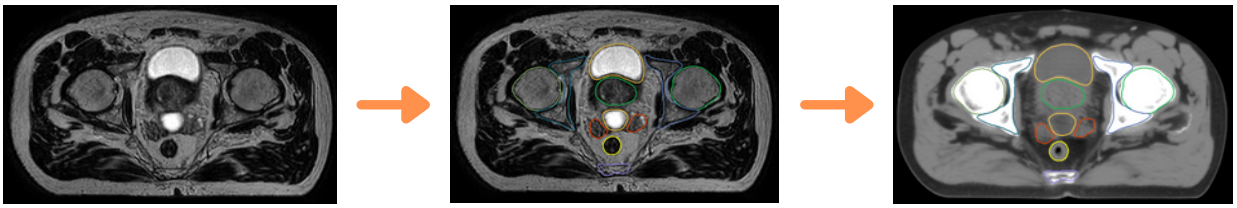

Delineate OARs on MR images → **Generate an MR-based pseudo-CT** → **Plan your treatment**

Our tools for MR-only workflow combine excellent soft-tissue contrast of MR images for OARs and target delineation, with the ability to generate tissue electron density for dose calculation from pseudo-CTs.

Our models include:

Brain T1/T1-Gd | **Pelvis T2** | **Abdomen & Pelvis Truefisp**

Clinical studies have demonstrated that dosimetric differences between planning CTs and pseudo-CTs were clinically insignificant for both PTVs and OARs. The results show that using ART-Plan™ for MRI-only planning is feasible for RT planning of brain and pelvis anatomies.*

Key Advantages of MR-only Radiotherapy Planning

- Better soft tissue contrast for improved delineation
- Reduced registration errors
- Reduced patient exposure to ionizing radiation
- Reduced overall treatment cost

www.therapanacea.eu

*References: MR-Only White Paper, TheraPanacea

SYMPOSIUM SPONSORS

Platinum

Elekta

VIEWRAY VISIBLY BETTER

PHILIPS

SUN NUCLEAR A MIRION MEDICAL COMPANY

SIEMENS Healthineers

MagnetTx

GE Healthcare

THERAPANACEA Reinventing cancer care through AI

Silver

PTW THE DOSIMETRY COMPANY

orfit

phantomlab

LinaTech Providing Superior Products for Cancer Treatment

mim SOFTWARE

LAP

MODUS QA an IBA Dosimetry Company

BluePhysics

medscint

SPECTRONIC MEDICAL MRI only treatment planning

QFix

Battled together CIVCO

TAKING MR IMAGING ANOTHER LEVEL UP WITH AIR RECON DL

Every so often, a new technology changes the status quo. In 2020, GE Healthcare introduced AIR™ Recon DL, a pioneering, deep-learning-based reconstruction algorithm that challenges the historic compromise between scan time and image quality in MR imaging.

AIR™ Recon DL improves image quality by making use of the raw data to remove image noise and ringing, improving SNR and image sharpness, and enabling shorter scan times. It has been heralded as one of the most significant innovations in MR technology in several decades.

Now, thanks to AIR™ Recon DL with true deep learning, there is simply a better way to achieve high SNR with shorter scan times.

TO LEARN MORE ABOUT AIR™ RECON DL,

SCAN THE QR CODE

AND WATCH THE MUST-SEE FILM, UNMISSABLE

ABSTRACTS

Meet AURORA-RT

PATIENT COMFORT

CLINICIAN BENEFITS

PATIENT SAFETY

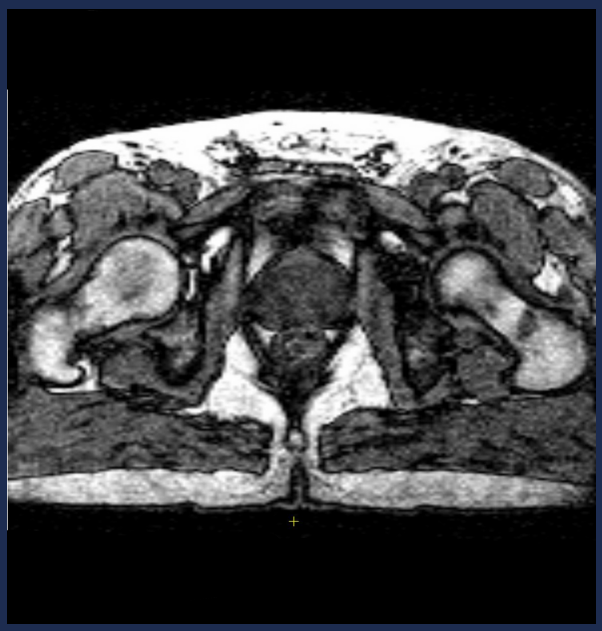

SOFTWARE COMPATIBILITY

BETTER FOR OUR PLANET

WIDER VARIETY OF TREATMENTS

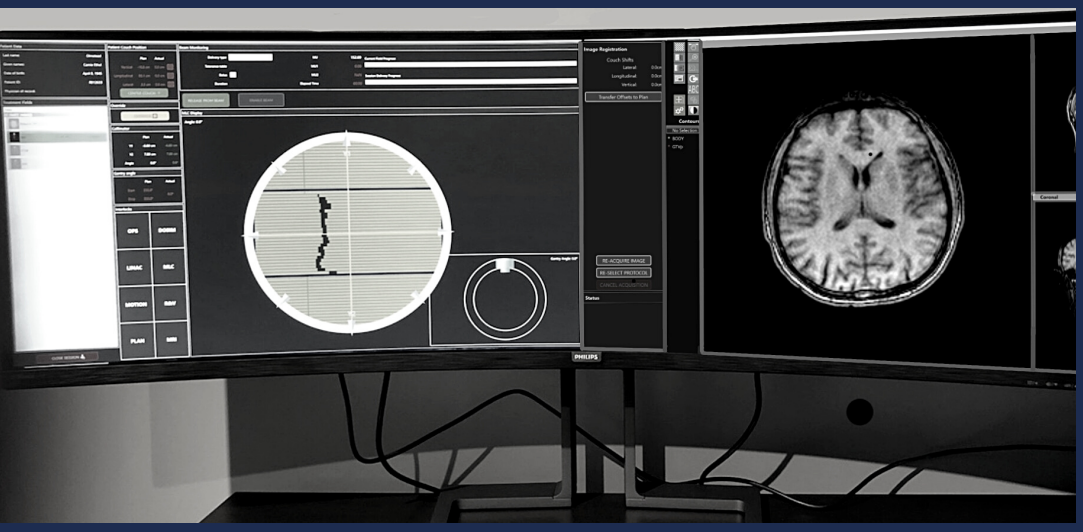

ADVANCED TECHNOLOGY FOR IMPROVED ACCURACY & PRECISION

BUILT SMARTER

2

Simulated adaptive re-planning during glioblastoma radiotherapy on a combination MRI-Linear accelerator.

Beatriz Guevara[1,2], Kaylie Cullison[1,2], Danilo Maziero[2], Gregory Azzam[2], Marcela De La Fuente[3], Karen Brown[2], Alessandro Valderrama[2], Jessica Meshman[2], Adrian Breto[2], Eric Mellon[1,2]

[1]Department of Biomedical Engineering,University of Miami, Miami, FL, USA. [2]Department of Radiation Oncology, Sylvester Comprehensive Cancer Center, University of Miami Miller School of Medicine, Miami, FL, USA. [3]Department of Neurology Sylvester Comprehensive Cancer Center, University of Miami Miller School of Medicine, Miami, FL, USA

Abstract

Purpose/Background: Cognitive function after brain radiation therapy (RT) is correlated with radiation doses to the normal brain and hippocampi. During RT of glioblastoma (GBM), daily MRI by combination MRI-linear accelerator (MRI-Linac) systems has demonstrated significant anatomic changes due to evolving post-surgical cavity shrinkage. Therefore, this study aimed to investigate if adaptive planning to the shrinking target could reduce normal brain RT dose with the goal of improving post-RT function.

Methods: We evaluated a cohort of 10 GBM patients treated on a 0.35T MRI-Linac with a prescription of 60 Gy delivered in 30 fractions over six weeks without adaptation ("static plan") with concurrent temozolomide. The patients analyzed were those with gross total or near total resection (n=21) and shrinking cavity during RT (47%). Resection cavity (RC), planning target volume (a total of 2.3 cm of expansions from RC), and organs at risk were contoured weekly on the set-up scans provided by the MRI-Linac. Six weekly plans were created per patient. The weekly plans were then summed, and the accumulated simulated adaptive dose was compared to the dose from the static plans.

Results: Reductions in radiation dose to uninvolved hippocampi (maximum and mean) and brain (mean) were observed for weekly adaptive plans. Dose (Gy) to hippocampi were for static vs. weekly adaptive plans: max 42.5±8.2 vs. 33.2±7.5 ($p=0.005$) and mean 24.2±6.3 vs 18.7±5.5 ($p=0.001$). The mean brain dose was 19.9±1.3 for static planning vs. 17.7±1.5 for weekly adaptive planning ($p=0.001$).

Conclusion: Weekly adaptive re-planning has the potential to spare the brain and hippocampi from high-dose radiation, likely reducing the neurocognitive side effects of RT. Future studies should evaluate the impact of MRI-guided adaptive RT on neurocognition.

3

Evaluation of using commercial deep learning-based MR image reconstruction for synthetic CT generation in radiation therapy of prostate cancer patients

Senior Medical Physicist Christian Jamtheim Gustafsson PhD[1,2], Senior Medical Physicist Jonas Scherman PhD[1], Senior radiation oncologist Adalsteinn Gunnlaugsson PhD[1], Professor Lars E Olsson PhD[2]

[1]Skåne University Hospital, Dept Haematology, Oncology and Radiation Physics, Lund, Sweden. [2]Department of Translational Sciences, Medical Radiation Physics, Lund University, Malmö, Sweden

Abstract

Purpose

The use of deep learning (DL) for magnetic resonance image (MRI) reconstruction has been implemented by several commercial vendors and allows for both image noise- and scan time reduction. This can provide several benefits when using MRI for radiotherapy planning purposes. The aim of this work was 1) to evaluate the compatibility between a commercial DL MRI reconstruction product and a commercial synthetic CT (sCT) generation software and 2) to quantitatively assess the Hounsfield (HU) and dosimetric integrity of sCT created from such MR images.

Methods

Twenty-four prostate cancer patients were prescribed ultra hypofractionated radiation therapy (RT) with 42.7 Gy, 7 fractions, in a clinical MRI-only treatment workflow using a General Electric (GE, Chicago, USA) 3T Architect MRI system together with a lightweight AIR receiver coil. Within the clinical MRI acquisition protocol, a large field of view (LFOV) T2 weighted MRI image volume was acquired for sCT conversion (sCT_orig) using Spectronic MRI planner v.2.4.14 (Spectronic Medical AB, Helsingborg, Sweden). This sCT generation has previously been validated against CT. In parallel, the MRI raw data from the LFOV acquisition was used in DL MRI reconstruction using the GE Air Recon DL product for host version MR29.1 and a new MRI image volume was created together with a corresponding sCT (sCT_DL).

To assess differences in HU values between sCT_orig and sCT_DL, HU differences outside the patient, in fat, muscle, spongy bone and compact bone was analyzed. To assess RT dose differences in target and organs at risk, clinical RT structures except the body structure were copied from the sCT_orig to the sCT_DL, clinical treatment plan was transferred with the same number of monitor units and dose was recalculated on sCT_DL. The created sCT_DL was visually inspected and the body volume for all sCT were calculated.

Results

HU difference outside the patient, in fat, muscle, spongy bone and compact bone had a mean absolute error (± 1 STD) in the cohort of 1.5±0.4, 1.5±0.3, 1.2±0.4, 4.9±1.1 and 7.4±2.2 HU (n=24), respectively. The mean dose differences for body, femoral heads, bladder, rectum, CTV and PTV were all positive and below 0.06 Gy (Fig.1, 0.1% difference, n=23). The sCT_DLs had a visually excepted appearance and the sCT body volume were larger for all patients but three compared to sCT_orig, with a median cohort difference of 15 cm3 (spread in cohort body volume was 11603-21542 cm3).

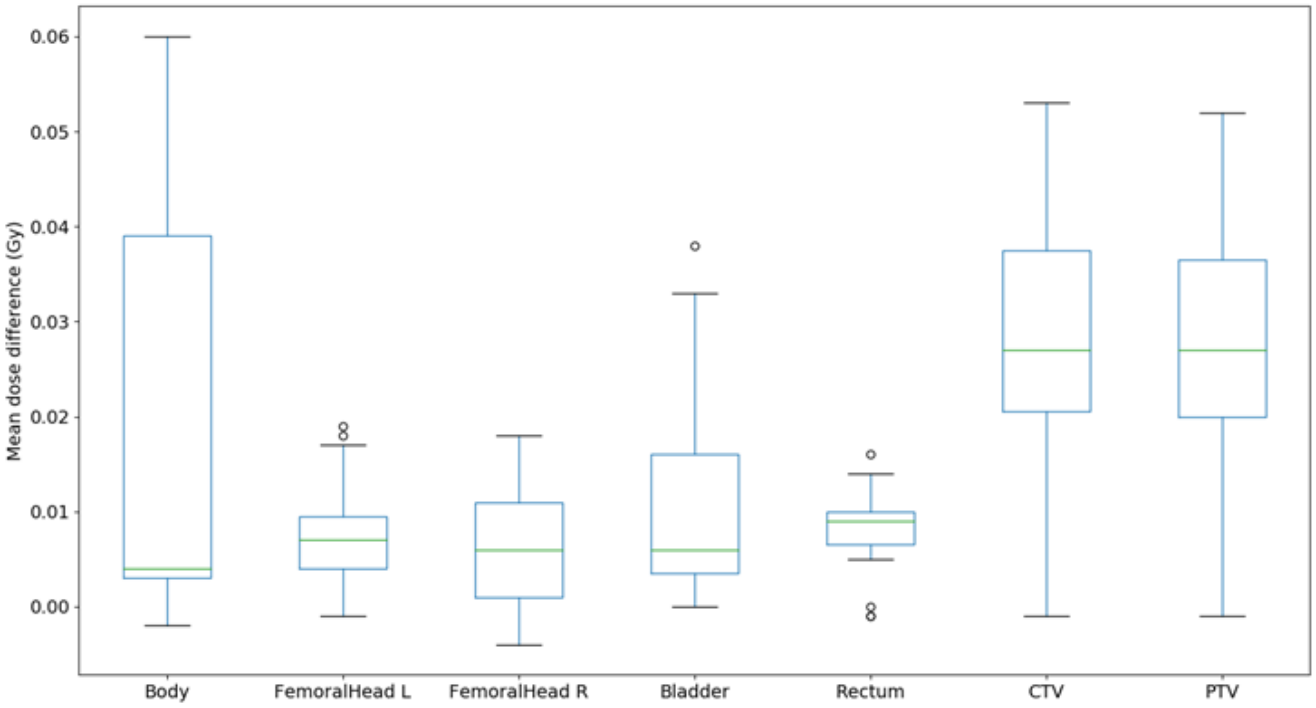

Fig.1. Mean dose differences for OAR and target (sCT_orig-sCT_DL). A small systematic shift towards a positive dose difference was observed. This was probably due to the larger sCT_DL volume, providing more radiation attenuation.

Conclusion

DL MRI reconstruction was suitable for sCT generation with only minor, clinically negligible, differences in HU and calculated dose. The differences were systematic and probably due to the larger size of the sCT_DL, which was believed to be the effect of improved MRI image quality, thereby affecting the sCT generation.

4

Deep learning cycleGAN MRI-only synthetic-CT generation for pelvis, brain and head and neck cancers

Dr David Bird PhD[1], Dr Richard Speight PhD[1], Sebastian Andersson[2], Jenny Wingqvist[2], Dr Basher Al-Qaisieh PhD[1]
[1]Leeds Cancer Centre, Leeds, United Kingdom. [2]RaySearch AB, Stockholm, Sweden

Abstract

Purpose: MRI-only planning relies on dosimetrically accurate synthetic-CT (sCT) generation to allow dose calculation from the MRI. A small number of commercial sCT generation products are available for pelvic and brain cancer sites, however they often rely on bulk density assignment techniques or are software packages attached to specific MRI scanners - meaning they cannot be easily implemented without purchasing a specific scanner. Deep learning approaches have potential for accurate use, but limited validation of commercial products has been undertaken.

A commercial deep-learning, cycle generative-adversarial-network (cycleGAN) sCT generation model, which can be applied through the TPS for enhanced utility, has been developed. Here we validated the dosimetric accuracy of sCTs generated using this algorithm for pelvic, brain and head and neck (H&N) cancer sites using variable MRI data from multiple scanners.

Methods: The commercial cycle-GAN sCT algorithm was used to train individual sCT generation models, using paired MRI-CT patient data, for the following input MRI sequences; T2-SPACE for pelvis, T1 with gadolinium (T1Gd) and FLAIR for brain and T1 for H&N. The pelvis, brain and H&N models were trained on 46 rectum data sets, 36 data sets and 57 data sets respectively.

The pelvis, brain and H&N model validation cohorts were comprised of 49 (16 anus, 28 rectum and 5 prostate), 30 and 25 patients respectively. All MRI scans were deformably registered to the planning CT prior to use and sCTs were generated using the appropriate model & MRI sequence (pelvis, brain or H&N). H&N patient externals and PTVs were cropped to the above the shoulders on CT and MRI as the field of view did not extend beyond this point. VMAT treatment plans, following local clinical planning protocols, were calculated on the planning CTs and recalculated on sCTs. HU and dosimetric differences were assessed between CT and sCTs, including DVH differences to target volumes and organs at risk as a percentage of the prescription dose (for example, PTV D95% dose difference) and gamma index (2%/2mm).

Results: Mean absolute error (MAE) HU differences were; 48.8 HU (pelvis), 118 (FLAIR brain), 126 (T1Gd brain) and 124 HU (H&N). Mean primary PTV D95% dose differences for all sites were <0.2 % (range: -0.9 to 1.0%). Mean 2%/2mm and 1%/1mm gamma indexes for all sites were > 99.6 % (min: 95.3 %) and >97.3 % (min: 80.1 %) respectively. For all OARs for all sites, mean dose differences were <0.4 %.

Conclusion: Generated sCTs had excellent dosimetric accuracy for pelvic T2-SPACE sequences, brain FLAIR and T1Gd sequences and H&N T1 sequences. The commercial deep-learning cycle-GAN model is a feasible method for sCT generation with high clinical utility due to its ability to use variable input data from multiple scanners and sequences.

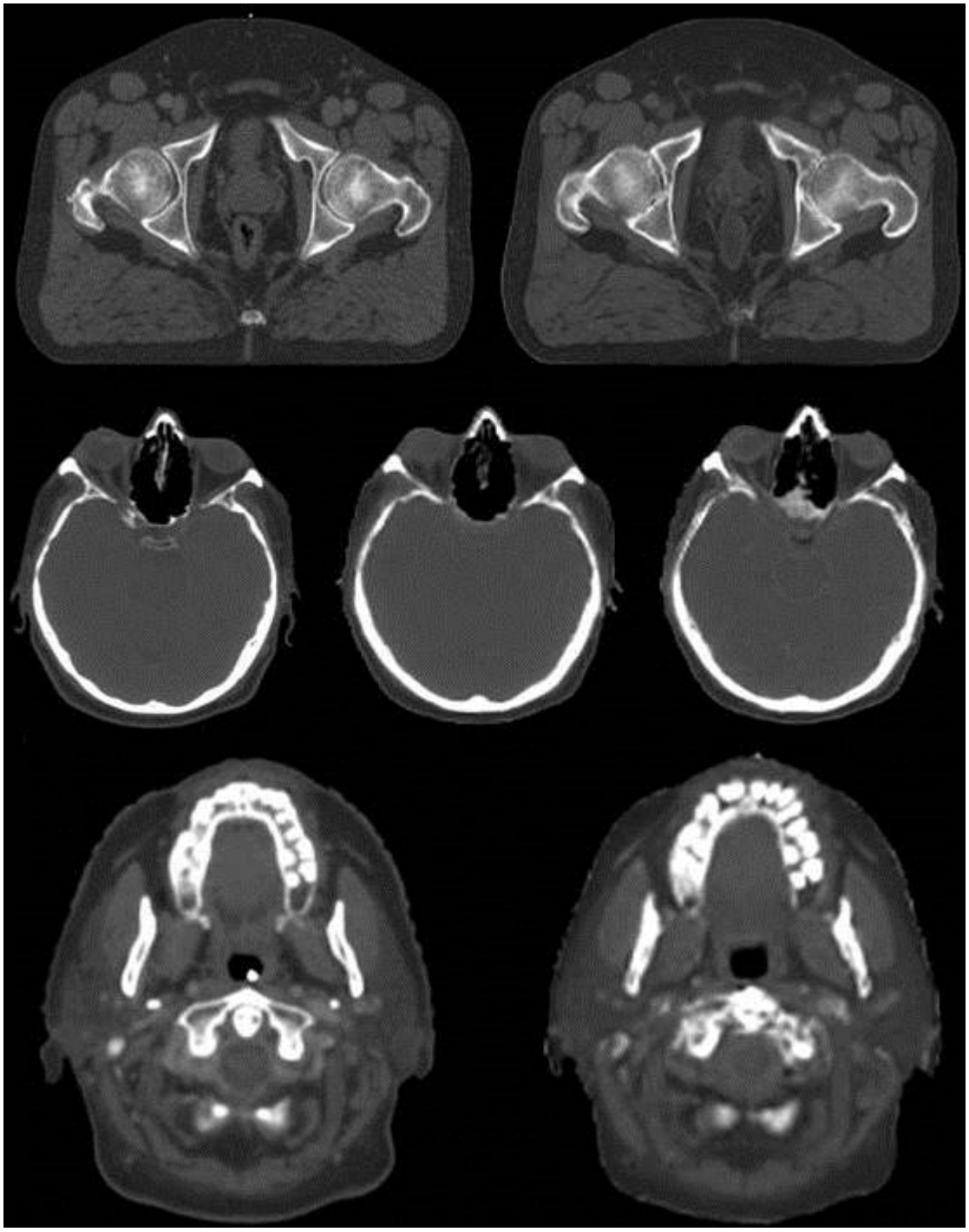

Figure 1. Axial slices of a pelvis CT and T2-SPACE sCT (top), brain cancer CT , T1Gd sCT and FLAIR sCT (middle) and H&N cancer CT and T1 sCT (bottom).

5

Deep learning-based Auto-Segmentation on Multi-sequence MRI for MR-guided Adaptive Radiation Therapy in Abdomen

Dr. Asma Amjad PhD[1], Dr. Jiaofeng Xu PhD[2], Dan Thill MS[2], Nicole O'Connell[2], Dr. Beth Erickson MD[1], Dr. William Hall MD[1], Dr. Eric Paulson PhD[1], Dr. Allen. X Li PhD[1]

[1]Department of Radiation Oncology, Medical College of Wisconsin, Miwaukee, WI, USA. [2]Elekta Inc, St. Charles, MO, USA

Abstract

Purpose: Rapid and consistent delineation of abdominal structures on daily MRI is generally challenging in MR-guided adaptive radiation therapy (MRgART) for abdominal tumors. Furthermore, the factor that the daily MRI is commonly acquired with multiple sequences in abdomen adds more complexity. To address this problem, we developed 2 deep learning-base auto-segmentation (DLAS) models to segment abdominal organs quickly on multi-machine, multi-sequence MRI.

Methods: 2 DLAS models were developed using a modified U-net, ResUnet3D, with end-to-end mapping, and were trained using 85 daily MRI sets acquired on a 1.5T MR-Linac (MRL-model) and 71 MRI sets acquired on a 3T MR-simulation (MRSim-model) for patients with abdominal tumors. For the MRL-model training, MRI data from 3 motion averaged sequences derived from 4D MRI, Fast Field Echo (FFE), Balanced Turbo Field Echo (BTFE) and TFE sequences, were used, while for the MRSim-model, 4 sequences, 2 T1 DXON_water and T2 HASTE/HASTE50% sequences, were used. All MRIs were pre-processed using bias field correction and intensity standardization and strategies including data pre-processing, z-normalization, and data augmentation were employed in training. For all MRIs, ground truth contours were created manually and randomly checked by two experienced oncologists. Each model was trained for 11 abdominal organs. Performance of the obtained models was evaluated on an Intel Xeon CPU (2.4 GHz, 64GB RAM) hardware using unique test datasets in terms of dice similarity coefficient (DSC), mean distance to agreement (MDA) and time efficiency.

Results: The time required to generate all organs on an MRI image set was < 20 seconds. Average DSC and MDA for the 11 organs from the MR-SIM and MRL models is shown in Table 1. DLAS of the two models on representative axial slices for the 4 image sequences is shown in Figure 1. Improved accuracy, especially for duodenum, pancreas and bowels is observed with the MRSim-model, and is attributed to the enhanced contrast, limited image artifact and homogeneous intensity seen in these images, when compared to the MRL images. Pancreas, duodenum, and small bowel segmentation with the MRL model is found to be dependent on image contrast.

Conclusion: We have developed deep learning auto-segmentation models based on multi-machine, multi-sequence MRI for abdominal organs. The model can be improved with further development using large datasets and may be integrated into MRgART workflow for fast re-contouring of abdominal organs.

Table 1: Accuracy metrics for the MRL and MR-Sim DLAS model.

		Aorta	Duodenum	Kidneys	Liver	Pancreas	Spinalcord	Spleen	Stomach	Bowel_large	Bowel_small
MR-SIM	DSC	0.94	0.75	0.96/0.96	0.97	0.81	0.8	0.97	0.93	0.85	0.84
	MDA/mm	0.75	2.92	0.9/0.84	1.24	2.01	1.21	0.97	1.5	3.85	2.81
MRL	DSC	0.92	0.66	0.91/0.91	0.94	0.6	0.84	0.92	0.88	0.74	0.73
	MDA/mm	0.65	6.2	1.58/1.13	1.7	6	0.87	1.3	1.8	6.4	5.5

Figure 1: Auto-segmentation on multi-contrast, multi-sequence MRI. Shaded contours are ground truth, line contours are DLAS.

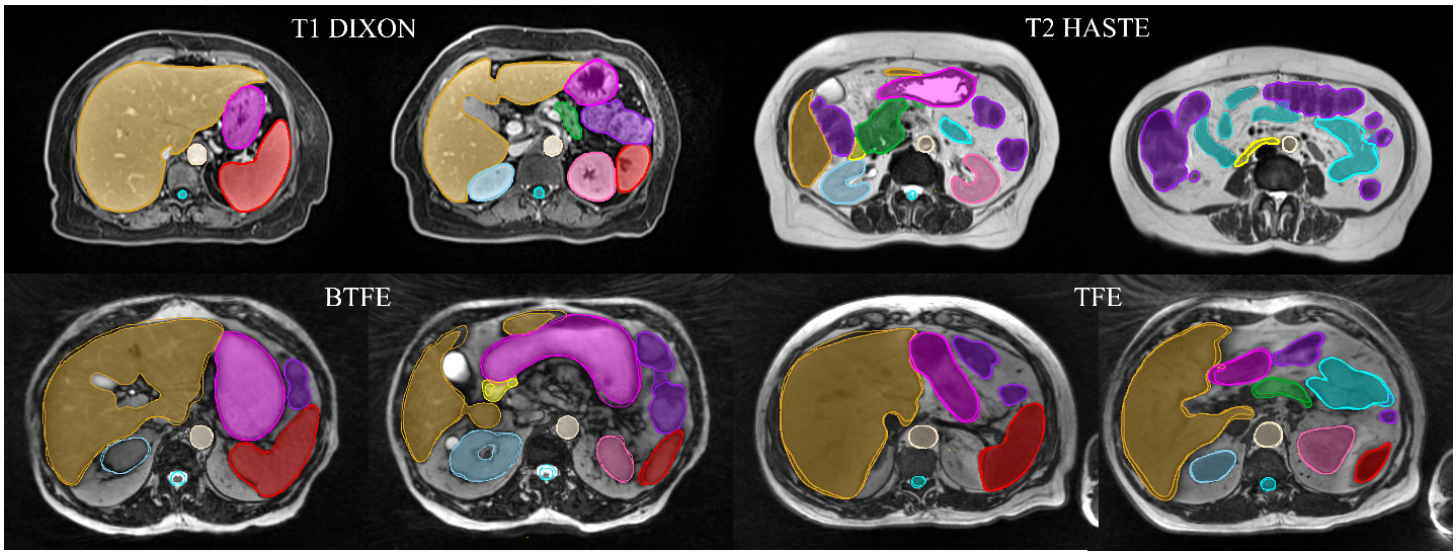

6

MR-Adaptive Hypofractionated Radiation Therapy for Locally Advanced Non-Small Cell Lung Cancer: Benefits and Challenges Learned from a Prospective Clinical Trial.

Gregory Vlacich MD, PhD[1], Shahed Badiyan MD[1], Aadel Chaudhuri MD, PhD[1], Clifford Robinson MD[1], Saiama Waqar MD[1], Olga Green PhD[1,2], Pamela Samson MD[1]

[1]Washington University in St. Louis, St. Louis, MO, USA. [2]Varian Medical Systems, Palo Alto, CA, USA

Abstract

Purpose:

In the definitive management of locally advanced non-small cell lung cancer (LA-NSCLC), the use of hypofractionation to improve locoregional control (LRC) over conventional fractionation has been limited by anticipated and observed toxicity with traditional technology. In a first-of-its-kind prospective study, we evaluate the role of magnetic resonance (MR)-guidance and intermittent plan adaptation to enhance the safety and feasibility of hypofractionation with concurrent chemotherapy. We present our preliminary experience using MR-guided technology in the treatment of LA-NSCLC.

Methods:

Patients with inoperable stage IIB, IIIA and select IIIB and IIIC NSCLC were enrolled on an ongoing single institution Phase II clinical trial with safety lead-in. As of October 2022, 20 of 27 planned patients have completed radiation therapy to 60 Gy in 15 fractions with concurrent carboplatin/paclitaxel followed by consolidation durvalumab. Radiation therapy was delivered using the Viewray MRIdian 0.35 T MR-linear accelerator and adaptive treatments were performed at fractions 6, 9, and 12. Both CT and MR were performed for initial simulation, but adaptation was performed online with only an MR dataset for adaptive planning.

Results:

There have been numerous distinct benefits to the use of MR-guided radiotherapy in the delivery of hypofractionated radiation for LA-NSCLC. These include the following: (1) improved soft tissue delineation with MR to better define and thus spare OARs such as esophagus, (2) ability to perform accurate respiratory gating on the primary tumor to further limit lung dose by tracking the tumor directly in real time, and (3) ability to adapt treatment in a relatively timely fashion to account for tumor response and/or relative OAR locations to help mitigate toxicity to mediastinal structures with hypofractionation. Considerable challenges, however, do exist when using this modality for LA-NSCLC, in particular for the treatment of often larger and discontinuous targets. The general lack of familiarity with thoracic MR imaging can lead to more uncertainty with tumor and OAR delineation, though this impact can diminish with more individual exposure and experience with MR planning. Adaptive treatments require considerable patient compliance, machine time, and staff and physician time with larger volumes for LA-NSCLC and preliminary analysis among our patient cohort suggests that even intermittent adaptation has limited benefit from a dosimetric standpoint. Finally, the absence of 4D capability with the MR imaging for adaptive treatments can result in uncertainty in the respiratory movement of non-gated targets if there has been changes in target size from initial simulation. Prospective modifications to the treatment workflow have helped to address some difficulties, but significant obstacles remain.

Conclusion:

The use of MR-guided radiation therapy in the treatment of LA-NSCLC with hypofractionated radiation can allow for unique approaches to help enhance target coverage or OAR sparing but accompanying limitations should be thoughtfully addressed to ensure appropriate allocation of workflow time and resources and safeguard adequate and accurate dosimetry.

7

Commissioning and image distortion analysis of an in-beam MR prototype system for MR-integrated proton therapy

Sergej Schneider[1,2,3], Aswin Hoffmann[1,3,4]

[1]OncoRay – National Center for Radiation Research in Oncology, Faculty of Medicine and University Hospital Carl Gustav Carus, Technische Universität Dresden, Helmholtz-Zentrum Dresden-Rossendorf, Dresden, Germany. [2]Technische Universität Dresden, Carl Gustav Carus Faculty of Medicine, Dresden, Germany. [3]Institute of Radiooncology-OncoRay, Helmholtz-Zentrum Dresden-Rossendorf, Dresden, Germany. [4]Department of Radiotherapy and Radiation Oncology, Faculty of Medicine and University Hospital Carl Gustav Carus, Technische Universität Dresden, Dresden, Germany

Abstract

Purpose: The physical integration of MRI with proton therapy (PT) into an MR-integrated PT (MRiPT) system is expected to improve the targeting accuracy of PT. The purpose of this project was to develop a prototype system combining an open low-field MRI scanner with a horizontal proton pencil beam scanning (PBS) beamline to enable a first MRiPT treatment. This contribution presents first results of the installation and commissioning of the MRiPT system where the positioning reproducibility, magnet shimming performance and image quality were analyzed.

Methods: The MRiPT setup consists of an open C-shaped 0.32 T MRI scanner (MRJ3300, ASG Superconductors SpA, Genoa, Italy) positioned in close proximity to the nozzle of a horizontal proton PBS beamline (Figure 1). The MRI scanner was encased in a custom-designed compact aluminum Faraday cabin. At the location of the PBS nozzle beam exit window, a beam entrance opening was incorporated in the wall of the RF cabin, which was sealed by a thin (20 µm) aluminum foil to combine high RF attenuation and small lateral spreading of the traversing proton beam. The scanner and RF cabin were mounted on top of an air-cushion-based transport platform, allowing the mobile system to be accurately positioned in the beam path exiting the nozzle. The maneuvering of the scanner into treatment position was thereby visually guided based on room lasers that intersect at the beam isocenter and project onto the outer wall of the cabin. The magnet was shimmed in treatment position close to ferromagnetic components of the nozzle where the B0 field homogeneity was measured using a magnetic field camera (MFC3045, Metrolab Technology SA, Geneva, Switzerland). During commissioning the MR image quality was assessed using the ACR Small MRI Phantom (American College of Radiology, Virginia, USA) with T1w multi-slice spin echo (SE) imaging, and the CIRS MRI-LINAC Dynamic Phantom (Computerized Imaging Reference Systems Inc., Norfolk, USA) with a T1w 3D spoiled gradient echo (GFE) pulse sequence dedicated for patient positioning verification in the MRiPT workflow. The CIRS phantom allowed for image distortion analysis based on 4 grid layers consisting of 5 concentric circles around the MR isocenter.

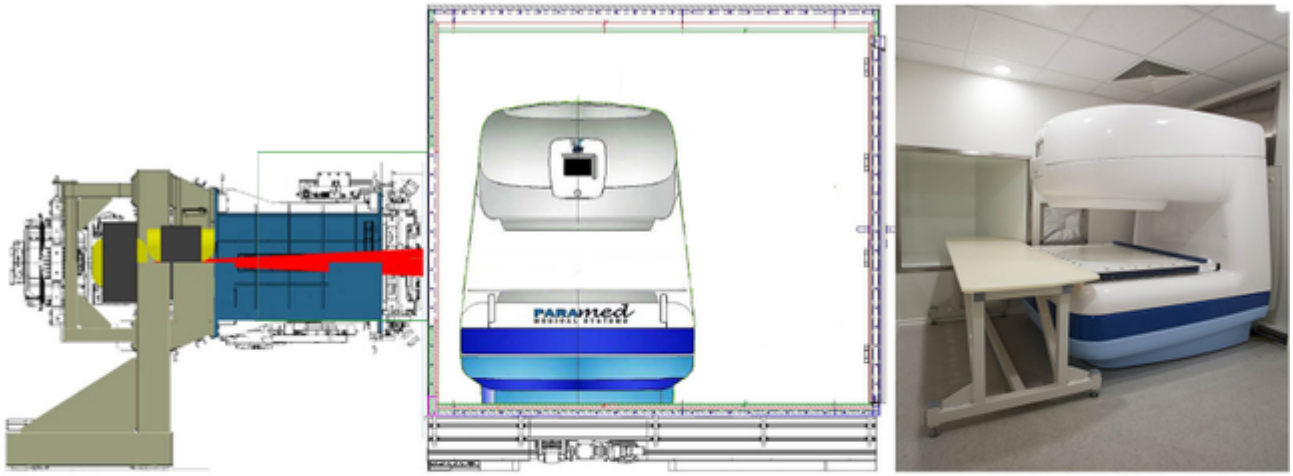

Figure 1. [a] Schematic of the MRiPT system, comprising a 0.32 T MRI scanner positioned inside a Faraday cabin on a mobile transport platform in front of the nozzle of a horizontal proton PBS beamline. [b] In-beam MRI scanner with a customized patient couch inside the Faraday cabin.

Results: The positioning accuracy and precision of the in-beam MRI system were below 1 mm. A peak-to-peak B0 field homogeneity of 43 ppm over a 25 cm diameter spherical volume (DSV) around the MR isocenter was achieved during shimming. The ACR QA protocol revealed a signal-to-noise ratio (SNR) of >80 and a geometric distortion of <1.5 mm over a 10 cm DSV around the MR isocenter. The CIRS phantom measurement showed that geometric distortion increased up to <8 mm at 20 cm DSV and <11 mm at 24 cm DSV.

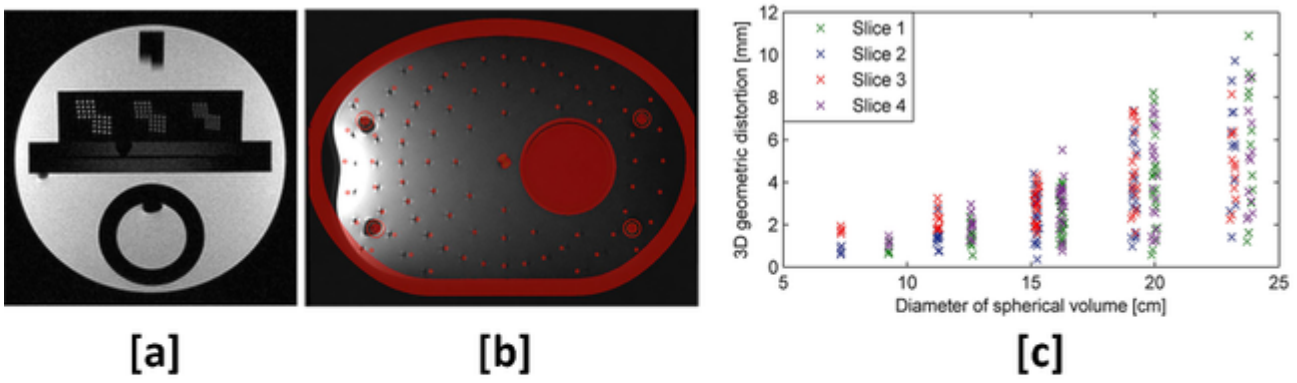

Figure 2. [a] T1w SE image of the Small ACR Phantom acquired in treatment position showing high SNR, high signal contrast and low geometric distortion. [b] 3D GFE image of CIRS large grid phantom overlayed with registered CT image (red) as reference for distortion measurement. [c] Distortion for 3D GFE sequence measured with CIRS phantom for different distances from MR isocenter along DSV.

Conclusion: A 0.32 T in-beam MRI scanner was successfully installed and commissioned in front of a horizontal proton PBS beamline in preparation for the development of a first prototype MRiPT system. Large volume image distortion measurements showed the necessity for geometric distortion correction algorithms in order to enable an accurate image guidance in a future MRiPT treatment.

8

Online adaptive MRI-guided radiotherapy for primary tumor and lymph node boosting in rectal cancer

Chavelli Kensen MSc, Anja Betgen, Lisa Wiersema, Femke P. Peters MD. PhD, Mutamba T. Kayembe PhD, Prof. Corrie A.M. Marijnen MD. PhD, Prof. Uulke A. Van der Heide PhD, Tomas M. Janssen PhD
The Netherlands Cancer Institute, Amsterdam, Netherlands

Abstract

Purpose. The purpose of this study was to evaluate motion and required treatment margins of the primary gross tumor volume (GTV_{prim}) and suspected mesorectal lymph nodes (GTV_{ln}) for two online adaptive MRI-guided strategies.

Methods. Thirty patients were treated on a 1.5T MR-Linac. GTV_{prim} and GTV_{ln} were delineated on T2-weighted images acquired for adaptation (MRI_{adapt}) and post irradiation (MRI_{post}) of 5 treatment fractions per patient. For Adapt to Shape (ATS), due to daily redelineation of the structures and plan optimization, the intrafraction motion of both structures between MRI_{adapt} and MRI_{post} is the primary remaining uncertainty. Therefore, to determine the treatment margins, the intrafraction center of gravity (COG) displacement of the GTV_{prim} and GTV_{ln} on MRI_{post} relative to MRI_{adapt} was determined for each fraction in left-right (LR), anterior-posterior (AP) and cranial-caudal (CC) direction. The effective intrafraction displacement during treatment was then estimated at ¾ of the total displacement. For Adapt to Position (ATP), translations of both GTV_{ln} and GTV_{prim} were corrected each fraction through an isocenter shift based on the position of GTV_{prim}. of a reference scan of a previous fraction. Due to the relative motion of GTV_{ln} with respect to GTV_{prim}, this results in a discrepancy between the planned position and actual position of GTVln, at the start of the treatment fraction. We therefore determined the interfraction motion of the COG GTV_{ln} w.r.t. the COG of GTV_{prim} on MRI_{adapt}, using the anatomy of fraction 1 as reference. The group mean (GM), systematic (Σ) and random (σ) error were calculated for each strategy and treatment margins were calculated using the Van Herk recipe. Significance of a non-zero GM was determined using a t-test.

Results. The results of the intrafraction motion of GTV_{prim} and GTV_{ln}, and interfraction motion of GTV_{ln} w.r.t. GTV_{prim} are shown in Table 1. A significant GM was found in AP direction for GTV_{prim} and AP & CC direction for GTV_{ln} as a result of time-dependent varying bladderfilling. The resulting margins were 1.7 mm (LR), 4.7 mm (CC) and 4.4 mm anterior and 5.6 mm posterior (AP) for GTV_{prim} and 3.5 mm (95% CI 3.4-3.7) LR, 4.4 mm (95% CI 4.2-4.6) cranial, 3.7 mm (95% CI 3.5-3.9) caudal, 5.3 mm (95% CI 5.1-5.5) anterior and 5.7 mm (95% CI 5.5-5.9) posterior for GTV_{ln}. The GM and Σ of the interfraction displacement of GTV_{ln} w.r.t. GTV_{prim} were largest in CC direction and σ were similar in all directions. The estimated margin was 10.6 mm (95% CI 10.3-10.8) in LR direction), 17.6 mm (95% CI 16.9-18.2) in CC direction and 11.4 mm (95% CI 10.9 -12.0) in AP.

Conclusion. Our study shows that ATP with a primary match on GTV_{prim} requires large margins for the mesorectal lymph nodes. ATS results in smaller margins and is preferred for this purpose. Based on this and other studies, GTV_{prim} margins should be in the range of 5-6 mm caudal-cranial and AP, with potentially smaller left-right margins (2-3 mm). For GTV_{ln} margins should be in the range of 3-4 mm (LR), 3-5 mm (CC) and 5-6 mm (AP).

Table 1: Summary information for GTV_{ln} (n=30) and GTV_{prim} (n=30) inter- and intrafraction motion calculated using van Herk PTV margin recipe. Translations are shown in left-right (LR), anterior-posterior (AP) and cranial-caudal (CC) directions. Positive values indicate motion in Right, Cranial, and Posterior direction. GM = mean of patient motion, Σ = systematic error, σ = random error

	Target volume		LR (mm)	CC (mm)	AP (mm)
Intrafraction displacement	**GTV_{prim} (n=30)**	GM	0.0	0.2	-1.2*
		Σ	0.6	1.7	1.6
		σ	1.0	1.4	1.3
		M_{PTV}	**1.7**	**4.7**	**4.4 (anterior) 5.6 (posterior)**
	GTV_{ln} (n=30)**	GM	-0.1 (-0.2 - 0)	0.7 (0.7 - 0.8)	-0.4 (-0.5 - -0.3)
		Σ	1.2 (1.2 - 1.3)	1.1 (1.0 - 1.3)	1.8 (1.8 - 1.9)
		σ	1.4 (1.3 - 1.5)	1.9 (1.8 - 1.9)	1.7 (1.6 - 1.8)
		M_{PTV}	**3.5 (3.4-3.7)**	**3.7 (3.5-3.9 |caudal) 4.4 (4.2-4.6 |cranial)**	**5.3 (5.1-5.5 |anterior) 5.7 (5.5-5.9 |posterior)**
Interfraction displacement w.r.t. GTV_{prim}	**GTV_{ln} (n=30)****	GM	0.4 (0.3 - 0.6)	0.8 (0.6 - 1.0)	-0.1 (-0.3 - 0.1)
		Σ	3.4 (3.3 - 3.5)	6.1 (5.8 - 6.3)	3.4 (3.2 - 3.6)
		σ	3.2 (3.1 - 3.3)	3.4 (3.3 - 3.5)	3.8 (3.7 - 4.0)
		M_{PTV}	**10.6 (10.3-10.8)**	**17.6 (16.9-18.2)**	**11.4 (10.9-12.0)**

*$p<0.001$

**Mean (95% CI) are reported based on 20 resampled datasets

9

Developing an intelligent solution for accurate MRI-based Stereotactic Radiosurgery

Dr Niloofar Yousefi Moteghaed Ph.D.[1,2], Dr Ali Fatemi Ardekani Ph.D.[3,2], Dr Daniel Low Ph.D.[4], Dr Dan Ruan Ph.D.[4], Dr Ahmad Mostaar Ph.D.[1]

[1]Department of Medical Physics and Biomedical Engineering, School of Medicine, Shahid Beheshti University of Medical Sciences, Tehran, Tehran, Iran, Islamic Republic of. [2]SpinTecx.LLC, Jackson, Mississippi, USA. [3]Department of Physics, Jackson State University, Jackson, Mississippi, USA. [4]Department of Radiation Oncology, University of California Los Angeles, Los Angeles, California, USA

Abstract

Purpose: Poor MRI image quality, including image noise, motion artifacts, and patient-specific geometrical distortion, are challenges for MRI-based brain stereotactic radiosurgery (SRS),. This work aims to develop a deep learning-based solution to improve MRI image quality for accurate SRS.

Method: We used an ensemble of deep convolutional auto-encoders (CAEC) and pix2pix Generative Adversarial Network (pix2pix-GAN) to propose an Auto-Encoder Generative Adversarial Network. The auto-encoder is a trained network to predict the uncorrupted data as its output from the artifact-ridden MRI dataset. We used the output of the AEC as the pre-model of the GAN network to generate fake images because the training procedure of a generator without a pre-model was too broad, and it generated poor results. The final output is referred to as “Modified” images. We trained our network using routine T1w and T2w MRI images of twenty-five brain tumor patients. We applied a binary head mask, Histogram matching to standardize image intensities from different MRI machines, and customized filters for contrast adjustment and sharpening reducing unwanted structure or inhomogeneity, such as noise or bias, to generate “ideal” images. We generated about 6000 2D slices of MRI images with synthetically added noise at the 10-20% level and motion artifacts at the moderate to high level to generate “artifact-ridden” images. The training and evaluation of the models were conducted on 5000 pairs of the "ideal" and "artifact-ridden" MRI images. The remaining 1000 images were used as synthetically unseen tests to evaluate the algorithm and find the best model. The quantitative analyses of the model between ideal, modified, and artifact-ridden MRI images were based on statistical measurements using five-fold cross-validation. Furthermore, to determine the generalization ability of the obtained model on “real motion” or “noise affected data," we performed the analysis of the no-reference image quality assessment such as Naturalness Image Quality Evaluator (NIQE), Blind Image Spatial Quality Evaluator (BRISQUE), and Perception-based Image Quality Evaluator (PIQE) score for five randomly selected patients.

Results: (Table 1) statistics on the entire head and regions of interest (ROIs) on artifact-ridden test data. **Figure 1** indicates visual analyses of the model on entire images and ROI. **Figure 2.** Results of patients with real noise and motion. The smallest (better quality) NIQE, BRISQUE, and PIQE score among five patients after correction were 6.9, 46.3, and 80.15 for T1W and 6.6, 46.6, and 74.12 for T2W images, respectively.

Conclusion: Our DL network improves MR images quality

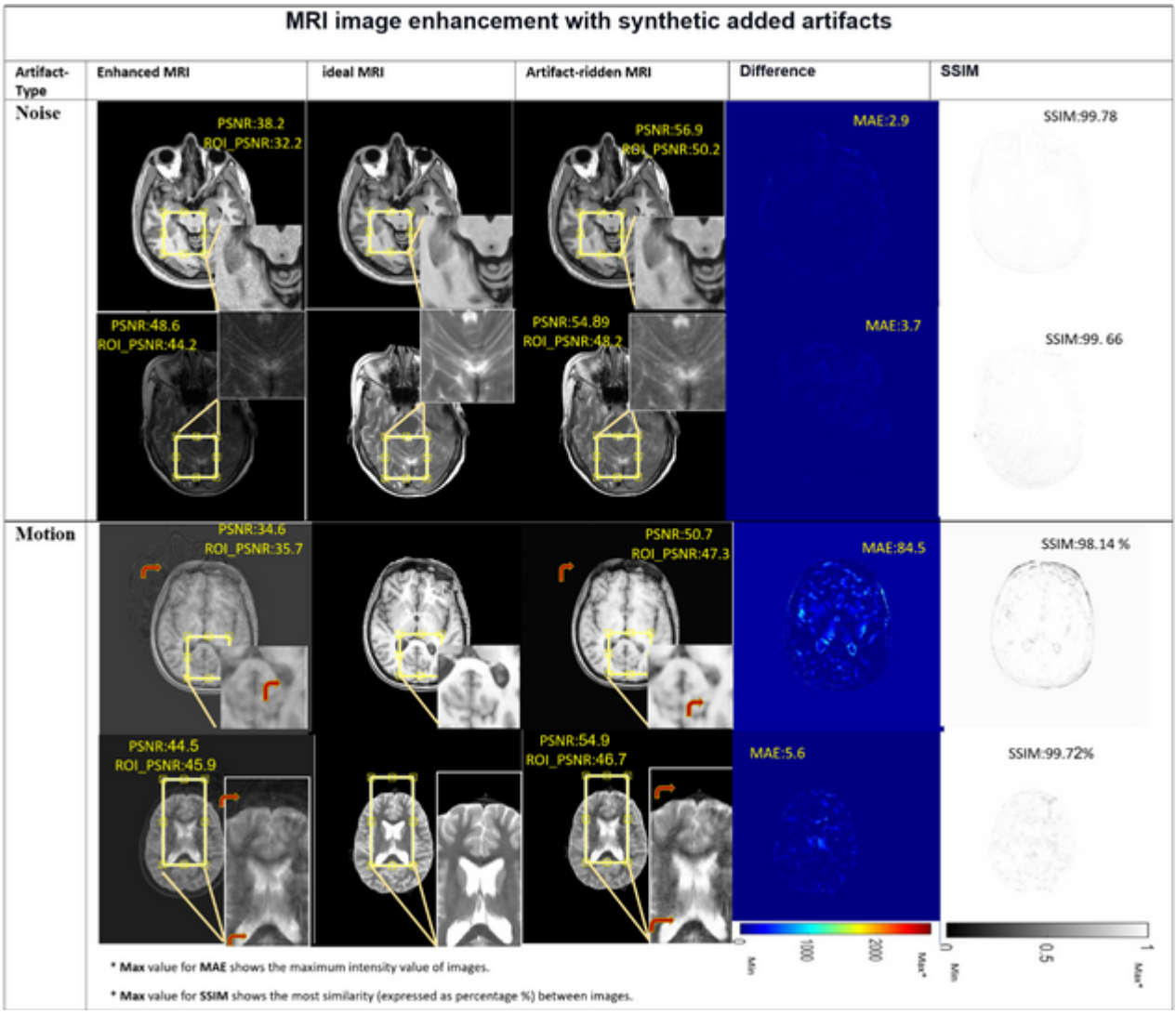

Figure 1: Comparison of "Modified " and "artifact-ridden" images with ideal images from different slices for T1W and T2W MR images by proposed DL mode

Statistical Measurements (Average ± SD) on Synthetic test data						
Artifact type	MRI-sequence	MAE	RMSD	ROI-PSNR	Total PSNR	SSIM %
Noise	T1w	20.48±2.7	88.25±3.9	58.00±0.4	54.77±0.5	99.70±0.02
	T2w	39.48±1.6	128.6±2.2	54.88±0.17	50.49±0.1	99.32±0.01
Motion	T1w	26.63 ±3.9	121.21±2.47	55.48±0.19	52.71±0.36	99.47±0.018
	T2w	25.24±5.05	135.83±4.6	54.49±0.34	49.29±0.31	99.29±0.04

Table 1: Statistical Measurements of "Modified" images with "ideal" images.

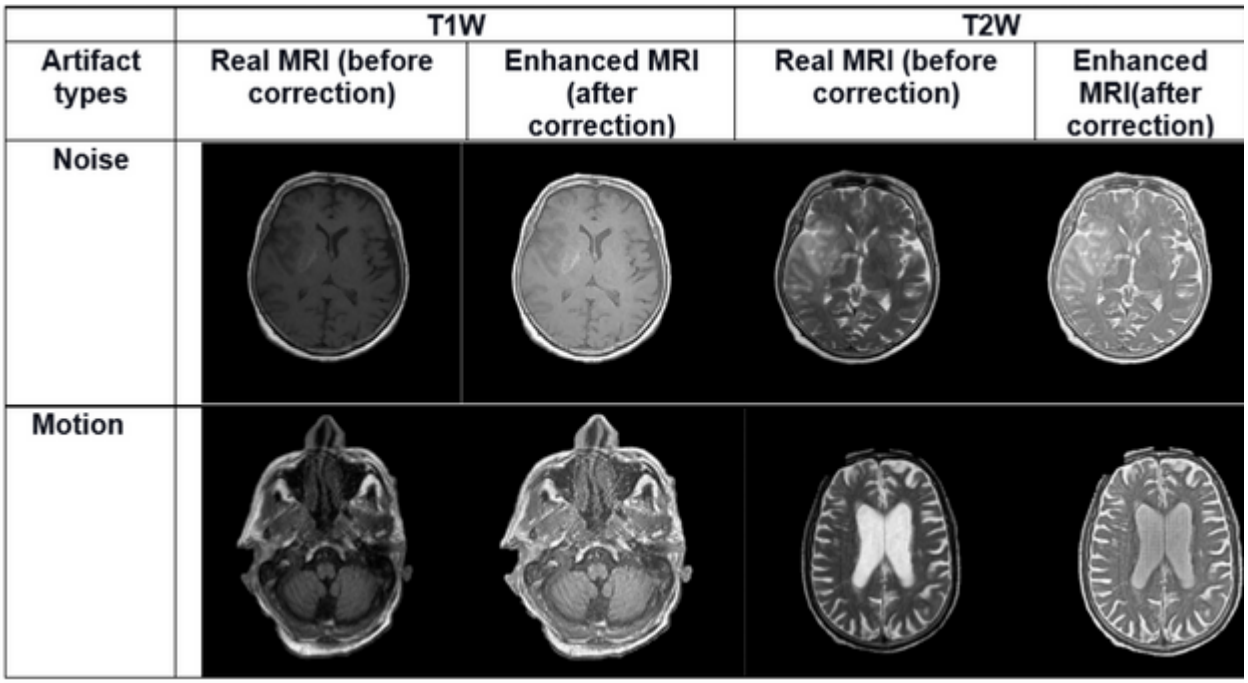

Figure 2: Result of selected patients

10

The Challenge of Model-Based B_0 Compensation in 0.35 T MRI-Linac During Gantry Rotation

H Michael Gach PhD[1], Austen Curcuru MS[1], Shanti Marasini PhD[1], Deshan Yang PhD[2], Taeho Kim PhD[1]
[1]Washington University in St Louis, St Louis, MO, USA. [2]Duke University, Durham, NC, USA

Abstract

Introduction: The ViewRay MRIdian 0.35 T MRI-Linac has a source-to-isocenter distance of 90 cm that requires the use of passive magnetic shielding in the gantry. The magnetic shielding causes B_0 fluctuations that depend on the velocity and position of the gantry. The B_0 fluctuations cause severe image artifacts and imaging isocenter shifts that can affect tumor tracking.

Currently, B_0 variations can be corrected for a stationary gantry during Step and Shoot treatment using a lookup-table method in which the B_0 offsets are measured at various gantry angles (e.g., 15° intervals) in a phantom and interpolated to cover the range of gantry angles. The transmitter and receiver frequencies are appropriately updated at each treatment gantry angle. The gantry angle is provided to the pulse sequence by the Linac's motion controller. However, the current B_0 correction method will not work with MRI-guided arc therapy in which the gantry rotates continuously while the beam is irradiating.

Methods: The center frequency (B_0) offset was measured at a rate of 7.4 frames/s using a free induction decay (FID) navigator integrated into a sagittal 2D balanced steady-state free precession (bSSFP) sequence. Data was acquired using a 24 cm diameter spherical phantom with the gantry of the 0.35 T MRI-Linac rotated both clockwise and counterclockwise for full (~360°) and partial (~180° and ~30°) continuous rotations. The body coil was used for transmission and reception. The center frequency offset was calculated from the time derivative of the FID phase. A sinusoidal model of the center frequency offset was constructed that addressed the long time-constant eddy current associated with the gantry interaction with the cryostat. The root mean square error (RMSE) between the model fit and data was calculated.

The real-time gantry angles were obtained from the inclinometer via the motion controller. The gantry velocity (speed and rotational direction) was calculated from the gantry angle using: 1) the derivative; and 2) a 10-point moving window slope. The gantry angle and velocity were input to the model to determine if the inclinometer data could be used to minimize the center frequency offsets.

Results: The dynamic B_0 model generally fit the B_0 offsets despite ignoring acceleration/deceleration of the gantry (Figs. 1-2). Table 1 summarizes the results of the model fits to the center frequency offsets. However, the gantry angle signal from the inclinometer appears to be nonlinear and noisy. The results of the model using the gantry angles and, especially, moving window slopes deteriorated with rotational arc angle or time. The results of the model using the derivative of the motion controller gantry angles were not satisfactory (not shown).

Conclusions: Integration of the baseline gantry-dependent B_0 offsets is needed in the model that occur when the gantry is stationary. Jitter in the inclinometer signal prevented an accurate representation of the B_0 fluctuations using the model approach despite using a moving window filter to smooth the nonlinearities. Improvement in the inclinometer signal linearity or signal processing is required.

Table 1. Results of Model Fits (Mean±Standard Deviation)

Variable	Full Rotation (358°)		Half Rotation (179°)		30° Rotation	
	CW (N=2)	CCW (N=2)	CW (N=2)	CCW (N=2)	CW (N=12)	CCW (N=12)
Amplitude (A)	271.25±17.72	306.40±9.34	266.00±12.19	249.31±2.05	260.27±10.30	241.58±16.84
Velocity (°/s)	3.43±.0.00	-3.43±0.00	3.43±0.00	-3.43±0.00	3.43±0.00	-3.43±0.00
Offset Angle (°)	-4.55±1.02	30.42±0.57	-2.42±1.73	31.02±0.85	-0.67±1.21	30.54±0.59
DC Shift (Hz)	6.47±0.56	1.38±0.36	5.49±3.05	2.33±9.23	3.64±6.73	4.35±7.72
Time constant (s)	1.55±0.13	1.17±0.04	1.59±0.10	1.50±0.02	1.66±0.09	1.64±0.13
RMSE (Hz)	13.98±0.03	16.08±0.13	12.49±0.05	11.98±0.48	4.53±0.76	4.10±0.78

N represents the number of data sets used to calculate the means and standard deviations.

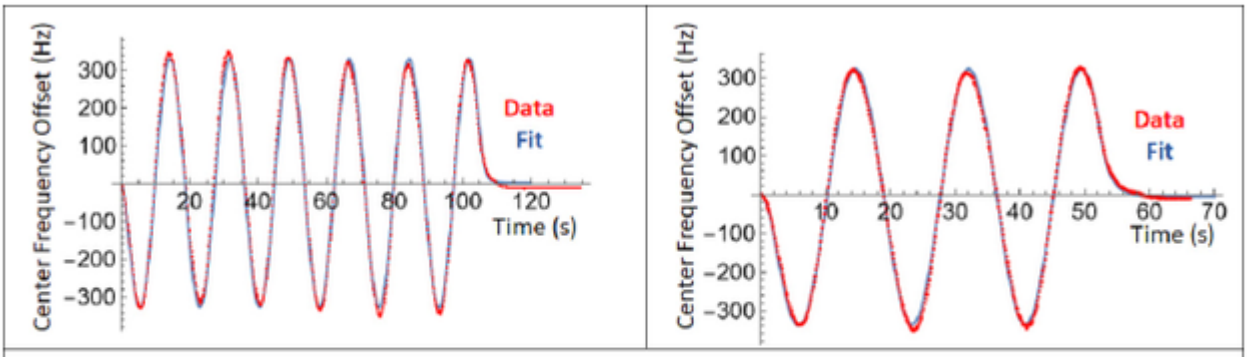

Figure 1. Examples of constant velocity model fit (-) to measured center frequency offsets (•) for counterclockwise gantry rotations from 30° to 33° (Left, rotational arc angle 358°, RMSE=16.17 Hz) and from 210° to 33° (Right, rotational arc angle 177°, RMSE=11.64 Hz)

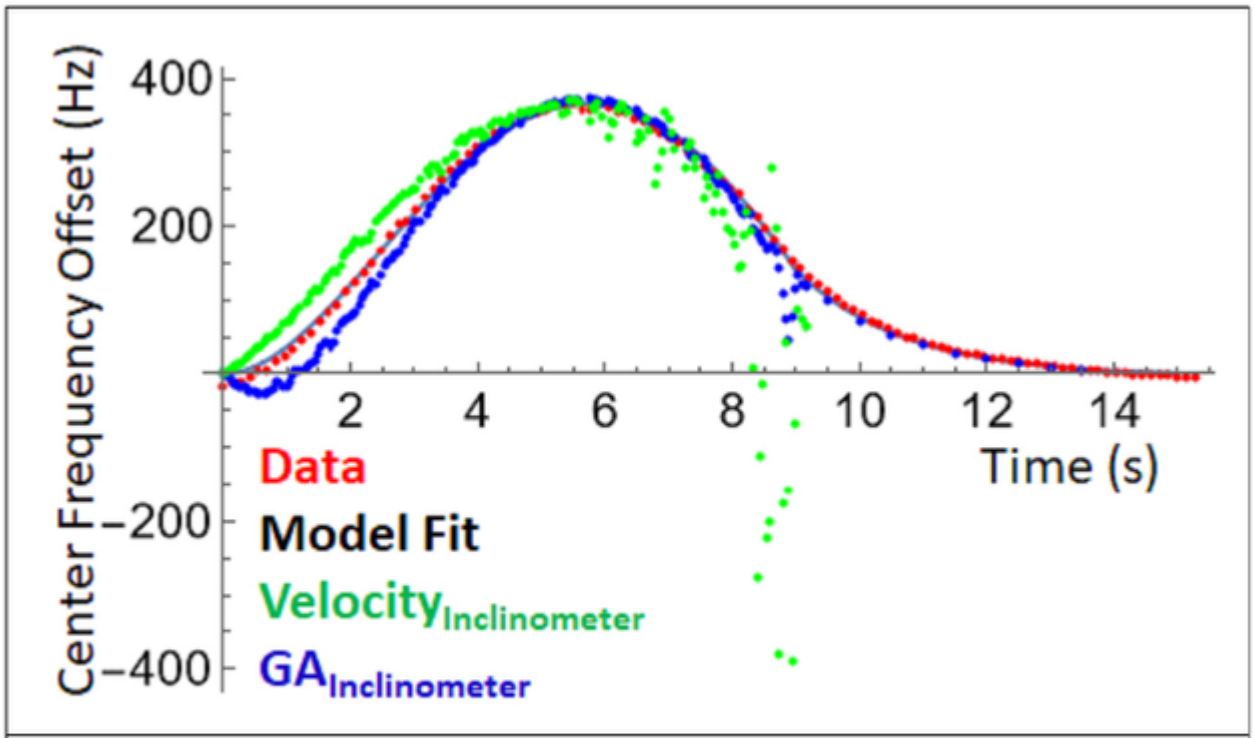

Figure 2. Example of the constant velocity model fit (-) to the measured center frequency offsets (•) for clockwise gantry rotations from 300° to 330° (rotational arc angle 30°, RMSE=5.93). In addition, the outputs of the model using the inclinometer data sliding window velocity and gantry angle (GA) are shown.

11

MR Motion Fingerprinting: A Novel Framework for High-Fidelity Real-Time Volumetric MRI with Sub-Second Latency

Li Feng PhD
Icahn School of Medicine at Mount Sinai, New York, New York, USA

Abstract

Purpose: Rapid real-time 3D MRI with ultralow imaging latency is highly desired for adaptive radiotherapy on an MRI-Linac system. The purpose of this work was to propose a novel framework called MR motion fingerprinting that enables high-fidelity real-time volumetric MRI with an imaging latency below 500 ms.

Methods: MR motion fingerprinting involves two imaging modes performed in two separate stages, one called off-view mode (first stage) and the other one called live-view mode (second stage). The off-view mode employs a new sampling strategy called Navistar for data acquisition (see supporting document for details about Navistar sampling), which embeds 2D motion fingerprints into 3D stack-of-stars golden-angle radial sampling. This mode acquires and reconstructs hundreds of time-resolved real-time 3D images to form a 4D motion database, in which each 3D image is uniquely linked to a 2D motion fingerprint, as shown in Figure 1. The live-view mode only acquires 2D motion fingerprints. At each time point, a live-view motion fingerprint is matched against all the available off-view motion fingerprints. The 3D image associated with the best matched off-view motion fingerprint is then selected for this time point. This two-stage imaging scheme places the typical acquisition and reconstruction burden of MRI to the off-view mode, allowing for real-time, low-latency 3D imaging in the live-view mode. The accuracy and robustness of MR motion fingerprinting was demonstrated in 17 subjects including both volunteers and HCC patients. MR motion fingerprinting was also compared with previous approaches using a similar two-stage imaging scheme but with 1D projection-based motion matching.

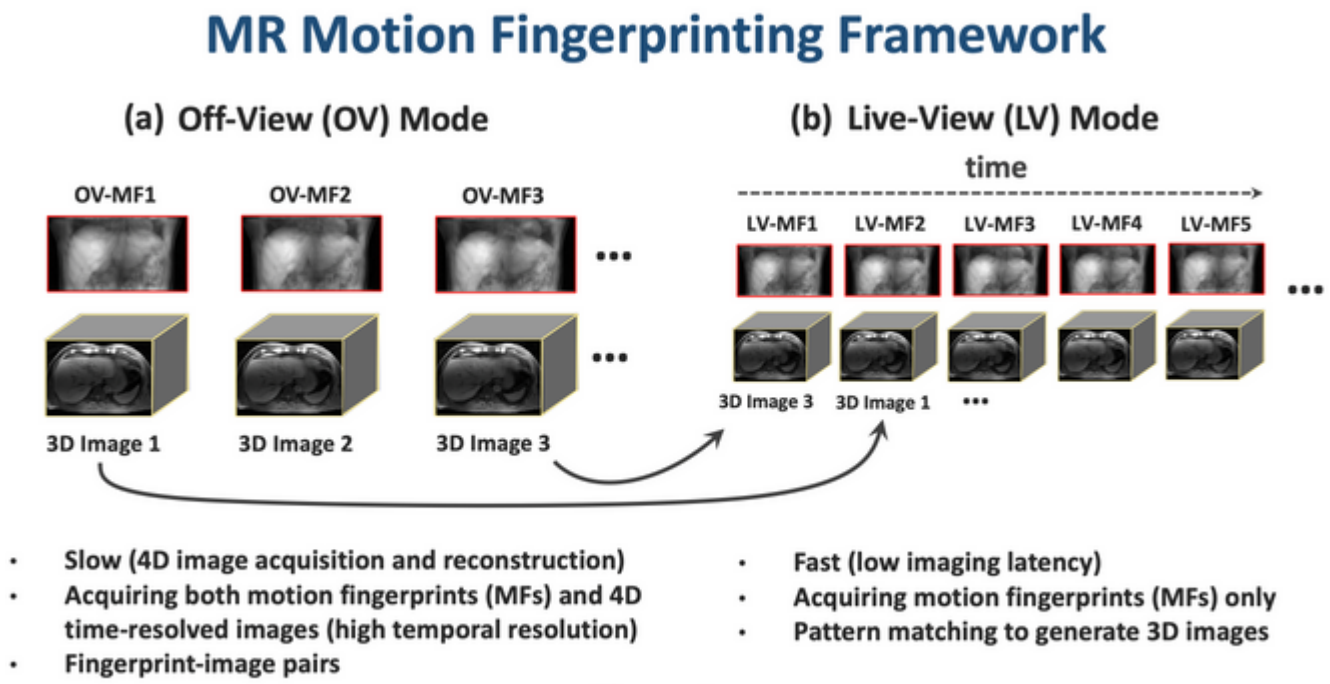

Figure 1

Results: MR motion fingerprinting was able to achieve a total imaging latency of ~0.4s with initial implementation in MATLAB, including time to acquire a 2D motion fingerprint (~0.11s), time to perform 2D FFT on the multicoil 2D motion fingerprint (~0.015s) and time of the motion fingerprinting (matching) process (~0.25-0.3s with parallel computing). Compared to references images, MR motion fingerprinting accurately and efficiently generates real-time volumetric images, as shown in Figure 2. Compared to previous approaches that are based on 1D projection matching, 2D fingerprint

matching is significantly more accurate and more robust towards movement that may occur during treatment (see supporting document for details).

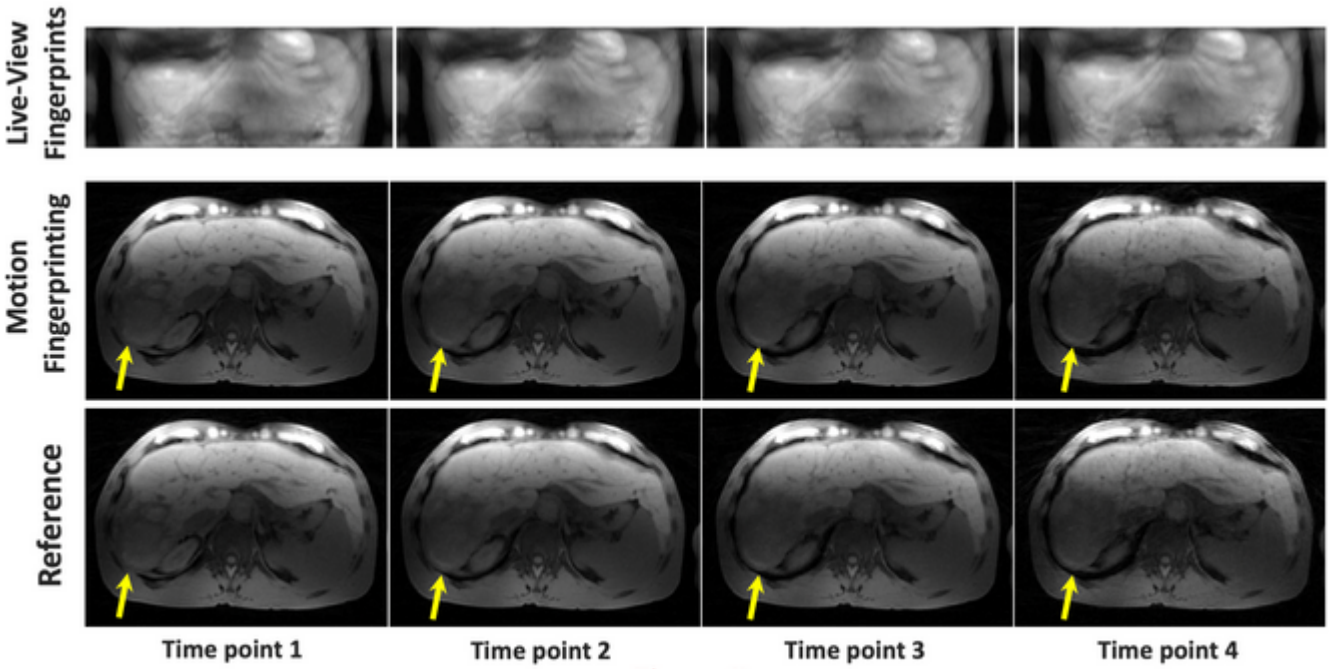

Figure 2

Conclusion: This work proposed a novel framework called MR motion fingerprinting, which enables real-time 3D imaging with low imaging latency and high imaging fidelity. Although the idea of two-stage imaging for real-time volumetric imaging was demonstrated before, prior approaches require motion detection and motion sorting that can lead to various uncertainties, such as sensitivity motion drift and/or body movement. MR fingerprinting proposes several novel components to implement this two-stage imaging framework, including (1) truly real-time 3D MRI acquisition and reconstruction without the need for motion detection and motion-guided data sorting, and (2) a new Navistar sampling strategy that acquires 2D motion fingerprints for more accurate and robust data matching in the live-view mode. These new components ensure that MR motion fingerprinting is robust to motion drift, body movement, and other uncertainties that we must take into consideration for motion management in MRI-Linac applications.

12

An end-to-end deep learning pipeline for radiotherapy auto-segmentation

Mr Wei Zhang Master[1], Dr Cungeng Yang Doctor[1], Mr Zhaocai Chen Master[1], Dr Qichao Zhou Doctor[1], Dr Yanle Hu[2], Dr Zhiwen Liang Doctor[3]

[1]Manteia Technologies Co.,Ltd., Xiamen, China. [2]Mayo Clinic Arizona, Arizona, USA. [3]Tongji Medical College, Huazhong University of Science and Technology, Wuhan, China

Abstract

Purpose

Accurate segmentation of the target and organs-at-risk (OARs) is an essential but time-consuming process in radiotherapy treatment of cancer. Deep learning (DL) has demonstrated great potential in significantly reducing the time required for target and OAR segmentation. But its application in radiotherapy is hindered by availability of DL expertise and IT resources. To expedite translation of DL to clinical radiotherapy practice, we evaluated a collection of data processing and model training methods. By combining these into an efficient pipeline, we provided accessible DL resources to a broad audience with minimal or even no DL and programing expertise.

Method

Our pipeline consists of four modules: data processing, model training, model evaluation, and model deployment. The image standardization and resampling are applied to image with adaptive rules based on image intensity range and distribution characteristics before training starts. During model training, data augmentation is first conducted on the loaded images, and then balanced cropping is performed according to the label area to generate the model input. The network structure does not need to be specified by the user. It is automatically constructed through the gradient feedback and the progress of the loss function during the training process. To ensure the stability of the model training, the variance of the model evolution process is restricted by KL divergence and optimized together with the default loss function. To demonstrate the feasibility of the proposed method, we used 5 open-access CT or MRI image datasets and one in-house MRI dataset, covering a variety of anatomical sites, to evaluate and benchmark the performance.

Results

The default model setting of the proposed method provided the best overall segmentation performance. Dice coefficients were greater than 0.9 for 16.7% of the segmented structures (GTVs or OARs) and greater than 0.8 for 63.3% of the segmented structures. Hausdorff distance 95% were less than 3mm for 26.7% of the segmented structures and less than 10mm for 71.7% of the segmented structures. For OARs, reasonable segmentation performance could be achieved with only 20 training cases. For the GTV, the performance kept improving with increased number of training cases. In extreme cases (e.g., MRgOART), acceptable performance could be achieved with very few training cases.

Conclusions

Our proposed method offers adequate performance with a small training sample size and short model training time. It brings DL to general community of radiotherapy and makes it feasible to build efficient auto-segmentation models that are customized to clinical practice of individual institutions.

Figure: the proposed end-to-end deep learning pipeline

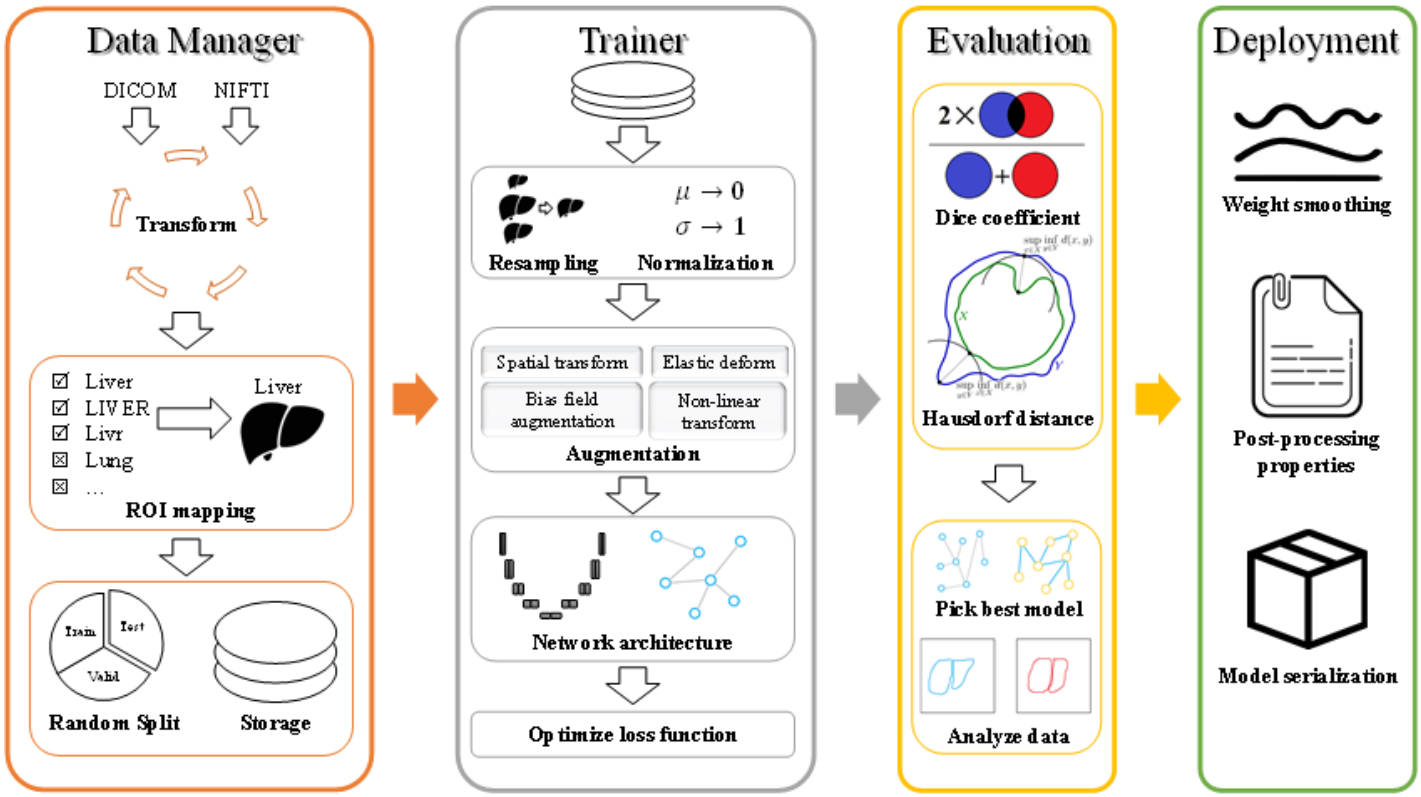
Data Manager
DICOM
NIFTI
Transform
Liver
LIVER
Livr
Lung
...
Liver
ROI mapping
Train
Test
Valid
Random Split
Storage
Trainer
$\mu \to 0$
$\sigma \to 1$
Resampling
Normalization
Spatial transform
Elastic deform
Bias field augmentation
Non-linear transform
Augmentation
Network architecture
Optimize loss function
Evaluation
2×
Dice coefficient
Hausdorf distance
Pick best model
Analyze data
Deployment
Weight smoothing
Post-processing properties
Model serialization

13

Dosimetric and geometric impact of on-patient placement of a lightweight receiver coil in a clinical MRI-only radiotherapy workflow for prostate cancer

Jonas Scherman PhD[1], Sacha af Wetterstedt MSc[1], Emilia Persson PhD[1,2], Lars E. Olsson Professor[1,2], Christian Jamtheim Gustafsson PhD[1,2]

[1]Department of Hematology, Oncology, and Radiation Physics, Lund, Sweden. [2]Department of Translational Medicine, Medical Radiation Physics, Malmö, Sweden

Abstract

For pelvic MRI-only radiotherapy treatment the use of one or multiple coil bridges for the anterior MRI receiver coil is recommended to avoid external patient contour deformation. In this work we evaluate the benefits and effects of light weight coil technology in a pelvic MRI-only radiotherapy workflow, with and without coil bridges. Anatomical and dosimetric quality measures were assessed as well as measurements of signal-to-noise ratio (SNR).

Twenty-one patients, referred to HYPO fractionated (42.7 Gy in 7 fractions) prostate MRI-only radiotherapy, were included in the analysis. Images were acquired with and without coil bridges. MR-Image acquisition was performed on a GE Architect 3.0 T (GE Healthcare, Chicago, Illinois, USA) using the large Anterior Array AIR Coil, revision 6. Two large field of view T2w sequences were used for synthetic CT (sCT) generation and treatment planning. Six fast T2w sequences were acquired throughout the image session to analyze anatomical variations and potential deformation from the on-patient air coil placement by measuring the anatomical change in anterior-posterior (AP) and left-right (LR) direction. SNR was measured both in a homogenous phantom and in vivo. Hounsfield Units (HU) for four different anatomical sites were measured on both sCTs.

For the dosimetric evaluation, a clinically approved treatment plan, created on the sCT with coil bridges, was transferred and recalculated on the rigidly registered sCT volume without the coil bridges. Delineated structures were transferred using the same image registration. The clinical dose metrics for the CTV, PTV, rectum, bladder and penile bulb were analyzed using the clinical structure set.

Anatomical differences after removing the coil bridges were observed with an average decrease in the AP measurement of 1.5 mm and an average LR increase of 2.5 mm, for all patients. No clinically relevant differences were measured for the HU (Figure 1).

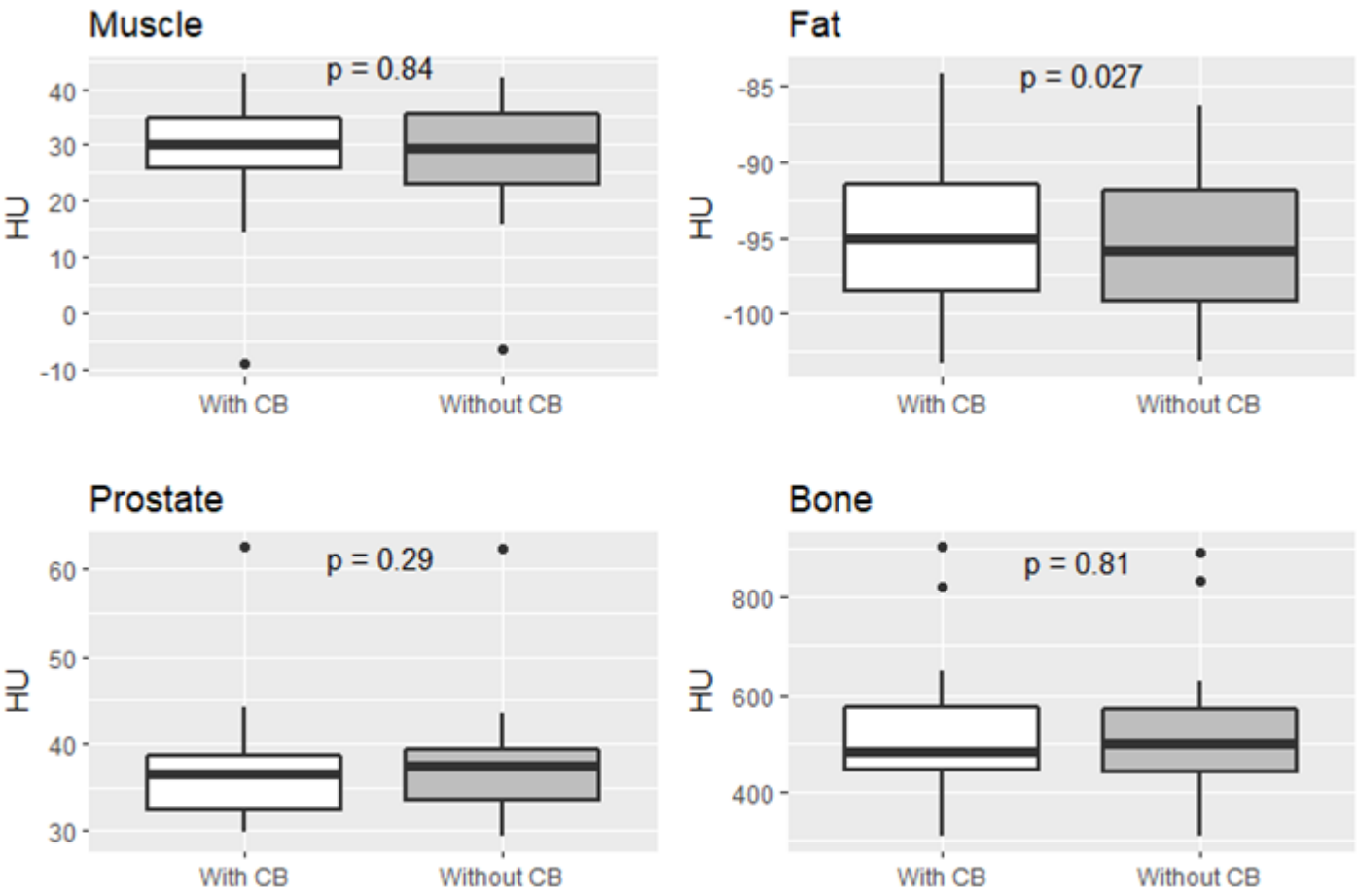

Figure 1: Measured mean Hounsfield Units (HU) in both sCTs (with and without coil bridge (CB)) for the four difference anatomical regions evaluated. Note the difference y-scales.

A statistically significant increase in SNR was seen in vivo (21% median increase). Additionally, dosimetric differences for the target structures were found negligible, but statistically significant. The difference in mean PTV and CTV dose for all patients were 0.19% (p= 0.0042) and 0.16% (p=0.0037) of the prescribed dose, respectively (Figure 2). No differences were observed for the organs at risk, except for the penile bulb.

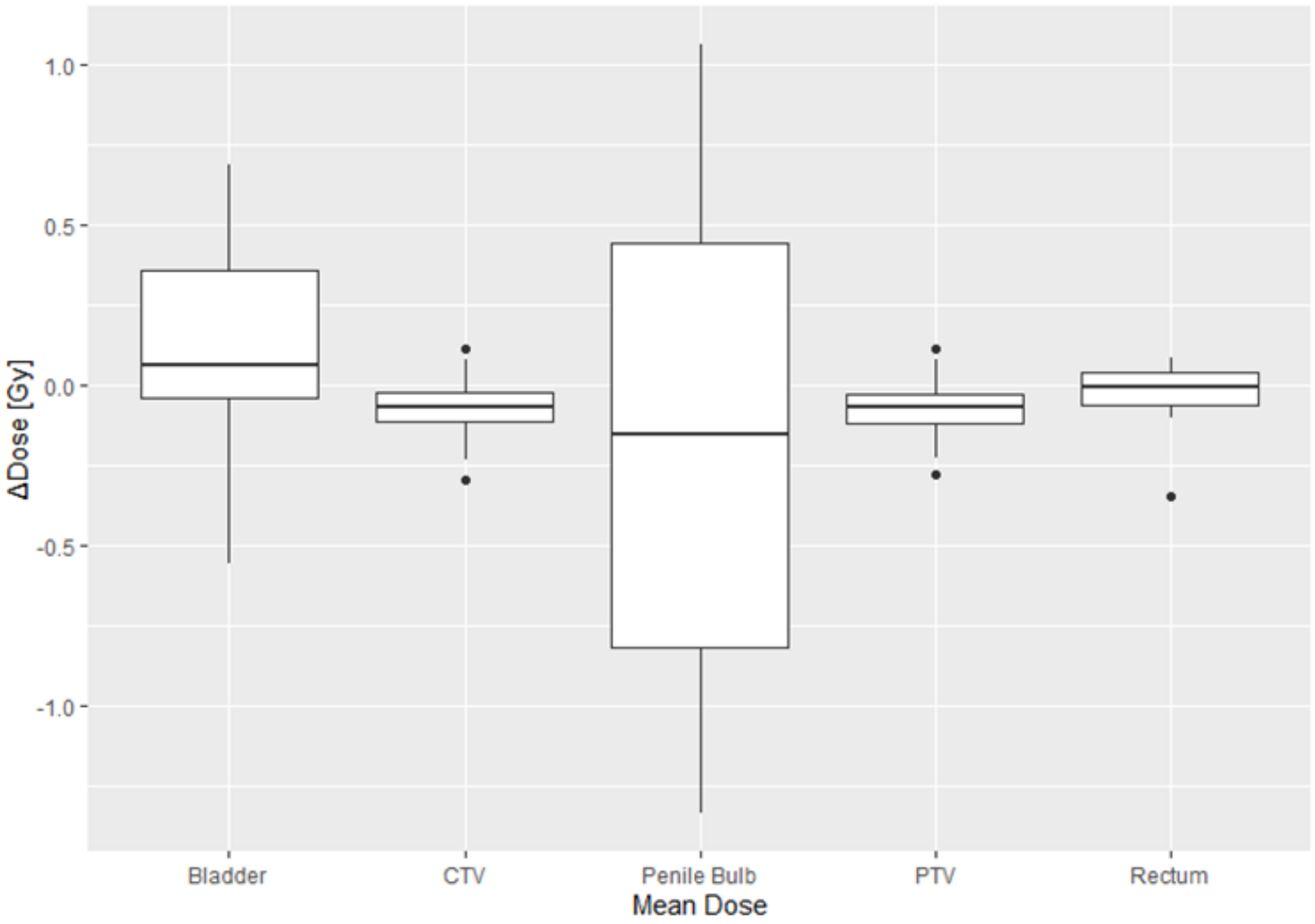

Figure 2: Mean dose differences for all mean dose criteria.

In this work we demonstrated that the anatomical change and the dosimetric differences, originating from scanning with no coil bridges, i.e., on-patient coil placement, were minor. The coil bridges can thereby be removed from the MRI-only workflow with no major concerns. This enables the benefits of easier patient positioning and increased image SNR when using AIR coils.

14

In vivo Microstructure Imaging in Oropharyngeal Squamous Cell Carcinoma

Prof Yue Cao Ph.D.[1], Siamak Nejad Davarani Ph.D.[2,2], Daekeun You Ph.D.[2], Thorsten Feiweier Ph.D.[3], Keith Casper MD[4,4], Ulysses Balis MD[5], Aaron Udager MD. Ph.D.[5], James Balter Ph.D.[2], Michelle Mierzwa MD[2]

[1]Radiation Oncology and Radiology, University of Michigan, Ann Arbor, MI, USA. [2]Radiation Oncology, University of Michigan, Ann Arbor, MI, USA. [3]Siemens Healthcare GmbH, Erlangen, MI, Germany. [4]Otolaryngology, University of Michigan, Ann Arbor, MI, USA. [5]Pathology, University of Michigan, Ann Arbor, MI, USA

Abstract

Purpose: Apparent diffusion coefficient, a bulk measure of effects of tissue microstructures on water diffusion, has limited sensitivity to changes during radiation therapy. To overcome these limitations, we developed in vivo microstructure imaging to measure cancerous microstructure parameters and assess cellular responses to RT.

Methods and Materials: Twenty-seven oropharyngeal cancer patients had MRI scans pre-treatment and 16 had second scans at fraction 10 during RT in treatment position on a 3T scanner (MAGNETOM Skyra, Siemens Healthcare GmbH, Erlangen, Germany). Diffusion weighted images were acquired within 10 minutes using a prototype oscillating gradient spin echo (OGSE) research application with sinusoidal trapezoid diffusion waveforms (Van, MRM 2014) at 50 and 35 Hz and b-values between 0.05 and 1 ms/um^2 and using a pulse gradient spin echo (PGSE) sequence with different diffusion times. Diffusion images were reconstructed with B_0 corrections. To estimate the free diffusion coefficient (D_0), ratio of cell membrane surface area to volume (S/V) and cell membrane permeability (κ) using the short-time limit of the random walk with barriers model (RWBM) (Novikov, 2011), effective diffusion times (t_{eff}) for both OGSE and PGSE were calculated according to Fordham (JMR 1996). The long-time-limit RWBM was used to estimate the bulk diffusion coefficient (D_{inf}). The averaged cell dimension in a image voxel can be estimated as 6V/S according to the RWBM. The parameters in gross tumor volumes (GTVs) defined on post-Gd T1 weighted images were correlated with clinical stages (p16+ clinical stage I-II, p16+ clinical stage III and p16- stage IV non-HPV-associated oral cavity squamous cell carcinomas) using 2-tail Spearman's rank correlation, and their changes from pre-treatment to the 10th fraction of RT were assessed.

Results: Table 1 summarizes pre-treatment averaged(+SEM) microstructures parameters in primary and nodal GTVs of 27 patients. We observed heterogeneous distributions of the microstructure parameters in both primary and nodal GTVs. V/S (proportional to cell dimension) and D_{inf} were significantly correlated with clinical stages ($p<0.02$). For the case with a corresponding tissue sample, *in vivo* estimated cell dimension was 12% greater than the estimation from digital pathological analysis of malignant tissue, within the anticipated tissue shrinkage rate due to fixation (10-15%). Figure 1 shows examples of D_0, V/S and κ maps. Averaged changes of the parameters from pre-RT to 10 fractions of RT were 54% (±41%) for κ, 34%(±14%) for D_{inf}, 14%(±5%) for D_0 and 10%(±5%) for V/S.

Conclusion: It is feasible to acquire diffusion weighted images at short diffusion times using the OGSE sequence on a clinical scanner to estimate microstructure parameters. Cell membrane permeability seems to be most significantly impacted early in RT. These microstructure parameters, with further pathological and clinical validations, may improve tumor delineation and therapy response assessment.

Table 1. Pre-Treatment microstructure parameters of 27 patients

	D_0 (um^2/ms)	V/S(um)	k(um/ms)	D_{inf}(um^2/ms)
primary GTV	2.72±0.50	2.37±0.45	0.058±0.034	0.55±0.26
nodal GTV	2.82±0.58	2.38±0.93	0.070±0.029	0.66±0.28
correlation with clinical	>0.8	<0.015*	>0.7	<0.012*

stages (p value)				

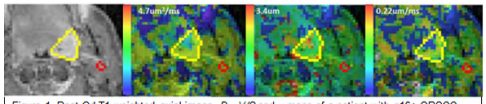

Figure 1. Post-Gd T1 weighted axial image, D_0, V/S and κ maps of a patient with p16+ OPSCC (from left to right). Yellow and red contours denote primary and nodal tumor volumes.

15

MRI Motion Artifact Reduction using 3D Deep Neural Network

Mojtaba Safari M.Sc[1,2], Dr. Daniel Low Ph.D., FAAPM, FASTRO[3], Dr. Ali Fatemi Ph.D., MCCPM, ABMP[4,5], Louis Archambault Ph.D.[1,2]

[1]Département de physique, de génie physique et d'optique, et Centre de recherche sur le cancer, Quebec City, QC, Canada. [2]Service de physique médicale et radioprotection, Centre Intégré de Cancérologie, CHU de Québec – Université Laval et Centre de recherche du CHU de Québec, Quebec City, QC, Canada. [3]Department of Radiation Oncology, University of California Los Angeles, Los Angeles, USA. [4]Department of Physics, Jackson State University, Jackson, USA. [5]Merit Health Central, Department of Radiation Oncology, Gamma Knife Center, Jackson, USA

Abstract

Purpose: Magnetic Resonance Imaging (MRI) image quality can be degraded by motion artifacts. MRI T1 weighted post-contrast sequence is the most often-used structural sequence with a 10.5% prevalence. Prospective motion correction methods require special hardware and sequences that limit their use in routine clinical settings. We proposed a deep-learning network to remove the artifact from MRI T1W post-contrast images.

Methods: We used a publicly available multicenter medical dataset (GLIS-RT, 230 patients) from the Cancer Imaging Archive with different imaging protocols and patients with various brain tumor types to improve our proposed model's generalization. During MRI signal collection, the frequency encoding time is generally short. Therefore, we assumed that the motion artifacts mainly resulted during the phase encoding direction. We simulated motion artifacts by randomly selecting a region of interest within the k-space (Figure 1). The randomly selected k-space lines within the specified areas were randomly displaced along the phase encoding direction. We modeled the displacement with pointwise multiplication in the given direction j ($\in\{x,y,z\}$) by e^{-2ikjt} where *kj* and *t* are the k-space line and the magnitude of the voxel translation, respectively. To restore the image, an Unet with residual layers was employed to minimize the loss between the recovered and the ground truth images. We tested our network on images with low, moderate, and heavy artifacts. Our proposed method was compared with the cycle-GAN network. Finally, our network was tested on real data extracted from the PACS system with real motion artifacts, which were not used in the training step of the network.

Results: The proposed network reduced the normalized mean squared error (NMSE) of the unseen data and improved the peak signal-to-noise ratio (PSNR) as well as the structural similarity index (SSIM) substantially for all the tested artifact levels. After the motion artifact correction, NMSE was reduced from 25.32±3.44% to 6.21±1.31% (p-value << 0.05), PSNR increased from 13.36±0.6to 37.47±0.96 dB (p-value << 0.005). Moreover, SSIM improved after motion correction from 0.66± 0.04 to 0.97± 0.01 (p-value << 0.005). Our network could remove the motion artifact from real data with motion artifact (Figure 2). Cycle-GAN reduced NMSE from 25.32±3.44% to 8.63±2.79% (p-value << 0.05) and increased PSNR and SSIM from 13.36±0.6to 32.54±0.82 (p-value << 0.05) dB, 0.66± 0.04 to 0.90± 0.02 (p-value << 0.05), respectively.

Conclusion: Motion artifacts were successfully modeled and removed. Removing the motion artifacts from data will possibly improve the MRI-guided radiation therapy by improving the accuracy and precision of the target and organ at risk delineations.

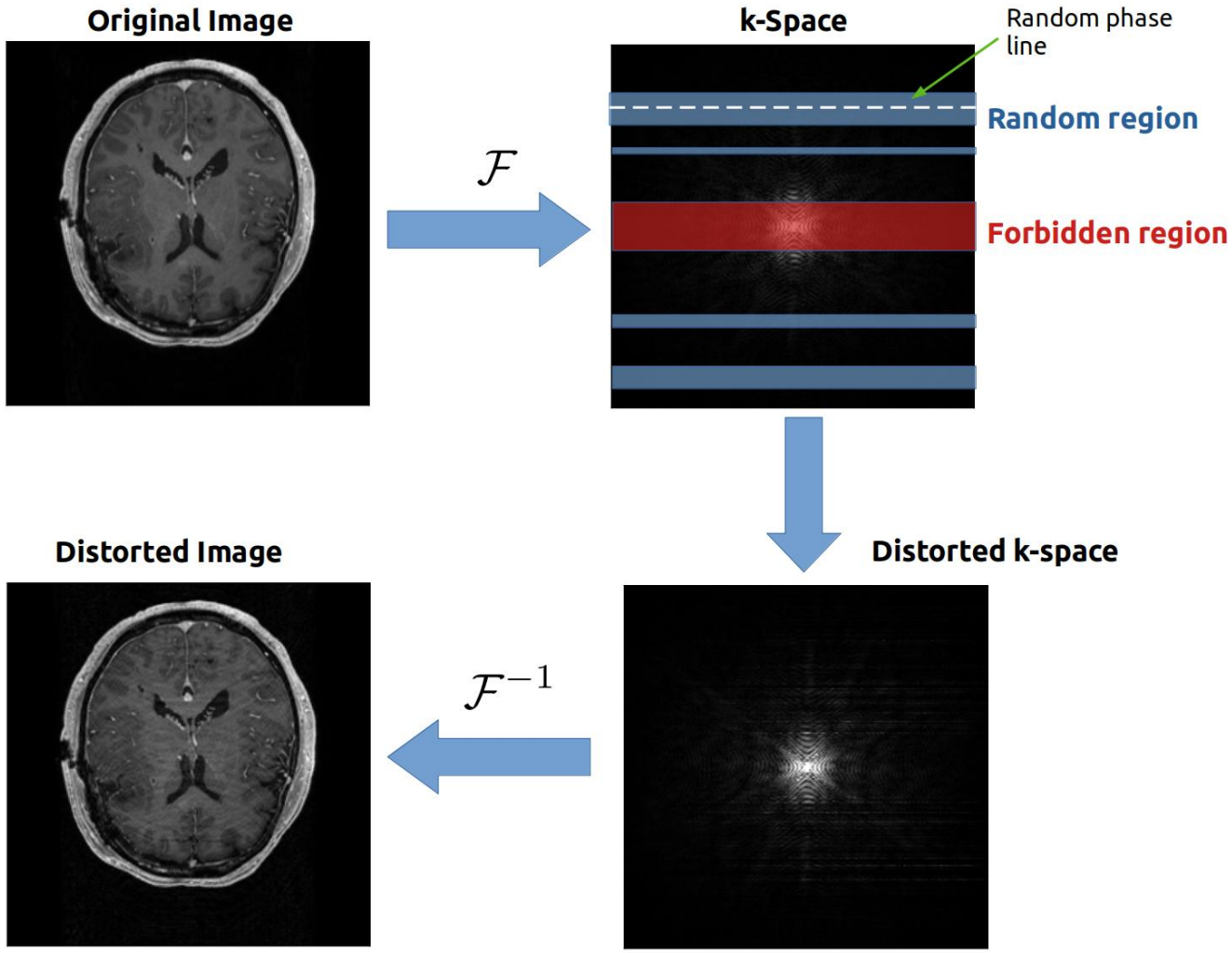

Figure 1. Flow chart of motion artifact simulation.

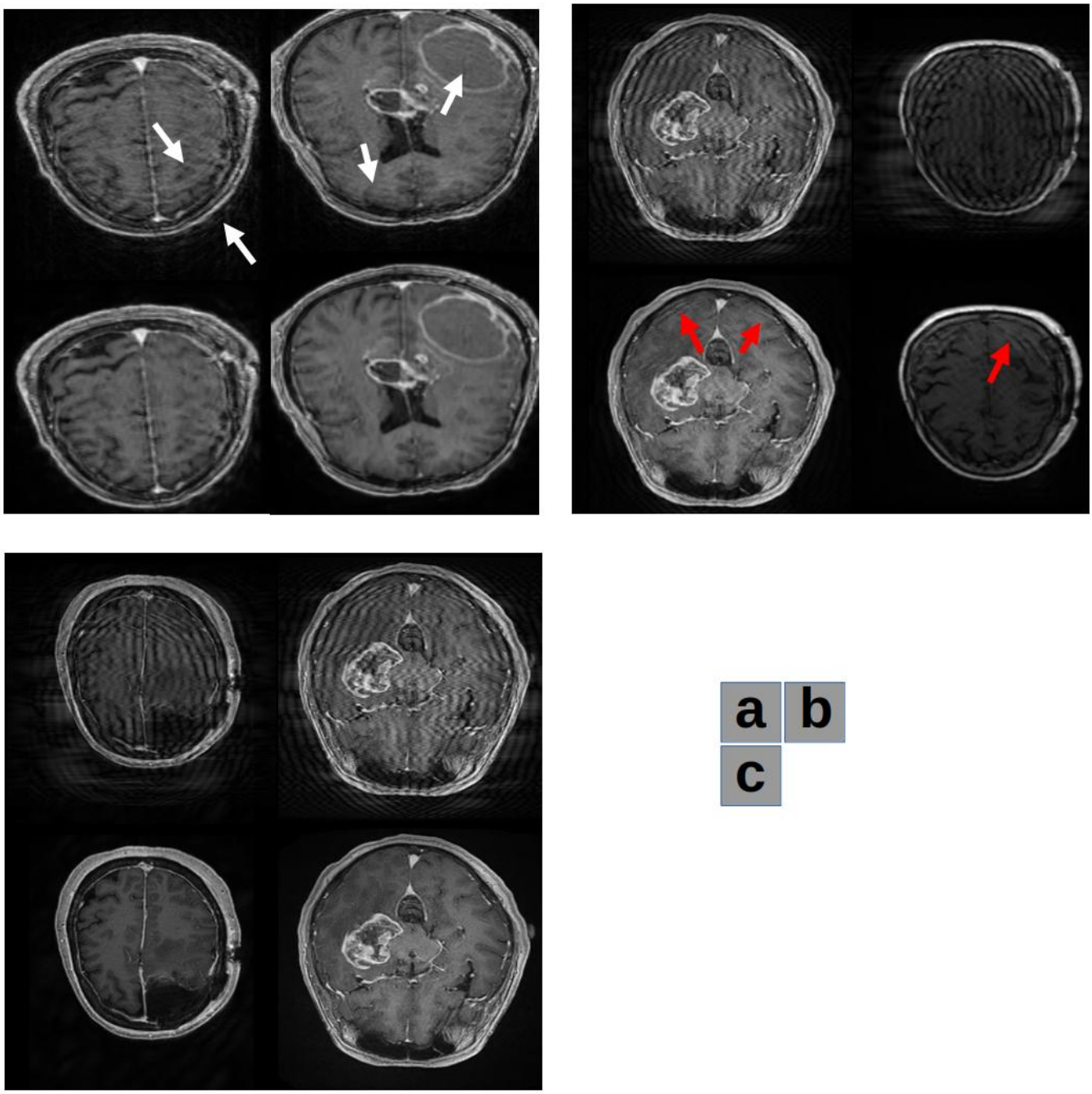

Figure 2. (a) Images with real motion artifact first row and motion-ridden images. White arrows illustrate the real motions. (b) The first row is an image with motion and the second row is the recovered image with Cycle-GAN. Red arrows show the regions where cycle-GAN did not recover completely. (c) The first row is an image with motion and the second row is the recovered image with our proposed method.

16

Multicenter MRI and CT Fusion using Unsupervised GAN Deep Learning

Mojtaba Safari M.Sc.[1,2], Dr. Daniel Low Ph.D., FAAPM, FASTRO[3], Dr. Ali Fatemi Ph.D. MCCPM ABMP[4,5], Dr Louis Archambault Ph.D.[1,2]

[1]Département de physique, de génie physique et d'optique, et Centre de recherche sur le cancer, Université Laval, Quebec City, QC, Canada. [2]Service de physique médicale et radioprotection, Centre Intégré de Cancérologie, CHU de Québec – Université Laval et Centre de recherche du CHU de Québec, Quebec City, QC, Canada. [3]Department of Radiation Oncology, University of California Los Angeles, Los Angeles, USA. [4]Department of Physics, Jackson State University,, Jackson, mississippi, USA. [5]Merit Health Central, Department of Radiation Oncology, Gamma Knife Center, Jackson, mississippi, USA

Abstract

Purpose: Computed tomography (CT) is the modality of choice for radiotherapy simulation and treatment planning. However, CT images suffer from poor soft tissue contrast for target and organ at risk delineation compared with magnetic resonance imaging (MRI) images. Using MRI-only images for radiotherapy is challenging due to the lack of electron density information for radiotherapy planning and the potential for geometrical distortion. One clinical solution is to co-register MRI and CT images. However, this increases the planning time and operational burden, which reduces the throughput of a radiation oncology clinic. Also, registration of MRI and CT images is always associated with the geometrical error. In this study, we proposed a novel unsupervised deep generative method to fuse CT and MRI images to improve tumor and organ at risk (OARs) delineation, reduce radiotherapy planning time and decrease the co-registration error.

Methods: We used a publicly available multicenter medical dataset (230 patients) from the TCIA with different imaging protocols and patients with different brain tumors, including metastases, to improve the model's generalization. Our proposed model consisted of one generator network and one discriminator network trained in an adversarial scenario. The generator was trained to produce an image with the information of the source images to fool the discriminator while the discriminator attempted to classify it to be different from CT and MRI. The patchGAN approach was employed in the discriminator network. Content, style, and L1 losses were used to preserve the texture and structure information of the source images.

Results: Our proposed unsupervised deep generative model achieved the highest amount of MRI soft tissue contrast and CT bony structure compared with traditional methods. Qualitative and quantitative comparisons were made with four different traditional techniques. The traditional methods were directional discrete cosine transform and principal component analysis, hybrid multiscale decomposition fourth-order partial differential equations and gradient transfer fusion. Qualitatively, one traditional method failed to preserve the soft tissue contrast, and one of them added lots of artifacts to the images (Figure 1). On the other hand, our method fused the source images with the highest spatial resolution without adding the image artifacts. Nine quantitative metrics were reported to quantify the preservation of the structural similarity, the statistical information, and the image edges (Table 1). Our method outperformed the traditional method on eight out of nine quantitative metrics (p-value < 0.05). And it got the second performance rank for the rest of the quantitative metrics. We can conclude from qualitative and quantitative comparisons that our automatic method could fuse multicenter CT and MRI images.

Conclusion: Our method was able to fuse the 3D T1-Gd and CT images with the highest amount of structural and content information of the source images and with a high amount of gradient information, improving tumor and OARs delineation. The contouring improvement will, in the end, improve the treatments. Our method is fully automatic, increasing the throughput of the radiation oncology departments and reducing the patients' waiting time.

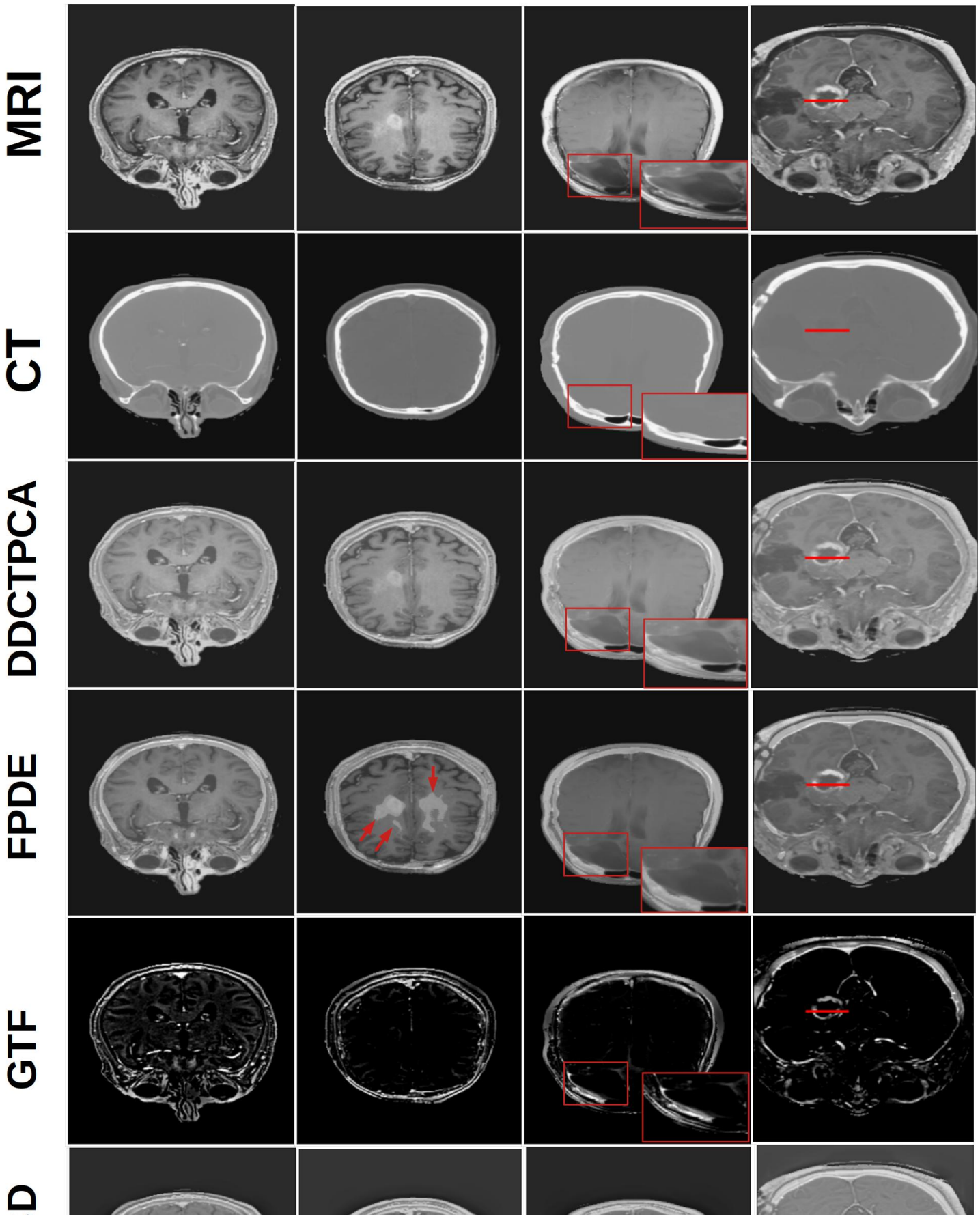

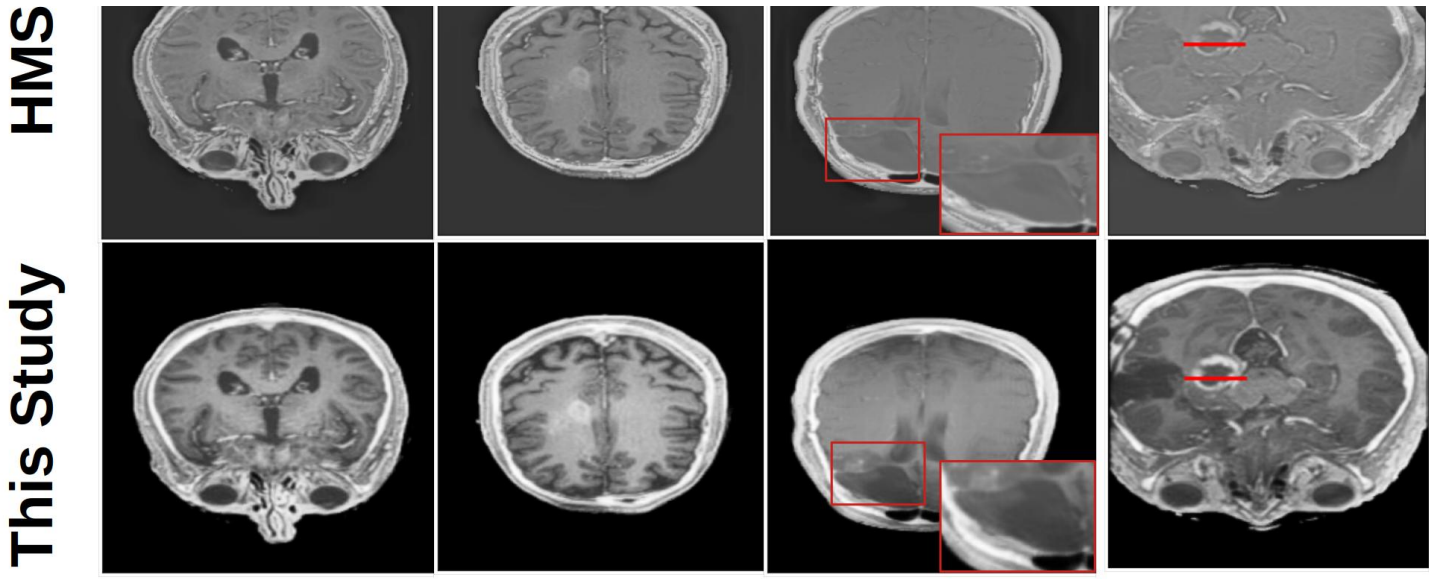

Figure 1. Qualitative comparison of our method with four state-of-the-art fusion methods

Table 1. Mean±STD of our GAN method and other methods are summarized

Method	ENT	STD	PSNR	$Q^{XY/F}$	MG	SF	NCC	MI	SSSIM
GTF	5.25±0.42	0.33±0.03	4.15±3.91*	0.6±0.06*	0.21±0.05	0.64±0.10	0.82±0.12*	0.39±0.21	0.29±0.37*
DDCTPCA	5.13±0.3	0.37±0.05*	5.98±1.65*	0.6±0.06*	0.18±0.04*	0.53±0.08*	0.85±0.11*	0.42±0.2	0.33±0.16*
FPDE	4.77±0.34*	0.27±0.05*	8.46±1.65*	0.37±0.1*	0.2±0.04	0.77±0.14*	0.3±0.28*	0.58±0.18*	0.25±0.26*
HMSD	5.58±0.23*	0.27±0.04*	5.75±1.86*	0.6±0.07*	0.21±0.05	0.61±0.1*	0.82±0.12*	0.35±0.22*	0.32± 0.17*
Our (GAN)	5.2±0.38	0.44±0.05	23.02±3.5	0.64±0.1	0.2±0.05	0.67±0.14	0.91±0.04	0.42±0.29	0.62±0.22

* is statistically different (p-value < 0.05) from our proposed GAN method. *Abbreviations:* GTF gradient transfer fusion, DDCTPCA directional discrete cosine transform and principal component analysis, FPDE fourth-order partial differential equations, HMSD hybrid multi-scale decomposition

17

TOWARDS MRI-GUIDED PROTON THERAPY: THE ULTIMATE CANCER TREATMENT?

Professor Paul Keall PhD[1], Dr Suzie Sheehy PhD[2], Professor Michael Barton MBBS MD FRANZCR[3,4,5], Dr Trang Pham BSc(Med) MBBS FRANZCR PhD[3,4,5], Professor Stuart Crozier PhD[6], Distinguished Professor Anatoly Rozenfeld PhD[7,8]
[1]University of Sydney, Sydney, NSW, Australia. [2]University of Melbourne, Melbourne, VIC, Australia. [3]Liverpool Hospital, Sydney, NSW, Australia. [4]University of New South Wales, Sydney, NSW, Australia. [5]Ingham Institute of Applied Medical Research, Sydney, NSW, Australia. [6]University of Queensland, Brisbane, QLD, Australia. [7]Centre for Medical Radiation Physics, Wollongong, NSW, Australia. [8]University of Wollongong, Wollongong, NSW, Australia

Abstract

Purpose: Radiation therapy (RT) is indicated to treat half of all cancer patients.[1] Today, RT is both effective and cost-effective. However, RT can be further improved by:

- improving image guidance which has been shown in randomised trials to improve outcomes[2,3]
- implementing adaptive radiotherapy[4]
- reducing treatment toxicity by reducing dose to normal tissues through proton therapy
- targeting additional focused radiation to the radioresistant, aggressive and metastatic-potential sub-volumes of the cancer.

A future RT system to maintain the strengths of RT and achieve the above improvements is MRI-guided proton therapy, arguably the ultimate cancer therapy. The aim of this research was to develop a plan to clinically realise MRI-guided proton therapy.

Methods: A multidisciplinary team of scientists and clinicians with experience to tackle this challenge was assembled. The team included members of large government-funded grant that designed and built an MRI-Linac. The team developed a 2-phase plan, a Research Planning phase, and a Research Implementation phase, to realise MRI-guided cancer therapy.

Results: The key Research Planning phase deliverable is a comprehensive Research Plan that includes the preliminary design, partner engagement, and site decision for a commercially attractive clinical MRI-Guided Proton Therapy system. The preliminary design will be informed by extensive consumer, clinician, health economics and public/private provider market engagement to maximise the product-market fit, clinical applications and workflow. A multi-institutional system-wide design exercise covering the interoperability and integration of the MRI and the proton system will be undertaken. Site selection and the tenders and selection of industry partners will be completed.

The key Research Implementation phase deliverables are the construction, research and development, and clinical demonstration of the MRI-Guided Proton Therapy system. This system will be a viable commercial prototype, with the clinical implementation advancing science, medicine and de-risking the commercial pathway.

Conclusions: We plan to unleash the clinical potential of proton beam radiation therapy for cancer patients by building a clinical magnetic resonance imaging (MRI) guided proton therapy device. This device should the most accurate and precise radiation therapy treatment system ever created.

Reference

1. Barton et al. Estimating the demand for radiotherapy from the evidence: A review of changes from 2003 to 2012. Radiother Oncol. 2014;112(1):140-144.

2. de Crevoisier et al. Daily versus weekly prostate cancer IGRT: Phase 3 multicenter randomized trial [published online ahead of print 2018/08/03]. Int J Radiat Oncol Biol Phys. 2018;102(5):1420-1429.

3. Tree et al. IMRT versus SBRT for prostate cancer (PACE-B): 2-year toxicity results from an open-label, randomised, phase 3, non-inferiority trial. Lancet Oncol. 2022;23(10):1308-1320.

4. Kishan et al. MRI-Guided vs. CT-Guided SBRT for Prostate Cancer (MIRAGE): Primary Endpoint Analysis of a Phase III Randomized Trial. International Journal of Radiation Oncology, Biology, Physics. 2022;114(3):S92-S93.

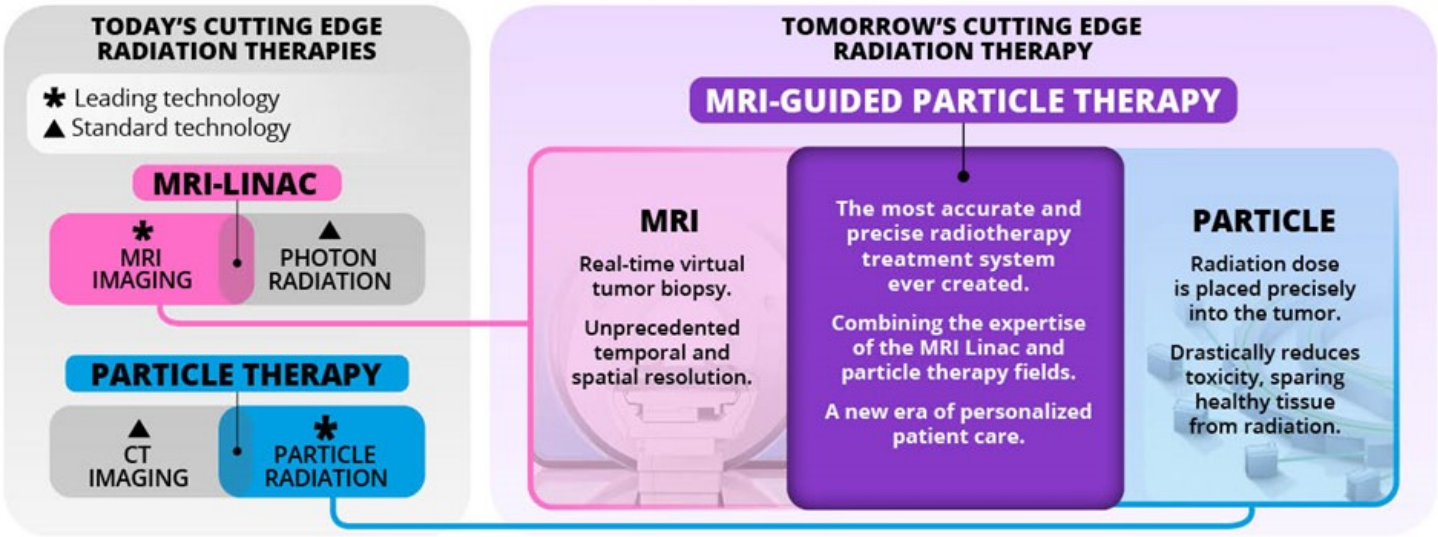

Figure 1. We plan to bring together the two most disruptive treatment devices in radiation therapy. We plan to design, build, and clinically pioneer MRI-Guided Proton Therapy.

18

ICRU REPORT ON MRI-GUIDED RADIATION THERAPY USING MRI-LINACS

Professor Paul Keall PhD[1], Associate Professor Carri Glide-Hurst PhD[2], Doctor Alison Tree MBBS BSc FRCR MD(Res)[3,4], Dr Percy Lee MD[5,6], Brad Murray MSc, FCCPM[7,8], Professor Bas Raaymakers PhD[9], Professor Uulke Van der Heide PhD[10], Clincial Professor Minsong Cao PhD, DABR, FAAPM[11]

[1]University of Sydney, Sydney, NSW, Australia. [2]University of Wisconsin, Madison, WI, USA. [3]The Royal Marsden Hospital, London, United Kingdom. [4]The Institute of Cancer Research, London, United Kingdom. [5]City of Hope Hospital, Irvine, CA, USA. [6]MD Anderson Cancer Center, Houston, TX, USA. [7]University of Alberta, Edmonton, Canada. [8]MagnetTx, Edmonton, Canada. [9]University Medical Center Utrecht, Utrecht, Netherlands. [10]The Netherlands Cancer Institute, Amsterdam, Netherlands. [11]UCLA, Los Angeles, CA, USA

Abstract

Purpose: The ICRU has been providing guidance for over 90 years to radiation medicine. An objective of the ICRU is the development of internationally accepted recommendations. Aligned with this objective, the ICRU report on MRI-guided Radiation Therapy (MRIgRT) using MRI-Linear Accelerators was commissioned.

Methods: A team with diverse country-of-origin, gender and expertise was assembled, noting that most of the MRIgRT development had been performed in high-income countries. The team focused on the differences in the radiation therapy process that the addition of MRI into the treatment room brings to the patient and to the treatment team. With the number of clinical systems growing rapidly, and the increase in feature availability and automation, the authors focused on the top-level concepts that will likely remain relevant amidst the ongoing technological changes. These top-level concepts include personalization of imaging, high-quality intra-treatment imaging, routine online adaptive radiotherapy, integrated intra-treatment imaging with beam gating, and integrated functional imaging capabilities. A summary of the key feature differences between MRIgRT and conventional X-ray image-guided radiation therapy (IGRT) are shown in Figure 1.

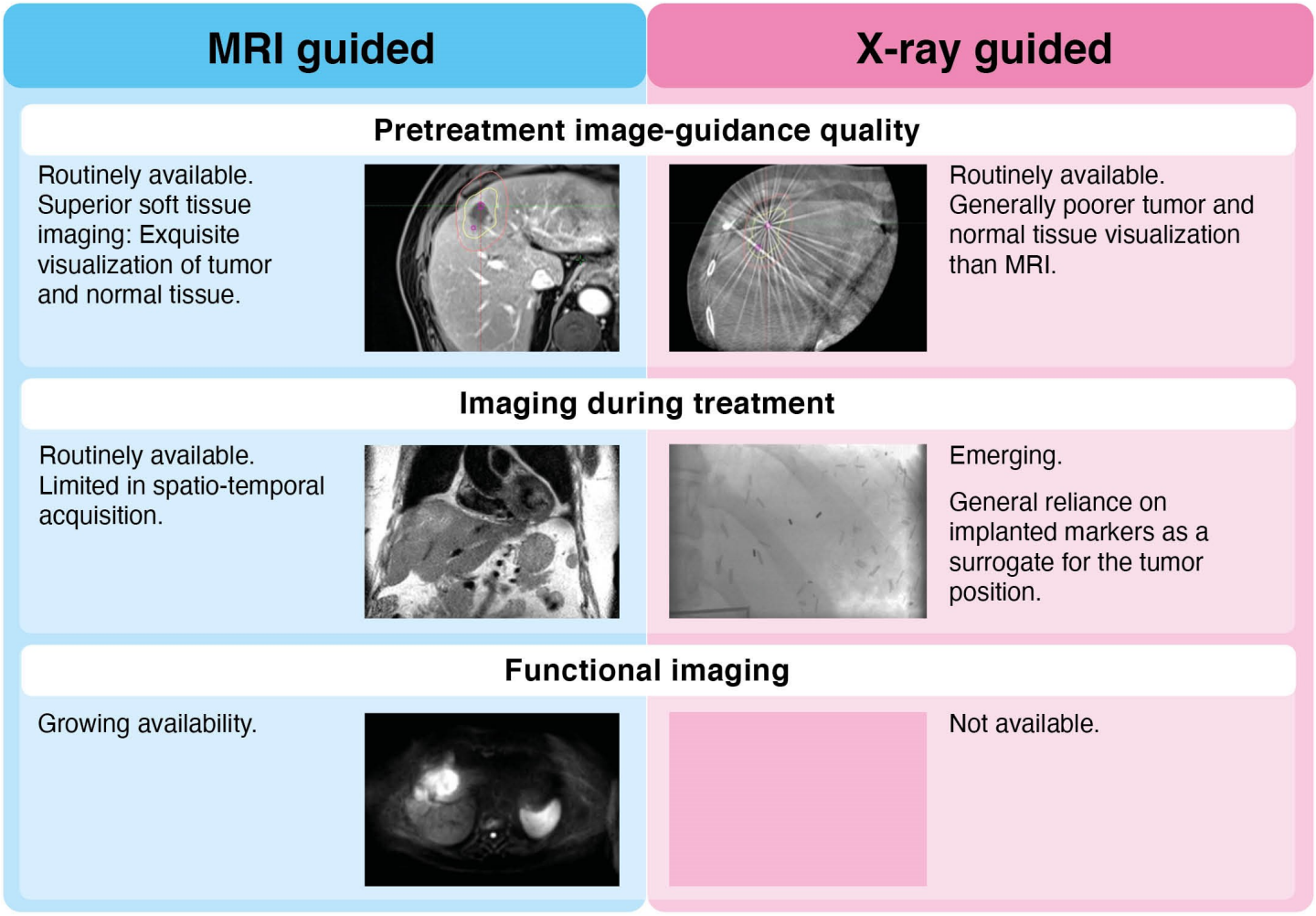

Figure 1. An illustration, using example liver cancer images, of some key differences between MRI-guided and conventional X-ray image-guided linear accelerator radiation therapy.

Results: The report begins with an overall rationale and status of MRIgRT, followed by the clinical indications for patient MRIgRT treatments across different cancer sites. A summary of the MRI-linac interoperability challenges and an overview of the MRIgRT systems to date is given. The MRIgRT process steps are given chronologically: treatment planning, image guidance, treatment adaptation and treatment delivery. The staff requirements, training and safety are discussed. A technical section reviews MRIgRT commissioning and dosimetry. The recommendations span multiple MRIgRT stakeholders: administrators, newer and expert users, industry and government. A future outlook and future needs of where MRIgRT may fit into the health care system, along with anticipated technological advances, are outlined. To give new users real-world examples of MRIgRT in practice, clinical case studies for a variety of sites and treatment complexity are given.

Conclusions: MRI-linacs are a rapidly emerging technology for radiation therapy that have undergone strong clinical adoption. MRI-linacs have higher capital, operating, staff and workflow costs than conventional X-ray guided linacs. However, MRI-linacs provide the radiation treatment team improved soft tissue discrimination and the ability to monitor patient anatomy prior to and during treatment without additional ionizing radiation risks. This additional information introduces many opportunities to improve patient outcomes. The CTV-PTV margins can be reduced, thereby reducing the likelihood and potential severity of treatment-induced side effects. MRI-linacs, particularly when coupled with online daily ART, have also enabled opportunities for hypofractionation, thereby mitigating the cost and time commitment for the patient and the healthcare system. As MRI-linacs combine two devices with their own risk profiles, and they are an emerging technology, the safe implementation requires skilled teams, ongoing training, a safety-first culture, comprehensive QA programs, and documented treatment workflow procedures.

19

Comparison of 4D-CT and 4D-MRI for volumetric and motion assessment in radiotherapy planning of lung cancer

Ms Amy Zerafa[1], Dr Satomi Higuchi[1], Dr Jane Ludbrook[1], Mr John Simpson[1], Ms Laura OConnor[1], Dr Jianing Pang[2], Dr Jonathan Goodwin[1]

[1]Calvary Mater Newcastle, Newcastle, NSW, Australia. [2]Siemens Healthineers, Erlangen, Germany

Abstract

Purpose

Identification of respiratory related tumour motion is an important consideration for radiotherapy planning for lung cancer. Minimising calculated dose to healthy lung while ensuring sufficient dose coverage to the tumour target typically involves 4DCT simulation to generate a series of 3D image volumes at separately defined stages of the patient's respiratory phase. These images provide visual confirmation of the extent of tumour motion, with both the average intensity projection (AveIP) across the whole image data set and for each respiratory phase bin. 4DMRI offers a potential alternative to 4DCT for treatment simulation, with potential improvement in accuracy of tumour motion identification and delineation due to superior soft tissue contrast, with less dependence on breathing regularity for image quality and phase binning accuracy. In this study we quantitatively evaluated the equivalence of 4DMRI and 4DCT in lung, with respect to tumour size and motion range, as well as dosimetric outcome compared to existing CT based treatment plans.

Methods

17 patients receiving radiation therapy for primary or metastatic malignancies in the lung, gave informed consent to participate in the trial. A phase based 4DCT scan was acquired, with the most appropriate respiratory rate determined for each patient (>6, >9, >12 breathes per minute) prior to scanning. The measured breathing trace was used to retrospectively bin 4DCT image data into separate 3D volumes across the respiratory cycle. MRI scans were performed following the CT simulation session on a 3T MRI scanner. Two separate scans were acquired using the prototype radial VIBE sequence, namely a transverse average, and a coronal acquisition, which was reconstructed with five respiratory phase bins from end exhalation to end inhalation, to generate a 4DMRI data set with a 3D image volume reconstructed for each respiratory phase bin. 4DMRI derived treatment volumes were compared to the patient's standard clinical treatment plans. Dosimetric differences between CT_PTVp and MRI_PTVp were compared and causes for discrepancy evaluated.

Results

4DMRI derived contours on the patients' existing treatment plan revealed clear differences in dose to target and healthy lung. We identified several causes for discrepancy between the two imaging methods in some patients. Most notably the use of a motion correction algorithm (MOCO) in tumours with large rapid movement gave an under representation of true motion extent in 4DMRI (Fig.1). Furthermore, a significant variation in breathing was observed for some patients between imaging modalities (Fig.2), as well as differences in patient positioning due to limitations on MRI bore space (Table 1).

Conclusion

While motion corrected 4DMRI had some limitations, clear benefits were observed with non-motion corrected 4DMRI in lower lobe lung cancer patients, particularly with irregular breathing patients. This study has demonstrated that 4DMRI may be a viable alternative to 4DCT in irregular breathing patients, or as part of an MRI only treatment planning workflow for lung cancer.

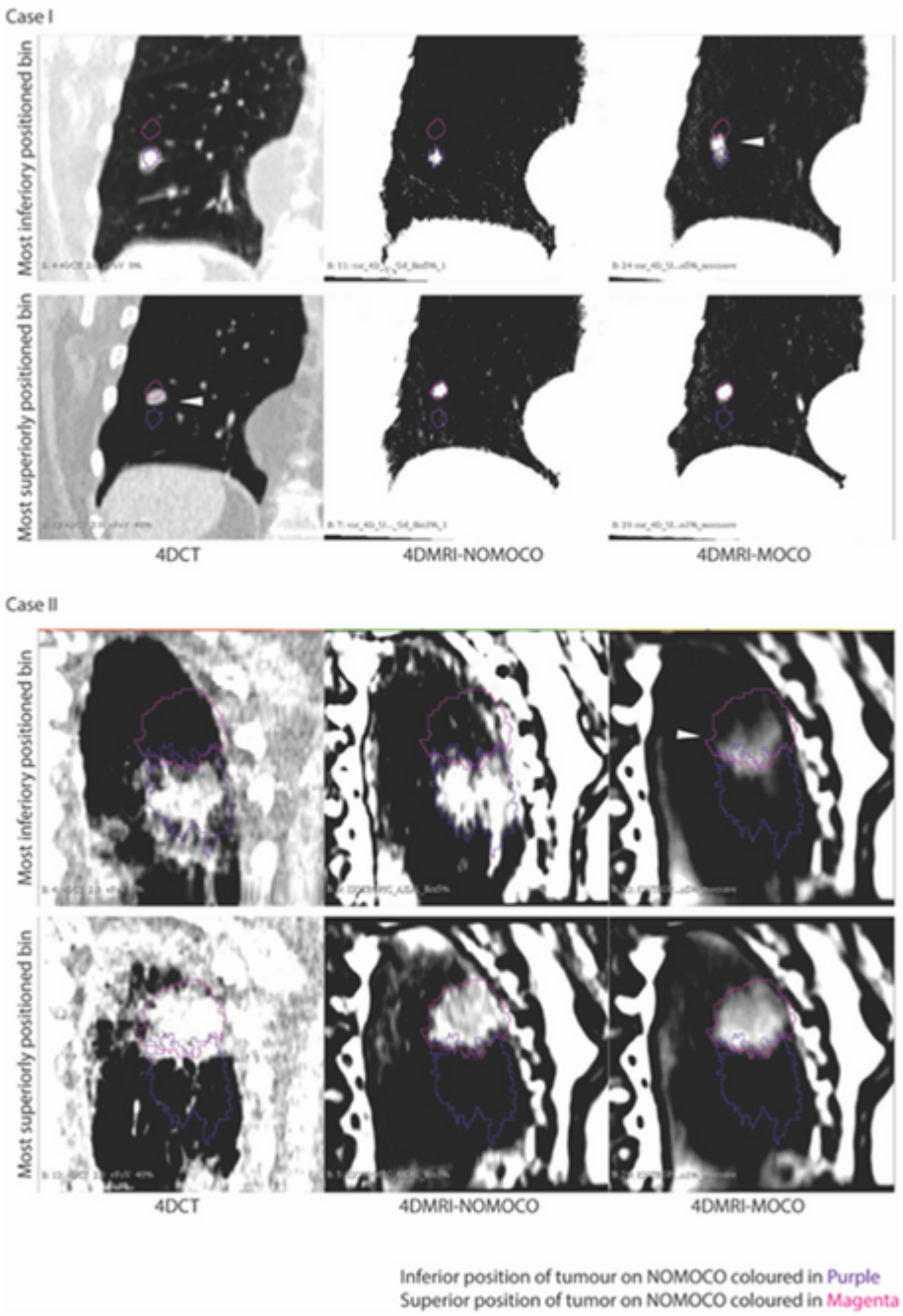

Figure 1. Shows discrepancies between MOCO and NOMOCO MRI, relative to equivalent 4DCT images. Significant positional differences were observed primarily in the most inferior tumour position.

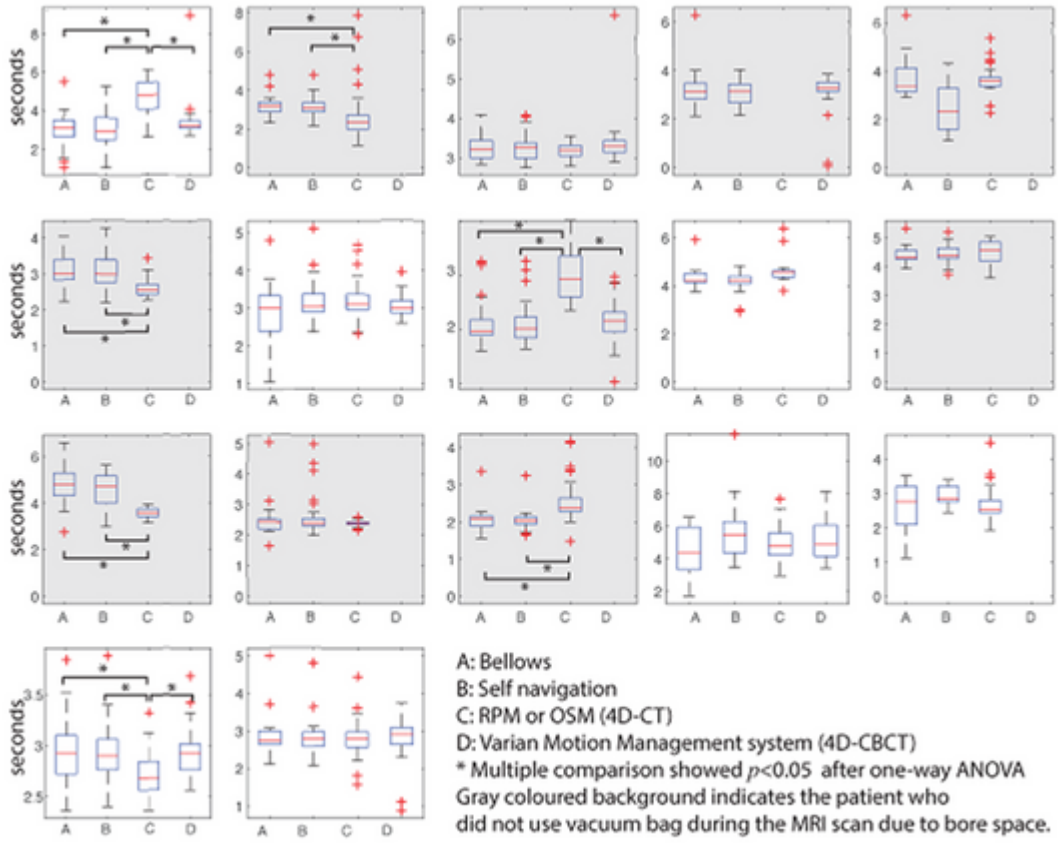

Figure 2. Statistical analysis of breathing patterns (CT, MR, CBCT) as well as 4DMRI self navigation signal.

Table 1. Summary of results showing measured tumour motion, volume and breathing equivalence between modalities.

	Average tumour volume at end exhalation and inhalation and SD [cm^3]			centroid motion [mm]					
	CT	MOCO	NOMOCO	CT	MOCO	NOMOCO	Breathing variance MRI vs CT	vacbag	
1	10.95±0.42	10.00±0.04	10.00±0.04	1.95	1.48	1.10	$p<0.05$	o	upper lobe
2	74.41±11.97	53.55±0.03	50.80±5.84	16.73	14.48	14.19	$p<0.05$	x	lower lobe
3	89.55±3.19	83.71±3.41	79.68±2.4	2.88	1.35	1.40		x	upper lobe
4	9.48±0.46	5.80±0.16	5.49±0.16	4.12	1.69	3.04		x	upper lobe
5	44.70±3.42	35.44±4.04	39.07±0.35	4.74	2.44	2.36		x	upper lobe
6	65.53±1.97	66.89±0.85		0.34	0.30		$p<0.05$	x	upper lobe
7	13.81±1.47	12.79±0.49	15.16±0.39	0.89	2.97	2.98		o	upper lobe
8	52.26±1.32	43.35±2.72	45.53±1.91	3.71	2.32	2.78	$p<0.05$	x	hilar
9	394.11±1.77		348.16±1.51	0.52		1.13		o	upper lobe
10	427.71±3.23	346.78±6.73	346.78±6.73	0.69	1.30	1.30		x	lower lobe
11	147.29±0.65	148.90±0.53	148.90±0.53	2.19	3.62	3.62	$p<0.05$	x	hilum
12	69.49±1.02	70.91±1.27	70.91±1.8	1.01	1.84	1.84		x	hilar
13	445.28±0.51		104.89±1.02	0.39		0.70	$p<0.05$	x	middle lung / Lingula
14	6.37±0.22	5.03±0.54	6.35±0.05	7.90	4.28	6.42		o	lower lobe
15	122.10±0.34	116.50±2.22	116.76±5.45	1.17	0.36	0.79		o	upper lobe
16	1.44±0.63	1.82±0.44	1.18±0.06	15.25	8.31	17.96	$p<0.05$	o	lower lobe
17	40.79±4.73	36.54±0.16	39.89±3.69	2.36	6.63	6.61		o	lower lobe

20

Determining the reproducibility of the apparent diffusion coefficient between three Elekta Unity MR-linacs using anatomy-specific sequences

Miss Madeline Carr[1,2,3,4], Miss Michaela Beavan[3,4], Dr John Baines[5], Dr Sarah Elliott[6], Professor Peter Metcalfe[2,3,4], Dr Lois Holloway[2,3,4], Dr Michael Jameson[1,2,3,4,7]

[1]GenesisCare, Sydney, NSW, Australia. [2]Wollongong University, Wollongong, NSW, Australia. [3]Liverpool and Macarthur Cancer Therapy Centres, Liverpool, NSW, Australia. [4]Ingham Institute for Applied Medical Research, Liverpool, NSW, Australia. [5]Townsville Cancer Centre, Townsville, NSW, Australia. [6]Austin Hospital, Heidelberg, NSW, Australia. [7]University of New South Wales, Sydney, NSW, Australia

Abstract

Purpose:

Diffusion-weighted imaging (DWI), a quantitative magnetic resonance imaging (qMRI) technique, has the potential to aid in disease characterization and treatment response monitoring [1]. MR-Linacs (MRL) provide the unique opportunity to simultaneously acquire DWI images of a patient whilst delivering radiotherapy. This enables large scale datasets to be collected efficiently, and without patient burden [2]. One factor currently limiting the clinical implementation of DWI derived imaging biomarkers, such as the apparent diffusion coefficient (ADC), is the unknown qMRI scanner performance variability. This study aims to quantify the inter-scanner accuracy and reproducibility of ADC between three Elekta Unity MRLs.

Methods:

An isotropic diffusion phantom [3] (at 0°C) and one healthy volunteer was scanned on three Unity MRLs. Elekta Consortium recommended DWI sequences, specifically designed to image brain, pelvis and abdomen anatomies, were used to image the volunteer and phantom at each Unity site. T1/T2-weighted volumetric images were also acquired for the volunteer. A radiation therapist used these images to contour organs of interest and overlaid the contours onto the scanner generated (inline) axial ADC maps. MiM was then used to extract each organs average ADC value. Python was also used to find the average ADC value of the phantom's isocentric water vial from the inline phantom ADC maps. A coefficient of variation (%CV) was used to measure inter-scanner reproducibility for each organ/phantom vial. Additionally, using the phantoms' known ADC vial values [3], the %bias could be calculated to determine the average inter-scanner ADC accuracy.

Results:

The ADC values measured for each contoured organ of the volunteer are presented in Figure 1. The average inter-scanner CV from these measurements for the brain, cerebellum, cervix, femurs and kidneys was 5.2%, 4.3%, 20.9%, 8.8% and 8.7%, respectively. For the phantom measurements of the brain, pelvis and abdomen sequences, the CV (and average %bias) was 0.3% (0.6), 0.6% (2.1) and 0.4% (-0.6), respectively. This was less than the QIBA Diffusion Profile phantom tolerance limits of 2.2% (±3.6%) for CV (and %bias) [3].

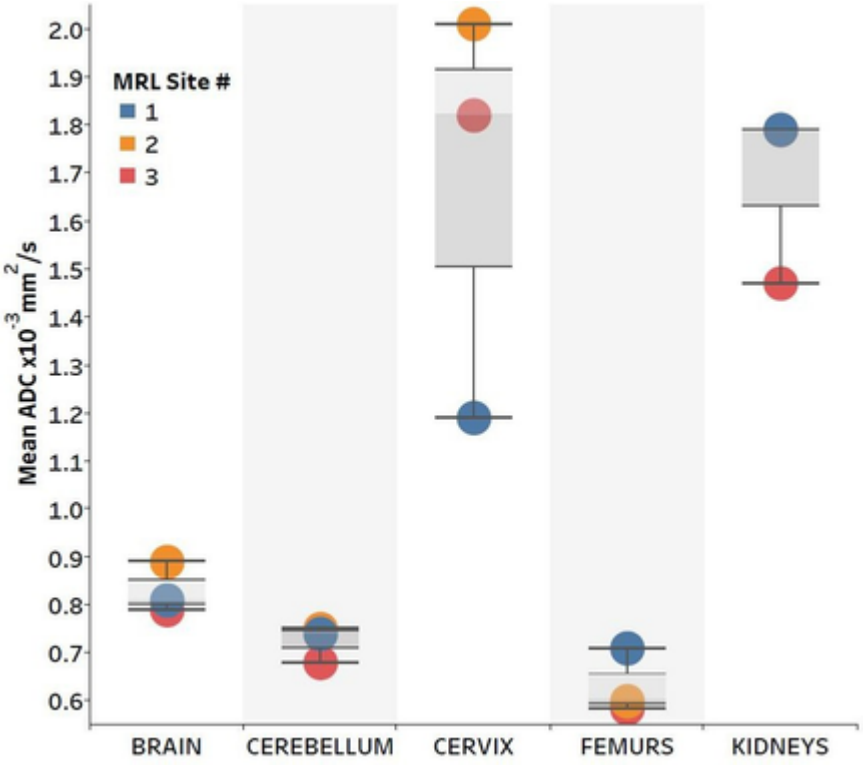

Conclusion:

This study demonstrated reasonable inter-scanner reproducibility and accuracy using the volunteer and phantom datasets. The cervix was found to have the largest variability in contoured volume, which could account for the larger %CV measured. Future investigations would involve incorporating multi-site patient-based imaging, assessing contour reproducibility and the effects of offline vs inline ADC map generation. This study suggests that qMRI techniques, such as DWI, could be a viable option for future multi-site studies utilizing MRLs.

References:

1. Diffusion-weighted magnetic resonance imaging as a cancer biomarker (AR. Padhani et al.), Neoplasia. 11, 102-125 (2009).

2. Integration of quantitative imaging biomarkers in clinical trials for MR-guided radiotherapy (PJ. van Houdt et al.), Eur. J. Cancer. 153, 64-71 (2021).

3. Conformance of a 3T radiotherapy MRI scanner to the QIBA Diffusion Profile (ME. Carr et al.), Med. Phys. 49, 4508-4517 (2022).

21

Impact of additional MRI scans on the training of supervised deep learning methods for automatic CTV delineation in head and neck cancers

Alexandra Walter[1,2,3], Cornelius Bauer[1,2,4], J. Pedro Rodrigues[1,2], Philipp Hoegen[2,5,6,7], Sebastian Adeberg[2,5,6,7,8,9], Thomas Welzel[2,5,7], Stefan A. Koerber[2,5,7], Katharina M. Paul[2,5], Sebastian Klüter[2,10], Oliver Jäkel[1,2,9], Martin Frank[3], Kristina Giske[1,2]

[1]Department of Medical Physics in Radiation Oncology, German Cancer Research Center (DKFZ), Heidelberg, Germany. [2]Heidelberg Institute of Radiation Oncology (HIRO) & National Center for Radiation Research in Oncology (NCRO), Heidelberg, Germany. [3]Karlsruhe Institute of Technology (KIT), Karlsruhe, Germany. [4]Department of Physics and Astronomy, University of Heidelberg, Heidelberg, Germany. [5]Department of Radiation Oncology, Heidelberg University Hospital, Heidelberg, Germany. [6]Clinical Cooperation Unit Radiation Oncology, German Cancer Research Center (DKFZ), Heidelberg, Germany. [7]National Center for Tumor diseases (NCT), Heidelberg, Germany. [8]German Cancer Consortium (DKTK), Partner Site Heidelberg, Heidelberg, Germany. [9]Heidelberg Ion-Beam Therapy Center (HIT), Department of Radiation Oncology, Heidelberg University Hospital, Heidelberg, Germany. [10]Department of Radiation Oncology, Heidelberg University Hospital, Heidelberg, Ghana

Abstract

Purpose

Since magnetic resonance images (MRIs) show better soft-tissue contrast, the segmentation of clinical target volumes (CTVs) for radiation therapy can be improved by adding MRIs into the planning procedure (1). Training a deep neural network model on computer tomography scans (CTs) only and another on CT and MRI combined data to predict nodal CTV, we investigated how additional MRIs might affect automatic nCTV segmentation.

Methods

We used 15 head and neck cancer patients with dual energy CTs (SOMATOM Confidence, Siemens) of which only the computed virtual mono-energetic images at 79 keV were used, and MRIs acquired with a T1-weighted in-phase Dixon sequence (SOLA 1.5T, Siemens). CTV labels were manually (man-nCTV) delineated on the CTs. The MRIs were registered to the CTs utilizing deformable image registration (2).

One nnUnet model (3) was trained (12 training and 3 test cases) with standard configurations on the CT data only and another on CT-MRI combined data, both to predict the nCTV. Pre-training on CTs of 70 other patients was performed in both cases.

Results

Table 1 shows the DICE coefficients of paired predicted CT-nCTV, predicted CT-MR-nCTV, and man-nCTV. Both predictions are more similar to each other than to the man-nCTV respectively, reflected in lower DICE values. Including MRI into the training shows no improvement in DICE between predictions and manual delineations.

The slices of large deviation between predictions and man-nCTV show high levels of patient-individual variations like the occurrence of GTVs (Figure 1), unsymmetrical segmentations which are caused by clinical circumstances (Figure 2), or the

extension over slices. The smaller differences between both predictions are frequently located along soft tissue boundaries, which the CT-MR-nCTV follows (Figure 2).

Table 1: Volumentric DICE coefficients of all paired predicted and manually delineated CTVs

	CT-nCTV vs. CT-MR-nCTV	CT-nCTV vs. manual	CT-MR-nCTV vs. manual
Patient 1	0.84	0.70	0.70
Patient 2	0.89	0.58	0.59
Patient 3	0.80	0.56	0.53
mean ± SD	0.84 ± 0.04	0.61 ± 0.06	0.61 ± 0.07

SD: standard deviation (1-sigma); CT-nCTV: CTonly-based nodal clinical target volume; CT-MR-nCTV: CT-and-MRI-based nodal clinical target volume

Conclusion

The volumetric DICE between man-nCTV and both predictions is comparable to the inter-observer variability of nCTV segmented on CTs (4), such that our model appears in-line with state-of-the-art achievable performance.

The advantage to only add MRIs to the networks training for its convergence towards the man-nCTV is negligible, because the man-nCTVs were delineated on the CTs only. Thus, MRIs' potential power to localize soft tissue boundaries is not reflected in the man-nCTV labels. Additionally, the impact of registration quality of the combined training data limits the performance of ANN-models (5), which was 0.71 ± 0.04 volumetric DICE for our data.

The fact that the 2D DICE of the predictions is low in slices with large individual adjustments in the man-nCTVs, matches the general concept of deep learning which is trained to infer commonalities within the training labels. Thus, the comparison of DL-predicted nCTVs and individually adjusted expert-generated nCTVs should be reconsidered.

Acknowledgments

This research is funded by xxx and partially by xxx.

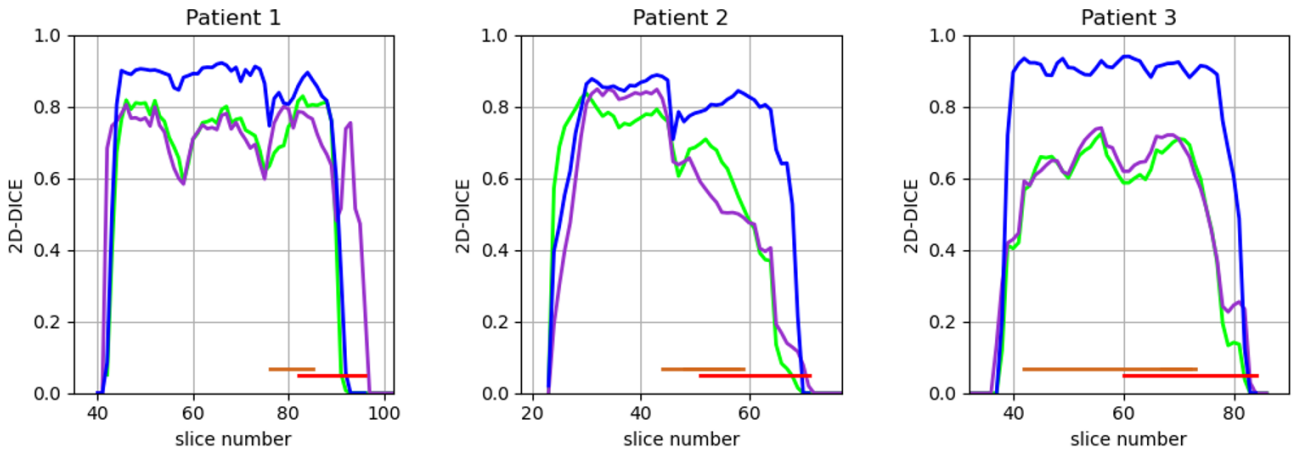

Figure 1: 2D DICE dependency on slice position along the body axis. CT-nCTV vs. CT-MR-nCTV in blue, CT-nCTV vs. manual in green, and CT-MR-nCTV vs. manual in purple for patient 1, patient 2, patient 3. Slices with primary GTV (nodal GTVs) are marked with red (brown).

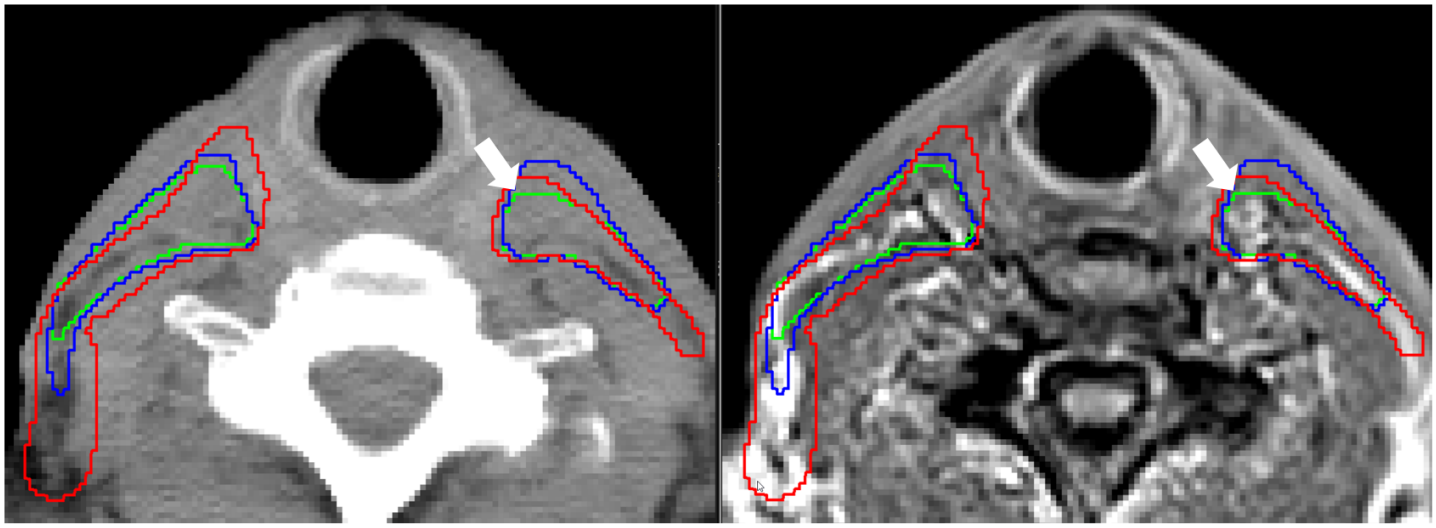

Figure 2: Exemplary transversal CT (left – soft-tissue-window) and MRI (right) slice (#57) of patient 1 with CT-nCTV (blue), CT-MR-nCTV (green), and man-nCTV (red). White arrows are pointing to the examples of the main difference between the predicted volumes coinciding with MRI soft tissue boundaries not contrasting in CT.

22

Pseudo-DECT Generation using 3D U-Net architecture for MRI-only Treatment Planning.

Ama Katseena Yawson[1,2,3], Cornelius Bauer[1,2,4], Katharina Maria Paul[2,5], Sebastian Klüter[2,5], Oliver Jäkel[1,2,6], Kristina Giske[1,2]

[1]Division of Medical Physics in Radiation Oncology, DKFZ, Heidelberg, Germany. [2]National Center for Radiation Research in Oncology (NCRO), Heidelberg Institute for Radiation Oncology (HIRO), Heidelberg, Germany. [3]Medical Faculty, Heidelberg University, Heidelberg, Germany. [4]Faculty for Physics and Astronomy University of Heidelberg, Heidelberg, Germany. [5]Department of Radiation Oncology, Heidelberg University Hospital, Heidelberg, Germany. [6]Heidelberg Ion Therapy Center (HIT), Heidelberg, Germany

Abstract

Purpose: To investigate the use of dual-energy CT (DECT); which can estimate stopping power map (SPR) with higher accuracy than conventional single-energy CT (SECT); by using a 3D U-Net architecture to generate pseudo-DECT from MRI for SPR calculation.

Methods: The proposed method was carried out using 16 head & neck cancer patients with MRI (VIBE Dixon Sequence) and DECT pairs. The DECT consists of high-energy CT (HECT – 140kVp) and low-energy CT (LECT – 80 kVp). Of the 16 datasets, 12 cases were used as training sets and the remaining held out as test (3) and validation set (1). N4 bias field correction was applied to all MRI images to reduce the inherent inhomogeneous intensity. Deformable image registration with the ability to preserve bony structures was utilized to align DECT images to their corresponding MRI images. Using a 3D U-Net architecture, two independent models for HECT and LECT synthesis were trained using the same parameter set with Adam optimizer, a learning rate of 2e-4, batch size of 4, 200 epochs, patch size of 64^3 with sliding overlap of 32^3. A combination loss of L1 and L2 loss was minimized as the objective function. From the predicted patches, a complete 3D volume was obtained via patch fusion of the predicted patches.

Results: The results for the mean absolute error (MAE), which can access the overall quality of the predicted pseudo-DECT between both pseudo-CTs and its target CTs for all test cases are summarized in Table 1. The MAE for pseudo-HECT showed lower HU differences within all the test cases than that of pseudo-LECT. Visual assessment of the generated pseudo-HECT and pseudo-LECT for one random test case is illustrated in Figures 1 and 2 respectively. The target CTs and the pseudo-CTs are generally not visually obvious without further analysis. However, from the difference map as indicated in Figures 1 and 2, large discrepancies can be observed in some bony structures.

Table 1: MAE between target DECT and pseudo-DECT

Patient ID	MAE for HECT (HU)	MAE for LECT (HU)
Patient 1	38.57	46.07
Patient 2	17.67	23.91
Patient 3	23.58	29.88
Mean ± STD	26.61 ± 10.77	33.28 ± 11.47

Conclusion: The proposed algorithm ensures a comparable pseudo-DECT to target DECT for all test cases with the largest deviations observed in bony structures, which is consistent with other published DL-based studies [1]. However, current predictions for bony structures cannot guarantee an accurate SPR calculation. Therefore, bone segmentation-guided training strategies will be investigated in future implementations.

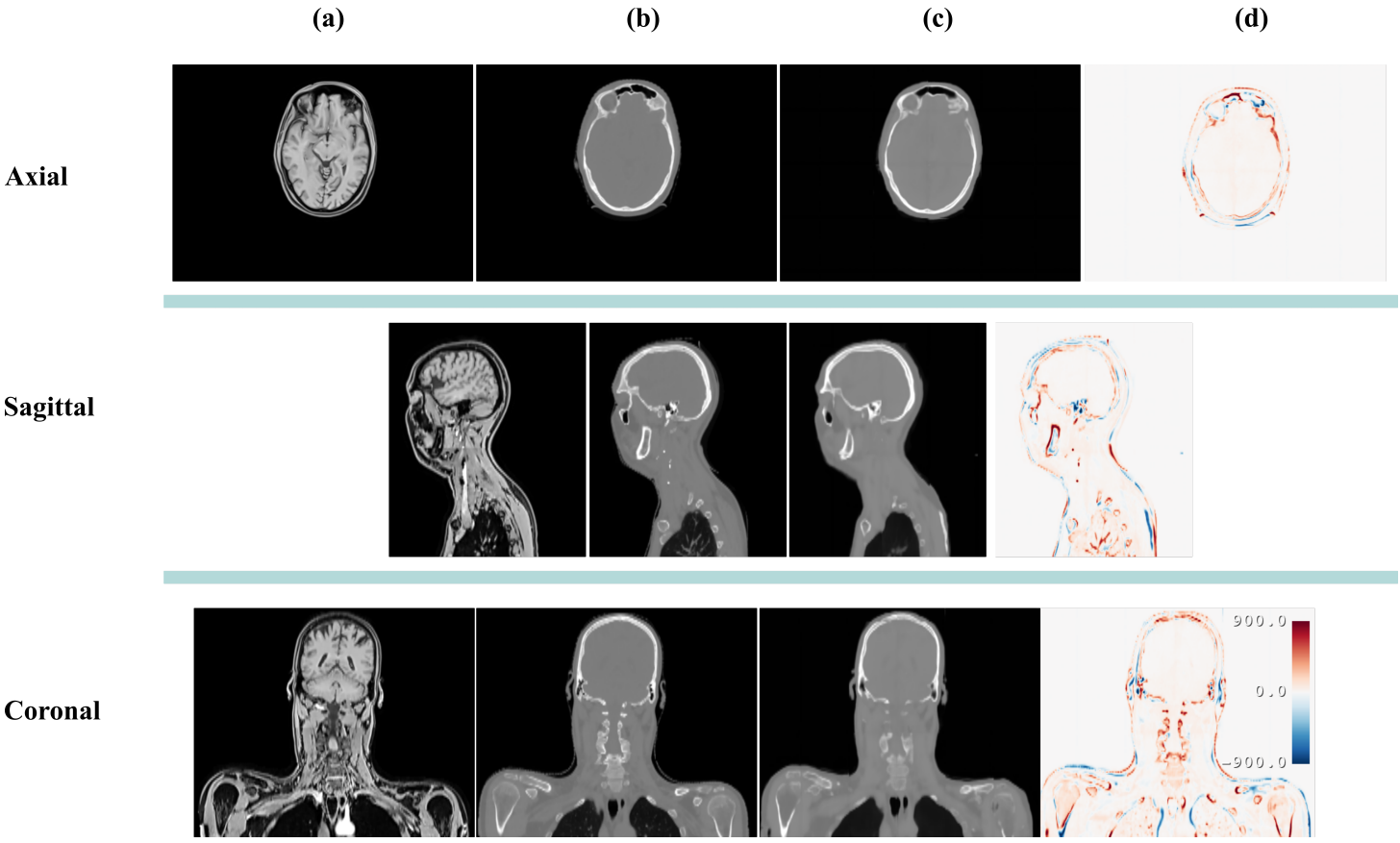

Figure 1: (a) Input MRI; (b) Target HECT; (c) Pseudo-HECT and (d) Difference map of the target HECT and pseudo-HECT

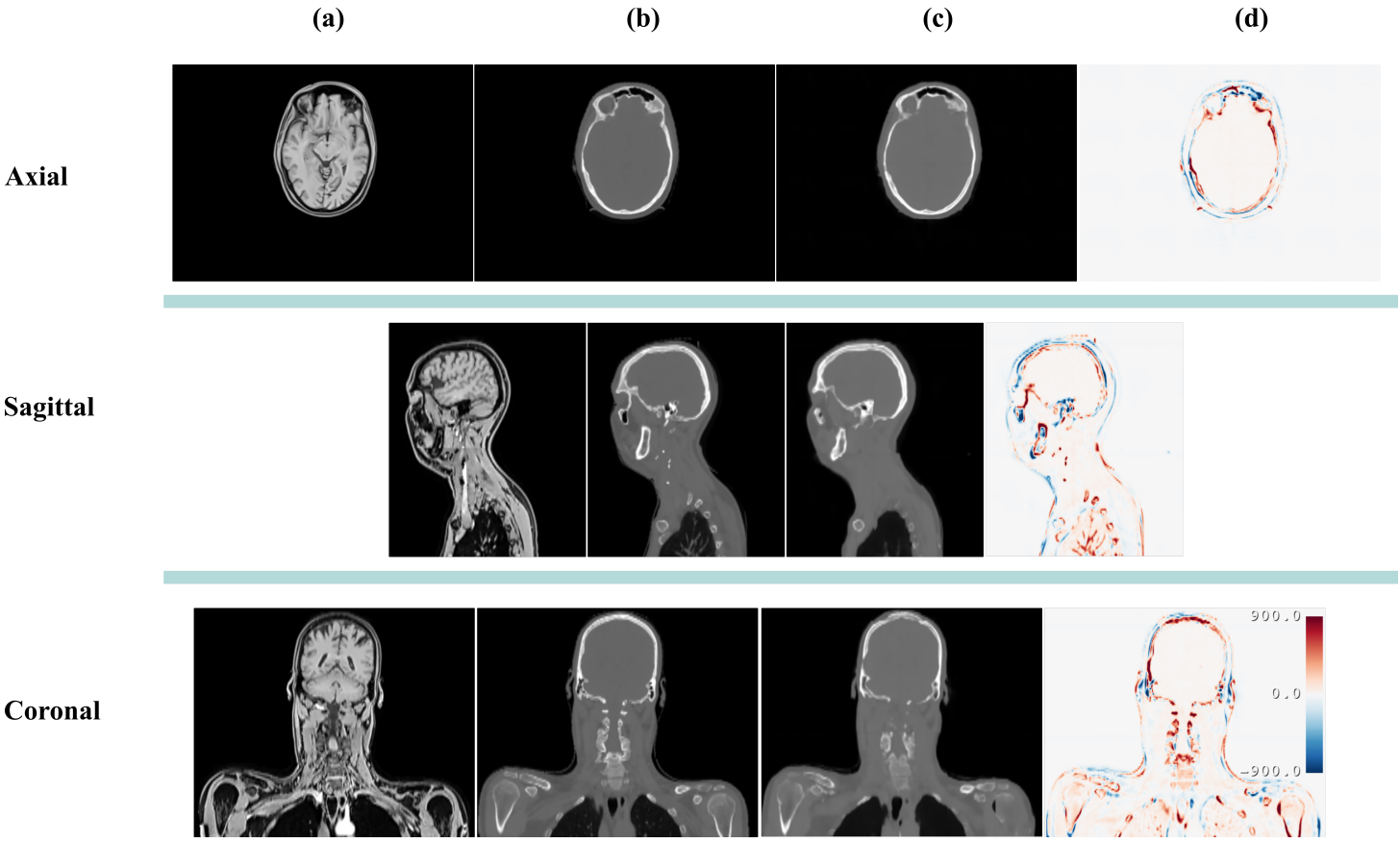

Figure 2: (a) Input MRI; (b) Target LECT; (c) Pseudo-LECT and (d) Difference map of the target LECT and pseudo-LECT

References:

[1] C. Wang et al., “Toward MR-only proton therapy planning for pediatric brain tumors: Synthesis of relative proton stopping power images with multiple sequence MRI and development of an online quality assurance tool,” 2022, doi: 10.1002/mp.15479.

Acknowledgement:

Funded by BMBF ARTEMIS #13GW0436

23

Quantitative MRI associated with patient-reported xerostomia after head and neck radiotherapy

Filipa Guerreiro[1], Robin Navest[2], Berit Verbist[3,4], Martin de Jong[1,4], Petra van Houdt[2], Nienke Hoekstra[1], Stefan Zijlema[2], Uulke van der Heide[1,2], Eleftheria Astreinidou[1]

[1]Department of Radiotherapy, Leiden University Medical Center, Leiden, Netherlands. [2]Department of Radiation Oncology, The Netherlands Cancer Institute, Amsterdam, Netherlands. [3]Department of Radiology, Leiden University Medical Center, Leiden, Netherlands. [4]HollandPTC, Delft, Netherlands

Abstract

Purpose: Radiation-induced damage to the salivary glands in head and neck (HN) cancer results in functional impairment and consequently in long-term toxicity (xerostomia or dry mouth) that can significantly reduce the patient's quality of life (QoL). The goal of this study was to validate quantitative magnetic resonance imaging (MRI) techniques associated with patient-reported xerostomia after radiotherapy in HN cancer.

Methods: Twenty-six healthy volunteers and sixteen HN cancer patients, who have completed radiotherapy 2 to 3 years before, were included. Subjects were divided into three cohorts: (1) healthy control group, (2) patients without xerostomia and (3) patients with xerostomia. Patients were distributed into cohorts 2 and 3 based on the self-reported xerostomia grade in the QoL questionnaire (EORTC H&N43, question 42), evaluated just before the MRI scanning session. Patients with xerostomia grade≥2 were included in cohort 3. All subjects underwent the same MRI protocol on a 3T MRI scanner (Ingenia, Philips, The Netherlands) using a 16-channel HN coil and including T_1-weighted mDixon QUANT for fat fraction (FF) quantification and T_2 mapping (Table1). Both FF and T_2 maps were computed at the scanner. Parotid and submandibular glands were delineated manually on a T_2-weighted turbo spin echo (TSE) sequence and were rigidly propagated to all maps. Average FF and T_2 values were calculated for all salivary glands. A one-way ANOVA test ($p<0.05$) was used to evaluate significant differences in the FF and T_2 values between the three cohorts. Moreover, the mean doses received by both parotid ($dose_{par}$) and both submandibular ($dose_{sub}$) glands were computed for each patient. To evaluate the effect of the radiotherapy dose on the quantitative MRI measures, the differences in the received dose (Δdose) and the quantitative values (ΔFF and ΔT_2) between ipsilateral and contralateral salivary glands were calculated per patient. A Pearson's correlation test ($p<0.05$) was performed to detect significant correlations between the ΔFF and ΔT_2 with respect to the Δdose.

Table 1. Detailed sequence parameters used for the two quantitative MRI techniques: (1) mDixon QUANT for fat fraction (FF) quantification and (2) T_2 mapping.

Parameter	mDixon QUANT, FF	T_2 mapping
Technique	3D FFE	multi-slice TSE
Orientation	transverse	transverse
Shot mode	-	multi-shot
FOV [mm^3]	400 x 350 x 180	250 x 205 x 180
Acquired voxel size [mm^3]	2.5 x 2.5 x 3	3 x 3 x 4
no. Echoes	6	12
TR / TE / ΔTE [ms]	5.6 / 0.97 / 0.7	7650 / 20 / 10
Flip angle [degree]	3	90
Acceleration factor	SENSE, 2	CS-SENSE, 4
NSA	1	1
Acquisition time [min]	00:24	05:52

Results: Ten patients reported xerostomia and six patients reported no xerostomia. The xerostomia cohort received higher average doses to the salivary glands ($dose_{par}$=19.7±11.4Gy, $dose_{sub}$=51.1±17.3Gy) in comparison with the non-xerostomia cohort ($dose_{par}$=15.5±12.6Gy, $dose_{sub}$=28.5±19.3Gy). The FF and T_2 values of both patient cohorts were significantly higher for all salivary glands ($p<0.05$) compared to the healthy control group (Figure1), whereas the differences between the patients' cohorts were smaller. Nevertheless, slightly higher FF and T_2 values were found between patients with and without xerostomia (Figure1), respectively. A significant correlation ($r>0.6$) was observed between the Δdose and both the ΔFF and ΔT_2 for the parotid and the ΔT_2 for the submandibular glands (Figure2).

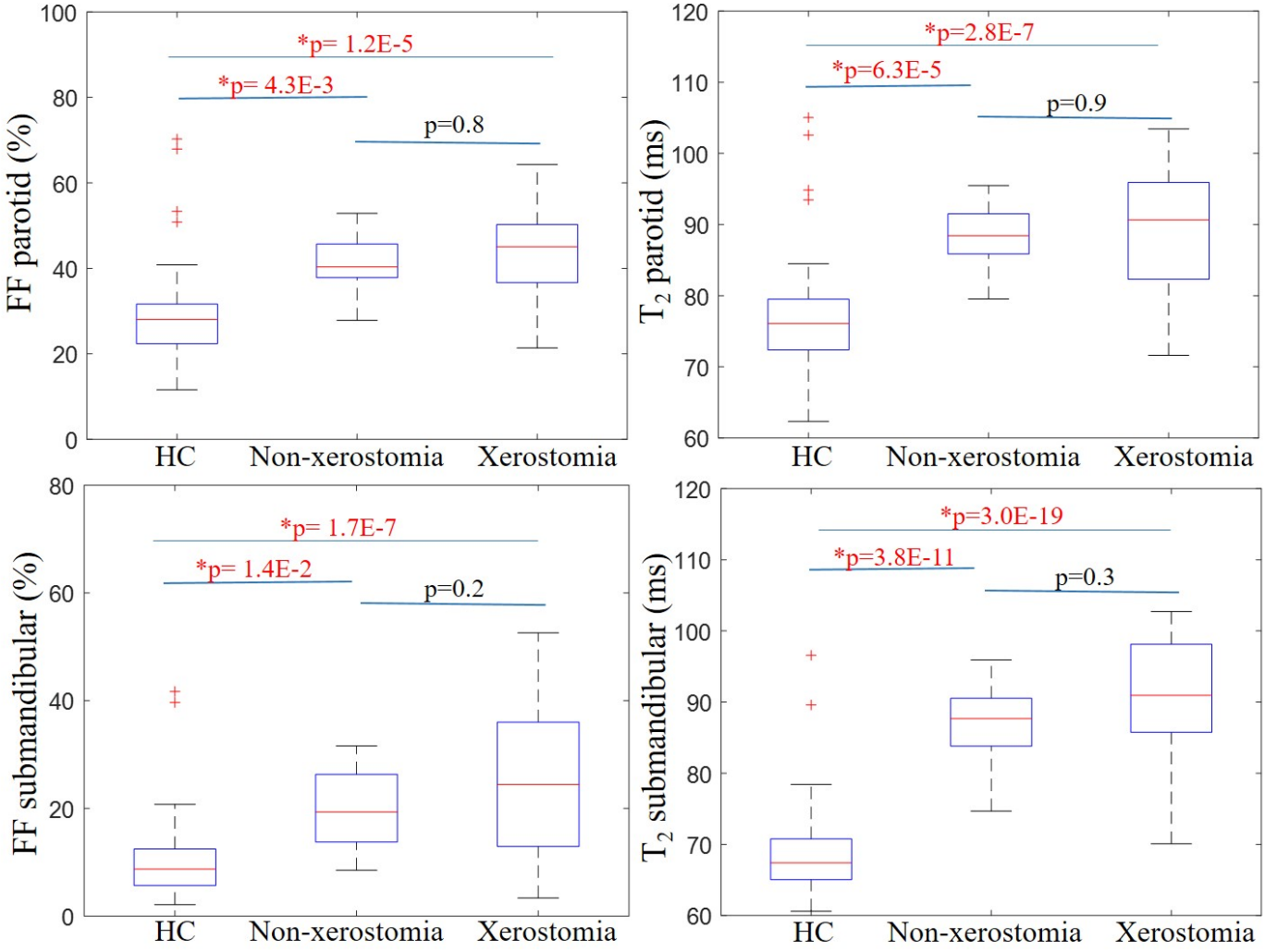

Figure 1. Boxplots of the FF and T_2 values of both parotid and both submandibular glands per cohort: (1) healthy control (HC), (2) patients without xerostomia and (3) patients with xerostomia. Horizontal bar, boxes, whiskers and circles represent median values, 50th and 90th percentiles and outliers, respectively. Significance between cohorts was evaluated using a one-way ANOVA test ($p<0.05$, in red).

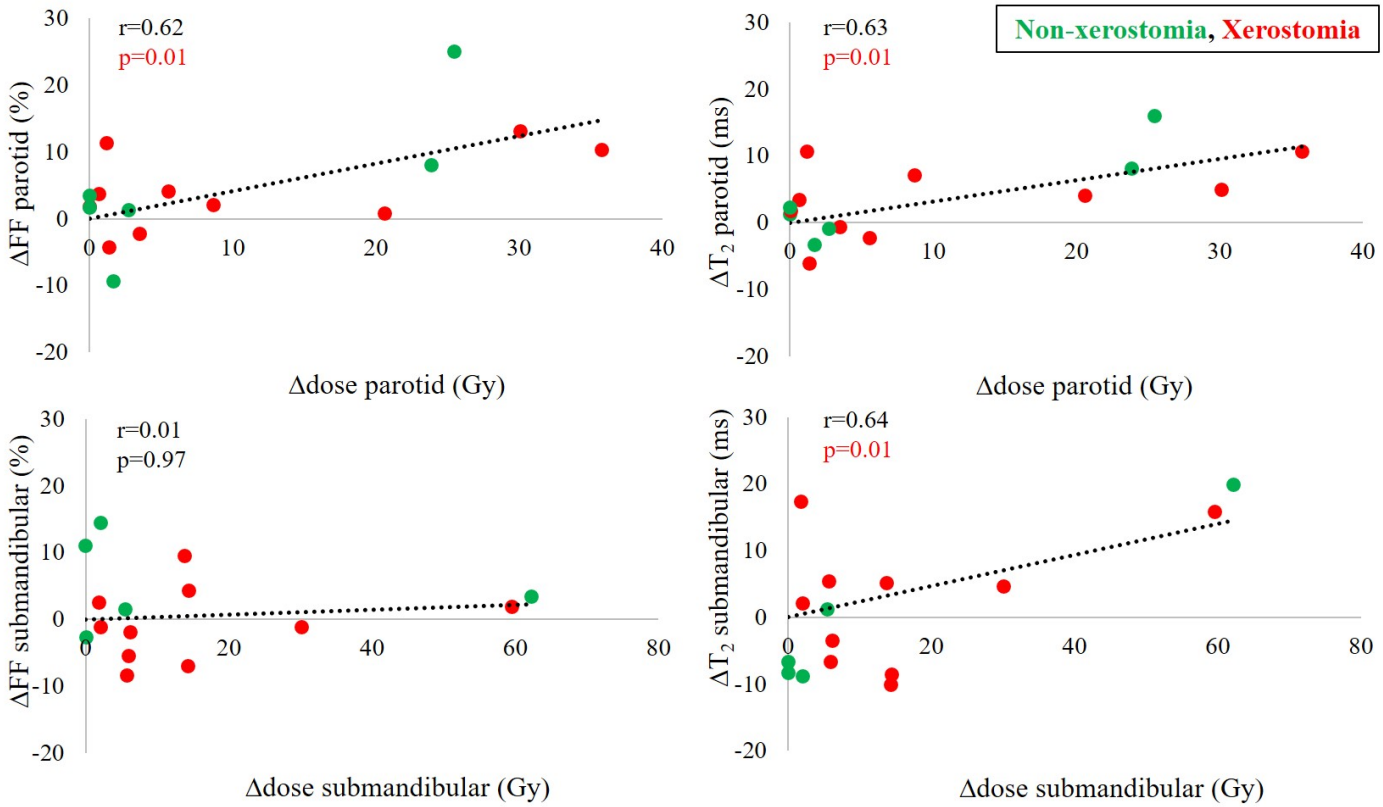

Figure 2. Pearson's correlation test between the differences of the MRI quantitative measures (ΔFF and ΔT_2) with respect to the received dose (Δdose) between ipsilateral and contralateral parotid and submandibular glands. Data points for patients with and without xerostomia are shown in red and green, respectively. Correlation coefficient (r) and p-value ($p<0.05$, in red) are shown.

Conclusions: Higher FF and T_2 values were found for patients reporting xerostomia after radiotherapy when compared to patients without xerostomia and healthy subjects. On a patient level, a positive correlation between the radiotherapy dose and the quantitative values was observed for the majority of the salivary glands. Therefore, FF and T_2 mapping could be potentially used as quantitative MRI measures for noninvasive estimation of radiation-induced salivary gland damage in HN cancer patients.

24

Incremental training strategy of auto-segmentation model for MR-guided adaptive radiotherapy

Mr Wei Zhang Master[1], Dr Cungeng Yang Doctor[1], Dr Zhenjiang Li Doctor[2], Dr Yinglin Peng Doctor[3], Dr Qichao Zhou Doctor[1], Dr Yong Yin doctor[2]

[1]Manteia Technologies Co.,Ltd., Xiamen, China. [2]Shandong Cancer Hospital and Institute, Jinan, China. [3]Sun Yat-sen University Cancer Center, Guangzhou, China

Abstract

Purpose: Accurate and efficient image segmentation is critical for high-quality plan adaptation in MR-guided adaptive radiotherapy (MRgART). Deep learning (DL) based contour propagation has the potential to surpass the registration-based methods, but its feasibility is limited by data availability and model generalizability. To address above issues, this study proposed a daily updated auto-segmentation strategy for MRgART based on incremental training with the patient's previous images and contours.

Methods: The proposed strategy first trained the base model for each patient respectively using the first set of MRI scan and the corresponding contours as inputs. This base model was used to make prediction for the next treatment fraction. With the completion of the current fraction, an incremental training was applied on the base model with the newly approved contours with corresponding images. During incremental training, the updates of the base model were constrained by consistency regularization. This helps the model learn the latest anatomical changes and volumes of the patient. To assess the feasibility of the proposed method, a collection of 8 abdominal patients (each with 5 fractions) underwent MRgART on a 0.35T MRI-Linac was utilized. The organ-at-risks (OARs) and the tumors were manually contoured by senior radiation oncologist and used as ground truth. The model performance was evaluated using Dice Similarity Coefficient (DSC) and Hausdorff Distance (HD).

Results: The proposed method achieved superior performance with DSC (0.854 95%CI:0.803-0.911) and HD95 (6.58mm 95%CI:4.32-8.76mm). As for target volume, the proposed method yielded a DSC of median (0.849, 95%CI:0.796-0.891) and a HD95 of median (3.97mm, 95% CI:3.21mm-4.59mm). The average performance increase in each fraction compared to the previous fraction was 3.2% (DSC) and 6.1% (HD95). It can be seen from the visualized images that the proposed method produces excellent contour smoothness and accuracy.

Conclusions: The proposed incremental training strategy is feasible for auto-segmentation in MRgART with superior performance. It has the potential to improve the efficiency of clinical workflow, reduce the workload of manual delineation and improve the utilization of medical resources.

Table: Evaluation of the auto-segmentation performance for fraction 2-5

* DSC (mean): 0~1, higher is better

* HD95 (mean): 0~INF, lower is better

	Fraction 2		Fraction 3		Fraction 4		Fraction 5	
ROI	DSC	HD95	DSC	HD95	DSC	HD95	DSC	HD95
GTV	0.78	4.24	0.79	3.00	0.80	3.35	0.83	2.99
CTV	0.85	4.24	0.89	3.00	0.90	3.00	0.89	3.35
Kidney_R	0.89	7.34	0.93	2.99	0.96	1.50	0.93	2.99
Kidney_L	0.93	2.99	0.93	2.12	0.94	1.50	0.94	2.12
Stomach	0.74	36.03	0.87	10.48	0.87	5.99	0.81	12.00

SpinalCanal	0.88	3.00	0.92	1.50	0.85	1.50	0.85	1.50
Liver	0.88	24.37	0.93	10.17	0.93	6.71	0.95	5.19
Duodenum	0.61	15.27	0.73	9.00	0.74	8.07	0.76	6.18
LargeBowel	0.70	16.29	0.80	8.06	0.86	3.00	0.79	21.46
V_Portal	0.88	1.50	0.89	2.12	0.88	1.50	0.88	1.50
Average	0.816	11.527	0.867	5.244	0.870	3.612	0.863	5.928

Figure: Visualization of one segmentation sample in fraction 2

* Green: Auto-segmentation

* Red: Manual segmentation

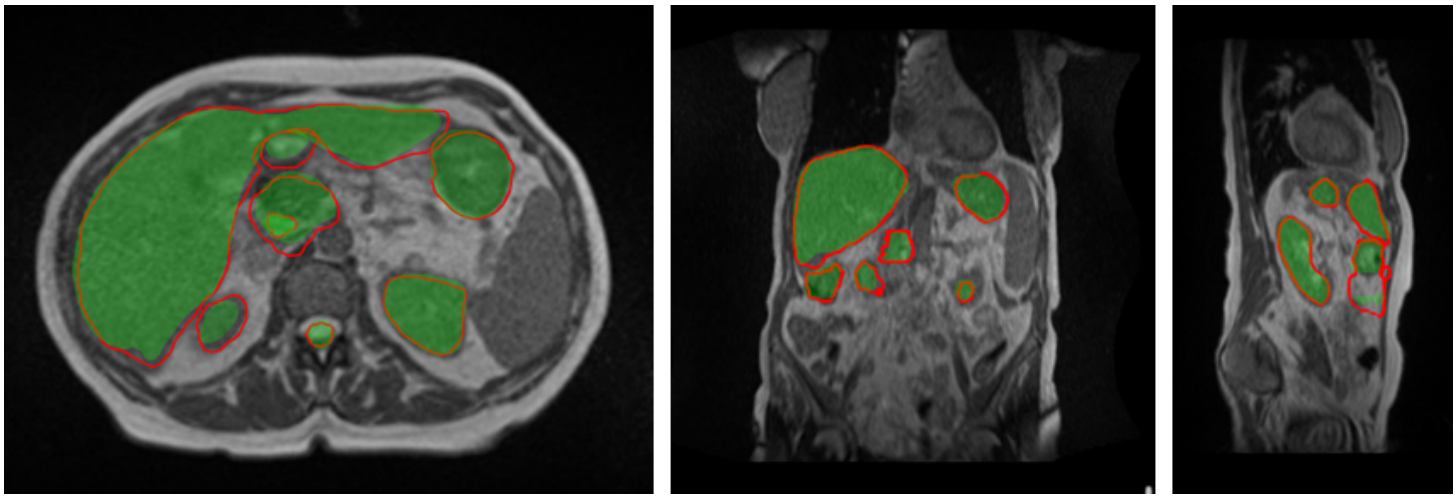

25

An injectable dosimeter for real-time, in-vivo verification of MR-guided radiation therapy

Leonard Kim[1,2], Kirstene Gultian[3], Geoffrey Ibbott[4], Sebastian Vega[3]

[1]MD Anderson Cancer Center at Cooper, Camden, NJ, USA. [2]Cooper Medical School of Rowan University, Camden, NJ, USA. [3]Rowan University, Glassboro, NJ, USA. [4]University of Texas MD Anderson Cancer Center, Houston, TX, USA

Abstract

Purpose: In-vivo patient dosimetry is currently limited to surface and intracavitary measurements, leaving most tumor locations and organs-at-risk inaccessible to dosimetric verification. Combining recent advances in patient-injectable hydrogels, gel dosimetry with MRI readout, and the recent advent of systems that integrate MRI and radiotherapy (MR-Linac), this project reports the development of an injectable hydrogel dosimeter with the possibility of real-time, in-vivo patient dosimetry for MR-guided radiation therapy (MRgRT). The dosimeter incorporates Fricke components into a self-forming, norbornene-tetrazine click chemistry-based hydrogel system. We characterize the system at body temperature over multiple irradiation sessions with clinically relevant injection-to-irradiation time intervals to evaluate radiation response under conditions relevant to in-vivo dosimetry.

Methods: Cuvettes were filled with injectable hydrogels containing Fricke dosimetry components, sealed, protected from light, and stored at room or body temperature. At zero, one-, or two-weeks post-manufacture, samples were irradiated to 16.8 Gy on a 1.5-T MR-Linac with a 7X FFF beam. T1-weighted 3D Fast Field Echo MR images (TR/TE = 11/3.8 ms, 8 signal averages) were obtained before, after, and twice during irradiation with the beam off. This was repeated weekly for a cumulative dose of 84 Gy over five fractions over five weeks. Short-term signal evolution was evaluated by acquiring multiple MR images of a sample up to 72 minutes post-irradiation and again at 24 hours. Finally, a porcine tissue phantom was injected, irradiated, and imaged. This simple experiment demonstrated the ability of our injectable dosimeter to detect a localized MR signal change within an irradiated region of soft tissue.

Results: The intra-fraction change in T1-weighted image intensity was linear with dose. Body temperature samples were twice as sensitive as room temperature samples (data not shown). Dose response decreased between the first and second fractions and was stable afterwards (Figure 1).

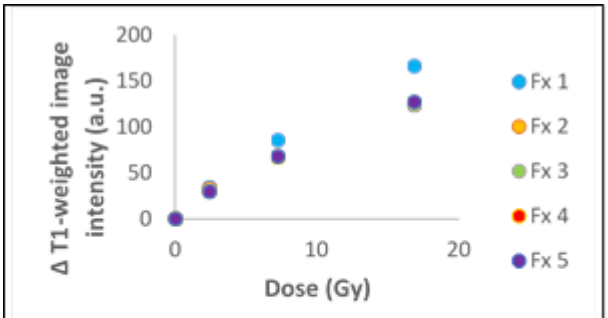

Figure 1 shows average change in T1-weighted image intensity values of the dosimeter at body temperature as a function of radiation dose for five fractions (Fx) delivered one week apart. Dose response decreased between the first and second fractions and was stable afterwards.

The dose responses of all body temperature samples were similar and unaffected by manufacture-to-first fraction time. The MR signal from body temperature samples returned to baseline intensity within 24 hours. Signal development reached 90% immediately post-irradiation and was complete within 3 minutes post-irradiation. Tissue phantom imaging showed the injected gel well-localized in the tissue with clear signal change after irradiation (Figure 2).

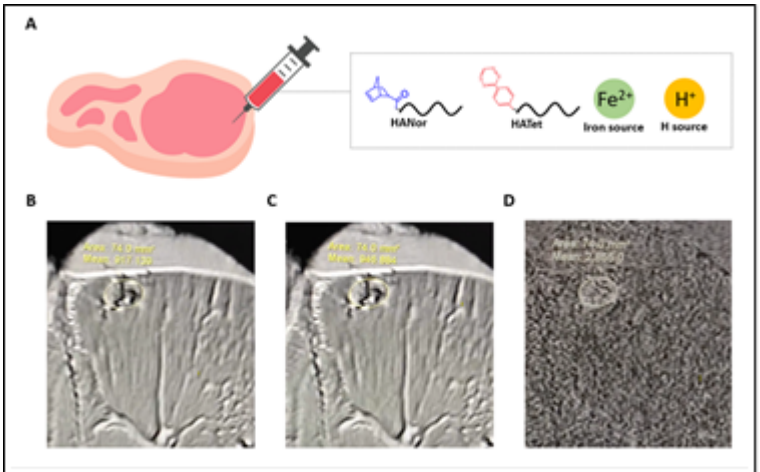

Figure 2 shows **(A)** pork phantom injection schematic followed by **(B)** pre- and **(C)** post-irradiation T1-weighted images. After irradiation, the mean pixel value (AU) within the region-of-interest increased from 917 to 946. **(D)** Rescaled difference image shows the clearly-localized dosimeter and signal change.

Conclusion: A novel injectable, MR-readable dosimeter has characteristics suitable for real-time in-vivo MRgRT dosimetry at clinically relevant dose levels and can be used for multiple irradiations over several weeks. Plans for evaluating cytotoxicity and efficacy in an in-vivo model are underway.

26

Daily 4DMRI motion assessment and the impact on planning target volume for non-gated MRI guided liver stereotactic body radiation therapy

Eenas Omari PhD, Hassan Jassar PhD, Eric Paulson PhD, Michael Straza MD, Xinfeng Chen PhD, Ergun Ahunbay PhD, William Hall MD, X. Allen Li PhD
Medical College of Wisconsin, Milwaukee, WI, USA

Abstract

PURPOSE: Treatment planning for thoracic or abdominal tumors, 4DCT is commonly used to assess the target motion and to generate the internal target volume (ITV) which is utilized for non-gated radiotherapy delivery. With the availability of daily pre-treatment 4DMRI during MRI-guided adaptive RT (MRgART), it is feasible to assess respiratory motion daily. Our objective is to assess daily variations of liver target motion from 4DMRI and to investigate its impact on ITV during non-gated MRgART for liver stereotactic body radiotherapy (SBRT).

METHODS: This work was approved by the Institutional Research Board (IRB) and is compliant with the Health Insurance Portability and Accountability Act (HIPAA) guidelines. A retrospective analysis was performed using 42 4D data sets acquired from 7 liver SBRT patients. 4DCT was acquired during simulation to generate the reference plan and daily respiratory-correlated 4DMRI was acquired pre-treatment using a 3D golden angle radial sequence for all treatment fractions on a 1.5 T MR-linac (Elekta AB). Motion analysis was conducted using MIM software and the maximum motion was defined in the superior-inferior (SI), left-right (LR), and anterior-posterior (AP) directions. The motion difference assessed during 4D CT sim and fractional 4DMRI were compared. Motion differences between simulation and treatment fractions were compared. T-test was utilized for statistical significance ($p<0.05$).

RESULTS: The difference between the SI motion assessed from 4DCT and 4DMRI ranged from -5 to 11 mm. The difference between the LR and AP motion assessed from 4DCT and 4DMR ranged from 0-4 mm The motion difference assessed during 4D CT sim and fractional 4DMRI is shown in Figure 1. 45% of the treatments had statistically significant ($p<0.05$) motion difference compared to the 4DCT. 17% of the fractions require a larger PTV to account for the daily respiratory motion changes based on 3-5 mm ITV to PTV margin.

CONCLUSIONS: Daily variation of liver target motion can be assessed using daily 4DMRI and should be used to generate daily motion adapted PTV for non-gated MRgART for SBRT liver cancer patients, improving tumor targeting and/or normal tissue sparing.

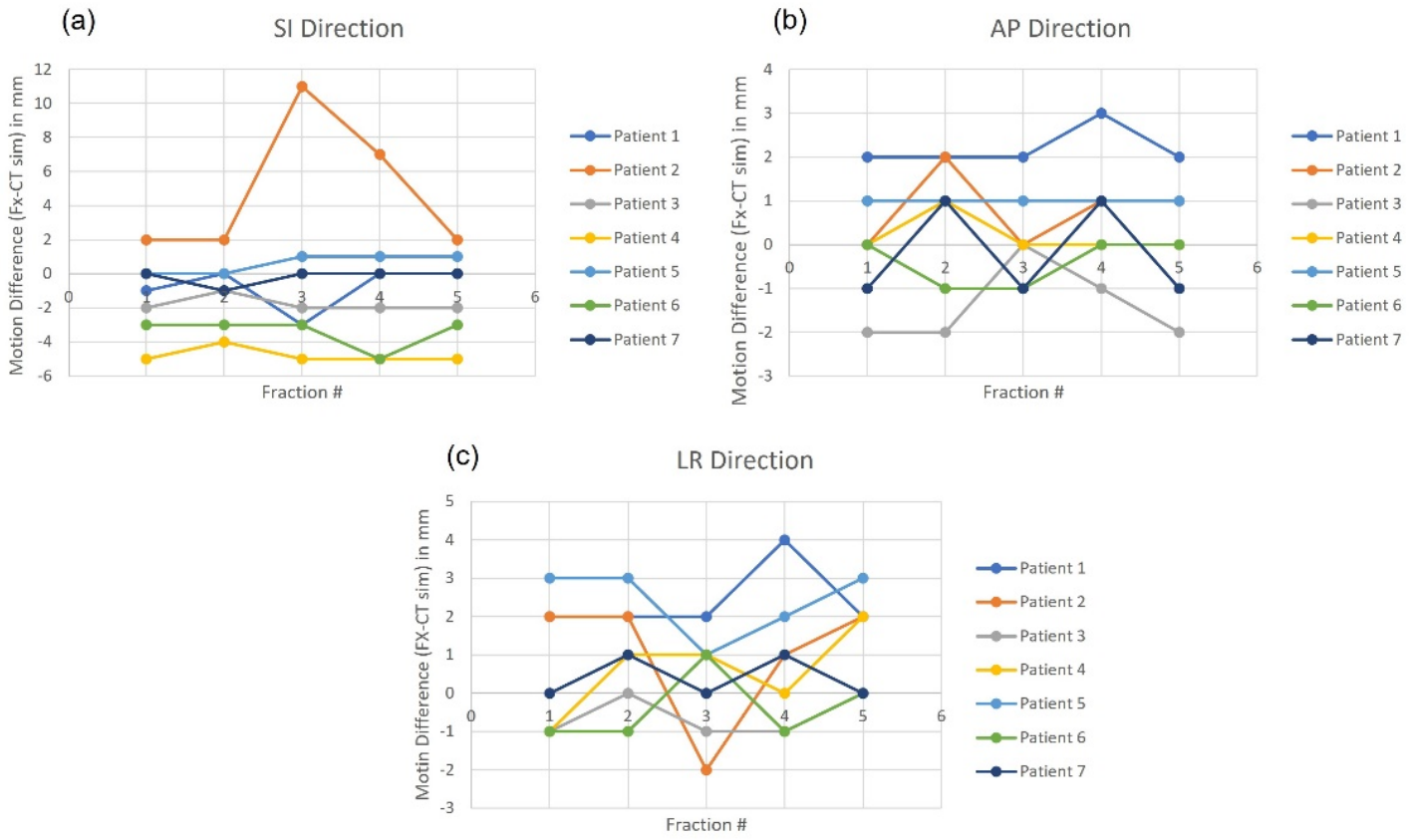

Figure 1: Motion difference between the planning 4DCT and treatment 4DMRI

27

Automated Segmentation of Skeletal Muscle for Sarcopenia Determination in Head and Neck Cancer Patients Using MRI

Medical Student Ali Mohamedi[1,2], Kareem Wahid[1], Dr. Mohamed Naser PhD[1], Dr. Abdallah Mohamed MD/PhD[1], Dr. Clifton Fuller MD/PhD[1]

[1]MD Anderson Cancer Center, Houston, Texas, USA. [2]McGovern Medical School, Houston, Texas, USA

Abstract

Purpose: Sarcopenia, the excessive loss of skeletal muscle mass and function is a well- validated negative prognostic factor for head and neck squamous cell carcinoma (HNSCC) patients. Sarcopenia has a remarkable impact on HNSCC patient survival, quality of life, and risk for post-operative complications, which can alter response to medical treatment. Thus, the determination of sarcopenia using objective measurements is crucial for determining clinically important outcomes in HNSCC patients. Typically, these measurements are made by calculating the cross-sectional area of skeletal muscle at a specific anatomic site using CT imaging. However, there is a growing interest in using MRI for this purpose as to avoid repeated radiation exposure to patients. Moreover, current approaches to determine sarcopenia require manual human curation and segmentation of images, which is time consuming and variable. While approaches have been developed to automate skeletal muscle segmentation for HNSCC patients on CT imaging, to-date, there have been no studies that utilize MRI. Therefore, sarcopenia-related clinical decision-making tools based on MRI are an unmet need.

Methods: Pre-radiotherapy T2-weighted MRI images from 117 patients in Digital Imaging and Communications in Medicine (DICOM) format from HNSCC patients at The University of Texas MD Anderson Cancer Center were curated from a large-scale clinical trial (NCT03145077, IRB: RCR03-0800). The sternocleidomastoid and paravertebral muscles at the C3 vertebral level were segmented on these images using the Velocity AI (Varian) treatment planning toolkit. The DICOM images were then converted to Neuroimaging Informatics Technology Initiative (NIfTI) format using Python v. 3.9. The patients were then further randomly divided into different train (n = 95) and test (n = 22) group sets. Images from the training set were used to develop a deep learning model to automatically determine the C3 vertebra level and subsequently segment skeletal muscle. Model training occurred using a 5-fold cross validation approach. For the final prediction of the test set, the 5 sub-model predictions were combined using an average consensus agreement, The Dice similarity coefficient (DSC) was used to compare the model's output data to the manual segmentation on the test set.

Results: The consensus prediction showed a median value of 2 mm with an interquartile range (IQR) of 2 mm for determination of the C3 vertebral level. Subsequently, the consensus prediction of our sub-models showed a median value of ~0.9 with an interquartile range (IQR) of +/- 0.025 for segmentation of the skeletal muscle.

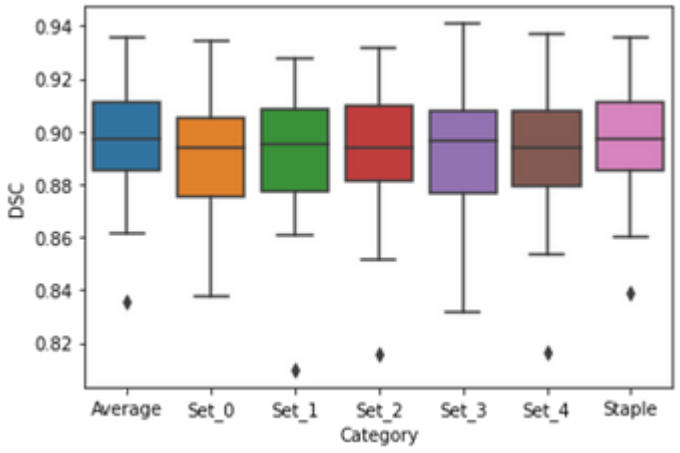

Figure 1. Performance of various models on test set. Dice similarity coefficient (DSC) value distributions shown for each model.

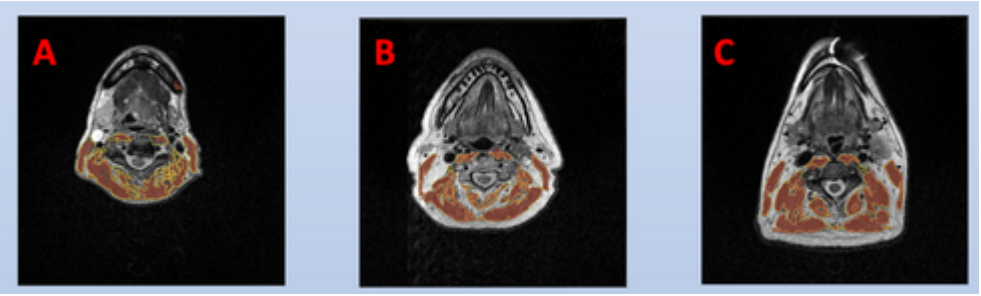

Figure 2. Model performance for skeletal muscle segmentation. [A] Low performance (DSC = 0.83). [B] Medium performance (DSC = 0.89). [C] High Performance (DSC = 0.93). Yellow = ground-truth, red = deep learning prediction.

Conclusion: We demonstrate a deep learning model that can automate the segmentation of skeletal muscle at the C3 vertebral level on MRI with high accuracy. This trained deep learning auto-segmentation model serves as good foundation to provide great benefit to physicians to efficiently assess sarcopenia in HNSCC patients.

28

Oxygen-enhanced (OE) and intravoxel incoherent motion (IVIM) MRI for detection of radiation therapy induced changes in head and neck cancer

Emilia Palmér[1], Jesper Brovall[2], Oscar Jalnefjord[1,2], Karin Petruson[3], Fredrik Nordström[1,2], Anna Karlsson[1,2], Maria Ljungberg[1,2], Maja Sohlin[1,2]

[1]Department of Medical Radiation Sciences, Institute of Clinical Sciences, Sahlgrenska Academy, University of Gothenburg, Gothenburg, Sweden. [2]Department of Medical Physics and Biomedical Engineering, Sahlgrenska University Hospital, Gothenburg, Sweden. [3]Department of Oncology and Radiotherapy, Institute of Clinical Sciences, Sahlgrenska Academy, University of Gothenburg, Gothenburg, Sweden

Abstract

Purpose

Relative changes of MR derived biomarkers for tumor oxygenation during treatment might be predictive for radiation therapy (RT) response and clinical outcome, and hence act as a noninvasive instrument for individualized RT. The aim of this study was to evaluate the feasibility of Oxygen-Enhance MRI (OE-MRI), intravoxel incoherent motion (IVIM), and diffusion kurtosis imaging (DKI) for early response assessment in head and neck (HN) cancers.

Methods

For seven HN cancer patients, morphological (T2W DIXON TSE and contrast enhanced T1W Dixon VIBE) and functional (OE-MRI, IVIM/DKI, and dynamic contrast enhanced (DCE)) MRI were acquired before and approximately two weeks after start of RT, using a 1.5 T Siemens Aera wide bore MR-system (Siemens Healthcare, Erlangen, Germany) and a 20-channel head coil. OE-MRI was performed by acquisition of five dynamic MP2RAGE images (TOLD-series) with breathing of 100% O2 during dynamic 2-4 and dynamic 5 acquired approximately 22 minutes after O2 breathing. A single shot echo planar imaging sequence with four b-values (b = 0, 110, 650 and 1500 s/mm2) and six diffusion weighting directions was used for the IVIM/DKI measurements.

The DCE-data was used to classify voxels as perfused or non-perfused. T1-maps were created from the TOLD data by simulations of the Bloch equations for the MP2RAGE sequence and subsequently used for derivation of longitudinal MRI relaxation rate (ΔR1) and fraction of voxels within each tissue classification (normoxia, hypoxia, and necrosis). The IVIM diffusion (D), capillary perfusion fraction (f), and kurtosis (K) effects were evaluated by segmented fitting of the data to the IVIM/DKI signal representation.

Results

OE-MRI and IVIM/DKI imaging were feasible in a clinical setting with successfully acquired OE-MRI data for six out of seven study patients (Figure 1), and IVIM/DKI data for all study patients. No clear change in population mean ΔR1 or in the fraction of hypoxic voxels for pre- and mid-RT tumors was identified in this small-scale feasibility study. A general increase in population means of D and f, and a decrease in population mean of K was noticed over the course of RT (Table 1 - supporting document), although not statistically proven. For one study patient, biomarker changes corresponding to a prediction of early locoregional control according to literature were observed. As the treatment outcome of the study patients so far is not known, no interpretation of unsuccessful/successful tumor response could be established.

Conclusion

The implementation of OE-MRI, IVIM/DKI imaging is clinically feasible, and changes of the derived biomarkers could be observed during the course of RT treatment. By introduction of parameter maps (Figure 1C; Figure 2) that have the

potential to visualize regions of hypoxia within the tumor, RT planning of localized treatment intensification or de-escalation strategies and thereby adaptive individualized RT may be enabled. Larger study cohort and future work regarding correlations of biomarkers changes to the treatment outcome are required to conclude the final prediction value of OE-MRI, IVIM/DKI imaging for early response assessment.

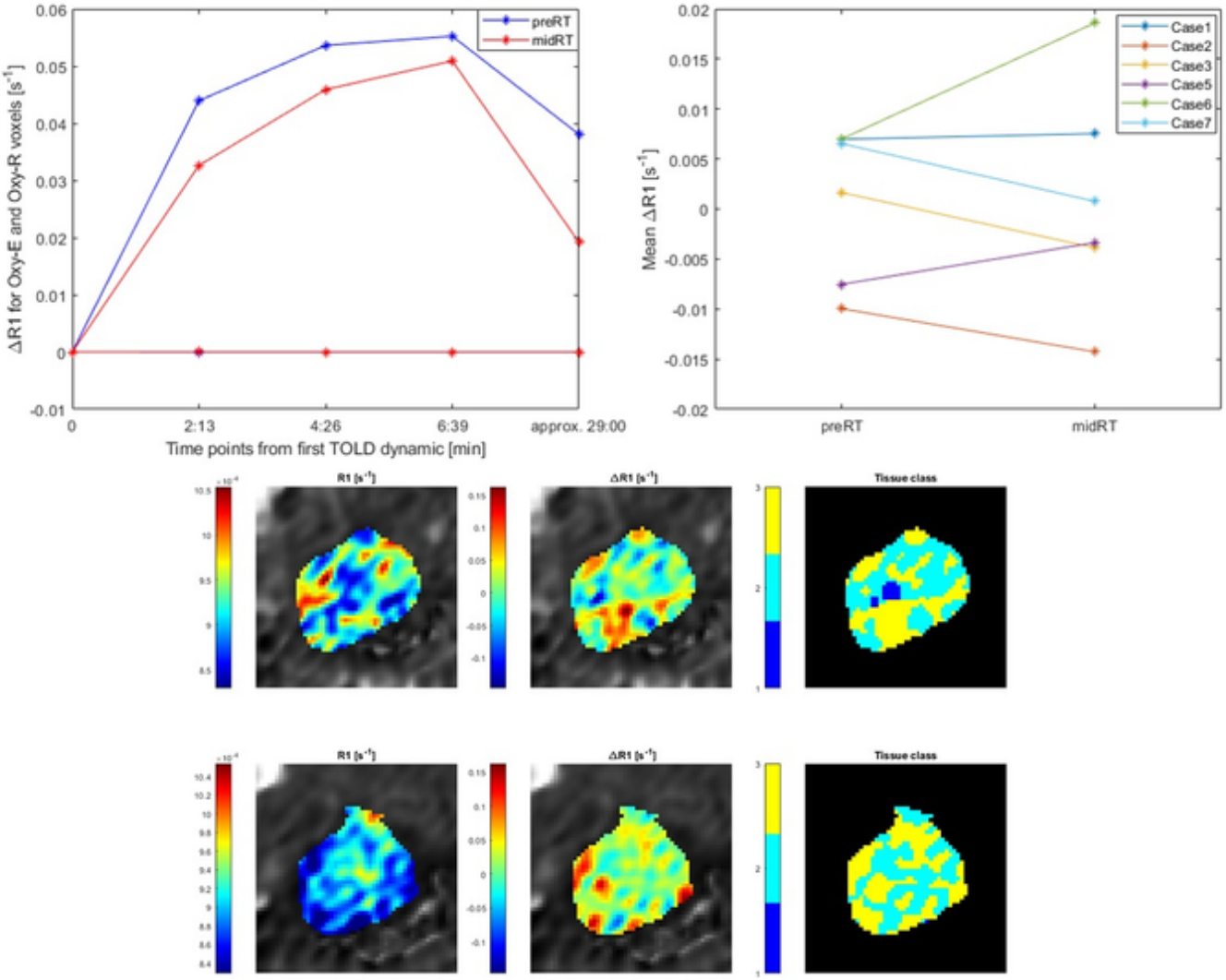

Figure 1. (A) The mean ΔR1 for Oxygen-enhancing (Oxy-E) classified voxels and oxygen-refractory (Oxy-R) classified voxels for each timepoint in the dynamic TOLD series for one included study patients. The blue curve represents mean ΔR1 estimated at the initial MRI session, and the red curve represents mean ΔR1 at the mid-treatment MRI examination. (B) Individual mean ΔR_1 within GTV reduced with a two-pixel thick outer shell to prevent impact of surrounding normal tissue (rGTV), potentially inaccurately included in the segmented GTV of the mean TOLD data, for both pre- and mid-radiation therapy (RT) MRI sessions for all study patients. (C) Pre-treatment (upper row) and mid-treatment (lower row) OE-MRI parameter maps of rGTV for the same study case as in (A). The values presented are R1-values of the first TOLD dynamic (left column), the ΔR1 in the MTOLD (middle column), and voxel tissue classification (right column). The classifications were Oxy-E (yellow), Oxy-R (light blue), and necrosis (dark blue) voxels. A decrease in the R1-values and an increase in the ΔR1 can be seen after 10 fractions of radiation therapy. Also, necrosis classified voxels was non-existing in the mid-treatment imaging session for this particular case. Note the different intensity scales for R1 and ΔR1-values.

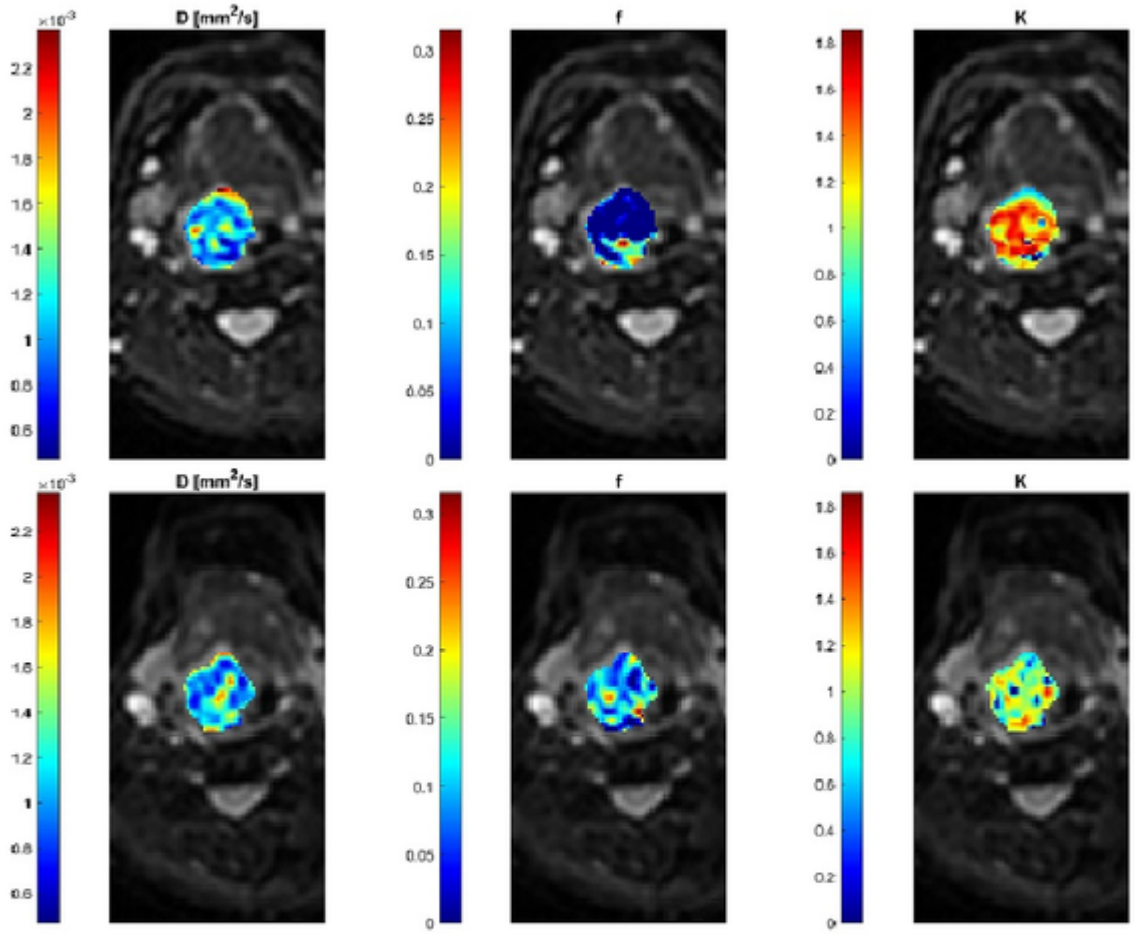

Figure 2. Pre-treatment (upper row) and mid-treatment (lower row) IVIM/DKI parameter maps for study the same study case as in figure 1. The values presented are diffusion (left column), perfusion fraction (middle column), and kurtosis (right column). An increase in diffusion and perfusion fraction can be seen at the mid-treatment imaging session. On the contrary, the kurtosis decreased in-between the two imaging sessions. Note the different intensity scales for diffusion, perfusion fraction and kurtosis.

Table 1. Pre- and mid-treatment intravoxel incoherent motion (IVIM) and kurtosis parameters. Data is presented as mean value and relative change within the modified gross tumor volume (mGTV).

	D [·10⁻³ mm²/s]			*f [%]*			*K*		
	Pre-RT	Mid-RT	Relative change [%]	Pre-RT	Mid-RT	Relative change [%]	Pre-RT	Mid-RT	Relative change [%]
Case 1	1.9 ± 0.6	2.0 ± 0.5	6.5	5.5 ± 7.2	7.0 ± 7.4	25.9	0.7 ± 0.2	0.6 ± 0.2	-14.3
Case 2	1.0 ± 0.3	1.3 ± 0.5	30.7	2.8 ± 5.5	4.6 ± 8.8	66.2	1.1 ± 0.7	0.7 ± 0.5	-32.0
Case 3	2.5 ± 0.6	2.6 ± 0.4	6.0	2.8 ± 5.1	2.0 ± 4.6	-27.9	0.4 ± 0.2	0.3 ± 0.2	-9.1
Case 4	1.1 ± 0.5	1.6 ± 0.4	41.4	13.8 ± 10.5	5.7 ± 6.1	-58.8	0.4 ± 0.4	0.9 ± 0.8	109.3
Case 5	2.0 ± 0.5	2.1 ± 0.8	6.2	16.7 ± 13.6	16.6 ± 14.9	-0.7	0.8 ± 0.3	1.1 ± 1.7	39.2
Case 6	1.0 ± 0.4	1.1 ± 0.4	16.0	6.2 ± 8.2	12.1 ± 8.4	94.2	1.1 ± 0.7	0.8 ± 0.4	-30.1
Case 7	1.2 ± 0.3	1.4 ± 0.3	16.9	8.7 ± 8.7	12.6 ± 10.3	44.1	1.1 ± 0.4	0.8 ± 0.3	-27.3
All cases	1.5 ± 0.6	1.7 ± 0.5	14.2	8.1 ± 5.4	8.7 ± 5.2	7.0	0.8 ± 0.3	0.7 ± 0.2	-6.3

29

A Workflow to Perform MRI-guided Adaptive Radiotherapy for Abdominal SBRT using Deformable Dose Accumulation with Confidence Intervals

Juan A. García-Alvarez PhD, Hualiang Zhong PhD, X. Allen Li PhD, Kristofer Kainz PhD
Medical College of Wisconsin, Milwaukee, WI, USA

Abstract

Purpose: When treating pancreatic tumors using MR-guided adaptive radiation therapy (MRgART), deformable image registration (DIR) based dose accumulation (DDA) potentially allows more accurate composite-dose calculation. We present a MRgART DDA workflow for pancreas SBRT, including DDA uncertainty confidence bounds.

Methods: The workflow requires an up-front definition and delineation of organs-at-risk (OARs) proximal to the PTV (typically duodenum and stomach for pancreas SBRT), an optimal MRI-to-MRI DIR algorithm, the resultant deformation vector fields used to map dose from different treatment fractions to a reference image, and DDA uncertainty calculations that can be performed in the absence of ground-truth registration. The optimal MRI-to-MRI registration algorithm was determined by comparing the Jacobian determinant (JD), mean distance-to-agreement (MDA), and Dice similarity coefficient (DSC) upon transferring the OARs using the contour-based (CB) and multi-modality image (MM) DIR algorithms implemented in MIM software (MIM, Inc., Cleveland, Ohio). Two methods were used to compute DDA uncertainties. The DVH overlay technique estimates the volumetric OAR accumulated dose uncertainty by comparing the source-image DVH calculated using native source-image dose and warped-image contours with the target-image DVH calculated using warped source-image dose and native target-image contours. The inverse consistency error (ICE) radius technique calculates an uncertainty in the dose warped to a given point (voxel) of interest (POI) by considering the dose grid points within a sphere centered at the POI landing coordinates in the source image; the radius of the sphere correlates with the ICE at the POI. Anatomical landmarks identified in a pair of daily MRs were utilized to validate the correlation between the target registration error (TRE) and ICE.

Results: The MM-DIR yielded the most favorable results based on JD variation and ICE, indicating more physiologically plausible deformations inside the abdominal structures. Smaller MDA and greater DSC are obtained with CB-DIR; higher DIR accuracy along the boundaries is advantageous for tracking and accumulating OARs maximum dose metrics. The ICE-TRE Pearson correlation coefficients were 0.67 and 0.62 utilizing MM-DIR and CB-DIR (P-values<0.001), and the TRE was greater than the ICE by approximately a factor of 2.0 (MM) and 1.4 (CB). Using the ICE-radius technique, uncertainties in the OARs D0.03cc and D1cc were around 1% to 2% (MM) and 3% to 4% (CB) for the duodenum and approximately 3% to 6% (MM) and 3% to 5% (CB) for the stomach. Using the DVH overlay technique, the uncertainty of the accumulated DVH across all OAR dose values was approximately 1% and 5% for the duodenum and stomach, respectively.

Conclusion: We demonstrated a clinical workflow to estimate DDA uncertainty during MRgART for abdominal tumors based on DIR of daily MRIs. The ICE-radius technique is useful for calculating the uncertainty of the OAR maximum point dose as well as tracking the maximum-dose location. The workflow's DDA uncertainty calculations improve upon the conservative summation of individual daily OAR maximum doses to estimate cumulative maximum dose. Accurate DDA uncertainty estimates potentially allow for more aggressive dose escalation during the treatment course, along with improved bias dose for retreatment planning.

31

Fast motion-resolved 4D MRI using deep learning reconstruction without explicit data consistency on an MR-Linac system

Victor Murray[1], Can Wu[1], Syed S. Siddiq[1], Ricardo Otazo[1,2]

[1]Department of Medical Physics, Memorial Sloan Kettering Cancer Center, New York, NY, USA. [2]Department of Radiology, Memorial Sloan Kettering Cancer Center, New York, NY, USA

Abstract

Purpose

Motion-resolved 4D MRI is a useful tool for radiation therapy of tumors affected by respiratory or cardiac motion. 4D MRI can be used to personalize treatment planning according to the motion range of the tumor and organs at risk [1]. The implementation of 4D MRI on an MR-Linac [2] system would enable to adapt radiation delivery to the motion of the day. However, current state-of-the-art 4D MRI methodology, such as XD-GRASP [3], requires relatively long acquisition times and particularly long reconstruction times, which prevent use in clinical practice.

The purpose of this work is to develop a deep learning-based 4D MRI reconstruction method named MRI-movienet to accelerate the acquisition and significantly reduce the reconstruction time compared to XD-GRASP. The main idea of MRI-movienet is to exploit space-time-coil correlations in the image domain without enforcing k-space data consistency.

Methods

Seventeen free-breathing datasets were acquired on 12 patients with pancreatic cancer (5 patients with two separate scans on different days) on a 1.5T MR-Linac system (Elekta) using a 3D T1-weighted golden-angle stack-of-stars acquisition (cartesian kz and radial ky-kx) with the following parameters: TR/TE = 5.0/2.1ms, flip angle = 12°, voxel size = 1.5×1.5×4.0mm3, number of radial spokes = 905, bandwidth = 720Hz/pixel, total scan time = 5:05min. XD-GRASP [3] reconstruction with 10 motion states, including motion detection, motion sorting, and iterative compressed sensing, was performed.

Our proposed deep learning reconstruction technique, MRI-movienet, replaces the iterative compressed sensing reconstruction in XD-GRASP. MRI-movienet uses a modified U-net architecture with residual learning blocks to exploit correlations in a 5D image space (x, y, z, time, coil) without enforcing data consistency in k-space to remove aliasing artifacts from undersampling accelerated data acquisition and reconstruct an unaliased motion-resolved 4D image. The network input is the 5D images from 600 spokes (acceleration factor = 1.5). The target is XD-GRASP reconstruction using 905 spokes (Figure 1). 14 datasets were employed for training, and 3 datasets (patients not included in training) were used to test the performance of the MRI-movienet. Training was performed slice-by-slice with about 700 slices total (50 slices per dataset).

Results

MRI-movienet reconstruction time of the entire dataset was only 1.65 seconds, which was significantly lower than the iterative XD-GRASP reconstruction time in the order of tens of minutes. The image quality of MRI-movienet is comparable to the one from XD-GRASP, despite the 1.5-fold acceleration of data acquisition and short reconstruction time (Figure 2). Table 1 presents quantitative metrics with a high structural similarity index measure (SSIM) [4] and peak-signal-to-noise ratio (PSNR) [5] for the three testing cases.

Conclusion

This work demonstrated the application of a novel deep learning architecture that exploits space-time-coil correlations without k-space data consistency to generate motion-resolved 4D MRI with 1.5x acceleration in data acquisition and significantly faster reconstruction times (about 1.65 seconds) than the standard XD-GRASP method on an MR-Linac system. The proposed MRI-movienet approach would enable 4D MRI with clinically feasible acquisition and reconstruction times to perform adaptive radiotherapy on an MR-Linac system.

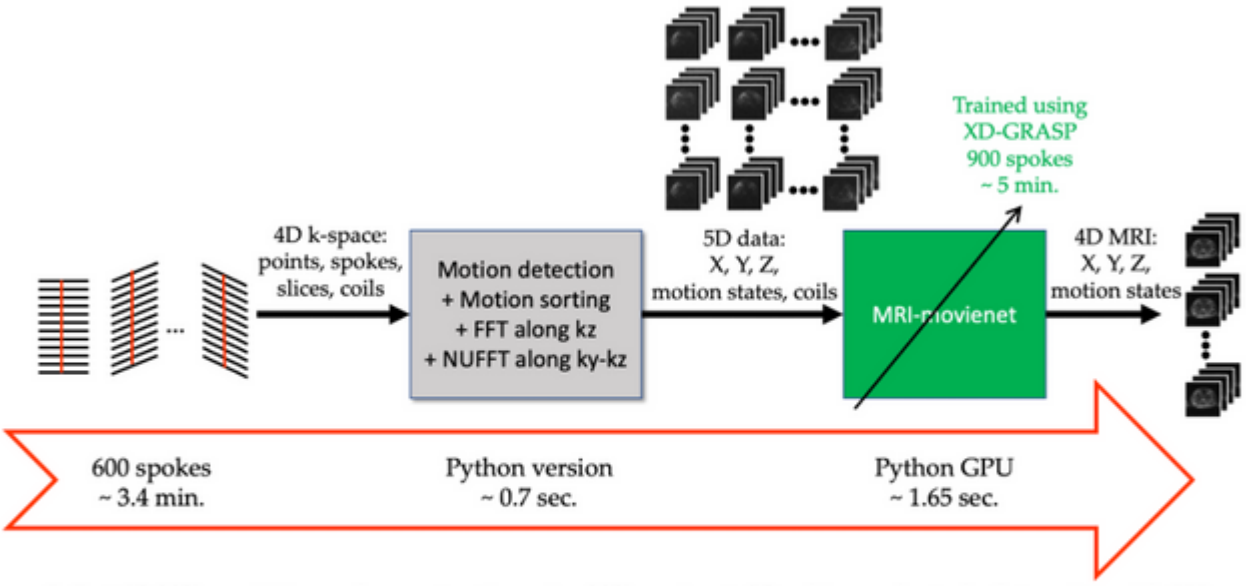

Figure 1. Fast 4D MRI acquisition and reconstruction using MRI-movienet. 3D golden-angle stack-of-stars data with 600 spokes are acquired during 3.4 minutes. Then, a motion signal is computed directly from the data (detection), the acquired data are sorted into motion states, FFT is applied along the kz dimension, and NUFFT is applied for each slice to produce a 5D array (x, y, z, time, coil) - total pre-processing time is approximately 0.7 seconds). Finally, MRI-movienet reconstructs the 4D image in about 1.65 seconds. More details about the MRI-movienet technique are presented in the attached supporting document.

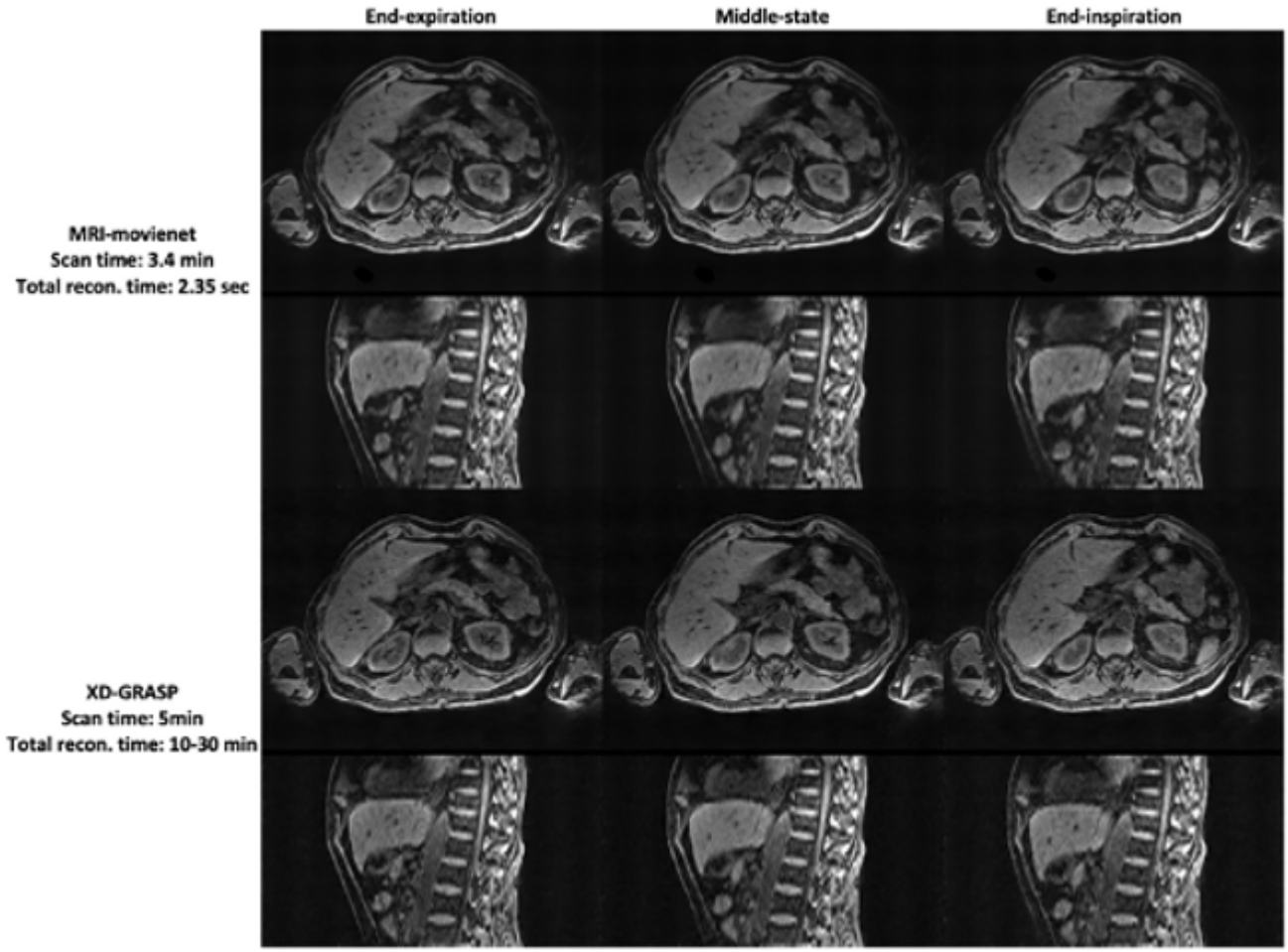

Figure 2. 4D MRI reconstruction for one patient using MRI-movienet and XD-GRASP. Three respiratory motion states (end-expiration, middle-state, and end-inspiration) for axial and sagittal orientations are shown for each reconstruction method.

Table 1. Quantitative metrics in the 3 testing cases between the proposed MRI-movienet with 600 spokes and the reference XD-GRASP with 900 spokes using structural similarity index measure (SSIM) and peak-signal-to-noise ratio (PSNR).

Test case	SSIM	PSNR
1	0.94	35.37
2	0.95	35.04
3	0.95	35.00

32

A comprehensive quantification of the dosimetric impact of electron streaming for MRI-guided proton therapy

Dr Bradley Oborn Medical Radiation Physics[1,2,3], Prof Paul Keall PhD[4,5]

[1]University of Wollongong, Wollongong, NSW, Australia. [2]Helmholtz-Zentrum Dresden-Rossendorf- Institute of Radiooncology-OncoRay, Dresden, Saxony, Germany. [3]Wollongong Hosptial, Wollongong, NSW, Australia. [4]Image X Institute, University of Sydney, Sydney, NSW, Australia. [5]Ingham Institute for Applied Medical Research, Liverpool, NSW, Australia

Abstract

Purpose: Electron streaming in MRI-linac systems is a well known phenomenon, and in certain cases can lead to undesirable increases in patient skin dose. The aim of this work is to investigate through accurate modeling the impact of electron contamination streaming on the patient beam entry side skin dose from therapeutic proton beams delivered in the context of real-time MRI-guidance.

Methods: To quantify the electron contamination streaming effects a physically rigorous Monte Carlo model was developed. The model utilized magnetic field maps directly derived from a suitable split-bore MRI system that would allow pencil beam scanning from either perpendicular or inline with the MRI imaging field. The electron streaming effects was computed with 5 variables: (1) inline and perpendicular beam orientation, (2) field strength (0-1.5T) (3) beam energy (70 - 214 MeV), (4) field size (5x5 cm - 20x20 cm) and (5) scanning treatment plans types (6 selected). The plans were simulated in a 30 cm3 water phantom located at MRI isocentre. The beam entry side skin dose was extracted at a depth of 70 um using scoring voxels of 10 um thickness.

Results: The electron contamination produced by therapeutic proton beams has the favorable property that their maximum energy is less than 1/10th of those produced by a 6 MV photon beam (0.35 MeV vs 5 MeV respectively). For the perpendicular orientation, the bulk of the electron contamination is swept away from the proton beam before reaching the surface. Therefore generally a reduction (1-5%) in skin dose is observed, with the only exception the 1.5 T plan with shallow treatment target (2% increase). For the inline orientation systems the electrons generated in the 10-20 cm above the phantom are confined by the magnetic field and propagate towards the entry surface without divergence. Of all the plans examined a maximum skin dose increase of 5% in seen in this orientation (see figure 1). There is no significant dependence of the small skin dose increases across the plans with different energy proton beams or field sizes.

Conclusion: This work presents for the first time detailed modelling of the beam entry side electron streaming effect that is predicted to occur in MRI-integrated proton beam therapy. From the broad array of scenarios modelled, no significant (> 5%) skin doses increases were predicted to occur at the 70 um epidermal layers of the skin structure. These results support the ongoing development of MRI-integrated proton therapy systems and dose planning optimisations that will be required.

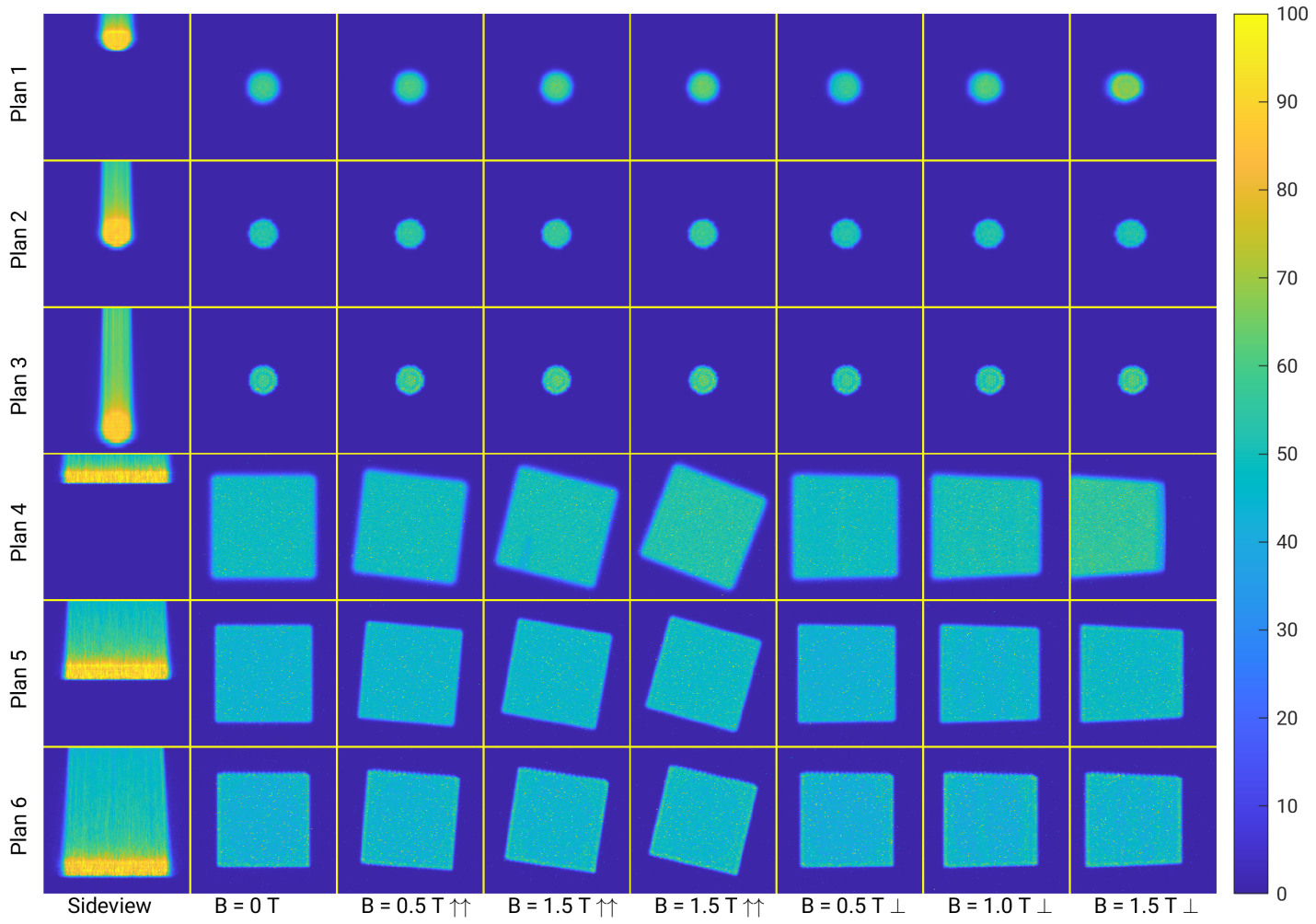

Figure 1. A summary of the 70 µm surface dose for the 6 plans created. The first (left) column shows a central slice from sideview of the dose in the phantom for each of the 6 plans as labelled on the left side. Columns 2-8 present a beam view of the dose in the 10 µm scoring volume centered at 70 µm depth for each of the magnetic fields as shown along the bottom.

33

Treatment margins for different adaptation strategies in MRI-guided online adaptive radiotherapy for prostate cancer

Mathijs Dassen[1], Tomas Janssen[1], Martijn Kusters[2], Floris Pos[1], Linda Kerkmeijer[2], Uulke Van Der Heide[1], Erik Van Der Bijl[2]

[1]The Netherlands Cancer Institute, Amsterdam, Netherlands. [2]Radboud University Medical Center, Nijmegen, Netherlands

Abstract

Purpose: In MRI-guided online adaptive radiotherapy of prostate carcinoma (PCa) various workflows are available for online plan adaptation. In the adapt-to-shape (ATS) workflow, delineations are adjusted online to the daily anatomy and the plan is re-optimized. A downside of this workflow, however, is that it is time-consuming, adding approximately 20 minutes to the total time per fraction. Simpler alternative strategies are the adapt-to-position (ATP) or adapt-to-rotation (ATR) workflow which do not require re-delineation and are considerably more time-efficient. The potential benefit of ATS over the other two strategies would be a gain in precision allowing for smaller treatment margins. However, the exact additional benefit in terms of the required margins in these respective workflows still needs to be established. Therefore, the aim of this study was to quantify the relative gain of online adaptive workflows used in MRI-guided adaptive radiotherapy for PCa by evaluating the margins required to accommodate intra-fraction motion of the GTV, CTV including prostate (CTVpros) and CTV including both prostate and seminal vesicles (CTVpros+sv).

Methods: Clinical delineations of 24 patients with intermediate- and high-risk PCa, treated using ATS on the 1.5T Unity MR-Linac were used for analysis. All delineations of the GTV, CTVpros and CTVpros+sv were extracted, which consisted of delineations of the planning-MRI and manually adjusted delineations of the adaptation- and during-MRIs. For the GTV, clinical delineations were evaluated as ATR structures. Since the ATP and ATR workflows were not clinically performed, we automatically generated the structures associated with these workflows using rigid transformations from the planning-MRI to the online MRIs (Fig.1). These clinical and simulated GTV/CTV delineations on the adaptation-MRI were used to define PTV structures with isotropic margins ranging 0-5mm in steps of 0.5mm. Subsequently, these were compared to their corresponding GTV/CTV delineations on the during-MRI. Target coverage was evaluated for each margin by calculating the mean volumetric overlap over 5 fractions per patient. For each margin we determined the overlap reached by >90% of the population.

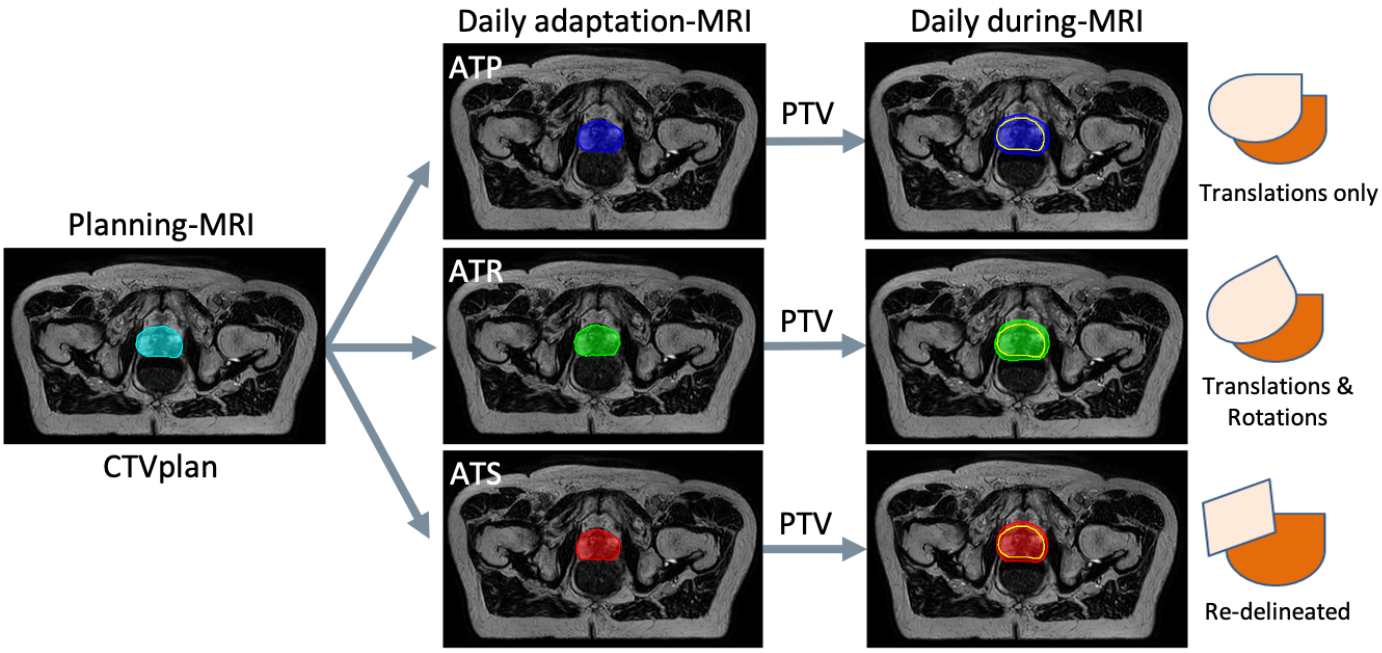

FIGURE 1. Schematic overview of the delineated and simulated contours. The CTV of the planning-MRI (CTVplan) and the re-delineated CTVs of the adaptation- and during-MRI were extracted from the clinical ATS data. The ATP and ATR CTVs were generated by either a rigid translations-only registration (ATP) or using both translations and rotations (ATR). PTVs were created for each CTV for the range of margins up to 5mm. Subsequently, the volumetric overlap of the PTVs as created for each of the adaptation strategies were evaluated with respect to their corresponding delineation on the during-MRI.

Results: The results are summarized in Fig.2. Analysis of the target coverage showed that the PTV margin required to cover ~95% of the CTVpros was equal (2.5mm) for all workflows. In case of the CTVpros+sv, the PTV margin required to cover ~95% increased to 5.0, 4.0 and 3.0 mm in the ATP, ATR and ATS workflow, respectively. For the GTV, for which usually no margin is used for integrated boosting, target coverage improved by 6.4%-point in the ATR workflow compared to the ATP workflow in case no margin was applied.

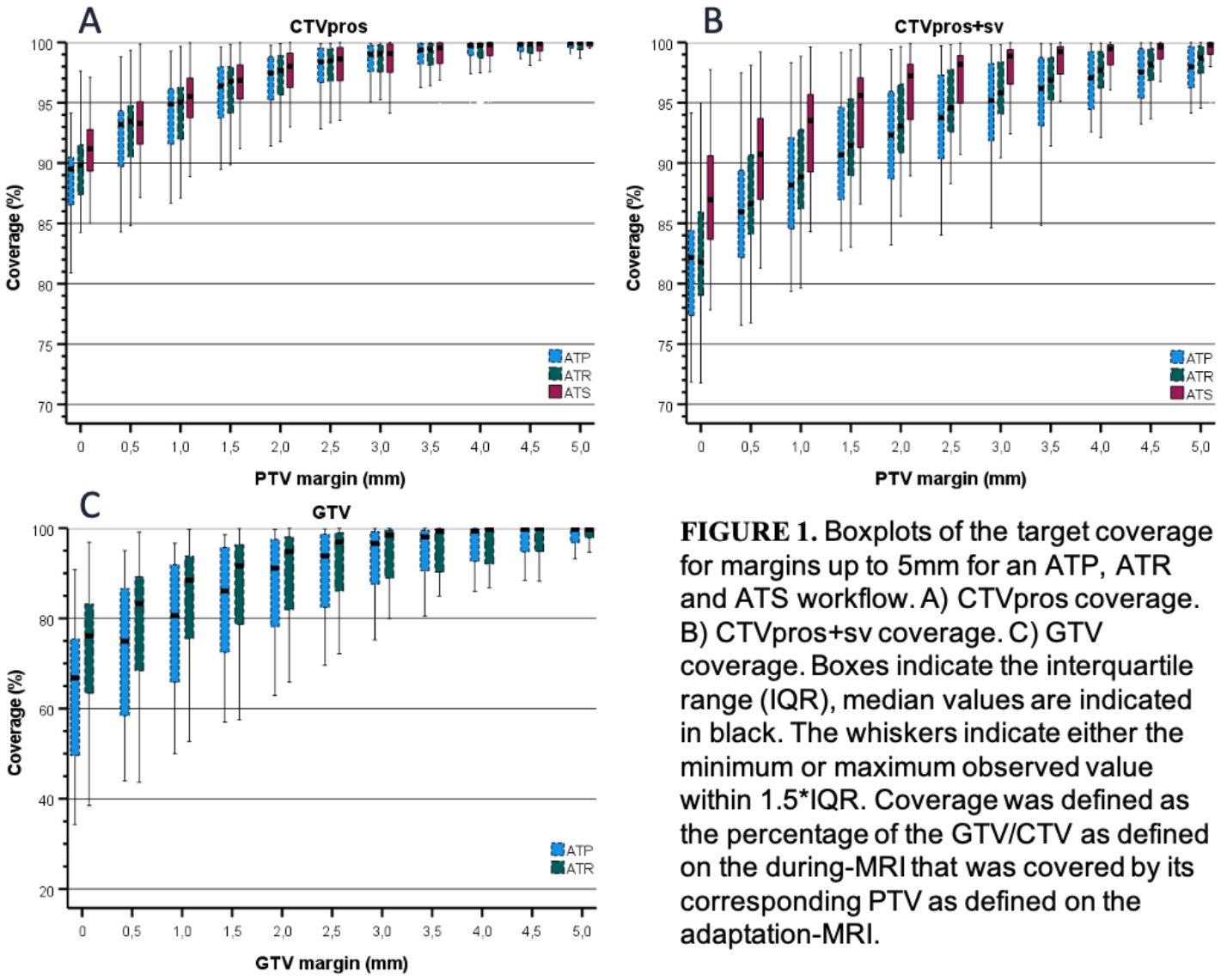

FIGURE 1. Boxplots of the target coverage for margins up to 5mm for an ATP, ATR and ATS workflow. A) CTVpros coverage. B) CTVpros+sv coverage. C) GTV coverage. Boxes indicate the interquartile range (IQR), median values are indicated in black. The whiskers indicate either the minimum or maximum observed value within 1.5*IQR. Coverage was defined as the percentage of the GTV/CTV as defined on the during-MRI that was covered by its corresponding PTV as defined on the adaptation-MRI.

Conclusion: In case only the prostate is considered as target volume, the ATS workflow does not reduce the necessary PTV margin to accommodate intra-fraction geometric variations during treatment. In case the CTV also includes the seminal vesicles, an ATS workflow allows for a margin reduction of 1 mm or 2 mm compared to an ATR and ATP workflow, respectively. GTV coverage can be improved by additional adaptation to any CTV rotations, which should be preferred in case of focal dose-escalation.

34

Measurements and Monte Carlo simulations of the response of a Farmer-type ionization chamber for proton beams in the presence of magnetic fields for the determination of k_B

Mathieu Marot[1,2,3], Sonja Surla[1,3,4], Elisa Burke[3,5], Stephan Brons[3,6], Fabian Jäger[1,4], Armin Runz[1], Steffen Greilich[7], Christian P. Karger[1,3], Oliver Jäkel[1,3,6], Lucas Burigo[1,3]

[1]German Cancer Research Center (DKFZ), Medical Physics in Radiation Oncology, Heidelberg, Germany. [2]University of Heidelberg, Faculty of Medicine, Heidelberg, Germany. [3]National Center for Radiation Research in Oncology (NCRO), Heidelberg Institute for Radiation Oncology (HIRO), Heidelberg, Germany. [4]University of Heidelberg, Facutly of Physics and Astronomy, Heidelberg, Germany. [5]Department of Radiation Oncology, Heidelberg University Hospital, Heidelberg, Germany. [6]Heidelberg Ion-Beam Therapy Center HIT, University Hospital Heidelberg, Heidelberg, Germany. [7]Berthold Technologies GmbH & Co. KG, Business Units Radiation Protection / Bioanalytics, Bad Wildbad, Germany

Abstract

Purpose: This work aims to determine the magnetic field correction factor (k_B) for proton beams using a Farmer-type ionization chamber. The k_B correction factor is the product of the k_{BMQ} and the c_B, correcting for the magnetic field effect on the chamber response and on the local dose difference respectively. The k_{BMQ} was determined via experimental measurements and crosschecked with TOPAS simulations to verify the Monte Carlo (MC) code accuracy. Based on our simulations of k_{BMQ} and c_B for magnetic field strengths of up to 1 Tesla, the correction factor k_B was calculated.

Methods: The measurements were performed using a Farmer-type cylindrical ionization chamber (PTW 30013, Freiburg, Germany) placed at 2cm depth of an in-house developed 3D printed (Vero Clear) water phantom. The detector response was measured with mono-energetic proton beams of 157.43 and 221.05 MeV/u, having a field size of 3x10cm2. The magnetic field was generated by an experimental electromagnet (Schwarzbeck Mess – Elektronik) providing field strengths from 0.1 to 1.0 Tesla. TOPAS version 3.7 was used for the MC simulations. For the determination of the k_{BMQ}, the geometry of the PTW 30013 chamber was adapted from a previous work[1] including a dead volume (i.e., volume within the chamber where charges are not collected) and was placed at 2cm depth in a water phantom, where an uniform magnetic field was applied. The energy was scored in the residual volume (i.e., residual volume = air cavity – dead volume). For the determination of the c_B, the proton beam was directed towards a 10x10x10cm3 water phantom and the dose was scored in voxels at 2cm depth with and without magnetic field.

Results: The measurements at both energies showed a small but significant deviation of k_{BMQ} from unity, depending of the magnetic field strength, first with an increase of the k_{BMQ} up to a maximum of (0.27±0.06)% (1 SD) at 0.2 Tesla, then followed by a decrease and stabilization around the unit value at high magnetic flux density. The simulated k_{BMQ} showed a good agreement to the measurements with a RMSE of 0.05% and 0.08% for the energy 157.43 and 221.05 MeV/u, respectively. The simulated k_B showed a maximum at low magnetic flux density of up to (0.28±0.16)% and (0.38±0.17)% (1 SD) at 0.2 Tesla, for the energy 157.43 and 221.05 MeV/u, respectively, and then decreases and stabilizes at high magnetic flux density.

Conclusions: The measurements have shown that the magnetic field has a small (<0.3%) but significant effect on the chamber response and the TOPAS MC simulations agree with the experimental measurements within 0.1%. The preliminary result of the magnetic field correction k_B factor shows that the overall correction factor is small (below 1%) and is mostly localized in the low magnetic field region (below 0.5 Tesla). To the best of our knowledge, this is the first work presenting an investigation of the magnetic field correction factor k_B using both experimental measurements and MC simulations, for proton beams using a Farmer-type ionization chamber.

[1]Spindeldreier et al. 2017 Phys.Med.Biol. 62:6708

35

Are early radiotherapy changes in quantitative MRI predictive of changes after treatment in soft-tissue sarcomas?

Imogen Thrussell[1,2], Jessica Winfield[2,1], Christina Messiou[2,1], Sadiq Usman[2], Jennifer Newman[2], Georgina Hopkinson[2], Aisha Miah[2], Shane Zaidi[2], Matthew Blackledge[1,2]

[1]The Institute of Cancer Research, London, United Kingdom. [2]The Royal Marsden NHS Foundation Trust, London, United Kingdom

Abstract

Purpose: Multi-parametric, quantitative MR provides an array of potential tumour response biomarkers, which may allow for the monitoring of early treatment response. In an effort to understand how early such changes can be observed, we explore whether changes in these biomarkers after 7-11 fractions are predictive of changes after treatment in soft-tissue sarcomas (STS).

Methods: 16 patients with extremity STS receiving neoadjuvant radiotherapy received multi-parametric quantitative MR imaging at 3 time-points: i) pre-treatment (PreRT), early treatment (fraction 7-11) (MidRT) and post-treatment (PostRT), as part of an ongoing prospective clinical trial. The imaging protocol included diffusion-weighted imaging (DWI), magnetization-transfer imaging (MT), Dixon imaging, and multi-echo, echo-planar imaging (T2-EPI). T2-EPI and DWI were pixel-matched, whilst the field-of-view and resolution of Dixon and MT imaging were matched as closely as possible; MT, DWI and T2-EPI had slice thickness (5.0mm) and Dixon imaging had slice thickness of 2.5mm. Regions-of-interest were drawn around the whole tumour in every slice that the tumour appeared on the DWI imaging (b=50 s/mm^2); these were converted to resampled binary masks for each parameter map. Four biomarkers were extracted at each time-point: (1) mean tumour Apparent Diffusion Coefficient (ADC), (2) mean tumour Magnetization Transfer Ratio (MTR), (3) mean tumour Fat Fraction (FF), and (4) mean tumour T2.

For each parameter, x, the correlation between changes at the early time-point ($\delta_{mid} = x_{mid} - x_{pre}$) and changes post-treatment ($\delta_{post} = x_{post} - x_{pre}$) were evaluated using a Pearson correlation test. Furthermore, Wilcoxon signed-rank tests were performed to determine whether population values of δ_{mid} or δ_{post} were statistically significant from zero. Finally, a Levene test was used to determine whether the variance of δ_{mid} was significantly different from the variance of δ_{post}. Significance level is set at $p = 0.05$.

Results: The Levene tests revealed significant difference in the variance between the (δ_{mid}, δ_{post}) for MTR (p=0.0067) and ADC (p=0.0044). No other significant changes were observed for the Wilcoxon or Levene tests. The Pearson correlation test revealed a moderate correlation between (δ_{mid}, δ_{post}) for FF only (r=0.526, p=0.036).

Conclusion: Our preliminary results show that patients with STS show heterogeneous change in a range of quantitative metrics (ADC, MTR, FF and T2) following radiotherapy. STS tumours typically demonstrate heterogeneous response patterns which is reflected in our results at both early-treatment and post-treatment time-points. Advancements in MR technology such as the MR-Linac allow for frequent monitoring of patient response, providing clinicians with a more diverse toolkit to make clinical decisions regarding treatment pathways. However, our results suggest that changes in such biomarkers may not be visible as early as at 7-11 fractions.

Figure 1: The MTR (top left), T2 (top right), FF (bottom left) and ADC (bottom right) for each time point (left to right: PreRT, MidRT, PostRT).

Figure 2: The quantitative maps for one patient at each time point (left to right: PreRT, MidRT, PostRT). Ascending order from top to bottom row: ADC, MTR, T2, FF.

36

A Feasibility Study on Pseudo-CT from Planning MRI in Single and Multi-fraction Stereotactic Radiosurgery of Brain

M.S. Xin Yang Master[1], M.S. Bin Feng Master[1], Ph.D. Fu Jin Doctor of Philosophy[1], Ph.D. Xiaoqi Wang Doctor of Philosophy[2], M.S. Han Yang Master[1], Ph.D. Huanli Luo Doctor of Philosophy[1], M.S. Haiyang Peng Master[1]
[1]Chongqing University Cancer Hospital, Department of Radiation Oncology, Chongqing, China. [2]Philips HealthTech, Beijing, China

Abstract

Purpose:

The generation of pseudo-CT from diagnostic MRI through deep learning is a well-established technique. However, due to the lack of radiotherapy-specific bedplate, coil, and body immobilization of diagnosis MRI, the pseudo-CT from it can't be used clinically. Planning MRI combined with AI-based pseudo-CT generation software (MRCAT Brain) solves this problem very well. This study aims to investigate the feasibility of the software for single and multi-fraction Stereotactic Radiosurgery (SRS/fSRS) in brain via multi-omics methods.

Methods and materials:

34 patients who had planning MR (34 mDixon-T1 and 30 mDixon-T1-CE) with Cone-VMAT or MLC-CRT SRS/fSRS were included. With a mean number of treated lesions by patient of 1 (range 1-4), 49 lesions were treated, with a mean PTV volume of 3.4 cm^3 (0.5-27.3). Each pseudo-CT was affiliated to its corresponding planning CT, using initial delineation, rigid co-registration, and treatment plans (Eclipse version： 15.6, following SABR 6.1 guidelines). For comparison purposes, the synthetic dose map was then transferred to the planning CT using the "Dose Accumulation -Rigid" workflow in MIM, and 3D gamma analysis (1-3%/2mm, 1%/1mm) was analyzed by 3DVH. After extracting original features for radiomics comparison, normal tissue complication probability (NTCP) was computed by Lyman-Kutcher-Burman model and tumor control probability (TCP) by Logistic model.

Results:

After Wilcox-test (α=0.05), we found there was no difference between two sets of pseudo-CTs generated from two sequences in all index, and dose-volume histogram (DVH) metrics for planning target volume (PTV) and organs at risk (OAR) between planning CTs and pseudo-CTs. The average gamma passing rate of 3D 1%/1mm local was 90.13%. In radiomic analysis of PTV and OARs, after excluding 47 outliers, we got 60 original features and found more than 85% of features have significant differences. And the average difference in TCP was 0.03%, the NTCP of brain-GTV was 0.16%, and other OAR's NTCPs were below 0.02%.

Conclusion:

It was a feasibility Study to analyze the difference between planning CTs and pseudo-CTs based on deep learning and planning MRIs. We found high similarity of DVH metrics, 3D gamma analysis, and TCP/NTCP between planning CTs and pseudo-CTs. These results proved that pseudo-CTs from planning MRIs can replace planning CT in SRS/fSRS of brain. It's a great benefit in reducing the treatment time of patients. But the poor radiomic results indicated that there are still differences in original features， which also proposed an improvement target for the image generation algorithm.

Keywords:

Planning MRI; Single and Multi-fraction Stereotactic Radiosurgery; Feasibility Study; Multi-omics Evaluation

37

Output factor measurements for small isocentric and off-axis photon fields at a 0.35 T MR-Linac

Sonja Surla[1,2,3], Sebastian Klüter[4,3], Katharina Renkamp[4,3], Carolin Buchele[4,3], Bernhard Rhein[4,3], Christian Karger[1,3]
[1]German Cancer Research Center (DKFZ), Heidelberg, Germany. [2]Faculty of Physics and Astronomy, University of Heidelberg, Heidelberg, Germany. [3]National Center for Radiation Research in Oncology (NCRO), Heidelberg Institute for Radiation Oncology (HIRO), Heidelberg, Germany. [4]Heidelberg University Hospital, Department of Radiation Oncology, Heidelberg, Germany

Abstract

Existing Code of Practice for small field dosimetry (TRS-483) has not yet addressed the application in magnetic fields. In MR-guided radiotherapy (MRgRT), dosimetry has to be performed in the presence of static magnetic field of MRI, which emphasises the need for investigation of small field dosimetry in magnetic fields. Aim of this work was to develop a procedure for output factor (OF) measurements in small isocentric and off-axis fields at 0.35 T MR-Linac.

Experiments were performed at 6 MV flattening filter free (FFF) photon beam of a MRIdian Linac (ViewRay Inc., Oakwood, USA) with PinPoint3D (PTW, Freiburg, Germany) chamber placed inside a BEAMSCAN MR (PTW, Freiburg, Germany) water phantom. The chamber axis was orientated parallel to the magnetic field and perpendicular to the beam. All values were measured at a depth of 5 cm and 85 cm source-to-surface distance.

Reproducibility of dose measurements at the MR-Linac and influence factors on charge collection in the chamber were investigated. Repeated measurements of chamber reading showed that the output variation of the MR-Linac varies within 0.65 % uncertainty from day to day, but only less than 0.07 % during one measurement session. Using the two-voltage method, the recombination correction factor, k_s, was found to be 1.0049 (± 0.0005) and 1.0046 (± 0.0008) for a field size of 10x10 cm^2 and 1.7x1.7 cm^2 field size, respectively. Measurements at opposing polarizing potentials led to the polarity correction factor, k_{pol}, of 0.9988 (± 0.0006) and 0.9990 (± 0.0005) for 10x10 cm^2 and 1.7x1.7 cm^2 field size respectively. OF for small isocentric and off-axis square fields (at ± 5 cm distance from isocenter in cross-plane and in-plane direction) were measured. Field size for each field was defined as full-with at half maximum (FWHM), obtained from profile measurements with reproducibility of 0.20 % and 1.41 % for 10x10 cm^2 and 1.7x1.7 cm^2 field size, respectively. For off-axis measurements, the chamber was positioned at the center of the field, and not at the maximum due to asymmetry of the field caused by the FFF-beam, and the nominal square field of side 10 cm at the same off-axis position was used as the reference field. OF measurements for 1.7x1.7 cm^2 field at off-axis positions agree with corresponding central field OF within 0.4 %.

In this work, consistency of small field OF measurements for 6 MV FFF photon beams in the presence of 0.35 T magnetic field was verified using PinPoint3D chamber. Measurements of OF from day to day showed a high reproducibility. Results for PinPoint3D chamber showed that recombination and polarity corrections were independent of field size. Preliminary OF measurements for small off-axis square fields showed that OF did not change significantly when the center of the field was 5 cm off-axis in cross-plane and in-plane direction.

38

Radial-RIM: accelerated radial 4D MRI using the recurrent inference machine

Chaoping Zhang[1], Matthan Caan[2,3,4], Robin Navest[1], Jonas Teuwen[1,5,6], Jan-Jakob Sonke[1]
[1]The Netherlands Cancer Institute, Amsterdam, Netherlands. [2]Amsterdam UMC location University of Amsterdam, Biomedical Engineering and Physics, Meibergdreef 9, Amsterdam, Netherlands. [3]Amsterdam Neuroscience, Brain Imaging, Amsterdam, Netherlands. [4]Computational Radiology and Artificial Intelligence, Division of Radiology and Nuclear Medicine, Oslo University Hospital, Oslo, Norway. [5]University of Amsterdam, Amsterdam, Netherlands. [6]Radboud University Medical Center, Nijmegen, Netherlands

Abstract

Purpose

To accelerate 4D radial MRI using the radial recurrent inference machine (radial-RIM).

Methods

We propose a 3D radial-RIM network to reconstruct 4D radially sampled k-space by adapting the forward model of the regular RIM[1] for the radial acquisition. The network architecture is presented in figure 1. Validation of the network was performed with reconstruction of free-breathing 3D golden angle stack-of-stars lung and liver scans of healthy volunteers in MR-Linac (Elekta Unity protocol details in the supporting document).

As preprocessing, we sorted the acquired 1344 k-space spokes equally into 10 motion phases[2]. For each of the sorted 3D radial k-spaces, we applied FFT in the slice direction to obtain the k-space slices. Due to limited GPU memory and the fact that the motion-state dimension is expected to be more redundant than the slice dimension, we focus on the 2D-slice reconstruction along with the extra motion-state dimension. The image size of a slice-over-time is 360x360x10.

The input image for the 3D radial-RIM network was the non-uniform (NU)FFT of 4x accelerated data (i.e., the first quarter of all spokes). The compressed sensing (CS) images using XD-GRASP[2] with all spokes (CS-full) were regarded as reference in training. In training/validation/testing of the radial-RIM, 7/2/2 subjects were used. Each subject includes one liver scan and one lung scan and each scan includes 87 slices. The L1-loss was used in training. For evaluation with the testing data, visual inspection was combined with RMSE and SSIM (w.r.t. CS-full reconstruction). The CS reconstruction on the 4x subsampled data (CS-subsampled) was also included as comparison.

To gain insight in the contribution from the extra motion-state dimension, we performed an ablation experiment with a 2D radial-RIM, where the convolutional kernel expanded only in two spatial dimensions and no shared information between motion phases was used.

Results

The reconstructed images of the test set are shown in Figure 2. Visual inspection shows that the 3D radial-RIM reconstructions largely preserve the visible image features of the reference CS-full reconstructions and meanwhile are less noisy. Note that the CS-full used all spokes and the 3D radial-RIM used a quarter (with scan time of 124s for lung and 80s for liver).

While the CS-subsampled reconstructions are noisier than the CS-full and already show low visibility for small image features, the 2D radial-RIM reconstructions are below the acceptable quality with strong blurriness and artifacts. While the SSIM might be influenced by noise and shows some inconsistency, the RMSE values largely agree to the visual quality.

For computation time, the MATLAB implemented CS reconstruction took around 2 minutes per slice (including all motion phases) on the CPU:AMD-EPYC-7402-SP3, whereas the PyTorch implemented 3D radial-RIM inference took around 1.9 seconds with the GPU:Nvidia-Quadro-A6000.

Conclusion

The radial-RIM can reconstruct images with better quality than compressed sensing in accelerated 4D radial free-breathing lung/liver acquisitions. The exploited signal correlation over the extra motion-state dimension contributes substantially to the image quality. The shorter acquisition time in combination with radically reduced reconstruction time would allow clinical implementation.

References 1.Lønning,K.et-al.MedIA.2019; 2.Feng,L.et-al.MRM.2016.

39

Promoting the Clinical Application of Deep Learning Auto-segmentation (DLAS) – an Automatic Contour Quality Assurance tool for MRI-guided online adaptive radiotherapy

Dr. Ying Zhang PhD, Dr. Nguyen Phuong Dang PhD, Dr. Asma Amjad PhD, Dr. Christina Sarosiek PhD, Dr. Mohammad Zarenia PHD, Dr. Renae Conlin PhD, Dr. William A Hall MD, Dr. Beth A. Erickson MD, Dr. Eric Paulson PhD, Dr. X. Allen Li PhD
Medical College of Wisconsin, Milwaukee, WI, USA

Abstract

Purpose

Fast and accurate segmentation is critical for MRI-guided online adaptive radiotherapy (MRgART). Recently, deep learning auto-segmentation (DLAS) tools are being increasingly developed to improve the efficiency and consistency of the image segmentation process. However, to deploy a DLAS in clinic, rigorous quality assurance (QA) and continuous monitoring of the model's performance are necessary, which is not yet available in practice. This work aims to develop a novel automatic contour quality assurance (ACQA) tool to assist the evaluation/commissioning and clinical application of DLAS tools.

Methods

The ACQA tool was designed to automatically validate the DLAS contour quality as acceptable, minor edit or major edit based on the expected edit time on a slice-by-slice basis. It includes two parts: (1) machine learning-based contour quality classification (CQC) method, and (2) deep learning-based contour quality evaluation (DL-CQE) method. The CQC method uses seven commonly used quantitative metrics (DSC, MDA, HD, surface-DCS, APL, relative-APL, and volume) extracted for each DLAS contour slice as compared to ground truth contours and trains organ-specific supervised classification models to identify the quality categories. While the DL-CQE method uses only the images and DLAS contours as inputs for a convolutional neural network (CNN) and is designed to reproduce the classifications from CQC models. All the models were trained and tested using the DLAS contours of five abdominal organs (large bowel, small bowel, stomach, duodenum, and pancreas) on 3T/1.5T MRIs. The performance was evaluated using AUC, accuracy, and risk rate (RR) (the percentage of unacceptable slices mislabeled as acceptable).

Results

The accuracy of the CQC models' prediction and majority vote labels from four independent observers was in the range of 91.5% to 100% and the RR was from 0.0% and 0.5% for the five organs. The DL-ACQA models were intentionally trained to minimize the RR, to be less than 1%. The AUC was in the range of 0.978 to 0.997 and the accuracy was in the range of 90% to 94%. The expected execution time on a daily MRI is less than 1 minutes.

Conclusion

The CQC model, relating three classes to seven calculable metrics, can accurately classify the quality of a contour slice based on its clinical applicability, thus, can be used to evaluate/compare the performance of any auto-segmentation algorithms, including DLAS. The DL-CQE models can automatically monitor the quality of the DLAS. The identified minor/major edit slices can be further manually/automatically corrected, reducing the workload and improve efficiency of the contouring process. The proposed integrated ACQA tool can promote the clinical application of the DLAS, facilitating the routine practice of MRgART.

Figure 1 Model prediction accuracy for four individual observers and the majority vote labels for the five DLAS organ contours

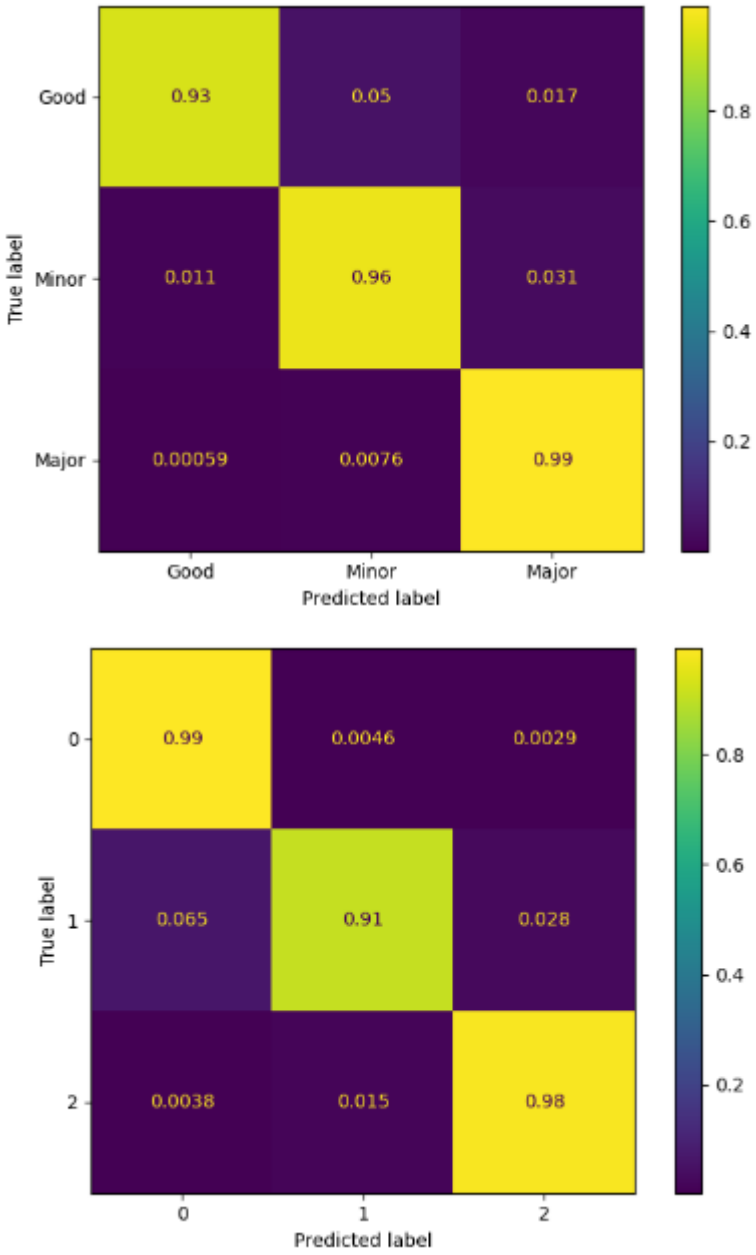

Figure 2 Representative Confusion matrices of CQE models for Large Bowel (left) and Pancreas (right). The label numbers 0,1, and 2 correspond to the acceptable, minor, and major edit categories

40

A New Framework for 3D MR Fingerprinting with Efficient Subspace Reconstruction and Posterior Distribution Estimation

Jiaren Zou, Yuchi Liu, Nicole Seiberlich, Yue Cao
University of Michigan, Ann Arbor, USA

Abstract

Purpose: MR fingerprinting (MRF) is an efficient quantitative MRI technique to simultaneous quantify multiple tissue parameters in a single scan. However, both k-space acquisition and reconstruction for 3D high-resolution MRF needs to be further improved by exploiting the spatiotemporal sparsity and developing an efficient computation algorithm to deal with a large quantity of MR data and computation expense. In this work, we propose a framework to efficiently reconstruct high-resolution parameter images and posterior distributions from 3D MRF.

Methods: Our 3D MRF reconstruction framework consists of two major components: 1) TR-decomposed stochastic gradient decent (SGD) subspace reconstruction to build coefficient maps of principle components of MRF-time series and 2) conditional invertible neural network (cINN) to estimate parameter maps and their posterior distributions. The previously proposed iterative 3D MRF subspace reconstruction requires large memory consumption and long reconstruction time. Our proposed method decomposes the objective function of the subspace reconstruction in the TR dimension first (instead of the whole volume-time series) and then optimizes the objective per-TR by SGD to accelerate computation and decrease memory demand. The cINN that is originally proposed to solve highly degenerate inverse problems in astrophysics is used as a general and fast way of estimating parameter maps and their posterior distributions. The network learns to minimize the Kullback-Leibler divergence between estimated and true posterior distributions from pairs of tissue parameters and corresponding MR signals. Also, the cINN has ability to characterize encoding capability of a MRF sequence for further acquisition optimization.

To validate the proposed image reconstruction method, digital brain phantoms were used for simulation with a FISP-based MRF sequence and then retrospectively undersampled using a 3D spiral trajectory (1mm-isotropic-resolution, FOV=$230*230*230mm^3$, acquisition time=1min). cINN was trained on a dictionary of noisy MRF signals. We validated the estimated posterior distribution with that using a Markov chain Monte Carlo (MCMC) method. The normalized root mean squared error (NRMSE) of the estimates was compared to two neural network-based point estimation methods, FCNN and RNN. Finally, image reconstruction was combined with cINN. SGD subspace reconstruction was compared to direct adjoint NUFFT image reconstruction followed by subspace projection and iterative subspace reconstruction using Primal-Dual Hybrid Gradient (PDHG).

Results: Similar estimated posterior distributions of cINN and MCMC are demonstrated in Figure 1. The MCMC method took ~60 mins to estimate the distribution for one voxel while cINN spent 0.81s. Table 1 shows that the NRMSEs of T_1 and T_2 of cINN are comparable with DRONE, while cINN can provide posterior distribution. Figure 2 shows comparisons of the parameter maps of one example slice using different reconstruction methods to cINN. The reconstruction with SGD shows the best visual quality. PDHG was run for 100 iterations (~4 hours) without convergence while 5000 iterations of SGD were performed within ~25 min.

Conclusion: Our method was able to efficiently estimate the posterior distribution and perform subspace reconstruction for 3D MRF, which paves the path towards deep learning-based reconstruction. An end-to-end deep learning based joint optimization of acquisition and reconstruction will be part of future work.

41

Volumetric MRI Reconstruction from Cine Acquisition Using Sparse Priors and Implicit Neural Representation Learning

Ridvan Yesiloglu[1], Liyue Shen[2], Lei Xing[1], Yue Cao[2], James Balter[2], Adam Johansson[3], Lianli Liu[1]
[1]Stanford University, Palo Alto, CA, USA. [2]University of Michigan, Ann Arbor, MI, USA. [3]Uppsala University, Uppsala, Sweden

Abstract

Purpose: To investigate the reconstruction of real-time volumetric MRI from orthogonal cine acquisition aided by sparse priors of 2 static MRI volumes with different breath-hold states via implicit neural representation learning, and to evaluate the reconstructed image volumes in supporting 3D motion tracking for MRI-guided radiotherapy.

Method: A multi-layer perceptron network was trained to learn the implicit neural representation (NeRP) of an image dataset, where the network takes image coordinates as inputs and outputs corresponding voxel values. By learning the NeRP of a sparse 4D MRI dataset created by stacking 2 static MRI volumes of a subject together, we embedded prior knowledge of the subject into network weights. The prior knowledge was further augmented by linearly interpolating and extrapolating the 4th dimension of the dataset coordinates. To reconstruct volumetric MRI from sparse samples, the 4th dimension coordinate corresponding to the sparse samples was first determined by minimizing mean-square-error between network outputs and sampled image values across different coordinate indexes. The prior-embedded network weights were further fine-tuned to fit network outputs to sparse samples. The final volumetric reconstruction was obtained by querying the fine-tuned network at 3D spatial coordinates. We evaluated the proposed method using 5-minute volumetric MRI time series with 340 ms temporal resolution collected from 7 liver carcinoma patients. The time series was acquired using golden-angle radial MRI sequence and reconstructed by retrospective sorting and breathing motion state assignment of radial samples. For each patient, one exhale state volume and one inhale state volume were selected from the first 30 seconds of the time series for prior embedding and volumes from the remaining 4.5 minutes were sampled to 2 orthogonal cine slices for testing. Peak signal-to-noise ratio (PSNR) and structural similarity index measure (SSIM) between reconstructed and ground truth image volumes were calculated. Three-dimensional motion tracking accuracy was evaluated by deforming a reference volume with gross tumor volume (GTV) contours to image volumes and calculating the GTV centroid position difference and 95-percentile Hausdorff distance between deformed GTV contours estimated using ground truth and reconstructed MRI volumes.

Results: Across the 7 patients evaluated, the PSNR and SSIM were 35.1 ± 3.6 dB and 0.97 ± 0.02 respectively. The mean absolute difference between GTV centroid positions was less than 1 mm in all 3 directions and the averaged 95-percentile Hausdorff distance was 2.55 mm, which is smaller than the in-plane image resolution (3 ~ 4 mm). Figure 1 shows example network reconstructed images. The network was able to reconstruct images with motion states in between the two priors and motion states outside the two priors.

Conclusion: Reconstructing volumetric MRI from orthogonal cine slices with sparse priors is feasible by embedding the prior knowledge into a neural network through NeRP learning. The proposed method removes the need of large-scale training datasets such as 4D MRI, which is not widely available on MR-Linac systems and takes long time to acquire. The reconstructed volumes showed image quality sufficient in tracking tumor motion in 3D and has the potential of supporting the clinical workflow of volumetric motion tracking.

42

Reduction of DIXON geometric distortions for HDR brachytherapy applicator imaging

Dr Evangelia Kaza PhD, Dr Christian Guthier PhD, Dr Ivan Buzurovic PhD
Brigham and Women's Hospital, Dana-Farber Cancer Institute, Harvard Medical School, Boston, MA, USA

Abstract

Purpose: CT is the standard surface applicator imaging modality for skin High-Dose-Rate (HDR) brachytherapy treatment planning, although MRI offers superior soft tissue contrast. Recently, DIXON MRI has shown the potential to simultaneously visualize skin and surface applicators, with empty hypointense catheters distinguished inside the brighter applicator spheres, particularly for opposed-phase images. To rely on MRI for HDR brachytherapy treatment planning, geometric distortions affecting catheter position should be minimized. We assessed spatial distortions of a surface applicator of known geometry on DIXON scans and investigated a distortion reduction approach using the available image sets.

Methods: A Freiburg flap applicator (31 catheters with 21 beads each) was fixed inside a 3D-printed holder surrounded by two plexiglass blocks. The applicator was positioned at the isocenter of a 3T Siemens Vida in the axial, coronal and sagittal plane, and scanned using an UltraFlexLarge18 and a Spine32 coil. A 3D DIXON VIBE sequence (TR\TE 4.61\1.65 ms, field-of-view (FOV) 346x346 mm^2, 0.9x0.9x1.2 mm^3 voxels, bandwidth 723 Hz/pixel, acquisition time 3min 43s) was acquired in the orientation of applicator placement. Subsequently the applicator was scanned on a helical CT in axial and coronal position (200 mA, 140 kV, 0.75x0.75x1.25 mm^3 voxels).

For each applicator placement the DIXON opposed-phase images were registered to CT images of the matching plane by point-based alignment in MIM 7.2.5, using one point at the center of each corner sphere. MR-CT distance between edge spheres was measured at six points along each applicator direction in checkerboard view (example measurements below):

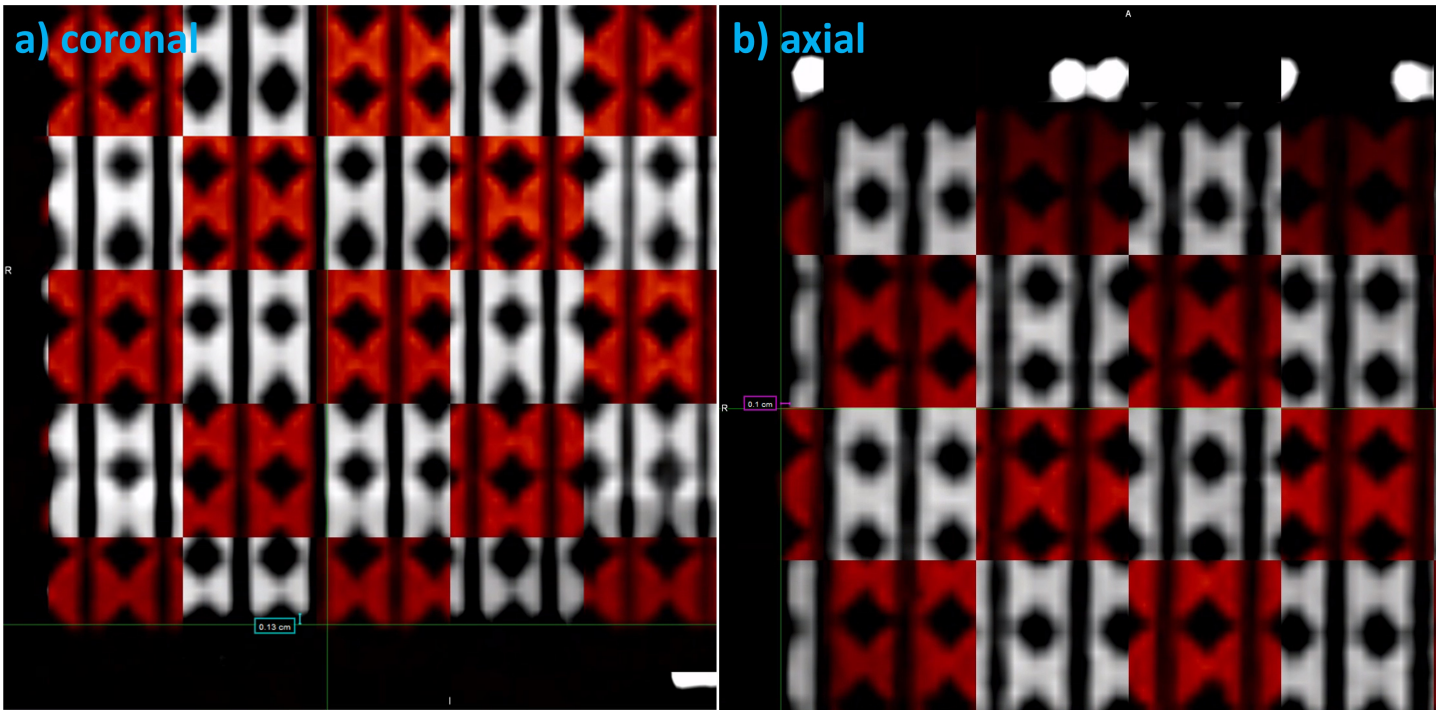

Additionally, the DIXON in-phase and opposed-phase images of each orientation were fused and the produced geometric mean image was registered to CT. Edge sphere differences between DIXON geometric mean and CT were measured in a similar way as for the original DIXON images.

Results: Combining the in-phase and opposed-phase DIXON images by building their geometric mean corrected their relative shear and preserved applicator-catheter contrast. The theoretical chemical shift for the applicator's silicon beads at 3T is 0.84 pixels for the employed bandwidth and silicon-water difference 4.7ppm. MR-CT positional agreement of applicator spheres improved for the geometric mean, as displayed by the example fusion of axial CT and DIXON opposed-phase and geometric mean images in edge detection mode:

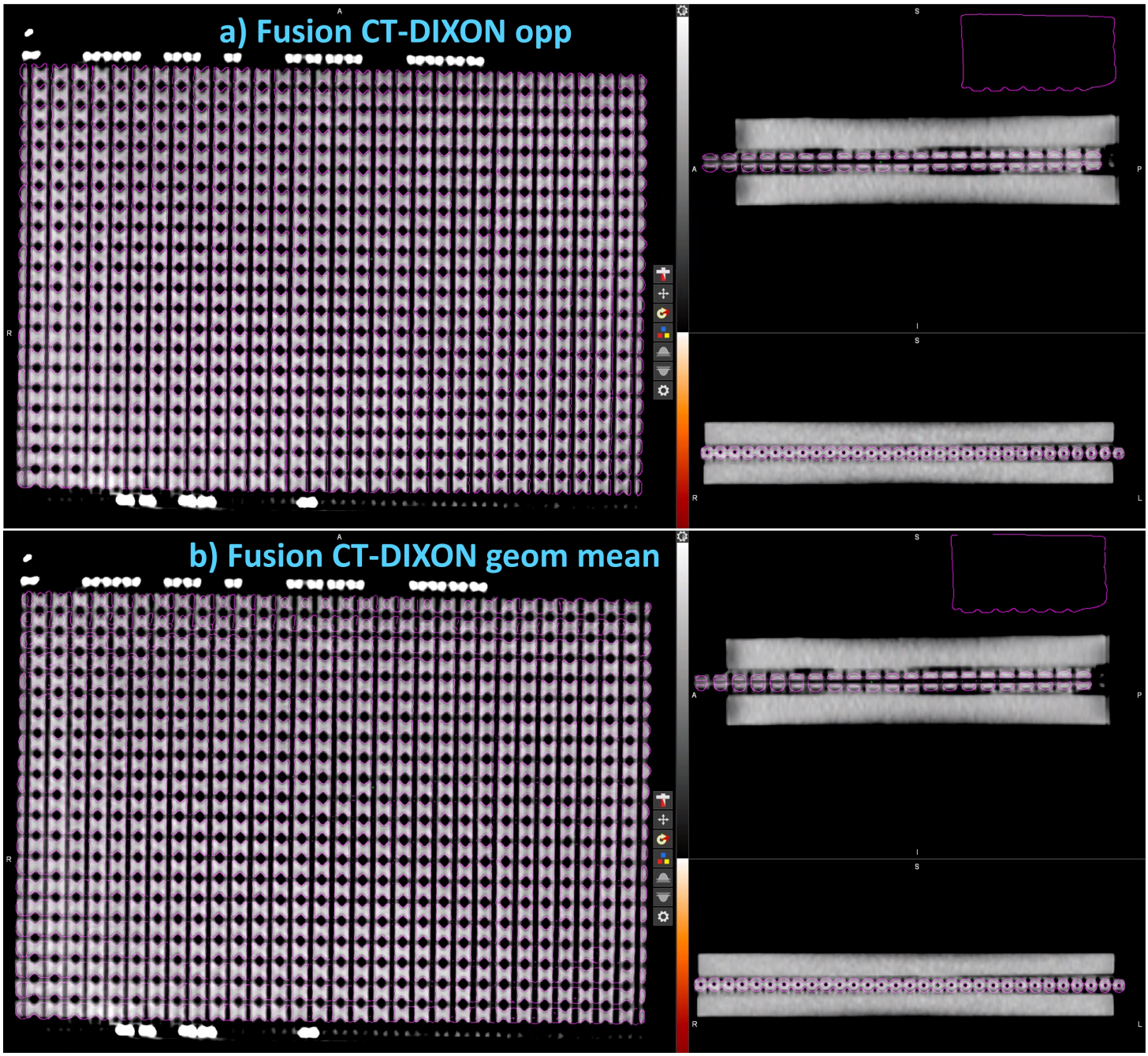

The mean and standard deviation of measured MR-CT distances for each applicator placement and side are displayed on table 1 for the original DIXON opposed-phase images and for the geometric mean of the in- and opposed-phase images. While in-plane geometric distortions were close to or above 1mm for the original images, they were substantially reduced to below 1mm or even 0.5mm for the geometric mean images.

direction	coronal DIXON opp	coronal DIXON geom mean	direction	axial DIXON opp	axial DIXON geom mean	direction	sagittal DIXON opp	sagittal DIXON geom mean
right	1.25 ± 0.27	0.20 ± 0.06	right	0.85 ± 0.26	0.40 ± 0.22	superior	0.83 ± 0.41	0.43 ± 0.34
left	0.98 ± 0.15	0.28 ± 0.08	left	0.65 ± 0.16	0.27 ± 0.15	inferior	0.87 ± 0.56	0.27 ± 0.19
superior	1.10 ± 0.28	0.40 ± 0.17	anterior	0.92 ± 0.34	0.27 ± 0.15	anterior	1.08 ± 0.25	0.49 ± 0.20
inferior	1.08 ± 0.49	0.82 ± 0.22	posterior	0.80 ± 0.22	0.38 ± 0.21	posterior	1.02 ± 0.68	0.32 ± 0.08

Conclusions: Comparing the CT and DIXON VIBE images of a Freiburg flap applicator suggested that geometric distortions mainly induced by chemical shift can be reduced well below the clinically acceptable 1mm threshold by building the geometric mean of the DIXON in- and opposed-phase images. Further investigation could help identify the clinical use of DIXON image combinations for MR-only treatment planning in skin HDR brachytherapy.

43

PSMA-PET/MRI for classification and delineation of intra-prostatic lesions

mr Tufve Nyholm Professor[1], mr Erik Nilsson MSc[1], ms Josefine Grefve MSc[1], Ms Kristina Sandgren PhD[1], mr Joakim Jonsson PhD[1], mr Lars Olsson Professor[2], mr Adalsteinn Gunnlaugsson PhD[3], mr Björn Zackrisson Professor[1], ms Karin Söderkvist Ph.D.[4], mr Mathieu Moreau[3]

[1]Umeå University, Umeå, Sweden. [2]Lund Univesity, Lund, Sweden. [3]Lund University, Lund, Sweden. [4]Umeå Univeristy, Umeå, Sweden

Abstract

Purpose

There is growing evidence for patient benefit of intra-prostatic radiation boost to the dominant lesion. Both mp-MRI and PSMA-PET are candidate image modalities for determining the geometric extent of the boost-region. In the present study we have investigated the connection between lesion ISUP grade and MR and PET image signatures, and the correspondence between segmented lesions and ground truth based on whole-mount histopathology.

Methods

55 men planned for radical prostatectomy with biopsy-proven prostate cancer were included in this study. [^{68}Ga]PSMA-11 PET/mpMRI and [^{11}C]Acetate PET/CT were performed prior to surgery. Prostate glands were delineated on T2-weighted (T2w) images and a shape-preserving mould was 3D-printed for each patient. Resected prostate specimens were placed inside the mould for ex-vivo T2w imaging, followed by histopathological preparation and subsequent evaluation. The evaluation resulted in digital annotations showing the location and extent of lesions and their ISUP grade groups (IGG). The in-vivo T2w images served as a common frame of reference for all image data. The histopathology was first registered to the ex-vivo T2w, which in turn was co-registered to the in-vivo T2w. The diffusion images were corrected for distortions using a deformable registration between the b0-image and the T2w anatomical image. All patients in the cohort were included in the analysis of the relation between IGG and PSMA and acetate SUV max and median relative ADC, k-trans and T2 relaxation time. The 15 of the patients with a clinically significant lesion of Gleason Grade 4+4 or higher were used to investigate the correspondence between delineations and ground truth extent of lesions. 4 radiation oncologists independently delineated GTV volumes based on ADC, T2w, early contrast enhancement and PSMA-images.

Results

For differentiation between ISUP 2 and ISUP 3 lesions we found that PSMA-PET gives the highest AUC in ROC analysis, but not significantly different from median relative k-trans. Bi-parametric MRI gave a combined AUC of 0.59, which was increased to 0.74 ($p<0.01$) when adding DCE-MRI and further improved to 0.81 when adding PSMA-PET ($p<0.05$) (figure 1). Delineations based on PSMA-PET imaging in cooperated on average 51% of Gleason grade 4 regions, while delineations based on diffusion MR, T2w images or DCE-MRI in cooperated below 40% of Gleason grade 4 regions on average. Combining diffusion, T2w and DCE-MRI resulted in an average Gleason Grade overlap of 55%. Gleason 3 regions in connection to the dominant lesion were included on average below 30% for all modalities.

Conclusion

The present study indicates that PSMA-PET and DCE-MRI (k-trans), can be used to differentiate between ISUP 2 and ISUP 3 lesions and provides independent information. PSMA-PET and mp-MRI appear equally good for delineation of high-grade regions.

Figure. 1 – ROC curves for classifiers using one modality (first column) or combinations of modalities (second column) for discriminating between IGG 3 and IGG 2 (first row) or IGG ≥ 3 and IGG ≤ 2 (second row).

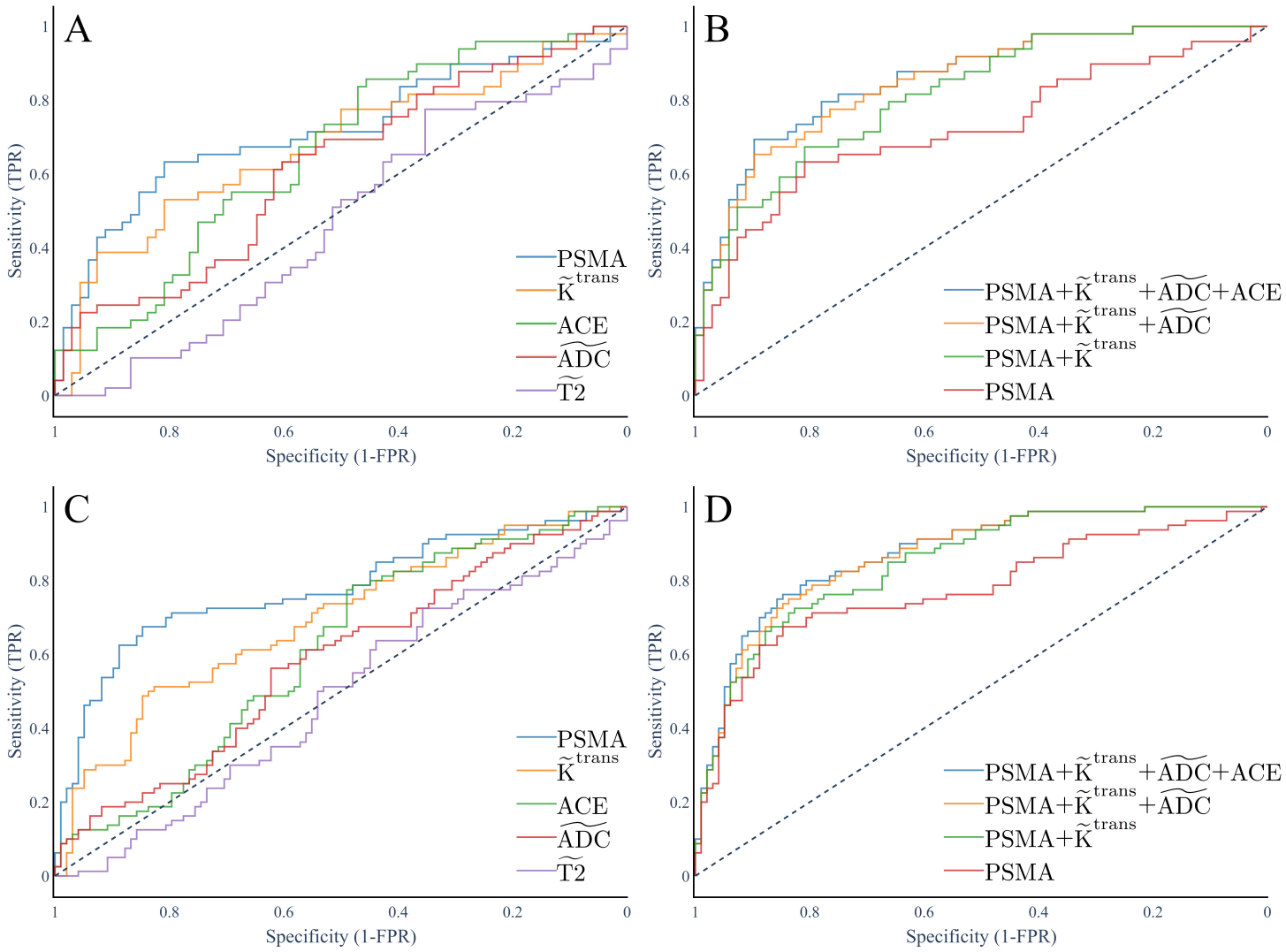

Figure 2 a) Histopathology slice with delineated lesion, b) PSMA-PET uptake, c) GTV delineations from the four different observers and d) the combined GTV (Staple).

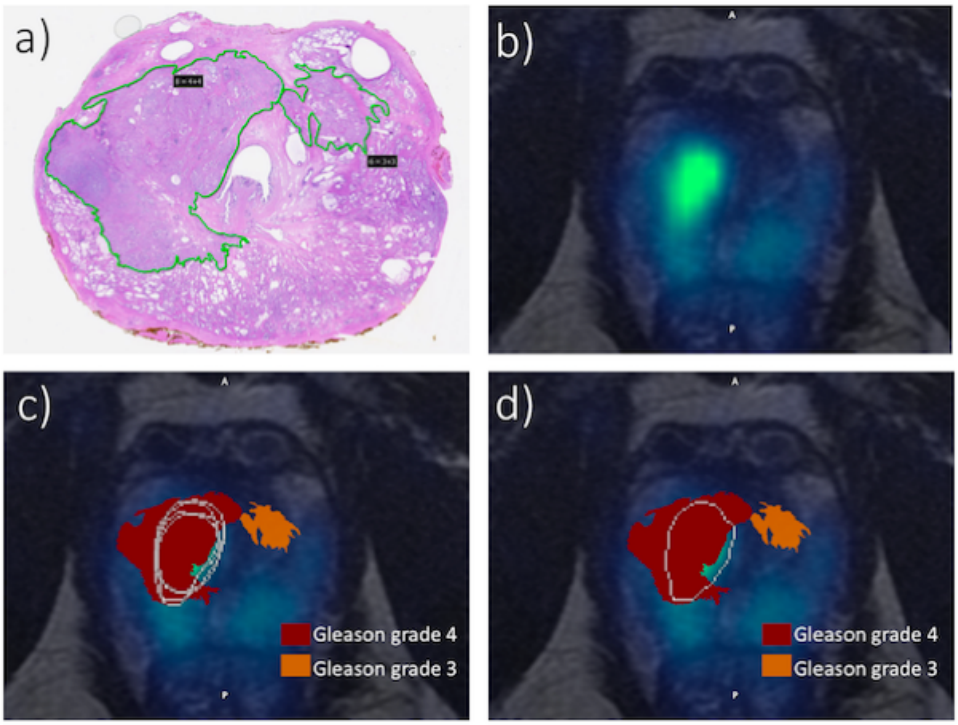

44

LapGM: A Fast and Accurate Multisequence MR Bias Correction and Normalization Method

Luciano Vinas[1], Arash Amini[1], Jade Fischer[2], Atchar Sudhyadhom[3,4,5]

[1]University of California, Los Angeles, Los Angeles, California, USA. [2]University of Victoria, Calgary, Victoria, Alberta, Canada. [3]Dana-Faber Cancer Institute, Boston, Massachusetts, USA. [4]Brigham and Women's Hospital, Boston, Massachusetts, USA. [5]Harvard Medical School, Boston, Massachusetts, USA

Abstract

Purpose: Deep learning of large imaging datasets requires fast and accurate preprocessing to be feasible and provide the best results. The state of the art methods that were developed over a decade ago for MR bias field estimation may be limiting in these respects as they may not take advantage of more recent methods and hardware technology. The purpose of this work is to develop and validate a fast and accurate two in one method to simultaneously estimate the bias field on each scan and normalize these MR scans across a population.

Methods: LapGM, a spatially regularized Gaussian mixture model, was developed that uses MR intensity information to segment the scan into a set of tissue classes. Bias field inhomogeneities are determined by contrasting spatial gradient information with tissue mean value and spread. The spatial regularization allows a user to fine-tune control between balancing bias field removal and preserving image contrast preservation for multi-sequence, magnetic resonance images. The fitted Gaussian parameters of LapGM serve as control values which can be used to normalize image intensities across different patient scans. LapGM is compared for speed and accuracy with the state of the art standard debiasing algorithm, N4ITK, in both the single and multi-sequence setting. As a normalization procedure, LapGM is compared with commonly used normalization techniques: max normalization, Z-score normalization, and the gold standard method of a region-of-interest normalization of a water region.

Results: LapGM provides faster results at similar or greater accuracy. LapGM bias field estimate was roughly 10-fold faster than N4 by CPU and up to 60-fold faster by GPU. Greater accuracy was achieved in the multi-sequence case by integrating data across multiple MR sequences which promotes convergence to true tissue classification resulting in RMSE errors that were 2-to-3 times lower compared to N4. LapGM normalization produced mutual information values superior to other normalization methods and in line with ground truth, water normalization.

Conclusion: In this work we have proposed a bias correction and normalization method which excels in tissue intensity recovery for multi-sequence MRI data. By computing both bias correction and normalization in one optimization step, we are able to minimize the effect of preprocessing artifacts in MR data pipelines. This is especially beneficial for MR deep learning tasks, where consistent and correct data is needed for superior learning. Lastly, Python package lapgm accelerated runtimes makes it a great candidate for large image workloads.

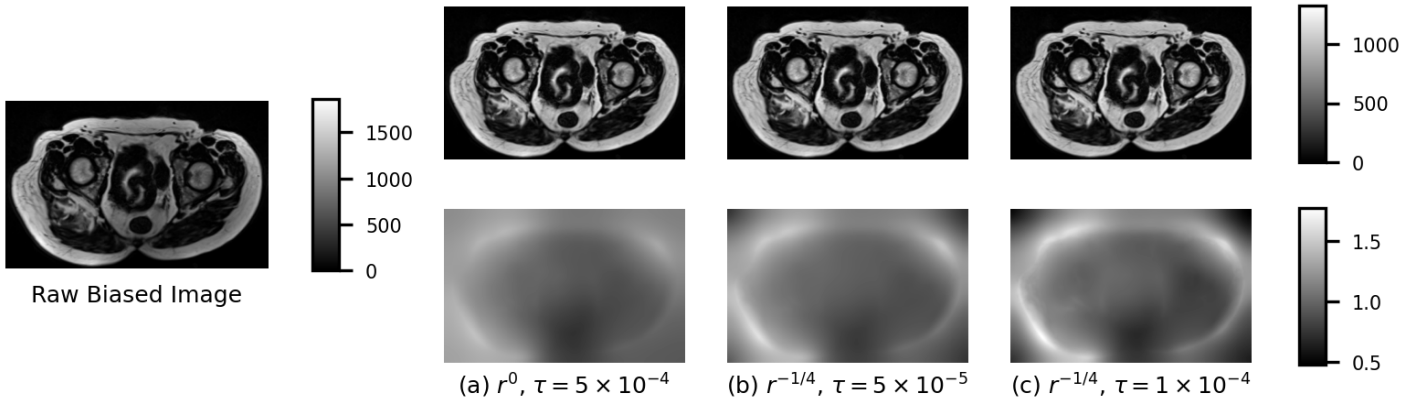

Figure 1: Debias and bias field comparison of LapGM on single sequence data for varying smoothness parameters τ and gradient weight penalties r^α.

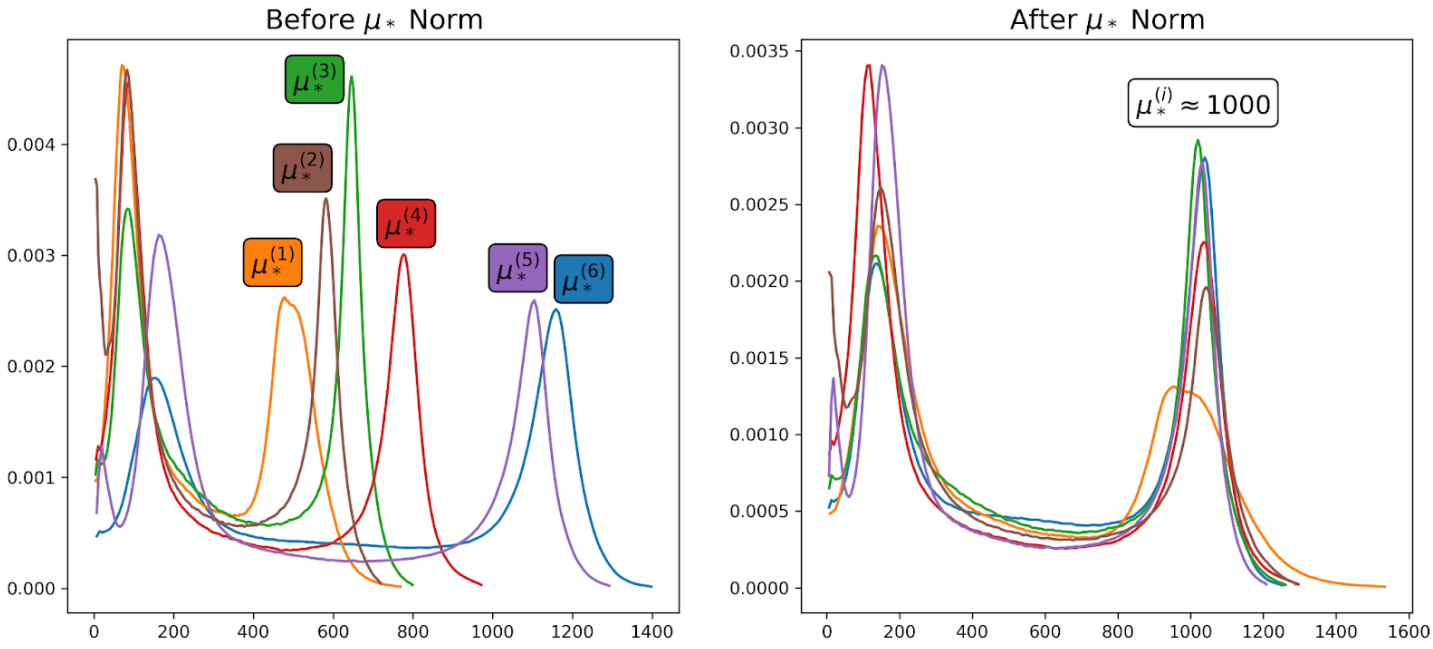

Figure 2: Visualization of LapGM's μ* normalization technique on real patient data. A target intensity of 1000 was specified for normalization.

45

MOLAR: Machine learning accelerated On-Line Adaptive Replanning for MRgART

X. Allen Li[1], Ying Zhang[1], Asma Amjad[1], Ergun Ahunbay[1], Jiaofeng Xu[2], Haidy Nasief[1], Abdul Parchur[1], Michel Moreau[2], Dan Thill[2], Nicole O'Connell[2], Jie Ding[1], Christina Sarosiek[1], Nguyen Dang[1], Xinfeng Chen[1], Eenas Omari[1], Mohammad Zarenia[1], Renae Conlin[1], Beth Erickson[1], William Hall[1], Eric Paulson[1], Chris Schultz[1]

[1]Medical College of Wisconsin, Milwaukee, WI, USA. [2]Elekta, St. Charles, MO, USA

Abstract

Purpose: Online adaptive replanning (OLAR) that generates a new plan based on the anatomy of the day and delivers the plan for the fraction has been shown to effectively address interfraction changes during MRgART. Major obstacles currently affecting the practice of OLAR include (1) impractical length of time required to segment the anatomy of the day, which can exceed 30 minutes in abdomen, (2) slow and/or inaccurate methods to generate synthetic CT (sCT) from abdominal MRI primarily due to randomly occurring air cavities, and (3) unavailability of a method to quickly and objectively determine when OLAR is necessary. To address these issues, we develop and test novel machine learning accelerated OLAR (MOLAR) solutions for MRgART of abdominal tumors.

Materials and Methods: Based on a variety of machine learning, including deep learning (DL), algorithms, the MOLAR solutions are developed to (i) quickly determine the necessity of OLAR immediately after a daily MRI is acquired without segmentation using machine learning based on either structural similarity index map or wavelet multiscale textures extracted from the daily MRI, (ii) rapidly generate accurate sCT by auto-segmenting air volumes on a daily MRI set specially designed to image air, and (iii) quickly segment organs at risk (OAR) on daily MRI using a multi-layer pipeline, which includes (1) auto-segmenting OAR using DL models trained with multi-sequence MRIs, (2) automatically validating and classifying the auto-segmented contours into three categories: acceptable, minor error and major error, defined based on editing effort, (3) automatically refining the identified inaccurate contours, (4) editing the remaining inaccurate contours using an interactive semi-automatic and a manually editing tools. The MOLAR solutions are designed and developed to be fully automated, except for the last editing step. The performance of the MOLAR was evaluated in terms of its execution time and accuracy (e.g., AUC of the ROC) or the agreement with the ground truth.

Results: Flowchart of MOLAR solutions is shown below. The necessity of OLAR was determined in less than 40 seconds with 100% agreement with the ground truth for the stested cases. The generation of sCT was less than 5 seconds with an accurcy of 98%. The DL auto-segemntaion yields Dice coefficints of greater than 0.7 even for complex organs, e.g., bowels, pancreas, duodenum, and stomatch. The auto-refinement results in up to 40% of inaccurate auto-segmented contours becoming acceptable. The 4-step segmentation pipeline can be completed within 5 minutes for the tested abdominal MRI sets.

Conclusions: The newly developed MOLAR solutions can automatically determine when OLAR is needed, rapidly generate accurate sCT, and substantially speed up segmentation on abdominal MRI. As a part of our on-going efforts, the MOLAR system is being implemented and integrated to substantially accelerate daily online adaptive replanning process in MRgART.

46

Progressively refined deep joint registration segmentation (ProRSeg) of gastrointestinal organs at risk for MRI dose accumulation

Jue Jiang Ph.D, Kathryn Tringale, Marsha Reyngold, Christopher Crane, Neelam Tyagi, Harini Veeraraghavan
Memorial Sloan Kettering Cancer Center, New York, NY, USA

Abstract

Purpose: Adaptive radiation treatment (ART) for locally advanced pancreatic cancer (LAPC) requires consistently accurate segmentation of the extremely mobile gastrointestinal (GI) organs at risk (OAR) including the stomach, duodenum, large and small bowel. Also, due to lack of sufficiently accurate and fast deformable image registration (DIR), accumulated dose to the GI OARs is currently only estimated, further limiting the ability to more precisely adapt treatments. The goal of our study if to develop a 3-D progressively refined joint registration-segmentation (ProRSeg) deep network to segment and align treatment MRIs, then evaluate the segmentation accuracy and feasibility for OAR dose accumulation.

Method: ProRSeg is implemented using deep neural network with convolutional LSTM layer in the encoder. ProRSeg was trained using 5-fold cross-validation with 110 T2-weighted MRI acquired at 5 treatment fractions from 10 different patients, taking care that same patient scans were not placed in training and testing folds. Segmentation accuracy was measured using Dice similarity coefficient (DSC) and Hausdorff distance at 95th percentile (HD95). Dose accumulation was performed by sequential alignment of the treatment fraction images and daily fraction doses (scaled to 5 fractions). DVF after each deformation was used to inter-fractionally accumulate doses for 5 patients who had daily dose maps available from online replanning. Intra-fraction dose accumulation was accomplished by aligning the pre-treatment MRI with the post-treatment MRI taken after completion of treatment on the same day.

Results: Segmentation accuracy of ProRSeg were significantly more accurate ($p<0.001$) compared to other deep-learning (voxelmorph) and non deep-learning (syN) methods, achieving a DSC of 0.94 ±0.02 for liver, 0.88±0.04 for large bowel, 0.78±0.03 for small bowel and 0.82±0.04 for stomach-duodenum from MRI (Table 1). ProRSeg based dose accumulation accounting for intra-fraction and inter-fraction motion showed that the organ dose constraints (D0.035cc = 33 Gy and D5cc = 25 Gy) were violated in 4 patients for stomach-duodenum and for 3 patients for small bowel (Figure 1). One representative deformation is shown in Figure 2. Out of these fibe, only one patient experienced grade 1 (mild abdominal) toxicity.

Conclusions: ProRSeg produced more accurate and consistent GI OARs segmentation and DIR of MRI compared to multiple available methods. Preliminary results indicates feasibility for OAR dose accumulation using ProRSeg.

Table 1: Segmentation accuracy (mean and standard deviation) of various methods applied to T2-w MRI. LG bowel: Large bowel, SM bowel: small bowel, Sto-Duo: stomach-duodenum. $*$: $p < 0.05$, +: $p < 0.01$, ‡: $p < 0.001$.

Method	DSC			
	Liver	LG Bowel	SM Bowel	Sto-Duo
SyN	0.89±0.04‡	0.59±0.13‡	0.61±0.09‡	0.66±0.08‡
Voxmorph	0.91±0.06‡	0.74±0.18‡	0.67±0.10‡	0.75±0.09‡
ProRSeg	0.94±0.02	0.86±0.08	0.78±0.07	0.82±0.05
	HD95 mm			
	Liver	LG Bowel	SM Bowel	Sto-Duo
SyN	9.17±3.55+	20.04±8.55‡	20.74±7.36‡	13.08±5.08‡
Voxmorph	7.85±3.85+	14.52±9.81‡	19.26±7.97‡	13.35±13.21‡
ProRSeg	5.69±1.72	7.00±5.14	12.11±5.30	8.11±3.54

Figure 1 Box plots showing accumulated dose metrics D0.035cm3(left) and D5cm3 (right) for stomach duodenum, small bowel and large bowel.

Figure 2 One representative example of MRI deformation.

47

Deep-learning based head-and-neck tumor segmentation for fully automated processing of MRI biomarkers

Daekeun You, Madhava Aryal, James Balter, Michelle Mierzwa, Yue Cao
University of Michigan, Ann Arbor, Michigan, USA

Abstract

Purpose: Automatic head and neck (HN) tumor segmentation is a crucial step in fully automated processing of image biomarkers for MRI-guided RT. Deep learning-based solutions have been proposed for HN tumor segmentation, with the most successful using PET and CT images. Approaches using MRI alone showed poor performance to date. In this study, we investigated fully automatic deep learning approaches for HN gross tumor volume (GTV) segmentation from MRI.

Methods and Materials: A total of 102 patients with p16- or p16+ HN cancers, including multiple HN cancer subsites, were used in this study. 74 patients were randomly selected for training and 28 patients for testing. We trained a 3D U-Net from the MONAI frameworks[1] with *DiceLoss* and *Adam* optimizer with a 5-fold cross validation. Two U-Net models were trained, one used post-Gd T1-weighted (T1w) images only as single channel input and another used T1w and T2-weighted (T2w) image volumes together as multi-channel input. To evaluate the segmentation performance, majority voting ensemble technique was used to generate a final segmentation map from five prediction maps and Dice similarity coefficient (DSC) and Mean Surface Distance (MSD) were computed between physician drawn GTVs and the prediction maps.

Results: Table 1 summarizes our testing results. The T1w U-Net model achieved a mean DSC of 0.60 and MSD of 3.82 mm. T1w and T2w combined model achieved better performance than the single input model, mean DSC of 0. 64 and MSD of 3.34 mm. The segmented GTVs from four patients showed very low DSC (<0.3). Investigations revealed that these cases had either small GTVs, low ratio of tumor-to-surrounding tissue, or blurred tumor boundary. Figure 1 shows two example results that achieved the highest DSC of 0.86 and lowest DSC of 0.00 by the T1w+T2w model.

Conclusion: Our study investigated automatic GTV segmentation of multiple types of HNC from MRI by deep learning without tumor location restrictions or expert initiation. Our initial segmentation performance is comparable with other studies targeting a single type of HNC (e.g., oropharyngeal in [2]). To improve the segmentation performance, further investigations will include designing new deep learning network architectures, increasing training data size, estimating posterior distributions of prediction, and incorporating multi-contrast inputs for complementary tumor characteristics. We will investigate the impact of automatically segmented GTVs on image biomarker processing.

Table 1. Performance of trained models

	Mean DSC	Mean MSD (mm)
T1w model	0.60 (0.69)	3.82 (2.49)
T1w+T2w model	0.64 (0.72)	3.34 (1.94)

Data in the parenthesis from 24 test cases.

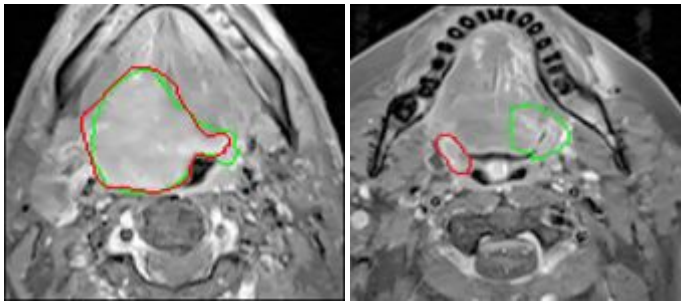

Figure 1. Segmentation results by T1w+T2w model. Left: Dice 0.86, right: Dice 0.0. Red and green contours are GTVs drawn by physicians and segmented by the model, respectively.

[1] The MONAI Consortium. (2020). Project MONAI. Zenodo. http://doi.org/10.5281/zenodo.4323059

[2] R. Rodríguez Outeiral et al., “Oropharyngeal primary tumor segmentation for radiotherapy planning on magnetic resonance imaging using deep learning,” Phys Imaging Radiat Oncol, 19 (2021), pp. 39-44

49

A Novel Deep Learning-based Workflow for Synthetic CT Generation Improves Dosimetric Accuracy for MRI-based Liver SBRT

Jin Uk Heo MS[1,2], Atallah Baydoun MD/PhD[3], Theodore Arsenault MS[3], Jennifer Dorth MD[3], Robert S. Jones[4,2], Shujin Sun BS[5], Yi Gu PhD[5], Yizhang Jiang BS[5], Pengjiang Qian PhD[5], Min Yao MD[6], John Nakayama MD[7], Bryan J. Traughber MD[6], Raymond F. Muzic Jr. PhD[1,2,4]

[1]Department of Biomedical Engineering at Case Western Reserve University, Cleveland, OH, USA. [2]Department of Radiology at Case Western Reserve University, Cleveland, OH, USA. [3]Department of Radiation Oncology at University Hospitals Cleveland Medical Center, Cleveland, OH, USA. [4]Department of Radiology at University Hospitals Cleveland Medical Center, Cleveland, OH, USA. [5]Jiangnan University, Wuxi, Jiangsu, China. [6]Department of Radiation Oncology at Penn State University, Hershey, Pennsylvania, USA. [7]Department of Obstetrics and Gynecology at Allegheny Health Network, Pittsburgh, Pennsylvania, USA

Abstract

Purpose

The purpose of this work is to investigate the feasibility of using deep learning-based synthetic computed tomography (sCT) generation for MR-only radiation treatment planning (RTP) for liver stereotactic body radiation therapy (SBRT). Due to the superior soft-tissue contrast of MRI compared to CT, MRI is crucial for target delineation in liver SBRT. Bypassing the use of CT in a MRI-only RT workflow can avoid MRI-CT registration errors, accelerate the clinical flow, and facilitate adaptive planning, eventually leading to improved tumor control. One major challenge in MRI-only RT is that, unlike CT, MRI lacks electron density information required for dose calculation. Therefore, recent efforts are made to generate sCT from MRI, and herein, we present and validate the clinical potential of a novel deep learning-based sCT generation method.

Methods

We designed a dedicated 4-channel conditional generative adversarial network (4C-cGAN) model where the generator organically integrates the well-known U-Net and the Residual neural Network. The channels correspond to the four volumetric DIXON images (fat, water, in phase, opposed phase) to maximize the available information. The discriminator (Markovian model) analyzes image patches.

A total of 34 data sets were acquired in a prospective trial that included patients undergoing routine whole-body (WB) clinical [18F]FDG-PET/CT scanning for whom [18F]-FDG-PET/MRI was also acquired. MRI were then registered to CT, and 4C-cGAN was used to generate sCT using a leave-one-out cross-validation.

Two methods were used as a reference for comparison: transfer fuzzy clustering with active learning-based classification (TFC-ALC) and 7-class segmentation. A simulated planning target volume (PTV) with a sphere of 25 mm diameter in liver segment V was selected for evaluation. An SBRT plan was generated using Pinnacle v16.2 to deliver 50 Gy in 5 fractions per the RTOG-1112 protocol. Fluence was copied into each sCT and the dose was recalculated.

The accuracy of the sCT compared to the measured CT (mCT) was evaluated using mean absolute error (MAE) and normalized cross-correlation (NCC). The dose distribution in sCT-based RTP was compared to that in mCT-based RTP using maximum dose and gamma evaluation.

Results

Full comparative metrics are provided in Table 1. Our proposed method (4C-cGAN) can generate sCT in approximately 5 minutes, and sCT is of superior quality compared to the TFC-ALC method and the 7-class segmentation method. For the liver SBRT plan, the proposed method achieves passing rates of approximately 99% of the voxels for 2%/2mm and 3%/2mm gamma criteria and even greater than a 95% for the very stringent 1%/1mm metric. In contrast, the generation using TFC-ALC or segmentation fails to achieve the customary 95% clinical acceptance rate for any of these gamma criteria.

Conclusion

Our 4C-cGAN generates a more accurate sCT and dosimetric distribution for MRI-only RTP for liver SBRT when compared with other sCT generation methods while achieving clinical acceptability of higher than 95% passing rate for all evaluated gamma criteria. These results suggest that using DCNN for sCT generation may be advantageous for MR-only workflow for liver SBRT, and warrants further development.

50

Dosimetric evaluation of plans from automated contours of elective target volumes and organs at risk for head and neck cancer patients for online adaptive MR-Linac treatments

Vesela Koteva[1], Alex Dunlop[2], Bjoern Eiben[1], Amit Gupta[2], Emilia Persson[1], Sebastiaan Breedveld[3], Uwe Oelfke[1]
[1]The Institute of Cancer Research, London, United Kingdom. [2]Royal Marsden Hospital, London, United Kingdom.
[3]Erasmus MC Rotterdam, Rotterdam, Netherlands

Abstract

Purpose: MR-Linac technology allows online daily adaptation of a radiotherapy treatment plan according to any anatomical changes detectable by daily MR imaging. This requires fast organ re-contouring, which is not feasible for head and neck cancer (HNC) patients if performed manually due to unacceptably long treatment times resulting in compromised patient comfort and low patient throughput. This study aims to develop and validate an algorithm for automated delineation executed in a time scale of less than a minute, that could be used for initial delineation and subsequent re-contouring for each treatment fraction.

Methods: A database consisting of 49 T2 weighted MR scans of 49 HNC patients was used. 38 scans were provided by the MOMENTUM study [1] and 11 by our hospital. The nodal elective clinical target volume (nCTV), parotid glands, spinal cord, brainstem, inferior pharyngeal constrictor muscle (IPCM), superior and middle pharyngeal constrictor muscle (SMPCM), and the mandible were manually delineated by a clinician. A deep convolutional neural network with a typical 2D U-Net architecture [2] was trained using 43 MR scans and their corresponding manually-delineated contours. Two MR scans were used for validation and four for testing. The time for generating a full set of contours by the algorithm was recorded. Geometric evaluation between the manually-delineated (ground truth) and algorithm-generated regions of interest (ROIs) was performed using Dice similarity coefficient (DSC). Dosimetric evaluation of the organs at risk (OARs) was also performed, whereby treatment plans optimised using the algorithm-generated ROIs were evaluated using the ground truth organs for the four tested patients. The mean dose and D95%, D50% and D5% for both algorithm-generated and manual OARs were recorded. The mean difference expressed as percentage of the prescribed dose of 65Gy was calculated for the investigated patient population.

Results: Example of the algorithm-generated structures overlayed with the manual contours is shown in Figure 1. Full delineation was performed in the order of 8 seconds. The DSC (± SD) were 0.75 ± 0.05 and 0.74 ± 0.02 for left and right nodes, respectively. Evaluated dose differences and DSCs for the remaining ROIs are shown in Table 1.

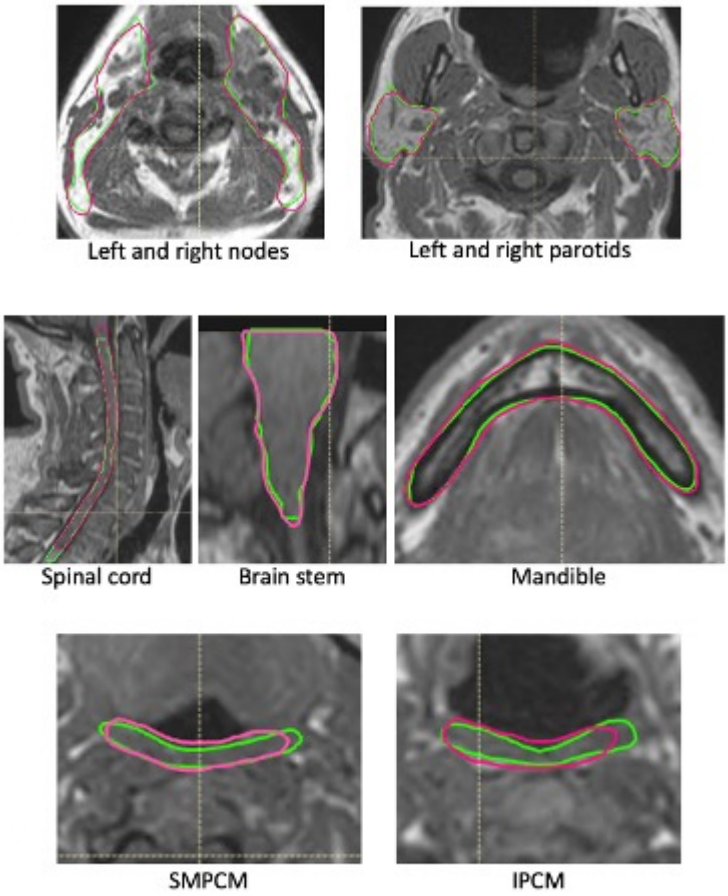

Figure 1: Examples of automatically generated contours (pink) overlayed with manually delineated contours (green)

	DSC	D95	D50	D5	DMean
Left parotid	0.84 ± 0.02	0.18 %	1.09 %	0.74 %	1.09 %
Right parotid	0.85 ± 0.03	0.09 %	1.43 %	0.62 %	0.95 %
Spinal cord	0.81 ± 0.06	0.86 %	0.86 %	1.09 %	1.22 %
Brain stem	0.89 ± 0.03	1.35 %	1.35 %	0.35 %	0.89 %
IPCM	0.55 ± 0.03	2.32 %	1.09 %	0.25 %	0.23 %
SMPCM	0.66 ± 0.04	1.09 %	0.83 %	0.49 %	1.06 %
Mandible	0.85 ± 0.02	3.17 %	0.06 %	0.88 %	1.29 %

Table 1: Geometrical evaluation showing the Dice similarity coefficient (DSC) ± standard deviation, which indicates how well the algorithm-generated contours overlap with the manually-delineated contours (1 being complete overlap and 0 being no overlap). Dosimetrical evaluation displaying the difference in mean dose (DMean) and dose delivered to 95% (D95), 50% (D50) and 5% (D5) volume of the manually and automatically delineated structures shown as a percentage with respect to the prescribed dose (65Gy).

Geometrical results indicate slight difficulty contouring the neck nodes and constrictor muscles. Regarding the nCTV, studies have shown that DSC for interobserver variability ranges between 0.67 – 0.82 when manually delineating the neck nodes [3]. Due to the small size of the constrictor muscles, DSC was expected to be lower than for the remaining ROIs. Dose analysis showed negligible difference in mean dose between the two sets of contours from plans based on automated ROIs with all relevant clinical goals fulfilled.

Conclusion: This study indicates the potential of clinically validated automated delineation of nCTV and OARs for initial and daily treatment planning for HNC patients executed in the order of seconds. Ongoing clinical trials will provide more data which will increase robustness and delineation accuracy.

References:

[1] S. R. de Mol van Otterloo et al., Frontiers in Oncology, 2020

[2] O. Ronneberger et al., MICCAI, 2015

[3] J. van der Veen et al., Radiotherapy and Oncology, 2019

51

Dosimetric comparison of MRI-guided vs CT-guided Stereotactic Body Radiotherapy to the Post-Prostatectomy Prostate Bed: A Post-Hoc Analysis of a Phase II Trial

Lauren M. Smith PhD[1], Yu Gao PhD[1], Stephanie M. Yoon MD[1], John N. Nikitas MD[1], Tommy Jiang BA[1], Ting Martin Ma MD, PhD[1], Leslie K. Ballas MD[2], Michael L. Steinberg MD[1], Amar U. Kishan MD[1], Minsong Cao PhD[1]

[1]University of California Los Angeles, Los Angeles, California, USA. [2]University of Southern California, Los Angeles, California, USA

Abstract

Purpose: To evaluate differences in target and organ-at-risk (OAR) dosimetry between CT-guided (CTgRT) and margin-reduced MRI-guided (MRgRT) stereotactic body radiation therapy (SBRT) delivered to the post-prostatectomy prostate bed.

Methods: SCIMITAR (NCT03541850) was a prospective phase II clinical trial evaluating stereotactic body radiotherapy (SBRT) for post-prostatectomy patients. 100 patients were enrolled onto this trial and treated with SBRT of 30-34Gy in 5 fractions to the prostate bed. 69 of these patients received CTgRT treatment on the conventional Linac (Truebeam, Varian) and 31 received MRgRT on a MR Linac (MRIdian, ViewRay). A 5mm isotropic expansion for the PTV was used for CTgRT treatment while a tighter margin of 3mm was adopted for the MRgRT treatment owing to improved soft tissue contrast and real-time motion management. Planning dosimetric metrics for the clinical target volume (CTV), planning target volume (PTV), and OARs listed in Table 1 were obtained for all 100 patients and compared between these two groups of treatments.

Results: Similar CTV and PTV coverage was achieved for both CTgRT and MRgRT in term of V95% and V100% as well as mean dose. The MRgRT plans showed significantly lower dose to several OARs including the rectum by multiple metrics (V27.5Gy, V32.5Gy, V33.75Gy), as well as lower doses to the rectal wall (V24Gy), sigmoid (V25Gy), and small bowel maximum dose, although bladder dosimetry did not significantly differ between platforms.

Conclusion: A post-hoc analysis of the planning dosimetry in patients treated with MRgRT and CTgRT showed similar target coverage, with MRgRT plans having lower OAR doses with respect to rectum, rectal wall, sigmoid, and small bowel. This is consistent with the observed lower rate of acute bowel toxicity in patients receiving MRgRT. Future work will evaluate actual delivered dose and correlate these dosimetric metrics with toxicity and efficacy.

Table 1. Planning dosimetric parameters achieved for CTgRT and MRgRT cohorts

	CT Mean	CT Median	CT Q1	CT Q3	MRI Mean	MRI Median	MRI Q1	MRI Q3	P-value
CTV V100%	98.49	99.41	97.73	99.82	99.01	99.31	98.60	99.89	0.2597
PTV V100%	94.68	94.75	94.40	95.78	95.83	96.30	94.71	97.13	0.0573
Rectum V27.5Gy	16.29	14.88	10.90	20.39	9.67	9.02	4.83	12.71	<0.0001
Rectum V32.5Gy	6.58	5.50	2.02	10.09	3.15	2.70	0.33	5.69	0.0011
Rectum V33.75Gy	3.76	2.24	0.10	6.31	1.47	0.62	0.02	1.90	0.0066
Rectal Wall V24Gy	25.34	25.75	19.56	30.71	18.46	18.37	12.21	24.29	<0.0001
Bladder V30Gy	77.57	71.36	54.45	98.77	82.93	80.87	47.60	103.92	0.4707
Bladder	19.44	18.51	9.70	31.56	18.28	18.14	10.24	23.85	0.6585

V32.5Gy									
Bladder Dose Maximum	35.96	35.42	34.63	35.78	36.60	35.56	35.40	37.64	0.2277
Bladder Wall V30Gy	20.80	19.78	16.63	23.90	21.75	23.28	16.20	25.99	0.4808
Bladder Wall V25Gy	24.10	22.33	19.02	27.31	25.68	26.34	19.32	29.12	0.3287
Bladder wall V20Gy	28.58	25.61	20.82	33.53	30.23	29.71	23.21	34.41	0.4947
Small Bowel V20Gy	5.81	0.74	0.00	7.16	1.57	0.00	0.00	0.04	0.2308
Small Bowel Dose Maximum	18.77	23.04	12.29	24.50	11.20	6.56	1.74	20.95	0.0013

52

Dosimetric Goals Versus Realities in Initial and Adaptive Plans from an Ongoing Phase II Clinical Trial of Online Adaptive MR-Guided Hypofractionated Radiation with Concurrent Chemotherapy for Locally-Advanced NSCLC

Gregory Vlacich MD, PhD[1], Alex Price[1], Olga Green[1,2], Clifford Robinson MD[1], Pamela Samson MD[1]
[1]Washington University in St. Louis, St. Louis, MO, USA. [2]Varian Medical Systems, Palo Alto, CA, USA

Abstract

Purpose:

To ensure the safety and efficacy for hypofractionated radiation therapy with concurrent chemotherapy in locally-advanced non-small cell lung cancer (LA-NSCLC), strict dosimetric guidelines were employed for tumor and organ at risk (OAR) dose within a prospective Phase II clinical trial. Here we assess the feasibility and the role of adaptation in achieving these dosimetric targets.

Methods:

Patients with inoperable LA-NSCLC were enrolled onto a single-institution Phase II clinical trial and received 60 Gy in 15 fractions on the Viewray MRIdian 0.35 T MR-linear accelerator. Online adaptation was performed at fractions 6, 9, and 12. For the initial and adapted plans, the prioritization for radiation planning was as follows: (1) achieve spinal cord and esophagus constraints, then (2) PTV coverage, then (3) constraints for other organs at risk (OAR). PTV coverage goal was 95% receiving 95% prescription (57 Gy) or to PTV-OPT (PTV carved 3-5 mm from OAR if overlapping with heart or esophagus). Minimum required PTV coverage was 51 Gy (EQD2 = 57 Gy) to ≥95%. Maximum dose of 105% prescription (63 Gy) was an acceptable variation to priority 3 OARs.

Results:

A total of 19 patients were evaluated and all completed concurrent chemoradiation as prescribed. For initial treatment plans, spinal cord constraints and an esophageal 5 cc volumetric constraint were met in all patients with esophageal maximum and mean dose constraints achieved in 89% (17 of 19 patients) and 95% (18 of 19 patients) respectively. Due to PTV proximity to mediastinal OARs, a PTV-OPT was necessary in 18 of 19 patients. Median PTV V57 was 79.25% (range: 67.53 to 98.22) and median PTV-OPT V57 was 98.5% (range: 67.84 to 99.96). Minimum required PTV coverage was achieved in 63% (12 of 19 patients) with a median V51 of 98.22% (range: 91.69 to 100), but all patients satisfied an acceptable variation of 48 Gy to ≥95%. For priority 3 OARs, a number of initial plans could not satisfy protocol constraints and 105% prescription maximum was utilized instead for heart (74%), great vessels (74%), and trachea/bronchial tree (47%). The median value of mean lung dose was 14.02 Gy (range: 8.17 to 21.75; protocol constraint <18 Gy) and median V20 was 22.96% (range: 12.81 to 48.56; protocol constraint <37%). Subsequent adaptive planning did not consistently improve priority 3 OAR sparing. Of OAR constraint violations at initial planning, these were resolved by fraction-12 adaptive plan in 7 of 23 initial trachea/bronchial tree violations, but only 1 of 15 lung violations, and 0 of 27 heart violations. This is primarily a consequence of inconsistent tumor response with median change in PTV volume (fraction 1 to fraction 12) of only -6.51 cc (range: +261.82 to -204.02 cc).

Conclusion:

The ability to achieve strict dose constraints to OARs while maintaining adequate PTV coverage is limited in hypofractionated radiotherapy for LA-NSCLC and intermittent adaptive planning does not appear to consistently improve OAR sparing. Further dosimetric analysis and correlation with subsequent clinical outcomes may identify more achievable constraints with acceptable toxicities and tumor control.

53

Regularizing breathing during 4D-MRI acquisitions on the MR-linac with visual biofeedback

Katrinus Keijnemans, Pim Borman, Bas Raaymakers, Martin Fast
University Medical Center Utrecht, Utrecht, Netherlands

Abstract

Purpose Motion management in the abdominothoracic region is important because of respiration. 4D-MRI is an efficient tool for providing respiratory-compensated daily imaging on the MR-linac, but its quality might suffer in case of irregular breathing. In this study, we investigate the efficacy of a novel method of providing visual biofeedback to regularize breathing during 4D-MRI acquisitions on a 1.5 T Unity MR-linac (Elekta AB, Stockholm, Sweden).

Methods A respiratory navigator (RNAV) was interleaved with a simultaneous multi-slice (SMS) 4D-MRI sequence. Data were acquired in six healthy volunteers with a T_2-weighted turbo spin echo sequence: 2(CC)x2.5(LR)x4–4.5(AP) mm^3 voxel size, 350(CC)x457(LR)x208–234(AP) mm^3 FOV. During 4D-MRI acquisitions, the RNAV position was used as surrogate respiratory signal for visual biofeedback and was displayed together with a guidance waveform on an in-room monitor (Figure 1), which was located at the cranial side of the MR-linac bore and could be viewed via a mirror. The guidance waveform was a $\cos^4$ with a peak-to-peak amplitude and period derived from an unguided acquisition. The latency between acquiring and displaying the RNAV was measured and accounted for during display.

Four 4D-MRI acquisitions were performed: 1) an unguided 4D-MRI acquisition to obtain the 'natural' peak-to-peak amplitude and period (4:27 min), 2) a guided acquisition with the subject-specific peak-to-peak amplitude and period (5:12 min), 3) a guided acquisition with 50% increased period to evaluate adaptability (5:12 min), and 4) a longer guided acquisition with the subject-specific peak-to-peak amplitude and period to evaluate the ability to maintain regular breathing (10:24 min).

The long acquisition was analyzed with a sliding window approach (4:27 min window size), resulting in 36 4D-MRIs. For all 39 4D-MRIs, the RNAV signals were split into individual respiratory cycles by detecting the end-inhale locations. Breathing regularity for peak-to-peak amplitude and period was quantified by calculating the coefficient of variation (CV, Equation 1). The reduction in variability (i.e., improved regularity) was determined by comparing the CV of guided acquisitions to the unguided acquisition (Equation 2).

$$CV_{a,b} = \sigma_{a,b} \,/\, \mu_{a,b} \quad [1]$$

$$CV_{red,b}\,[\%] = (CV_{Guided,b} - CV_{Unguided,b}) \,/\, CV_{Unguided,b} * 100\% \quad [2]$$

where $a \in$ (Unguided $\vee$ Guided) and $b \in$ (Amplitude $\vee$ Period).

Furthermore, the stability of the end-exhale, end-inhale, and mid-position locations was quantified.
The SMS images were saved for retrospective 4D-MRI reconstruction using the acquired RNAV positions as sorting signal.

Results The latency of displaying the RNAV position was 356±6 ms. The median (min:max) CVred was −23.2 (−57.7:31.8)% for the breathing peak-to-peak amplitude and −60.0 (−85.0:3.6)% for the breathing period (Figure 2).
The median (min:max) position standard deviation was 2.3 (2.0:2.9) mm for end-inhale and 1.5 (0.7:3.5) mm for end-exhale in the unguided acquisitions. For acquisitions with guidance, this reduced to 2.0 (1.1:3.1) mm and 1.1 (0.4:2.9) mm respectively. The median (min:max) absolute mid-position drift during the long acquisition was 0.2 (0.0:3.6) mm.

Conclusion Visual biofeedback during 4D-MRI acquisitions drastically reduces breathing variability, resulting in a more predictable moving anatomy.

54

Exploring physiological changes after conformal radiation therapy in orthotopic U251 glioma model as potential biomarkers of response using DCE-MRI

O. Grahm Valadie[1,2], Dr Stephen Brown Ph.D[1], Glauber Cabral[1], Dr Tavarekere Nagaraja Ph.D[1], Katelynn Farmer[1], Prabhu Acharya[1,3], Dr Robert Knight Ph.D[1], Dr George Divine Ph.D[1], Dr. James Ewing Ph.D[1,3]

[1]Henry Ford Health System, Detroit, MI, USA. [2]Wayne State University, Detroit, MI, USA. [3]Oakland University, Rochester, MI, USA

Abstract

Purpose: Early predictors of tumor response would allow for altered treatment and potentially better outcomes. As a first step, this work aims to identify physiology that might signal long-term radiation treatment (RT) response in orthotopic, small animal models of gliomas using dynamic contrast-enhanced MRI (DCE-MRI). Studies exist suggesting a strong relationship between tumor exudate flux and the distribution volume of the outer rim of the tumor (V_D) in U251 tumor models [1]. This relationship was explored as a potential marker of survival after conformal RT.

Methods: RNU athymic rats were stereotactically implanted with human U251 cells. At ~18 days, rats were irradiated with a single fraction of 20 Gy delivered via four non-coplanar arcs with an identical isocenter using a Small Animal Radiation Research Platform (SARRP). The SARRP operated at 220 kV and 13 mA, with effective energy of ~70 keV and dose rate of ~2.5 Gy/min. The treatment field conformed to the tumor identified by contrast-enhanced MR with no margin. DCE-MRI studies were performed before, ~3 hrs after, and ~8 days following RT. Study endpoint was animal survival at 200 days with no health deterioration. Established model selection paradigms [2,3], and Patlak [4] and Logan [5] plots applied to DCE-MRI data were used to estimate the VD and exudate flux from the inner rim of the tumor through the outer rim. Survival studies are ongoing.

Results: Initial analysis revealed a significant ($p<0.05$) pre-irradiation relationship between flux and V_D (Fig 1A). This relationship did not deviate significantly at 3 hrs post-irradiation (Fig 1B) but did 8 days post-irradiation (Fig. 1C). Wilcoxon rank-sum tests comparing the percent flux change (depicted in Fig 2) from the pre-RT baseline showed that, while the short-term changes were not significant, the long-term changes were significantly different from baseline values.

Figure 1 additionally depicts the relationship between Flux vs VD distinguishing between survivors and non-survivors. While pre-irradiation regression lines (Fig 1A) do not deviate greatly from each other, both short- (Fig 1B) and long-term (Fig 1C) regression lines did. A general trend is the slope from animals that survived 200 days is greater than that from the animals that did not. Wilcoxon rank-sum tests did not show any significant flux change differences between survivors and non-survivors at any time point.

Conclusion: Preliminary analyses indicate that changes in flux are significant 8 days post-RT. The relationship between two physiological biomarkers appears to both change after treatment and vary depending on the long-term therapy outcome. The discriminator between eventual survivors from non-survivors is greatest at high flux and VD values suggesting an area of future study: pharmacologically increasing flux and/or distribution volume at the tumor boundary.

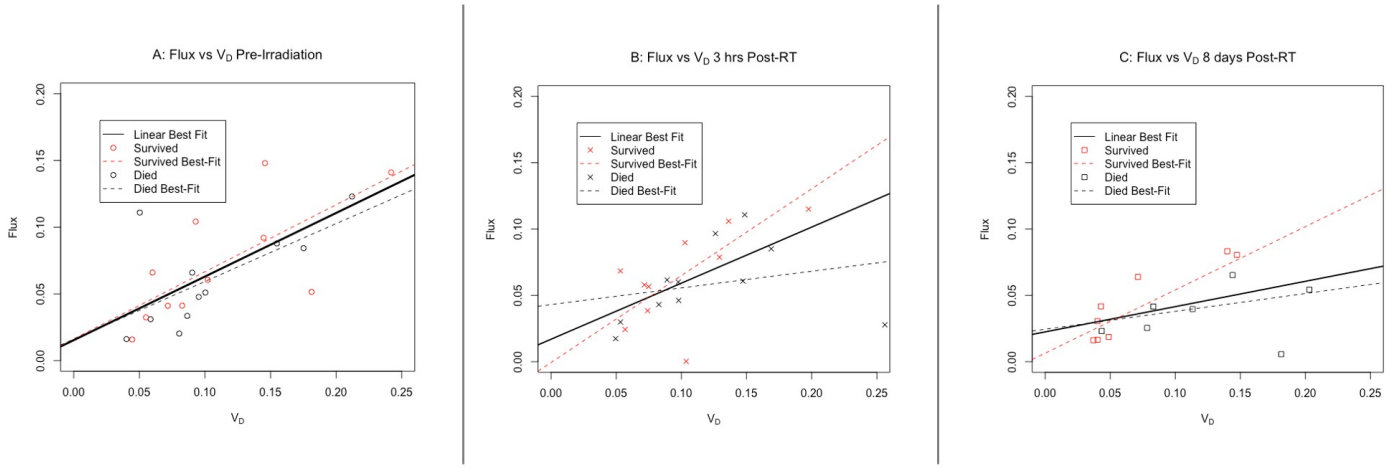

Figure 1 – Tumor exudate flux versus the distribution volume in the outer rim of the tumor (V_D) based on A) Pre-RT values, B) 3 hrs post-RT values, C) 8 Days-Post RT values. Values are distinguished on each plot by color (red = survived to 200 days, black = died before 200 days). The best linear fit of all points (solid black) is plotted alongside the best linear fit from the survivor data (red dashed) and non-survivor data (black dashed).

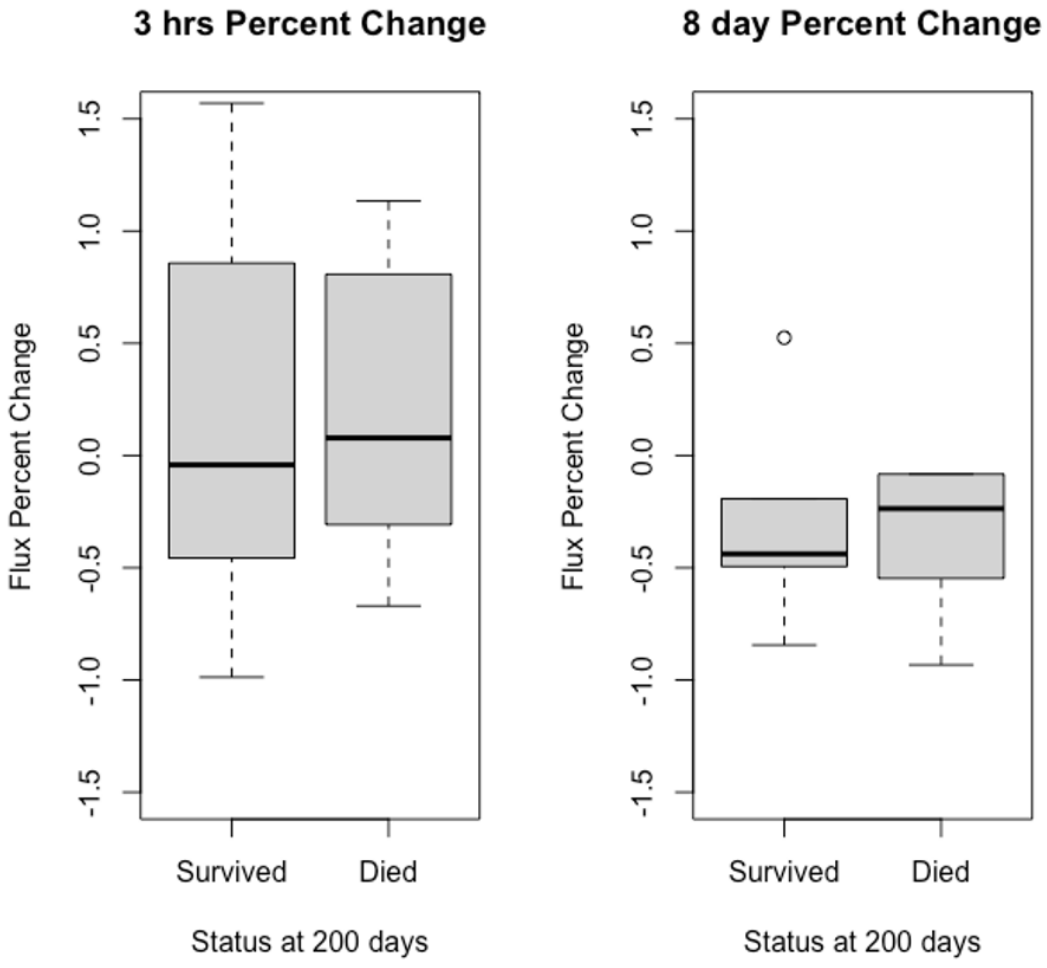

Figure 2 – Box and whisker plots showing the percent change of the flux from pre-irradiation baseline at the 3 hrs post- and 8 days post-RT separated by survival to study end at 200 days.

55

Development and clinical implementation of a novel MRI-only planning workflow for prostate cancer external beam radiotherapy

Boyu Meng PhD, Xiao Liang PhD, Chenyang Shen PhD, Andrew Godley PhD, Junjie Wu PhD, Paul Medin PhD, Ti Bai PhD, Mu-han Lin PhD, Steve Jiang PhD, Yulong Yan PhD, Jie Deng PhD
UT Southwestern Medical Center, Dallas, TX, USA

Abstract

Purpose: There is widespread recognition that MRI provides superior soft tissue contrast for target and normal tissue delineation and improved interobserver contouring consistency for prostatic cancer. In most clinics, multi-modality imaging is used for prostate external beam radiation therapy (EBRT) planning in a combined workflow, where MRI is utilized as secondary imaging modality for visualization and segmentation of anatomical features, and co-registered to CT for treatment planning. However, CT-MRI combined workflow introduces systematic error from image registration inaccuracy and temporal changes in anatomy between image acquisitions. Hence, adopting a MR-only workflow would mitigate registration limitations and improve treatment plan quality. Herein, we described the development and clinical implementation of an MRI-only planning workflow for prostate radiotherapy using novel sCT generation algorithm and automatic detection of gold fiducial markers (FMs).

Methods: The proposed MRI-only workflow is demonstrated in Figure 1. The MRI simulator utilized in this study is a 1.5T Philips MRI scanner. The novel sCT generation algorithm utilized a multichannel CycleGAN model with fat and in-phase (IP) images acquired by a T1-weighted Dixon MRI sequence to improve the bony structure accuracy in sCT. The sCT quality, including boney structure generation, hounsfield unit (HU) accuracy, and sCT-based plan quality was examined retrospectively using 11 clinical patients' data, where CT-MRI combined workflow were used. Automated FM identification was achieved by using quantitative susceptibility mapping (QSM). QSM maps were computed based on the magnitude and phase images of gradient echo MRI to distinguish gold FMs from prostate tissues based on the substantial difference in their magnetic susceptibility. Other developmental work included auto-contouring of prostate for automatic FM detection process, as well as coordinates conversion system to ensure accurate patient setup during treatment. The MRI-only workflow was fully integrated into the Eclipse treatment planning system (TPS) via Eclipse Scripting API (ESAPI).

Results: Visual inspection and quantitative comparison demonstrated a strong similarity between CT and sCT (Figure 2A-F). The average HU difference between sCT and CT was determined to be -0.25 ± 5.90 HU, and bony anatomic structures showed the largest HU deviations, 55.16± 24.31 HU. Dosimetric study showed that the sCT plan qualities were comparable to CT plan qualities for planning-target-volumes (PTVs) and organs-at-risk (OARs) (Figure 2G, H). The detection rate of 66 FMs in 22 patients using the QSM algorithm was 89.4%, with an average displacement of 2.6mm compared to FMs identified on CT by a clinician. Six prostate EBRT patients were included in the initial clinical trial, and 4 patients were successfully treated with MRI-only planning workflow, including 1 SBRT and 3 non-SBRT treatments.

Discussion: Clinical implementation of MR-only radiation therapy simulation and planning for prostate cancer is still in its infancy. Currently, only a few centers have adopted the MR-only workflow with limited publication focusing on clinical workflow. In this study, we demonstrated a novel MRI-only planning workflow by utilizing in-house developed sCT generation and FM localization algorithms. The proposed workflow offers a unique perspective that could be leveraged in MRI simulation development, patient stratification, and treatment improvement.

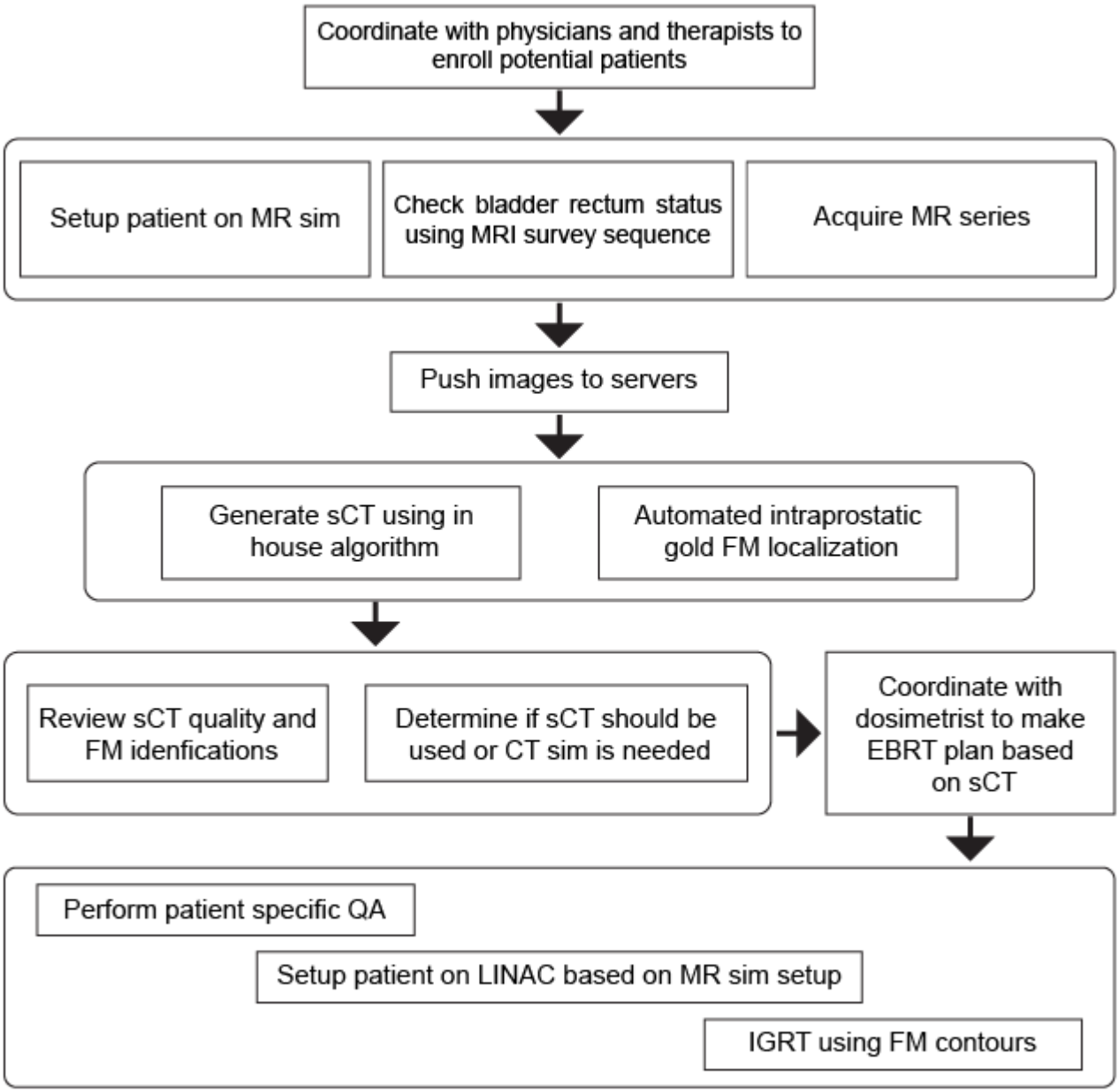

Figure 1: Flowchart of MRI-only planning workflow

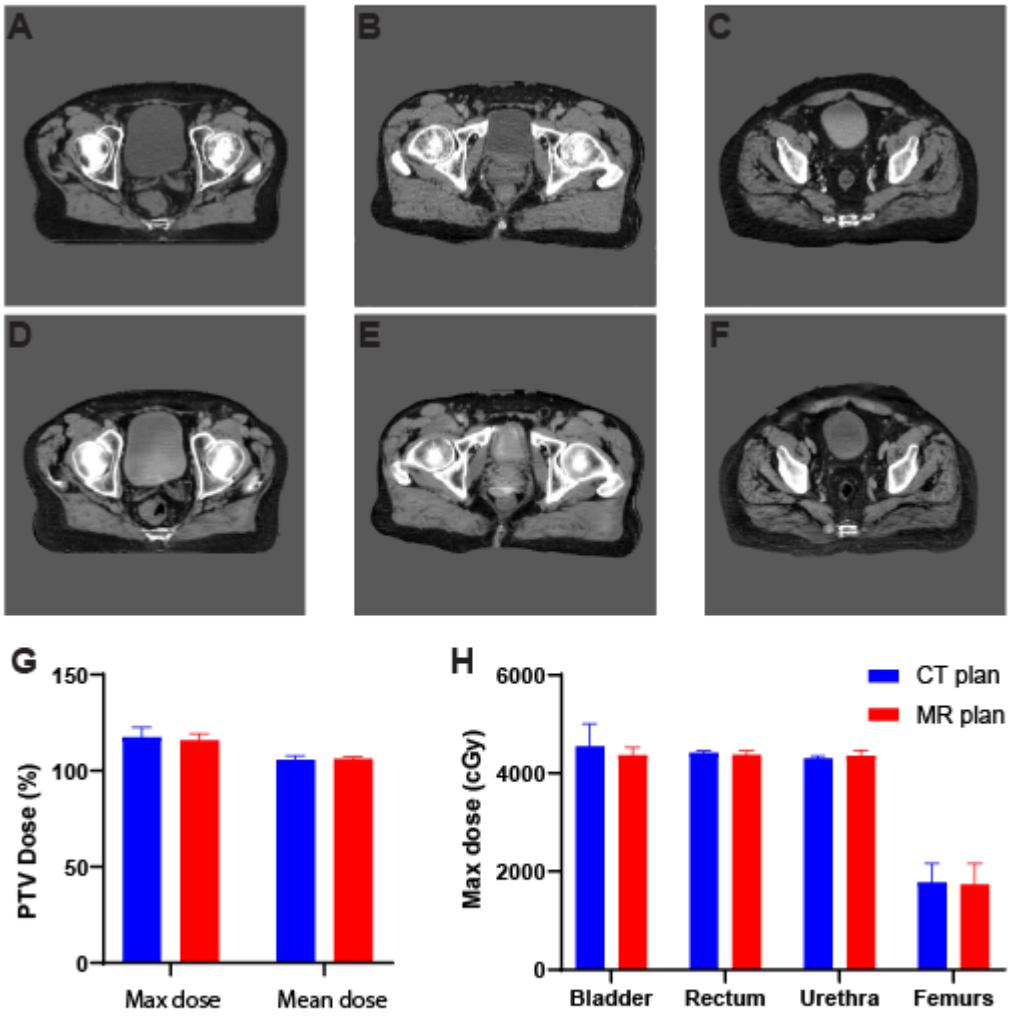

Figure 2: sCT quality assessment. (A)-(C): Axial view CT images of 3 different patients. (D)-(F): Corresponding sCT images. PTV (G) and OARs (H) dosimetric comparisions between CT-MRI combined workflow plans (blue) and MRI-only workflow plans (red)

56

Real-time dose reconstruction with differential target and OAR motion and inter-beam replanning

Dr Björn Eiben PhD, Dr Emilia Persson PhD, Edmund Goodwin MSc, Dr Simeon Nill PhD, Prof Uwe Oelfke
Joint Department of Physics, Institute of Cancer Research and Royal Marsden NHS Foundation Trust, London, United Kingdom

Abstract

Purpose

Real-time delivered dose reconstruction is a prerequisite to leverage the advantages of online adaptive radiotherapy, for instance by inter-beam replanning. Many studies for motion-including dose reconstruction assume the patient anatomy rigidly shifts with the target. However, this approach implemented as a simple iso-centre shift cannot account for differential motion of two or more anatomical structures.

We introduce a method to track and accumulate organ doses which accounts for differential motion between the primary radiation target and an organ at risk (OAR). The calculated delivered dose is subsequently used to perform inter-beam replanning for a simulated MR-linac treatment.

Method

We developed a software framework that integrates the research treatment planning system Monaco (Version 6.09.01, Elekta) via the research interface (C++ API), with our in-house treatment delivery simulation platform and a dose calculation engine (GPUMCD, Elekta). Figure 1 shows an overview of the essential software components and the main data exchanged. Initial treatment plans are generated in Monaco according to clinical protocols. To simulate treatment delivery, the plan and patient geometry including tissue properties are sent to our control entity which starts the treatment simulation, including motion management and motion trace selection. During the simulation the dose to the selected anatomical structures and to the overall anatomy is calculated in real-time as follows. Point clouds (PCs) are generated that cover two configurable region-of-interest (ROI) groups plus a margin. During online dose calculation MLC shapes and patient geometry are used by the dose calculation engine to first calculate the dose to the full anatomy. Then the PCs are moved to their positions reported by the treatment simulation and usually detected by real-time MRI. There the dose is sampled and then accumulated at each point. After each beam both PCs project the accumulated dose onto the overall dose cube using their last sampling positions. This reconstructed delivered dose is passed back into Monaco, structures are moved to the respective point cloud positions. Optionally, a bias dose plan accounting for the delivered reconstructed dose can be created and optimised for the remaining beams. A 5-fraction, 9-beam IMRT MR-linac treatment plan for a prostate patient was created with 36.25Gy prescribed to 95% of the PTV. Zero and linear motion of the target from zero to about 1cm in IEC-y direction (superior) was simulated. The OAR was kept in its initial position and MLC tracking was enabled.

Figure 1: Data flow and processing components. Data on a beam-by-beam basis is shown as colour arrows, whereas continuous data streams are shown in grey.

Results

Figure 2 shows the differential DVHs for the PTV (top) and for the rectum (bottom) after beams 1/5/9 (140°/0°/220°) for zero (orange) and drifting motion (blue). D98 for the PTV was 34.57Gy/ 34.15Gy for zero/drifting motion. A decrease in V36Gy from 1.99cm^3 to 0.025cm^3 for the rectum could be observed due to differential motion.

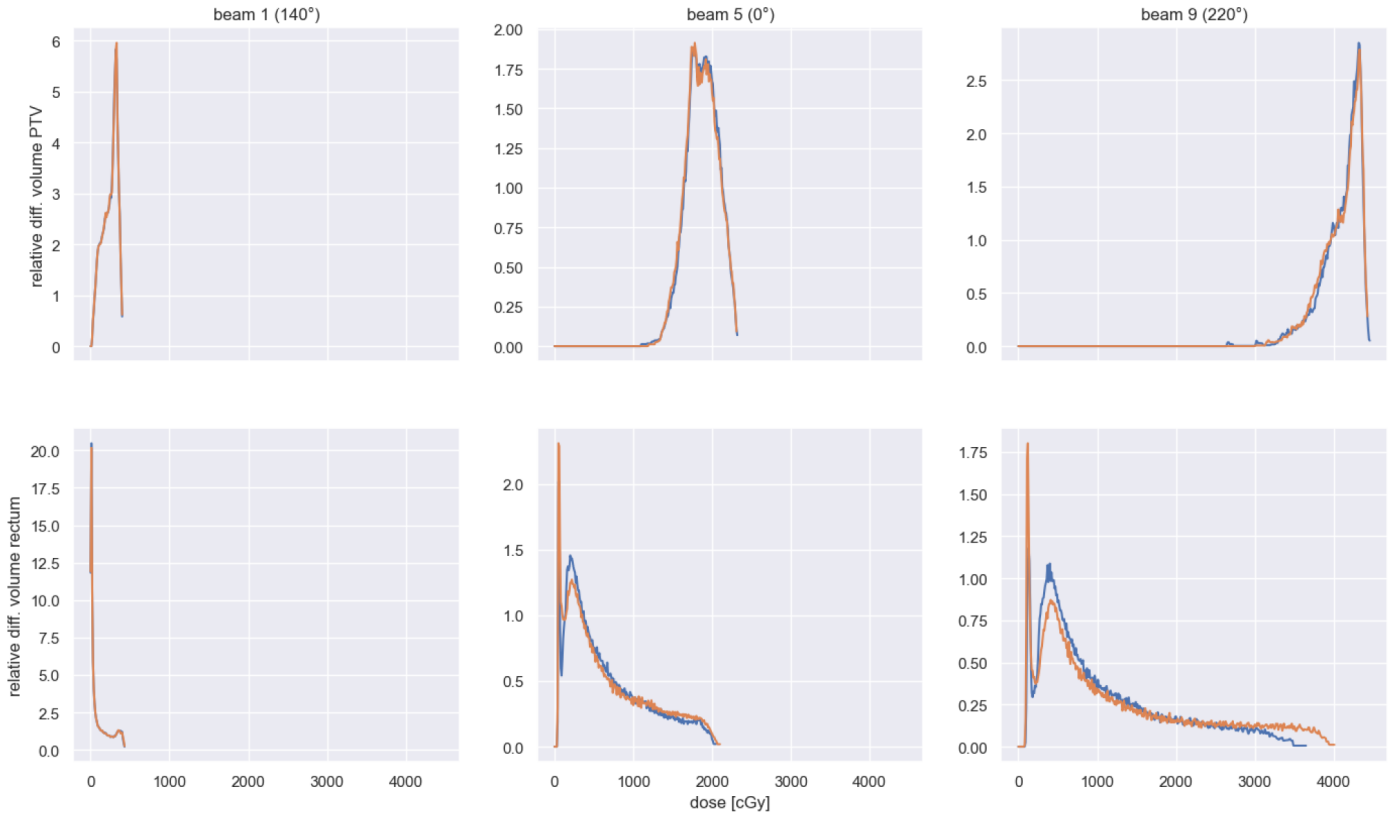

Figure 2: Differential dose-volume histograms for accumulated organ doses after beams 1, 5, and 9 (140°, 0°, and 220°). The PTV moved with linear motion in the IEC-y direction over the course of the delivery whilst the rectum (OAR) stayed in its initial position.

Conclusion

We have designed and implemented a software framework enabling investigation of various dose delivery strategies such as tracking or gating with a real-time dose reconstruction method that allows for differential motion of two ROI groups. This paves the way to investigate scenarios which will benefit from inter-beam replanning.

57

Dosimetric impact of gating and MLC tracking in MR-guided ultra-hypo fractionated prostate radiotherapy

Emilia Persson PhD[1], Björn Eiben PhD[1], Edmund Goodwin MSc[1], Alison Tree PhD[2], Andreas Wetscherek PhD[1], Simeon Nill PhD[1], Uwe Oelfke Professor[1]

[1]Joint Department of Physics, Institute of Cancer Research and Royal Marsden NHS Foundation Trust, London, United Kingdom. [2]Royal Marsden NHS Foundation Trust and the Institute of Cancer Research, London, United Kingdom

Abstract

Purpose

MR-guided radiotherapy gives the opportunity to carefully tailor the treatment to the daily patient anatomy and to monitor intra-fraction motion. Given the trend in radiotherapy to move towards fewer fractions with higher fraction doses, motion management strategies will play a vital role in ensuring target coverage and avoidance of organs at risk (OARs). Depending on the magnitude of intra-fraction motion, the delivered dose will be affected by the chosen motion management strategy and must be considered accordingly.

The purpose of this study was to investigate the dosimetric impact of introducing gating and multi-leaf collimator (MLC) tracking for MR-guided ultra-hypo fractionated prostate radiotherapy.

Methods

Daily treatments for the first three patients included in the two-fraction arm of the HERMES-trial (prescription dose: 24Gy) were retrospectively analysed. Patients had received treatment using the Elekta Unity MR-linac (Elekta AB, Stockholm, Sweden) with a daily adapt-to-shape workflow. In this study, the first treatment for each patient was simulated and the delivered dose reconstructed using a tracking and adaptation software developed in-house.

The software enables an automated workflow for real-time motion including dose reconstruction and simulates treatment delivery with gating and MLC tracking on the Elekta Unity MR-linac. Connection to research Monaco TPS (v.6.09.01, Elekta AB, Stockholm, Sweden), enables use of daily treatment information, including treatment plan, MR-images, and delineated target and OARs. The delivered dose is automatically reconstructed with the GPUMCD-library (Elekta AB, Stockholm, Sweden) by assigning bulk densities to the daily MR. Two previously reported prostate motion traces, representing erratic and stable motion (Figure 1), were used to investigate the impact of rigid target motion of different magnitude on the delivered dose.

For each patient and motion trace, treatment delivery was simulated with the following motion management strategies; 1) No motion management, 2) Gating with a 3mm window from the original target position, 3) MLC tracking in 1D (motion restricted to leaf travel direction), and 4) MLC tracking. A treatment delivery with zero motion was simulated and used as a baseline. The reconstructed doses for the three fractions were compared using DVH-analysis.

Results

The DVH-analysis is presented in Figure 2. The erratic motion showed larger variations between the motion management strategies compared to the stable motion. MLC tracking performed closest to the baseline for most cases. The overall highest target doses for both motion traces were seen for MLC tracking. With respect to target dose, 1D tracking performed closest to no motion management for the erratic case. Restricting MLC tracking to 1D or enabling gating lowered the rectum dose in comparison to MLC tracking.

Conclusion

This first evaluation shows that the dose delivered to the target and OARs is sensitive to the choice of motion management strategy. The dosimetric impact is more pronounced for large intra-fraction motion and MLC tracking results in the highest target dose. Restricting the MLC motion to the leaf travel direction will lower the overall dose when large motion is predominant in the anterior-posterior direction. Increased dose to OARs need to be considered for MLC tracked treatment delivery.

58

Characterization of MR image quality for simultaneous ion beam scanning in particle therapy

Stefan Dorsch[1,2,3], Katharina Paul[1,2], Alina Elter[1,2,3], Cedric Beyer[1,2,3], Jakob Naumann[4], Thomas Hansmann[4], Eike Feldmeier[4], Christian P. Karger[1,3], Jürgen Debus[1,2,4,5,6]

[1]National Center for Radiation Research in Oncology (NCRO), Heidelberg Institute for Radiation Oncology (HIRO), Heidelberg, Germany. [2]Department of Radiation Oncology, University Hospital Heidelberg, Heidelberg, Germany. [3]Department of Medical Physics in Radiation Oncology, German Cancer Research Center (DKFZ), Heidelberg, Germany. [4]Heidelberg Ion-Beam Therapy Center (HIT), Heidelberg, Germany. [5]Clinical Cooperation Unit Radiation Oncology, German Cancer Research Center (DKFZ), Heidelberg, Germany. [6]core center Heidelberg, German Cancer Consortium (DKTK), Heidelberg, Germany

Abstract

Purpose

MR-guided particle radiotherapy (MRgPT) holds the potential to increase therapy precision by daily control of location, volume and shape of tumor and organs at risk. Furthermore, the ability to gate the beam application to breathing motion has been shown to be beneficial in MR-guided photon therapy1,2. Although, no commercial MRgPT system is available to date, experimental setups have been reported3,4,5. In this work, we present the characterization of an open MR scanner positioned in-line to an ion beam, focusing on the MR image quality during the simultaneous operation of MR imaging and particle irradiation.

Material and Methods

An open MR scanner with a field strength of 0.25 T from a permanent magnet in vertical direction (Esaote, Italy) was positioned within a radiofrequency-shielded cabin in front of a horizontal ion beamline. Several image quality parameter like signal-to-noise ratio (SNR) and ghosting ratio were assessed in dedicated phantoms during simultaneous irradiation with and without beam scanning in horizontal and vertical direction (protons and carbon ions) and acquisition of MR images (2D Spin Echo (SE), 2D-CINE and 3D Gradient Echo (GRE)). To mimic beam scanning during in-vivo knee imaging in a healthy volunteer, the beam scanning magnets were operated remotely with a continuously changing current pattern but without having an active beam. Maximum beam currents were set equivalent to a beam deflection of ±10 cm for carbon ions at the highest energy (430 MeV/u).

Results

In accordance to other publications3,5 no dependency of MR image quality on the beam-energy of a central spot was found. However, the fringe field of the horizontal beam-scanning magnet leads to an additional frequency component within the isocenter of the MR-device causing ghosting artefacts (Figure1) and reducing SNR in 3D GRE images. The extent is correlated to the spot duration or ramp rate of the scanning magnet – with amplified artifacts for high currents and fast switching of the scanning magnet. Significantly less or no artefacts were found in the 2D SE images. Likewise, the 2D-CINE revealed no ghosting artefacts for the in-vivo measurement (Figure2), suggesting that the fringe field of the horizontal beam scanning magnet may be neglected when using therapy-relevant beam scanning parameters and fast CINE MR imaging. For 3D images, an optimization of treatment plans to avoid short spot durations, scanning mainly in the vertical direction or additional magnetic shielding of the scanning magnets may further improve image quality.

Conclusion

Our experiments revealed that the presented setup of an MR scanner in front of a horizontal beam line enables high quality MR imaging while simultaneously irradiating a target using active beam scanning. One limitation of this study is the small range of analyzed MR pulse sequences that needs to be adapted towards a more realistic clinical application. These experiments pave the way for further studies on the road to MR-guided particle radiotherapy.

1. Green et al. 2018 MedPhys.45(8):3728-3740.

2. Hoffmann et al. 2020 RadiationOncology15:129

3. Schellhammer et al 2018 Phys.Med.Biol.63;23LT01

4. Gantz et al 2020 Phys.Med.Biol.65;215014

5. Paul et al 2022 ESTRO2022,OC-0778

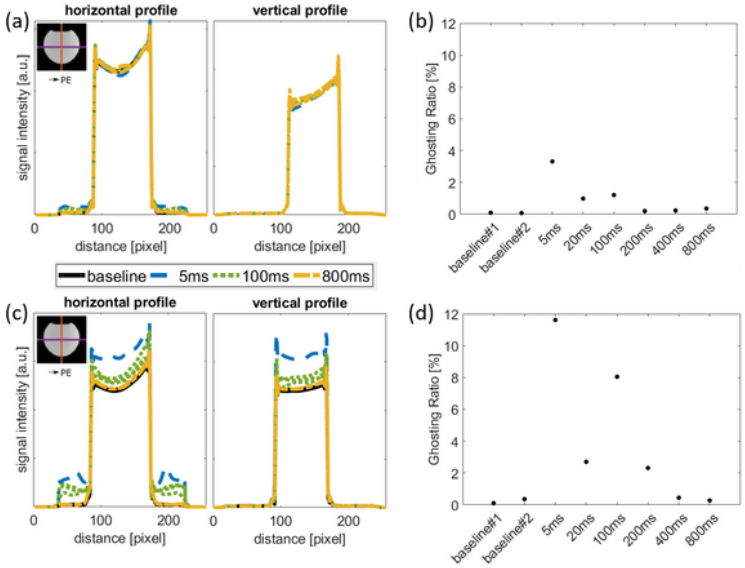

Figure 1: Line profiles of 3D MR image of a homogeneous phantom for simultaneous irradiation with horizontal beam scanning of (a) protons (221 MeV/u) and (c) carbon ions (430 MeV/u) using different spot durations. Ghosting ratios are shown for the (b) proton and (d) the carbon experiment for one central slice.

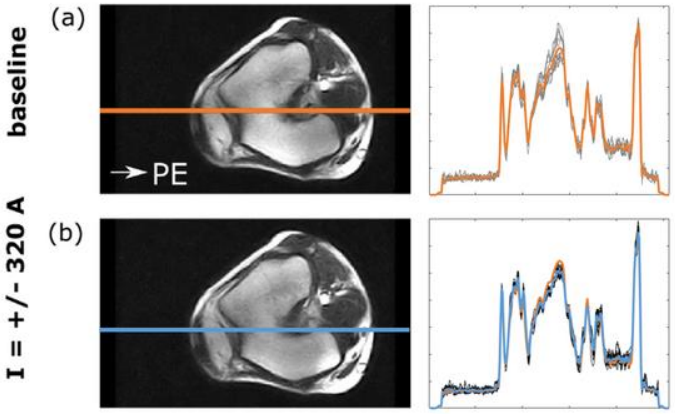

Figure 2: Images and corresponding profiles along a line in phase encoding direction for 2D CINE *in-vivo* knee imaging. (a) Baseline and (b) triangle shaped current pattern for the horizontal beam scanning magnet from -324 A to +324 A with a ramp rate of 1620 A/s. Fifteen CINE images were acquired for both (a) (grey) and (b) (black), which are all superimposed. Further, the mean profiles for baseline (orange) and scanning (blue) are shown.

59

Does Stereotactic Online Adaptive MRgRT Obviate the Need for Rectal Spacer?

Dr. Aharon Feldman MD, Dr. Jennifer Dolan Ph.D, Justine Cunningham MS, Dr. Daniel Chapman MD, Dr. Jadranka Dragovic MD, Dr. Mohamed Elshaikh MD, Dr. Benjamin Movsas MD, Dr. Parag Parikh MD
Henry Ford Health, Detroit, MI, USA

Abstract

Purpose: Hydrogel rectal spacers have been shown to decrease rectal wall dose in prospective studies of fractionated prostate cancer. However, with the advent of stereotactic online adaptive MR guided radiation (MRgRT), it is not clear that these improve the need for plan adaptation.

Methods: A prospective database of MRgRT patients were queried for intact prostate cancer patients who received stereotactic online adaptive MRgRT. Patients were reviewed for the presence of a hydrogel rectal spacer present on the planning images. The number of adaptive fractions and the organs at risk out of tolerance were noted for each patient. Comparisons between the number of fractions adapted, as well as the number of fractions adapted for rectal constraints, were noted.

Results: 25 patients were treated with stereotactic online adaptive MRgRT from 2020 to 2022. 6 patients had a hydrogel rectal spacer. Out of the 95 fractions delivered to non-hydrogel patients, 78 were adapted, with 52 for urethra, 31 for bladder, 5 for bladder neck, and 35 for rectum. For the 30 fractions for patients with a hydrogel spacers, the corresponding numbers were 9 for urethra, 16 for bladder, 6 for bladder neck, and 8 for rectum. Although the percentage of patients requiring adaptation for rectal constraints was greater in the non-hydrogel patients (36.8% vs 26.7, this was not found to be statistically significant (p=0.101).

Conclusion: The presence of a rectal spacer did not reduce the need for online plan adaptation of the rectum for stereotactic online adaptive MRgRT. Furthermore, patients with rectal spacers often required adaptation to meet other prescription constraints. Further work is necessary to better select patients who would benefit from hydrogel spacers in the setting of online adaptive MRgRT.

60

4D-MRI reconstruction for radiotherapy treatment planning of liver tumors

Dr. Jessica Scholey PhD[1], Dr. Horatio Thomas MD, MSc[1], Dr. Xin Miao PhD[2], Dr. Dianne Ferguson PhD[3], Dr. Wensha Yang PhD[1], Dr. Michael Ohliger MD, PhD[1], Dr. Mary Feng MD[1]

[1]University of California San Francisco, San Franscisco, CA, USA. [2]Siemens Healthcare, Malvern, PA, USA. [3]Harvard Medical School, Boston, MA, USA

Abstract

Purpose: Stereotactic body radiotherapy (SBRT) has demonstrated improved local control of liver tumors while minimizing toxicities. Respiratory-correlated 4D-MRI is an active area of research due to its excellent soft tissue contrast and ability to account for tumor motion with respiration. However, it is not widely used in the clinic because it requires specialized acquisition protocols, reconstruction techniques, and hardware. Furthermore, binning strategies and image reconstruction methods, such as compressed sensing (CS) acceleration, could affect 4D-MRI quality and compromise radiotherapy planning. In this work, we developed a novel respiratory-correlated volumetric MRI protocol and investigated the impacts of respiratory binning and CS acceleration for radiotherapy planning.

Methods: Twelve patients (17 tumors) were prospectively recruited and received same-day 4D-CT and 4D-MRI simulation using identical positioning. 4D-CTs were acquired over a single respiratory cycle using 8-phase retrospective binning. 4D-MRIs were acquired continuously over multiple respiratory cycles using a T1-weighted 3D fast gradient-echo sequence with a golden-angle stack-of-stars sampling trajectory (3T MAGNETOM Vida, Siemens Healthcare, TE/TR=1.5/3ms, 1.3x1.3mm^2, 3mm slice thickness, FOV=380x380mm^2, 64–72 slices). A self-gating signal was extracted from k-space center and used as a respiratory motion surrogate. Prototype phase-, amplitude-, and two-directional amplitude-binning algorithms were applied to the 4D-MRIs. Acceleration was simulated by retrospectively under-sampling k-space data. The first 1500 (2x-acceleration) or 1000 (3x-acceleration) out of 3000 ('original') acquired radial spokes were used for CS reconstruction, which simulated half (~5min) or one-third (~3.3min) of the original scan time (~10min). Image quality was assessed using a qualitative 4-point Likert score (1=diagnostic quality, 4=undefinable) and quantitative sharpness score. Targets were independently contoured on CTs and MRIs by two radiation oncologists. Treatment planning was performed using 10MV volumetric-modulated-arc-therapy (50Gy in 5 fractions) and optimized separately on CTs and MRIs to assess dosimetric differences.

Results: Tumor clarity scores using two-directional binning were consistently equivalent to or better than amplitude and phase binning at end-inspiration (1.47,1.53,1.53, respectively) and end-expiration (1.24,1.35,1.53, respectively). Two-directional binning demonstrated significantly higher sharpness scores compared to phase-based binning ($p<0.05$) and captured an additional 2.3mm (range: 0.5-5.6mm, $p<0.001$) of anterior tumor motion. Image sharpness and tumor clarity scores are shown in Table 1 for original, 2x-accel, and 3x-accel. At end-expiration, clarity and sharpness scores were not significantly different for 2x-accel and 3x-accel versus original 4D-MRIs. At end-inspiration, sharpness scores were not significantly different, but clarity scores were rated lower quality ($p<0.05$) for 2x-accel and 3x-accel versus original. On average, there was no significant difference between volumes of MRI-derived and CT-derived targets (39cc vs. 44cc, $p=0.44$). A comparison of target coverage on CT-optimized plans revealed significantly lower coverage of MR-derived versus CT-derived targets (75.56% vs. 89.38%, $p=0.002$), indicating that planning to 4D-CT-derived targets could result in tumor underdosing and increased risk of marginal misses.

Conclusion: 4D-MRI can be used to delineate liver tumors for radiotherapy. Two-directional binning renders high-quality images and captures tumor hysteresis, and adopting 4D-MRI over 4D-CT may improve liver SBRT and reduce risks of

marginal misses. While acceleration decreases acquisition time, it may reduce tumor clarity on inspiratory phases and warrants further investigation.

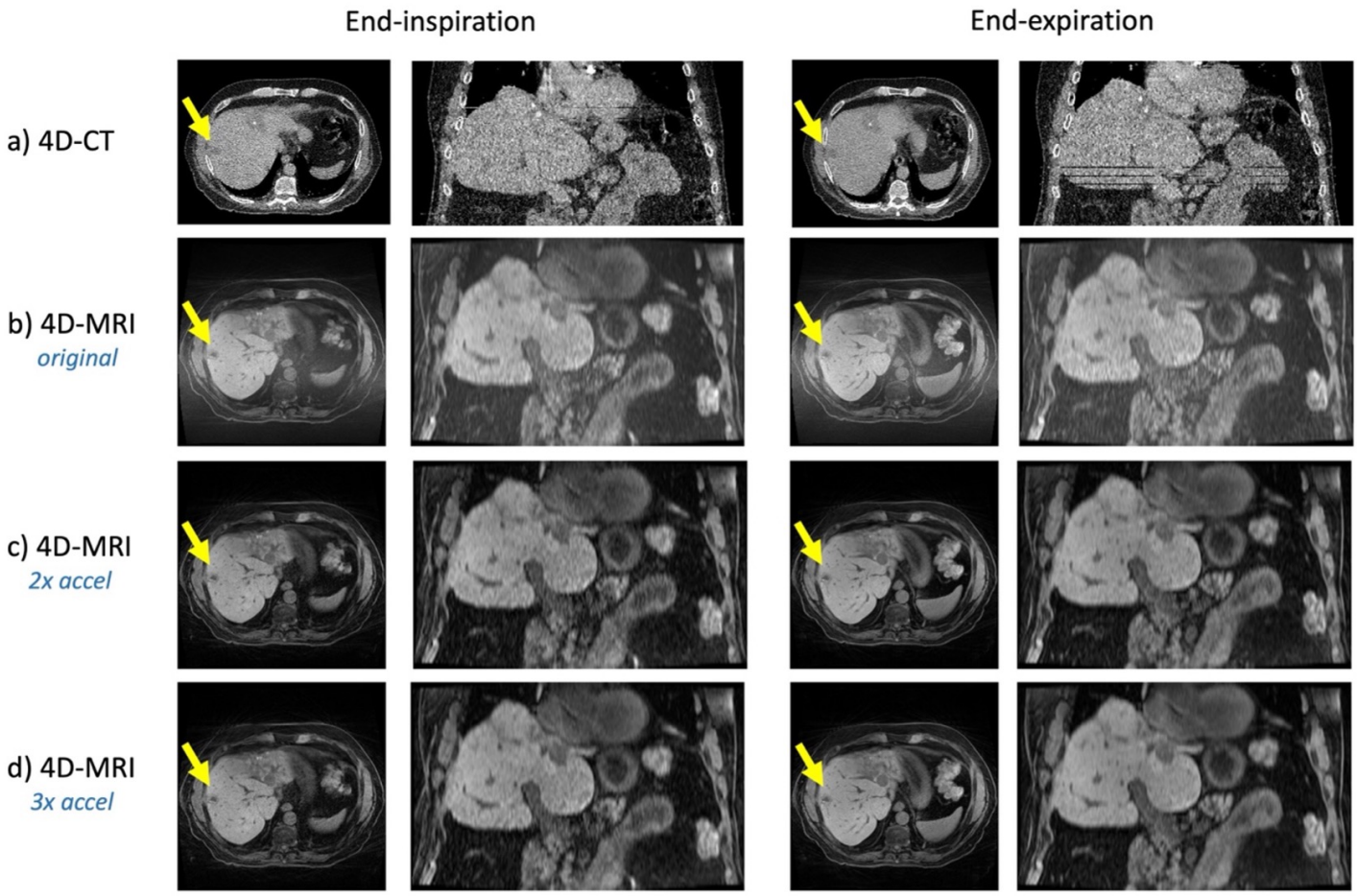

Figure 1: End-inspiration and end-expiration a) 4D-CT and 4D-MRIs reconstructed using b) original 3000 spoke sampling, c) 2x acceleration, and d) 3x acceleration. The liver tumor is annotated using the yellow arrow in all axial planes. Note that the 4D-MRI improves tumor contrast and resolves respiratory-induced motion artifacts relative to the 4D-CT.

Patient	Breathing pattern	End expiration						End inspiration					
		original (3000 spokes)		2x acceleration (1500 spokes)		3x acceleration (1000 spokes)		original (3000 spokes)		2x acceleration (1500 spokes)		3x acceleration (1000 spokes)	
		Sharpness	Tumor Clarity	Sharpness	Tumor Clarity	Sharpness	Tumor Clarity	Sharpness	Tumor Clarity	Sharpness	Tumor Clarity	Sharpness	Tumor Clarity
1	irregular	0.21	1,2	0.35	1,1	0.49	1,2	0.74	1,2	0.56	2,3	0.63	2,4
2	regular	0.53	1	0.5	1	0.53	1	0.45	1	0.45	1	0.34	1
3	irregular	0.42	2	0.45	1	0.43	1	0.42	2	0.42	2	0.43	2
4	regular	0.4	1,2	0.38	1,3	0.39	2,4	0.27	1,2	0.29	2,4	0.31	2,4
5	regular	0.43	1	0.41	1	0.43	1	0.47	1	0.44	1	0.39	1
6	irregular	0.19	2	0.23	2	0.28	2	0.18	3	0.19	3	0.19	3
7	regular	0.33	1	0.33	1	0.41	1	0.33	1	0.34	1	0.36	1
8	irregular	0.35	1	0.34	1	0.32	1	0.24	2	0.24	2	0.21	2
9	irregular	0.28	1	0.22	2	0.22	2	0.18	2	0.16	2	0.18	2
10	irregular	0.38	1	0.38	1	0.39	2	0.29	2	0.3	2	0.22	2
11	regular	0.41	1	0.44	1	0.4	2	0.29	1	0.3	2	0.24	2
12	regular	0.35	1,1,1,1	0.38	1,1,1,1	0.36	1,1,1,1	0.33	1,1,1,1	0.33	1,1,2,1	0.31	1,1,2,2
Average		0.36	1.24	0.37	1.24	0.39	1.53	0.35	1.47	0.34	1.88	0.32	2.00
Paired t-test, p value				0.472	1.000	0.254	0.096			0.383	0.014	0.059	0.008

Table 1: Image sharpness and tumor quality scores for end-inspiration and end-expiration 4D-MRIs using original 3000 spoke sampling, 2x acceleration (1500 spokes), and 3x acceleration (1000 spokes). At end-expiration, clarity and sharpness scores were not significantly different for 2x and 3x acceleration versus original 4D-MRIs. At end-inspiration, sharpness scores were not significantly different, but clarity scores were rated lower quality for 2x and 3x acceleration versus original 4D-MRIs.

61

Prospective dose accumulation to assess target coverage gain for locally advanced pancreatic cancer (LAPC) patients undergoing ablative MR-guided adaptive radiotherapy

Dr Neelam Tyagi PhD, Sarah Burleson MS, Dr Jue Jiang PhD, Dr Sadegh Alam PhD, Dr Christopher Crane MD, Dr Harini Veeraraghavan PhD
Memorial Sloan-Kettering Cancer Center, New York, NY, USA

Abstract

Purpose: MR-guided radiation therapy (MRgRT) has enabled delivery of ablative prescriptions with improved outcomes for locally advanced pancreatic cancer (LPAC) by adapting daily treatment to the changes in the configuration of highly mobile and radiosensitive luminal gastrointestinal (GI) organs. Even with MRgRT, varying and often conservative dose constraints are used for GI organs at the cost of sacrificing therapeutic dose to the target. This is partly due to the lack of reliably accurate deformable image registration (DIR)-based dose accumulation methods to measure the dose delivered to these organs from daily adaptive fractions. Our recent analysis of first 30 pancreas patients treated with 50Gy in 5 fractions has shown coverage of median tumor volume of 67% (range: 44.0% to 95.6%) with ablative prescription and no grade 3 or higher GI toxicities. The goal of our study was to use DIR-based dose accumulation to perform prospective dose accumulation using the initial delivered fractions to assess the feasibility of increasing target dose while keeping the OAR doses the same for LAPC patient population.

Methods: Five LAPC patients undergoing five-fraction MRgRT using abdominal compression and daily online plan adaptation to 50Gy in 5 fractions on 1.5 Tesla Unity MR-linac were analyzed. A pre-treatment, verification, and post-treatment MRI for each of the five fractions (75 total) were used to calculate intra and interfraction deformation. We used our published multi-stage integrated b-spline regularized method called symmetrized large deformation diffeomorphic metric mapping (LDDMM) developed for LAPC patients to accumulate doses to stomach_duodenum, small bowel (SB) and large bowel (LB). Dose accumulation was done by voxel-wise summation of the scaled and warped doses using trilinear interpolation with the DVFs computed to sequentially align treatment fractions at intra- (pre-treatment to post-treatment) and inter-fraction MRIs. Prospective dose accumulation using the first four delivered fractions was performed. The accumulated dose metrics computed after treatment fraction 4 were subtracted from our institutional OAR dose volume constraints ($D_{0.035cc}$ = 33 Gy and D_{5cc} = 25 Gy). The dose difference was then added to the inverse planning objectives of the last (fifth) treatment fraction. The new objectives were used within the clinically used Monaco TPS for reoptimization and the coverage to target volume was measured.

Results: Our results show that large inter- and intrafraction motion (up to 4 cm) occurs for GI organs (Figure 1). Using LDDMM based DIR, accumulated doses for first four fractions, the Dmax to stomach duodenum and the SB decreased by 3.4±0.74 Gy and 3.7±0.78 Gy, respectively compared to the clinical adaptive plans, which does not use DIR dose accumulation. Prospective dose accumulation showed an average increase in PTV coverage (volume receiving prescription dose) of 11.2±1.8% (Figure 2).

Conclusion: Prospective dose accumulation using the first delivered fractions can potentially be used to optimize MRgRT for the remaining fractions to further increase target coverage without increasing the OAR.

62

Developing a 3D printed phantom and analysis software to quantify MRI radiomic features' consistency and variations between institutions and sessions

Suong Duong MS[1], Danny Lee Ph.D[1], Carri Glide-Hurst Ph.D[2], Bhudatt Paliwal Ph.D[2], Michael Boss Ph.D[3], Jennie Crosby Ph.D[2], Yungeng Cui Ph.D[4], Mi Huang Ph.D[5], Heng Li Ph.D[6], James Monroe Ph.D[7], Ying Xiao Ph.D[8], Jason Sohn Ph.D[1]
[1]Allegheny Health Network, Pittsburgh, PA, USA. [2]University of Wisconsin, Madison, WI, USA. [3]American College of Radiology, Philadelphia, PA, USA. [4]Duke University, Durham, NC, USA. [5]Mayo Clinic, Jacksonville, FL, USA. [6]Johns Hopkins University, Baltimore, MD, USA. [7]VA Hospital, St. Louis, MO, USA. [8]Univ of Pennsylvania, Philadelphia, PA, USA

Abstract

Purpose: This study aims to design a 3D printed radiomic phantom and create a data assessment software to automatically analyze large datasets from multiple radiomic calculations. Radiomic parameter consistency can vary between MRI imaging sessions and scanners. Characterizing radiomic consistency requires a standard radiomic phantom and data assessment software which process multiple radiomic data sets and present the results in graphical and tabular formats.

Methods: We designed and printed a radiomic phantom with three mesh objects, and two egg shaped objects. As shown in Figure 1, the first object (1) (designated as Grid 3x3x2) consists of a mesh object with 3×3×3 mm3 interiors formed by 2 mm thick framing. The 7×7×5 mesh forms a frame 30mm wide, 30mm long, and 25mm high. Grid 5x5x1 (2) and Grid 5x5x2 (3) consisted of 5×5×5mm3 interiors formed by 1 mm and 2 mm thick framing, respectively. They were stacked to 7×7×5 mesh forming objects 42x42x30mm and 49x49x35mm. The two hollow egg-shaped objects were printed. Egg 5x2 (4) is 5cm long, 2 cm maximum diameter formed by a 1 mm thick shell. Egg 5x4 (5) is 5 cm long, 4 cm maximum diameter, formed by a 1 mm thick shell. Both egg objects were packed with vitamin D3 capsules (125mcg, 5000 IU, Nature Wise brand) and filled with olive oil in the gaps between the capsules to remove any air remaining in the egg objects. Prior to MR scanning, the 5 objects are placed in a container and filled with distilled water.

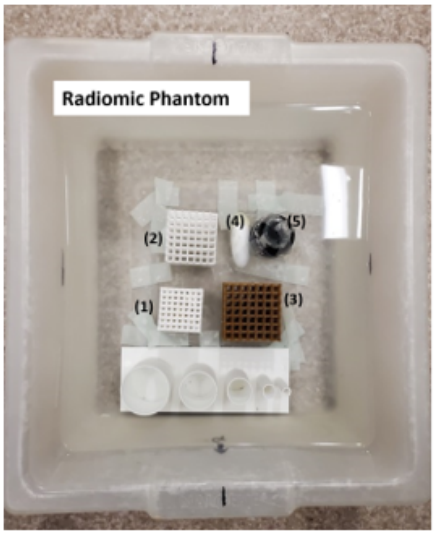

FIGURE 1: Image of the 3D printed objects of the radiomics phantom. (1) Grid 3x3x2, (2) Grid 5x5x1, (3) Grid 5x5x2, (4) Egg 5x2, (5) Egg 5x4.

The 3D printed radiomic phantom was scanned ten times per protocol using: (1) a 1.5T Philips MR equipped in Unity MR-Linac at Institution A with T1, T2, and (2) a 1.5T GE MR scanner and (3) a 0.35T ViewRay MR at Institution B with T1 and T2. Using Pyradiomics in 3D slicer, 107 radiomic features were extracted per MR image set. Coefficients of variation (CV(%)) were computed for each object and each radiomic feature in 10 repeated MRI scans for each sequence. The new assessment software was created using Python 3 (version 3.9), and the matplotlib library. PyQt5 was used to build the interface for the software.

Results: Three MR scanners were used to image the 3D Phantom using 2 sequences. Scans were repeated 10 times, producing a total of 60 scans. 107 radiomic features were extracted via PyRadiomics and analyzed by our assessment software. A sample subset the data analyses are shown below in table and graph formats. The mean Coefficient of Variability (CV) as shown in Table 1, showed the highest variability between scanners occurs using T1.

Table 1. Mean coefficient of variation (%) between scanners

	T1			T2		
Object	**1.5 T Philips**	**1.5T GE**	**0.35 T Viewray**	**1.5 T Philips**	**1.5T GE**	**0.35T Viewray**
1	8.6	1.3	29.7	19.2	3.7	2.8
2	8.0	1.3	23.3	13	3.7	2.5
3	3.6	1.4	8.9	9.5	1.7	1.7
4	5.1	2.9	7.1	8.7	1.8	1.7
5	5.7	1.1	21.7	7.8	1.7	0.9

The Figure 2 below demonstrates the graphical analysis of extracted features from the 60 scan, multi-MR study of the standardized 3D phantom.

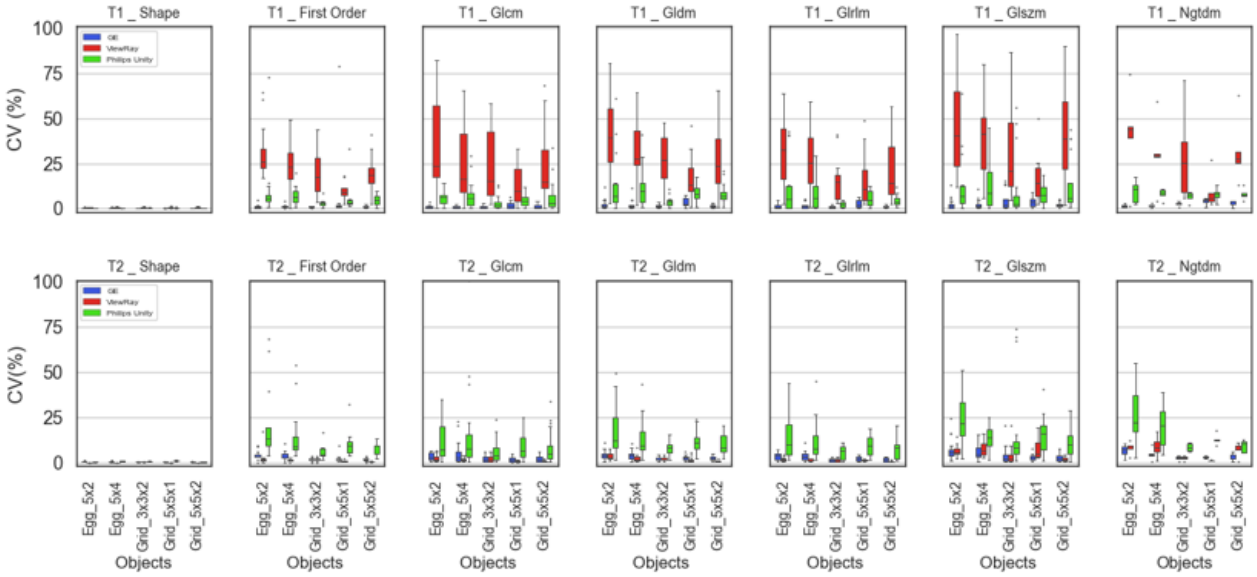

FIGURE 2: Examples of feature intercomparisons showing variability of five objects in each feature class and 3 scanners. The variability is shown by the distribution of coefficient of variation in radiomic feature classes. In both top and bottom rows, from left to right are the plots of feature classes including shape, first order, glcm, gldm, glszm and ngtdm feature classes.

Conclusions: This study demonstrated a standardized 3D printed radiomic phantom and auto-analyzing software to characterize scanner-to-scanner variability and single scanner imaging variability. This is a desirable approach for establishing baseline radiomic features prior to multi-institutional radiomic studies.

63

Assessment of intrafractional prostate motion in MR-guided online adaptive radiotherapy

Xiao Tan MS, Dr Ergys Subashi PhD, Dr Neelam Tyagi PhD
Memorial Sloan-Kettering Cancer Center, New York, NY, USA

Abstract

Purpose: To evaluate intrafractional prostate motion captured during MR-guided adaptive radiotherapy (MRgART) for prostate cancer on 1.5 Tesla MR-linac system.

Methods: Eighty prostate patients, each undergoing five fraction MRgART of 40 Gy to prostate and a boost of 45 Gy to the dominant intraprostatic lesion treated were analyzed. An empty bladder and empty rectum protocol was strictly followed by each patient. Multiplanar 2D cine MRI, placed at the centroid of the planning target volume (PTV), were acquired at 1.6Hz/cine frame during treatment (average beam-on time = 8.9 mins). 2D coronal and sagittal cine images acquired at the start of beam-on (first 90 frames) were registered with a vendor provided software to 3D pre-treatment MRI used to create a template (Figure 1). Rigid registration was performed within a chosen region-of-interest (eg PTV). The subsequent frames were registered to the template frame and center of mass shift (Mean±standard) of the ROI in anterior-posterior (AP), superior-inferior (SI) and left-right (LR) directions were calculated. The motion profiles over the entire beam-on timeframe were generated by recording the centroid shift of each frame. The time-dependent coordinates of the centroid were filtered with a moving average filter using a window of 5 seconds. In each direction the filtered signal was baseline corrected by subtracting the coordinate at time zero. The analysis was performed for the signal in the range 1-10 mins, in steps of 0.5 minutes. In each patient, the motion signal for all pairs of combinations over five fractions was compared to determine significant correlations. A correlation was considered to be significant if $|\rho|>0.7$ and $p<0.05$, where ρ is the Pearson correlation coefficient. The variance-ratio test was used to assess whether the speed of the centroid in each direction can be modeled by a random walk process. The magnitude of displacement from baseline was estimated by determining the total number of fractions in which the shift was greater than 1 mm, 2 mm, and 3 mm.

Results: A total of 400 cine data were analyzed. The mean prostate motion for all patients and fractions was -0.14 ± 0.16, 0.42 ±0.36 and -0.64 ± 0.49mm in LR, AP and SI direction respectively. Time evolution of shifts in any direction showed that at 10 minutes after the start of treatment, the probability of shifts > 3mm was < 8% (AP), > 2mm was < 12% (AP), and 1mm was < 40 % (SI) (Figure 2). The correlation between the motion signals was dependent on beam-on time. The maximum correlation was for the displacement in the AP direction, happening in less than 20% of the cases. A similar trend was observed for the SI direction. A correlation in the LR direction was observed for only 7% of cases.

Conclusion: Analysis shows that prostate shifts were within 3mm CTV-to-PTV margin for a majority of patients and patients were effectively treated with ablative doses using MRgART. Future studies will investigate the dosimetric impact of these intrafractional shifts.

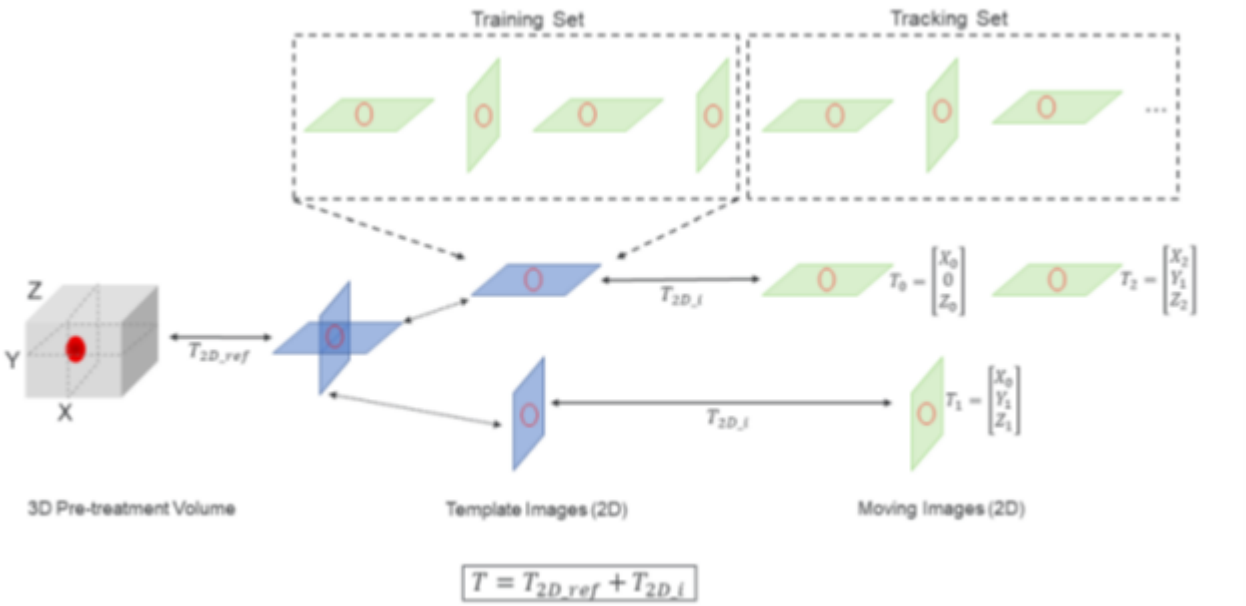

Figure1: 2d-3D Registration algorithm details

Figure 2: A) Representative cine motion pattern. B-D) Probability vs time for shifts > 1mm, 2mm and 3mm

64

An error estimator for intra-fraction dose accumulation: introduction and evaluation

Lando Bosma[1], Dr. Mario Ries[1], Dr. Baudouin Denis de Senneville[2], Prof. Bas Raaymakers[1], Dr. Cornel Zachiu[1]
[1]University Medical Center Utrecht, Utrecht, Netherlands. [2]Université de Bordeaux, Bordeaux, France

Abstract

Purpose

The introduction of the MR-linac allows continuous imaging during radiotherapy delivery, permitting to reconstruct the delivered dose by taking organ motion during delivery into account. This increases the accuracy of therapy-response estimates and opens up the possibility of intra-fraction replanning after major motion events [1]. While motion-compensated dose accumulation (DA) has generally been shown of good accuracy [2], potential uncertainties/errors in the deformable image registration (DIR) can nevertheless introduce/accumulate errors over time. As a consequence, an independent estimate of the magnitude and location of these DA errors is highly desirable for clinical decision-making based on motion-compensated DA. Here, we introduce and validate an intra-fraction dose accumulation error estimate (DACE) for prostate cancer treatments.

Methods

We introduce a DACE model in Gy, which is computed as the product of the spatial dose gradient (in Gy/voxel) and an estimate of the registration error magnitude in voxels. We found the latter can be determined using the structural similarity metric of the reference and registered images.

To test our DACE model, we performed a series of “virtual EBRT-experiments” and compared the true dose accumulation errors with our DACE estimates. For this, motion was synthesized using biomechanical finite-element simulations, modelling clinically observed organ deformation patterns, and subsequently used to create a series of synthetic cine-MRIs/Hounsfield-maps by deforming a reference dataset. Subsequently, we simulate delivery of one EBRT-fraction under motion [3]. The simulation allows to reconstruct the true accumulated dose (trueDA) as a gold standard, and a motion compensated DA or non-motion compensated DA (estDA).

We evaluate the DACE model using the gamma pass rate between DACE and the true dose accumulation error, and by investigating for which voxels the trueDA is in the range [estDA-DACE, estDA+DACE]. Details on the model, simulations, and evaluations are provided in the supporting document.

Results

An example of the estDA and DACE for different DIR algorithms is shown in Figure 1. The mean gamma pass rate (2%/2mm) is 86%. The percentage of voxels in the range is on average at least 92%. The voxels outside the range are located mainly to the side of the prostate and near the edge of the beam, not in crucial regions close to the organs-at-risk. This allows for the interpretation of the DACE as a confidence interval. Using DACE as a bandwidth on the estDA, all cases where the planning constraints were violated in the trueDA were correctly identified.

Conclusion

We introduce a model for dose accumulation error estimation. From our experiments on simulated data, it proves a useful estimator of the true dose accumulation error and it can be used as a confidence interval on the motion-compensated accumulated dose. This may inform the clinician if a reliable decision can be made based on this dose, which may in turn aid the clinical implementation of reconstructing motion-compensated delivered doses on an intra-fraction basis.

[1] Kontaxis et al (2015), PMB 60 7485

[2] Bosma et al (2020), PMB 66 065002

[3] Wieser et al (2017), MedPhys 44(6)

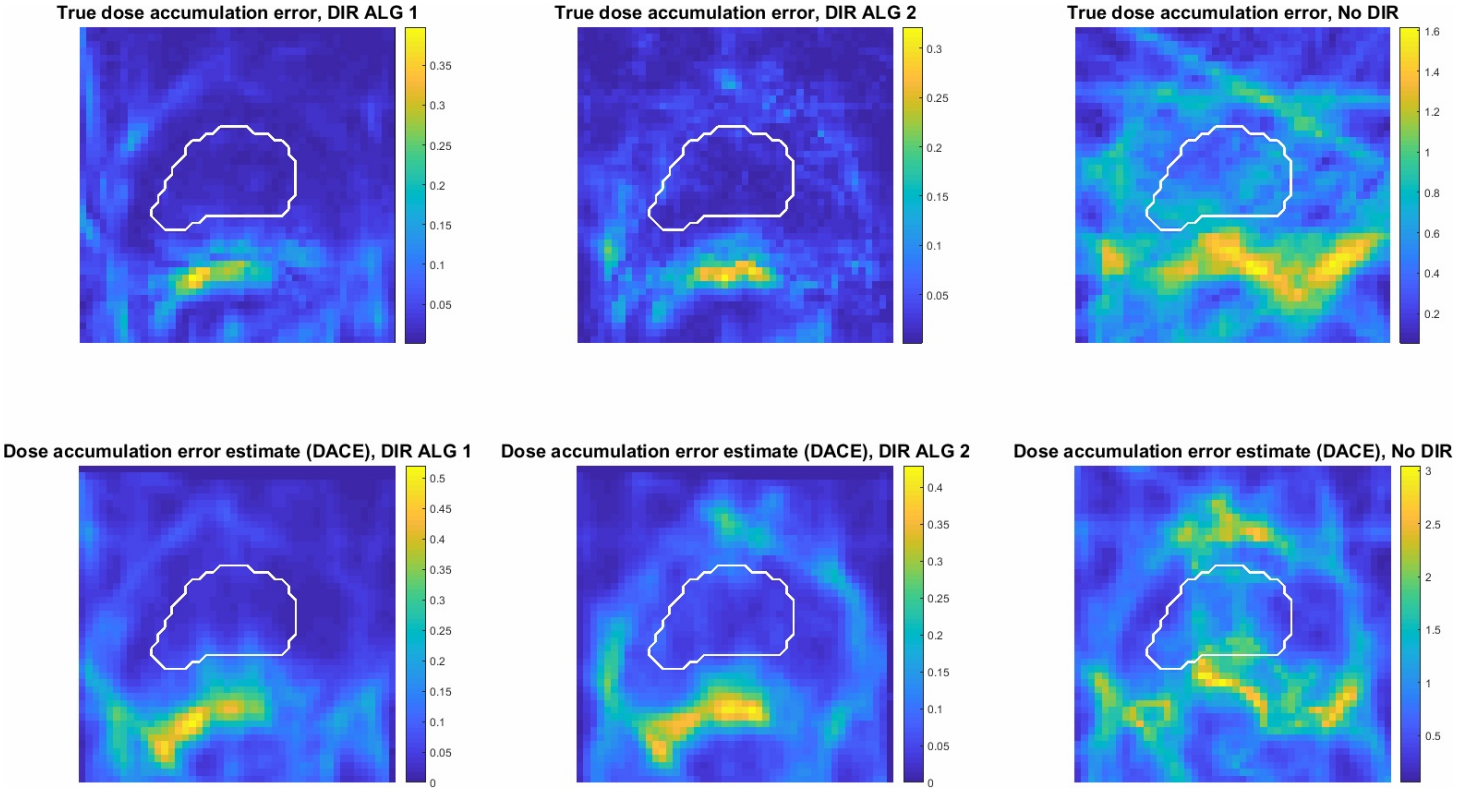

65

Initial experience with MR-only workflow validation for accelerator-based stereotactic radiosurgery/radiotherapy of brain tumors

Medical Physicist Hyeri Lee PhD, Assistant Professor Xiangyu Yang PhD, Associate Professor Ahmet Ayan PhD, Medical Physicist Dominic DiCostanzo, Medical Physicist Michael Weldon, Dosimetrist Wesley Zoller, Radiation Oncologist Evan Thomas PhD, MD, Radiation Oncologist Joshua Palmer MD, Professor Nilendu Gupta PhD
The Ohio State University Wexner Medical Center, Columbus, OH, USA

Abstract

Purpose: In radiation oncology, CT images play a pivotal role in dose calculation. Due to its superior soft tissue contrast, MRIs are commonly used as secondary images to visualize targets and organs-at risk (OARs) in anatomical areas such as the brain. The objective of this study is to validate the use of MR-only workflow for linear accelerator-based stereotactic brain radiotherapy. In this talk, we are reporting our initial experience with this study as we are still enrolling participants.

Methods: Before replacing the current (CT-based) workflow withthe MR-only (synthetic CT [sCT] derived from MRI) workflow, the quality of CT-based and sCT-based radiotherapy plans (RTPs) should be compared to verify that sCT-based RTPs are dosimetrically equivalent and/or clinically acceptable. Subjects will undergo MR scans while immobilized in the custom mask. Non-contrast MRI sequences specifically designed to produce sCT images will be acquired prior to a contrast enhanced Standard-Of-Care (SOC) Brain MRI protocol. For the MR scans, a mask-compatible MR receiver coil will be used. According to an experienced Radiologist's assessment, MR image qualities using the mask-compatible coil are comparable to those obtained using the standard head coil. From the MR images, sCT images will be reconstructed using a manufacturer's advanced postprocessing workstation. The sCT images will be used for RTP calculation purposes and the quality of the plan will be analyzed. We have acquired Institutional Review Board approval to recruit 33 patients. In addition, we are developing quality assurance procedures for MR only workflow including an end-to-end test.

Results: We have established the workflow including the MR scans with the immobilization masks for brain stereotactic radiation. To date, we have recruited two patients who completed their treatment, which is not enough to provide the dosimetric evaluation between CT-based and sCT-based plans. However, we have identified various issues to improve. One is the limited field of views for the treatment plan which is not enough to add the couch top and the mask support. Another is the visibility of simulation markers, where the MR markers are not visible in synthetic CT to place the CT reference point because the sCT algorithm was not trained with any fiducial markers.

Conclusion: We have identified areas to improve on before implementing the MR-only workflow for brain stereotactic radiation and will continue to collaborate with the vendors to refine the sCT generation and treatment planning process. We will also keep recruiting patients to show the dosimetric equivalence or clinical usage for sCT-based brain stereotactic plans.

66

Diffusion-weighted MRI derived imaging metrics for MR-guided ablative radiotherapy of pancreatic ductal adenocarcinoma

Dr Neelam Tyagi PhD, Xiao Tan MS, Dr Ergys Subashi PhD, Dr Amita Shukla-dave PhD, Dr Christopher Crane MD, Dr Marsha Reyngold MD
Memorial Sloan-Kettering Cancer Center, New York, NY, USA

Abstract

Purpose: Pancreatic ductal adenocarcinoma (PDAC) is characterized by complex microarchitecture, dense fibroblastic stroma and heterogenous vascularization, which can create considerable challenge for therapy planning and response assessment. Multiple studies have shown superior outcomes, including overall survival, when PDAC patients received stereotactic body radiation therapy (SBRT) doses of > 40 Gy in 5 fractions. Biomarkers of early response could further facilitate adaptive replanning of ablative SBRT and/or help inform post-SBRT management. The goal of our study was to assess longitudinal changes in quantitative imaging metrics derived from diffusion-weighted (DW-) MRI for pancreas patients undergoing MR-guided ablative radiotherapy (MRgART).

Methods: 45 PDAC patient undergoing 50 Gy in 5 fractions and daily adaptive replanning on 1.5 Tesla MR-linac system were analyzed. 17 patients were on an immunotherapy protocol with durvalumab whereas patients remaining were not. For each treatment fraction, DW-MRI was acquired using a single-shot spin-echo EPI imaging sequence using four b-values (0, 30, 150 and 500 s/mm^2). Scan time was ~4 minutes. Multiple repeat acquisitions were acquired for each patient during fraction 1 to calculate patient-specific repeatability data. Figure 1 shows the DWI acquisition schema during MRgRT. DWI data were fitted on a voxel-by-voxel basis to a monoexponential model to generate apparent diffusion coefficient (ADC) and segmented biexponential model or intravoxel incoherent motion (IVIM) using a cut-off value of b= 100 s/mm^2 to generate true diffusion (D), pseudo diffusion coefficient (D*) and perfusion fraction (f). Median values within the clinical delineations for GTV were obtained. Within subject repeatability data using coefficient of variation (%COV) was calculated for ADC, D, D* and f. Last review of first 30 patients showed that six out of 30 patients had failed locally. During treatment response of immunotherapy vs non-immunotherapy patients as well as patients who failed locally was performed.

Results: Within subject %COV for ADC, D, D* and f was 3.98%, 6.9%, 6.9 and 9.14%. Baseline ADC was lower for non-immunotherapy patients compared to immunotherapy patients (1.64 vs 1.86 mm^2/s). Change in ADC post RT was higher for immunotherapy group (14% vs 10%). Similar trend was seen in true diffusion values as well. Change in D post RT was significantly higher (19.8% vs 8.7%) for immunotherapy group (Figure 2) compared to ADC. Changes in perfusion fraction were inconclusive. Patients who failed locally showed minimal to no changes in all the diffusion metrics.

Conclusion: Literature has shown robust DWI data for COV of 5% indicating strong confidence in ADC and D. DWI-derived quantitative metrics changes during MRgART and show potential to be useful biomarkers to evaluate longitudinal changes to SBRT. Future work will show correlation of these metrics with overall survival as the outcomes data matures.

Figure 1: DWI acquisition schema for PDAC patients undergoing five fraction MRgART

Figure 2: Longitudinal trend in IVIM derived true diffusion (D) metric - comparison of immunotherapy vs non-immunotherapy group shown for all fractions (top row) and Fx1 and last fraction only (bottom row)

67

REAL-TIME MR SIGNATURE MATCHING (MRSIGMA) FOR VOLUMETRIC MRI WITH LESS THAN 300MS LATENCY ON A MR-LINAC

Syed Saad Siddiq[1], Victor Murray[1], Can Wu[1], Pim T.S. Borman[2], Bas W. Raaymakers[2], Ricardo Otazo[1,3]

[1]Department of Medical physics, Memorial Sloan Kettering Cancer Center, New York, NY, USA. [2]Department of Radiotherapy, University Medical Center Utrecht, Utrecht, Netherlands. [3]Department of Radiology, Memorial Sloan Kettering Cancer Center, New York, NY, USA

Abstract

Purpose

The MR-Linac offers a unique platform to adapt and monitor treatment of tumors affected by motion [1, 2]. However, current real-time MRI technology is restricted to 2D imaging. MR Signature Matching (MRSIGMA) is a novel technique that enables the ability to perform real-time 3D MRI [3-5]. However, MRSIGMA was only tested as a proof-of-concept in a non-real-time scenario. This work develops a real-time implementation of MRSIGMA on the Elekta Unity MR-Linac to perform volumetric MRI with an imaging latency of less than 300ms.

Methods

MRSIGMA has two steps: motion learning and signature matching. Motion learning computes a dictionary of 3D motion images and corresponding signatures. Signature matching acquires signature-only data and finds the closest signature in the motion dictionary. This work optimized all MRSIGMA components to perform real-time imaging on the MR-Linac system, including raw data transmission to a high-performance computer, 4D reconstruction using deep learning, and correlation-based signature matching (Figure 1).

Data acquisition: T1-weighted golden-angle stack-of-stars acquisition with 905 angles was performed for motion learning with a scan time of 5:05mins. Signature matching scan time for each angle was 250ms.

Raw data transmission: ReconSocket[6] was employed to send each radial k-space line to the reconstruction computer with minimal latency as acquisition and transmission occur simultaneously.

Motion learning: A novel deep learning 4D reconstruction named MRI-movienet was employed instead of iterative compressed sensing to significantly reduce reconstruction time of the original XD-GRASP method [7]. MRI-movienet operates in the image domain without data consistency. Motion detection computes a respiratory motion signal directly from the central k-space points using principal component analysis. Raw k-space data is sorted into 10 respective motion states. FFT along k_z and Non-Uniform FFT (NUFFT) transform raw data into aliased 5D images (x-y-z-motion-coil), which are sent to the MRI-movienet network to obtain unaliased 4D images.

Signature matching: Motion projection correlation analysis was used to reduce matching time. FFT of received k_z lines from each angle provides the new motion projection. The 3D motion state in the motion dictionary whose signature presents the highest correlation with the new motion projection is selected as output.

Results

Real-time MRSIGMA implementation was tested on a healthy volunteer. Latencies corresponding to motion learning and signature matching are shown in Table 1. Deep learning-based MRI-movienet minimized 4D reconstruction time to 4±1 seconds, a significant reduction from tens of minutes for iterative compressed sensing. Signature data transmission latency was 3ms±2ms. Total signature acquisition (250ms), transmission (3ms) and matching (15ms) time was lower than 300ms, which enables real-time 3D MRI of organs affected by respiratory motion. Figure 2 shows 4D images of the volunteer.

Conclusion

The combination of simultaneous data acquisition and transmission, deep learning-based 4D reconstruction and correlation-based matching enabled real-time implementation of MRSIGMA on a MR-Linac to perform 3D MRI with a latency lower than 300ms. This development would enable the potential of MR-Linac systems to adapt and monitor treatment of mobile tumors in real-time.

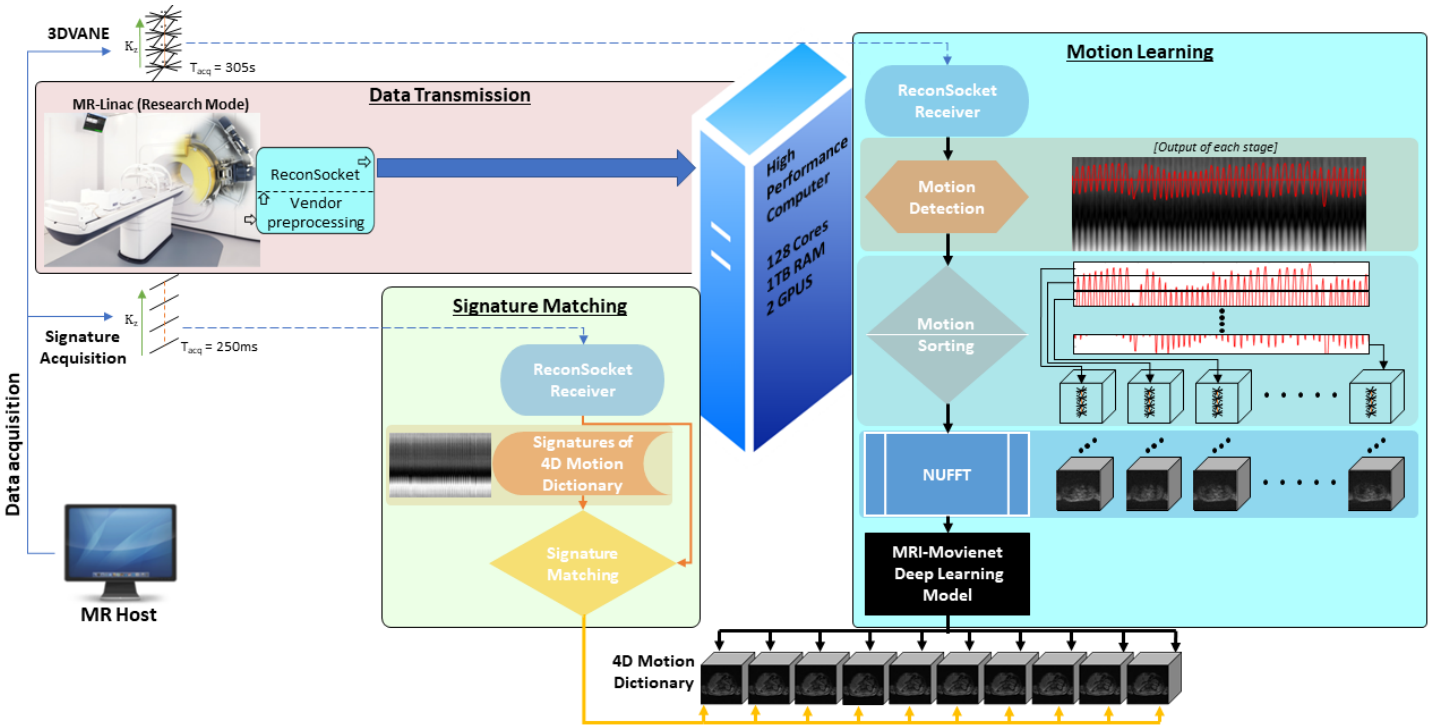

*__Figure 1__: **Data Transmission** (highlighted in red background) setup of real-time MRSIGMA implementation consists of MR-Linac (1.5T Unity, Elekta AB, Stockholm, Sweden) in research mode connected to High Performance Computer (Dell Inc., Round Rock, Texas, USA) via a 10GBit Ethernet. Two data reconstruction pipelines were implemented in Python (Python Software Foundation, Wilmington, DE, USA). **Motion Learning** data pipeline (highlighted in blue background) comprising of five processing blocks described in abstract is illustrated with their adjacent corresponding output. 4D motion dictionary consisting of 3D images of 10 motion states is generated by the motion learning step. **Signature Matching** data processing pipeline (highlighted in yellow background) consists of three blocks. The signature matching block selects one of 10 motion states in the training dictionary based on new signatures acquired from MR-Linac in real-time.*

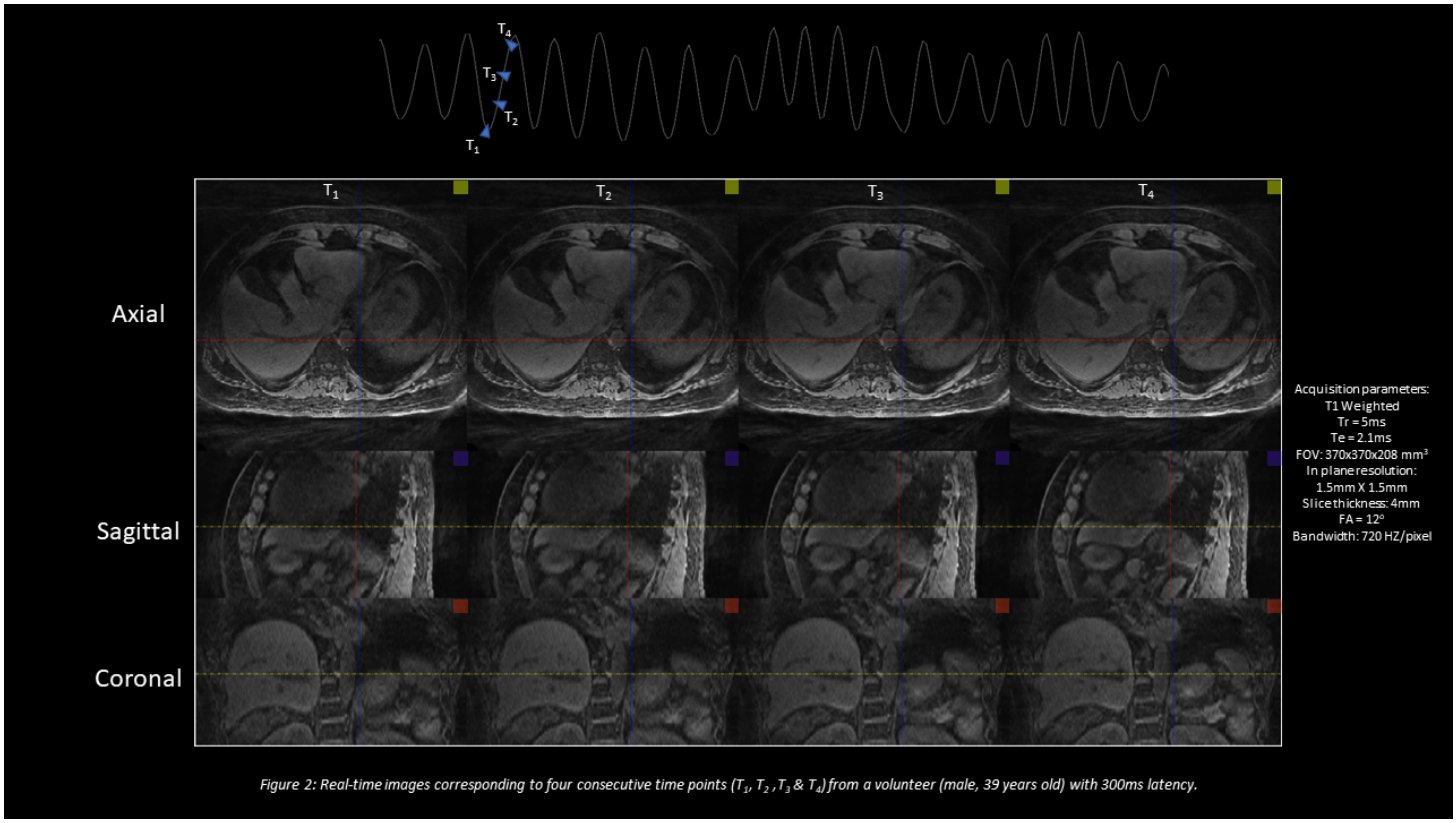

Figure 2: Real-time images corresponding to four consecutive time points (T_1, T_2, T_3 & T_4) from a volunteer (male, 39 years old) with 300ms latency.

Table 1

Motion learning Data Acquisition: 305s	**Signature Data Acquisition:** 250ms
Motion learning reconstruction times	**Signature matching times**
Motion Detection: 11.8ms ± 111us Motion Sorting: 482ms ± 262us NUFFT: 619ms ± 172ms MRI Movienet model: 4s ± 1 s	Signature Matching: 15ms ± 5ms

68

CT-MR-Deformable Image Registration for MR-Guided Radiotherapy using a Biomechanical Skeleton Model

Cornelius J. Bauer[1,2,3], Pasit Jarutatsanangkoon[1,2], Alexandra Walter[1,2,4], Thomas Welzel[2,5], Stefan Koerber[2,5], Sebastian Klüter[2,5], Oliver Jäkel[1,2,6], Kristina Giske[1,2]

[1]Department of Medical Physics in Radiation Oncology, German Cancer Research Center (DKFZ), Heidelberg, Germany. [2]Heidelberg Institute for Radiation Oncology (HIRO), National Center for Radiation Research in Oncology (NCRO), Heidelberg, Germany. [3]Department of Physics and Astronomy, University of Heidelberg, Heidelberg, Germany. [4]Karlsruhe Institute of Technology, Steinbuch Center for Computing, Eggenstein-Leopoldshafen, Germany. [5]Department of Radiation Oncology, Heidelberg University Hospital, Heidelberg, Germany. [6]Heidelberg Ion Beam Therapy Center (HIT), University Hospital Heidelberg, Heidelberg, Germany

Abstract

Purpose

MR-guided adaptive radiation therapy for cancer requires accurate tumor and organ at risk localization along the treatment course. A biomechanical registration approach can provide an accurate and physiologically consistent transformation. We scrutinize the accuracy of an articulated kinematic skeleton model for CT-MR registration (KinematicDIR) of the head and neck region.

Methods

The proposed patient individual skeleton model is build up from manually segmented individual bones on a planning CT and rule based joint positions. The dependencies of bones and joints is modelled using a multibody physics engine via inverse kinematics [1]. We utilize a hierarchical optimization scheme and a simplex optimizer for the transformations of individual joint-connected bones [2].

Deformable image registration was performed for three patients between planning CT (Siemens Somatom Confidence) and same-day MRI scan (Siemens Magnetom Sola: Vibe Dixon in phase) using a binary overlap similarity measure within the manually delineated skeleton (Figure 1).

Evaluation is based on 50 landmark pairs positioned on the skeleton for each scan used to calculate the target registration error (TRE).

Results

Single-threaded deformable registration takes (20±5) minutes on a workstation (Xeon W-2145 CPU (3.7 GHz), 128 GB RAM). The landmarks on each scan were compared after manual rigid alignment and after application of KinematicDIR.

The landmark based median TRE within the skeleton for three considered patients was consistently reduced to (2.0±0.1) mm with an interquartile range below 2.0 mm for each dataset (Figure 2). There are few outliers that can be associated with limited bone contrast impeding the positioning of landmarks but not deteriorating the overall distribution.

Conclusion

With our landmark-based analysis, we could show that our biomechanical model enables kinematic deformable registration with an accuracy sufficient for radiation therapy. Registration errors below 2 mm can be considered accurate enough for adaptive workflows.

Future work will address the potential to build-up the model from auto-segmented bony structures on both CT and MRI using deep learning semantic segmentation and its effect on the registration accuracy.

References:

1. Simbody: multibody dynamics for biomedical research (Sherman, M. A., et al.) Procedia IUATM, 2, 241-261.

2. Construction of a biomechanical head and neck motion model as a guide to evaluation of deformable image registration (Teske, H., Bartelheimer et al.), Phys in Med & Bio, 62(12), N271. (2017)

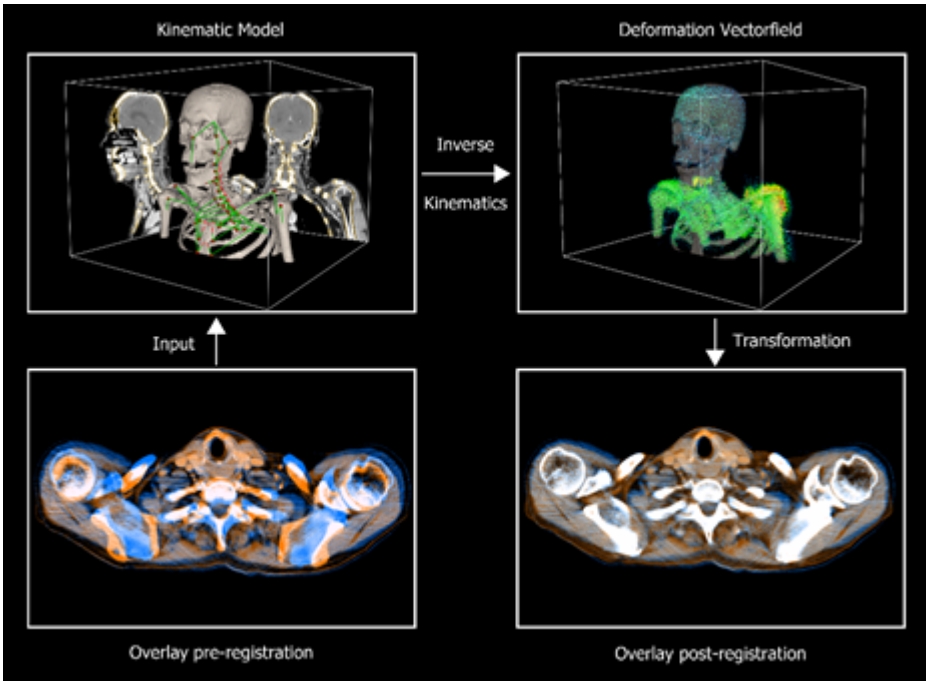

Figure 1. Biomechanical Model and Registration Pipeline: Two images are used as input for model build-up and registration. After transformation using the deformation vector field, both images align well.

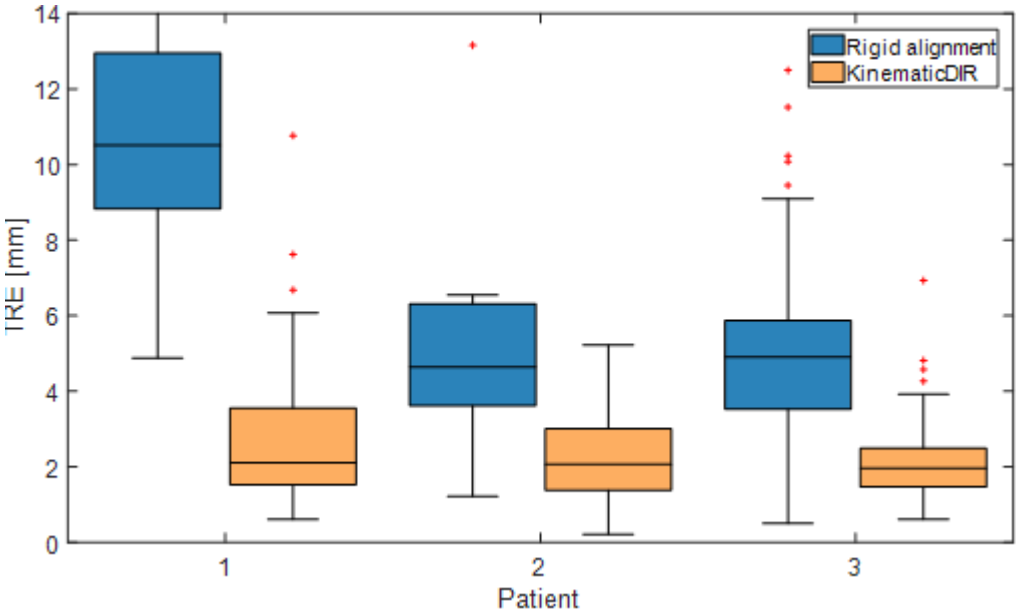

Figure 2. Target Registration Error without registration and after application of KinematicDIR: TRE before registration varies due to patient positioning in the MRI. After registration, the TRE is comparable for all patients and reaches (2.0±0.1) mm accuracy in the median.

69

Evaluation of the magnetic field effect on scintillator response to megavoltage photon beams.

Yunuen Cervantes Espinosa PhD[1,2], Ilias Billas PhD[3], Simon Lambert-Girard PhD[4], Yoan LeChasseur[4], François Therriault-Proulx PhD[4], Louis Archambault PhD[1,2], Hugo Bouchard PhD[5,6], Luc Beaulieu PhD[1,2]

[1]Département de physique, de génie physique et d'optique et Centre de recherche sur le cancer, Université Laval, Québec, QC, Canada. [2]Service de physique médicale et de radioprotection, Centre intégré de cancérologie, CHU de Québec –Université Laval et Centre de recherche du CHU de Québec, Québec, QC, Canada. [3]National Physical Laboratory, Chemical, Medical & Environmental Science Department National Physical Laboratory, Teddington, United Kingdom. [4]Medscint inc., Québec, QC, Canada. [5]Département de physique, Université de Montréal, Montréal, QC, Canada. [6]Centre de recherche du Centre hospitalier de l'Université de Montréal, Montréal, QC, Canada

Abstract

Purpose: In magnetic resonance-guided radiation therapy (MRgRT), dosimetry is performed in the presence magnetic fields. This field amplifies the electron fluence perturbations in detectors, especially when they have density heterogeneities. Plastic scintillation dosimeters (PSD) are ideal for MRgRT since they are homogenous and water-equivalent in terms of density, stopping power, and mass energy absorption coefficients. However, the effect of magnetic field on their dose response and on the Cherenkov, light must be characterized. In MRgRT beams, the average trajectory of charged particles is modified by the magnetic field strength and direction. As such, Cherenkov light will vary with irradiation conditions. The goal of this study is to evaluate the impact of magnetic fields on three different base core scintillation dosimeters.

Material and method: Three scintillation probes were built with different scintillation materials: BCF-60, BCF-10 and EJ-204. All scintillators have a 1 mm diameter and 1 mm length. Each detector was placed at 5 cm depth in a water tank, inside the gap of an electromagnet. Six magnetic field strengths and 2 polarities were used: 0 T, ±0.2 T, ±0.35 T, ±0.5 T, ±1 T, ±1.5 T. The irradiation was performed by a 6 MV Elekta photon beam, using a 7 x 7 cm2 field. The magnetic field was perpendicular to the irradiation beam and the detector axis. The detector axis was perpendicular to the photon beam. Depending on the current polarity, the Lorentz force pointed towards the stem (orientation 1) or towards the tip (orientation 2).

The Hyperscint RP-200 research platform (Medscint Inc.) was used for readout to perform dose measurements. To quantify the impact of the magnetic field, the dose was normalized to the 0 T value. A hyperspectral analysis was performed to determine the Cherenkov abundance from the measured spectra for each magnetic field.

Results: The normalized dose is presented in figure 1. The dose increases with the magnetic field in both orientations. The dose increases by up to 6.3%, 5.0% and 4.2%, for the EJ-204, BCF-10 and BCF-60, respectively. The largest increase occurs when electrons are deflected towards the stem, for the three scintillators. The difference between the two orientations is less than 1%. The variation is larger between 0.5 - 1 T and smaller at 1.5 T.

In figure 2, results show that the Cherenkov abundance increases with magnetic field when the Lorentz force point towards the stem and it decreases in the opposite orientation. The variation is not symmetrical, and it is more important when electrons are deflected towards the stem, up to 2.3 times the 0 T value. The largest Cherenkov variation occurs for the EJ-204 and it is significantly larger (50% more at 1.5 T) than for the other scintillators.

Conclusion: Cherenkov light contribution is highly dependent on magnetic field strength and orientation and, to a lesser extent, scintillator core material. For the irradiation conditions, the dose increases with the magnetic field. A difference of less than 1% on the magnetic field effect among the two orientations.

70

MRI simulation for breast cancer radiotherapy planning in poorly defined cavities

Jonathan Massachi MS[1], Catherine Lu Dugan BA[2], Xin Miao PhD[3], Rita Freimanis MD[4], Christina Calvin MR Technologist[2], Kamal Singhrao PhD[2], Catherine Park MD[2], Nicolas Prionas MD, PhD[2], Jessica Scholey* PhD[2], Lisa Singer* MD, PhD[2]
[1]UCSF School of Medicine, San Francisco, CA, USA. [2]UCSF Department of Radiation Oncology, San Francisco, CA, USA. [3]Siemens Healthineers, Boston, MA, USA. [4]UCSF Department of Radiology and Biomedical Imaging, San Francisco, CA, USA

Abstract

Purpose:

Following breast conserving surgery, radiation therapy (RT) is an important part of multidisciplinary management of breast cancer. For patients requiring a tumor cavity (TC) boost or partial breast irradiation, RT planning requires accurate delineation of the TC. Delineation of the TC can be challenging due to poor contrast on computed tomography (CT) between the normal glandular tissue and the TC. Magnetic resonance imaging (MRI) provides excellent soft tissue contrast and may be especially helpful in the delineation of TCs, motivating use of MR simulation for breast RT planning. In this retrospective study, we examine the impact of MR simulation on RT planning and factors impacting MR image quality.

Methods:

A breast MRI simulation protocol was developed on a 3T MRI simulator (MAGNETOM Vida, Siemens Healthcare) in collaboration with radiology, and utilized in patients with poorly defined TCs, as determined by the treating radiation oncologist (RO). In this retrospective IRB-approved study, patients who underwent breast CT and MRI simulation were identified in the electronic health record (EHR) and the following information was collected: patient demographics, surgery type, tumor histology and staging, TC volume, and MRI parameters. Sequences investigated include: T2 fat-saturated free-breathing (FS FB), T2 HASTE breath-hold (BH), and T2 BLADE BH. Overall image quality for the T2-weighted sequences was assessed by two ROs specializing in breast cancer, and a medical physicist specializing in MRI, blinded to sequence type. The two ROs also assigned a cavity visualization score (CVS) based on CT vs CT+MRI, when unblinded. Descriptive statistics were calculated in Microsoft Excel.

Results:

8 patients underwent breast MRI simulation over a 6-month period (Table 1). Median CVS was unchanged for both raters with median CVS of 2, range [1-4]. The addition of MRI improved visualization of the TC margins in 3/8 (38%) cases by one rater's assessment. The T2 FS FB sequence was identified as the most useful sequence by all raters for all but one case, citing improved contrast and sharpness, with Krippendorff's Alpha of 0.718. A representative image of the comparison between sequences is shown in Fig 1. MRI produced images of sufficient quality for cavity delineation in 6/8 patients. Of these, 5 patients had TC volumes contoured before and after the availability of MRI data. For 80% of patients with available contour volumes (4/5), including MR in RT planning contributed to an adjustment in the contoured TC volume > +/-25%.

Discussion:

In our initial experience of MRI simulation for breast RT planning, MRI contributed to changes in TC volume in the majority of cases. This study was restricted to poorly-defined cavities, likely contributing to low CVS ratings in both modalities. For cases where MRI was not immediately helpful, later protocol optimization addressed issues encountered with both patients who had poor imaging results. This cohort of cases with poorly-defined TCs will provide important guidance to prospective studies using our finalized imaging protocol to investigate feasibility and efficacy of breast MRI simulation for RT planning.

(* Denotes co-last author)

71

Future-Proofing our Radiation Therapy Workforce: Development of an MR-Integrated Radiation Therapy Training Program

Darby Erler MHSc[1,2], Laura D'Alimonte MHSc[1,3], Mikki Campbell MHE[4], Nicole Harnettt MEd[1,5]

[1]University of Toronto, Department of Radiation Oncology, Toronto, ON, Canada. [2]Sunnybrook Odette Cancer Centre, Toronto, ON, Canada. [3]Windsor Regional Hospital, Windsor, ON, Canada. [4]Canadian Association of Medical Radiation Technologists, Ottawa, ON, Canada. [5]University Health Network, Toronto, ON, Canada

Abstract

Purpose

Due to its superior soft-tissue contrast, the integration of magnetic resonance imaging (MRI) into the radiation therapy (RT) care pathway has increased dramatically over the last decade. This has prompted many RT departments to invest in MRI simulators (MRSIM) and integrated MRI-guided treatment systems (MR-Linac). The adoption of MRI into the RT workflow is not trivial as significant challenges exist extending beyond MRI safety requirements including the imaging literacy of radiation therapists (RTTs) which remains a limiting factor for wider adoption. The purpose of this work was to design an education program specifically for RTTs to acquire the knowledge, skills and judgement to safely operate MRI within a therapeutic oncology context.

Methods

A needs assessment was conducted in November 2017 to understand MRI in the RT landscape across the country, including the projected uptake of these systems over the next 5-10 years, proposed health human resource models and related training needs. To better articulate the knowledge and skills required for RTTs to safely use and operate MRI in RT practice, a modified Delphi process was undertaken to obtain expert consensus from multi-disciplinary international experts including radiation oncologists, medical physicists, RTTs, MRI technologists (MRTMR) and RTTs also certified in MRI. The results of this Delphi exercise were used by an expert panel to undertake a curriculum mapping exercise to identify the key learning outcomes and programming for a comprehensive continuing education program for practicing RTT to develop competence to use MR in the radiation therapy domain.

Results

Results of the needs assessment indicated that a significant number (~40% of respondents) of clinical departments across the country planned to implement MRSIM and/or MR-Linac. A large variation in staffing models existed, whereby the units may be operated by: dual certified RTT/RTMRI, RTT with specialty MRI training, or a team comprised of individual RTT and RTMRI, likely due to the limited formal MRI training opportunities available to RTTs. Consistent themes emerged with respect to training needs, including: MRI safety, MRI-based anatomy, MRI image quality and MRI quality control.

The Delphi process yielded a final inventory of 49 knowledge and skill statements in 4 domains including: MRI Image Formation and Interpretation, Patient Care and Safety, Quality Assurance and Quality Control and Practical Integration and Application of MRI. These knowledge and skills statements were incorporated into 7 learning objectives addressing safety, imaging literacy and application of MRI in the RT environment. In order to address these learning objectives, a 31 week spiral curriculum was developed employing a blended learning format and incorporating didactic, simulated and experiential learning approaches. The majority of the part time program is delivered virtually (26 weeks) while the final weeks are comprised of in person practical experiences with MRSIM and MR-Linac as well as in diagnostic imaging departments.

Conclusion

A comprehensive, learner-centred, multi-faceted curriculum was designed for RTTs to acquire the confidence and competence to integrate MR-technology into their practice and support departments in their efforts to implement safe and high quality MRI into the radiation therapy care pathway.

72

3D-Printed Multi-Contrast Phantom for Quality Assurance of Adaptive Radiotherapy Delivery in a High-Field MR-Linac

Ergys Subashi[1], Horatio Hamkins[2], Justin Kuligowski[3], Samuel Hellman[3], Neelam Tyagi[3]

[1]Memorial Sloan Kettering Cancer Center, New York, NY, USA. [2]University of Bath, Bath, United Kingdom. [3]Memorial Sloan Kettering Cancer Center, New York, USA

Abstract

Purpose: Independent end-to-end testing and verification of online adaptive radiotherapy delivery in a high-field MR-linac is challenging due to the lack of MR/CT compatible phantoms. This work aims to design an anthropomorphic phantom that approximates the patient-specific MR/CT properties needed for verification of online adaptive radiotherapy delivery in a 1.5T MR-linac.

Materials and Methods: Digital models of human anatomy were created based on the extended cardiac torso (XCAT) phantom. For a given anatomical site, a list of structures representing common organs-at-risk (OARs) was generated by combining structures available in XCAT. Physiological movement was modeled by implementing respiratory, cardiac, and GI tract motion. These motility modes can be implemented individually or in combination. For a given motion state, the OARs were first converted to binary masks, then to high-resolution stereolithography (STL) files. The STL assembly was used to guide the insertion of dosimeter holders in specified anatomical points. Holders were designed for OSLD, film, and ion chamber dosimeters. The dosimeter-embedded STL assembly was used as an input for 3D printing. The following materials were evaluated as surrogates for estimating patient-specific MR/CT properties: gel matrix (GM), tissue matrix (TM), bone matrix (BM), radio matrix (RM), agilus (AG), vero white (VW). Samples of various mixtures ranging from 10% - 60% were printed and evaluated in a clinical CT simulator and in a 1.5T MR-linac.

Results: For treatments of gastrointestinal (GI) targets, a phantom with the following organs was selected: lung, esophagus, heart, vessels, stomach, liver, gallbladder, pancreas, small bowel, large bowel, kidneys, bones, spinal cord, skin, connective tissue, muscles, and body. An example is shown in Fig. 1. Dosimeter slots were designed in the STL assembly by identifying a path that traverses the least number of organs. The dosimeter holders were designed with materials that match the tissue in the slot. The analysis of the sample mixtures reveals that HU values are modulated by the presence of radio matrix while MR signal intensity is modulated by a mixture of gel and tissue matrix, shown in Fig. 2. These findings are complemented with relaxometry measurements in the MR-linac.

Conclusion: We demonstrate the ability to generate realistic 3D printed anthropomorphic phantoms for verification of online adaptive radiotherapy delivery in a 1.5T MR-linac. Future work will evaluate long-term radiation properties and material stability.

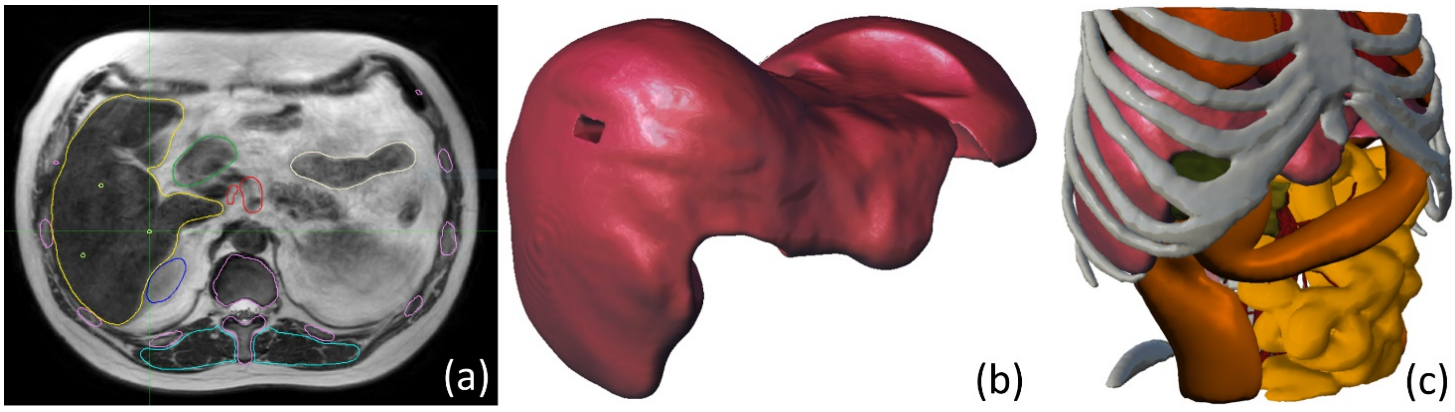

Figure 1. (a) Representative example of patient T2-weighted MRI used in planning the placement of a dosimeter in the liver. (b) Model of liver showing the planned position of dosimeter holder. (c) Assembled STL model prepared for 3D printing.

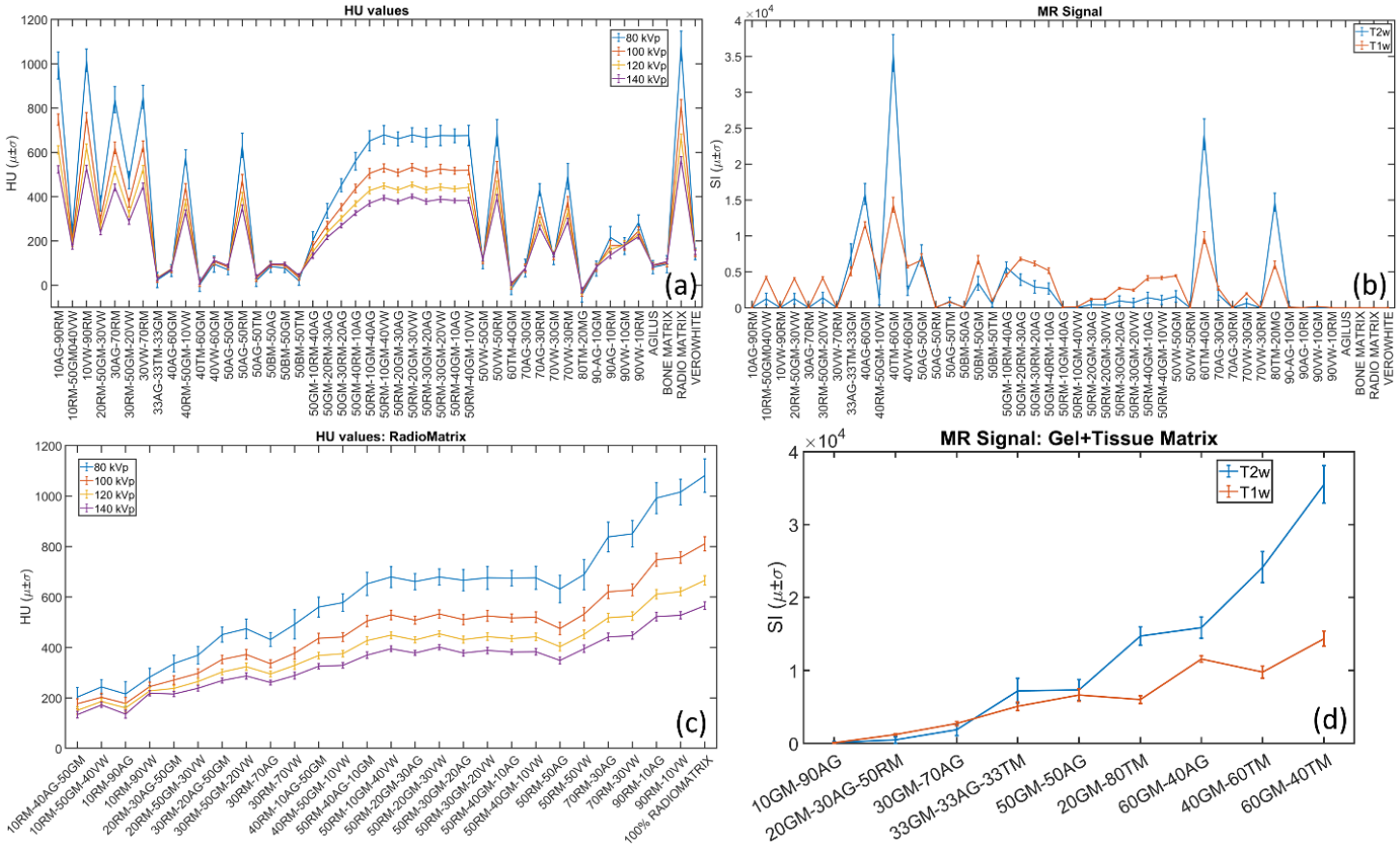

Figure 2. (a) Hounsfield unit measurements in a clinical scanner at four tube voltages (80, 100, 120, 140 kVp) for all material compositions considered in this study. (b) Signal intensity values using two clinical T1/T2-weighted sequences for all material compositions. (c) HU values as a function of amount of radio matrix showing the dynamic range achievable with mixtures up to 100%. (d) T1/T2-weighted signal intensity for mixtures of gel and tissue matrix showing the dynamic range achievable with mixtures up to 60%.

73

Study of correlation between patient specific QA gamma index passing rate and IMRT plan complexity for a ViewRay MR-Linac System

Zhifei Wen PhD, Annamarie Minion MS, Benjamin Rusk MS, Jay Zheng PhD
Hoag Memorial Hospital Presbyterian, Newport Beach, CA, USA

Abstract

Purpose: The primary goal of patient specific QA for IMRT is to verify that the machine-delivered dose is in good agreement with the treatment planning system (TPS) calculated dose. The degree of agreement can be quantified by the gamma index passing rate. Low gamma passing rates are often seen in highly modulated IMRT plans, which may contain large numbers of small treatment field segments, causing increased inaccuracy in dose calculation and delivery. The TPS of the MRIdian system (Viewray, USA) uses Monte-Carlo based dose calculation algorithms, which can maintain high accuracy for small fields. In this study, we present the IMRT QA gamma passing rates for SBRT plans as a function of plan complexity, which is quantified as a simplified parameter, MUs/Gy, the ratio of the monitor units per fraction (MUs/Fx) in the plan to the prescribed dose per fraction (Gy/Fx).

Methods: 125 SBRT plans (3-5 fractions) were selected with disease sites including the brain, lung, liver, pancreas, and prostate. IMRT patient specific QA was performed with a MRIdian system and an MR-compatible Delta4 phantom (ScandiDos, Sweden). The gamma index was calculated using 2 mm/2% with a dose threshold of 10% of the maximum dose. The phantom position was optimized in the software to maximize the gamma index passing rate. The gamma index passing rate was plotted as a function of MUs/Gy. A linear regression line was fitted to the plot to show the trend.

Results: The plan complexity parameter ranged from 155 to 840 MUs/Gy. Among the 125 plans, 3 IMRT QAs (MUs/Fx= 371, 467, 662) had gamma index passing rates < 95%. The gamma index passing rate was 98.5% for the most highly modulate plan (MUs/Fx=840). The linear regression of all QA cases was y = -3E-05 * x + 0.9987 (y: gamma passing rate in decimal, x: MUs/Gy), with R^2=0.1052, showing a poor correlation between the gamma passing rate and plan complexity.

Conclusion: 122 of the 125 SBRT plans in this study had gamma index passing rates >=95% with 2 mm/2% criteria, showing excellent agreement between delivered and calculated dose for our MRIdian system. The gamma passing rate does not seem to be correlated with the plan complexity, demonstrating the high accuracy of Monte Carlo dose calculation for highly modulated treatment plans.

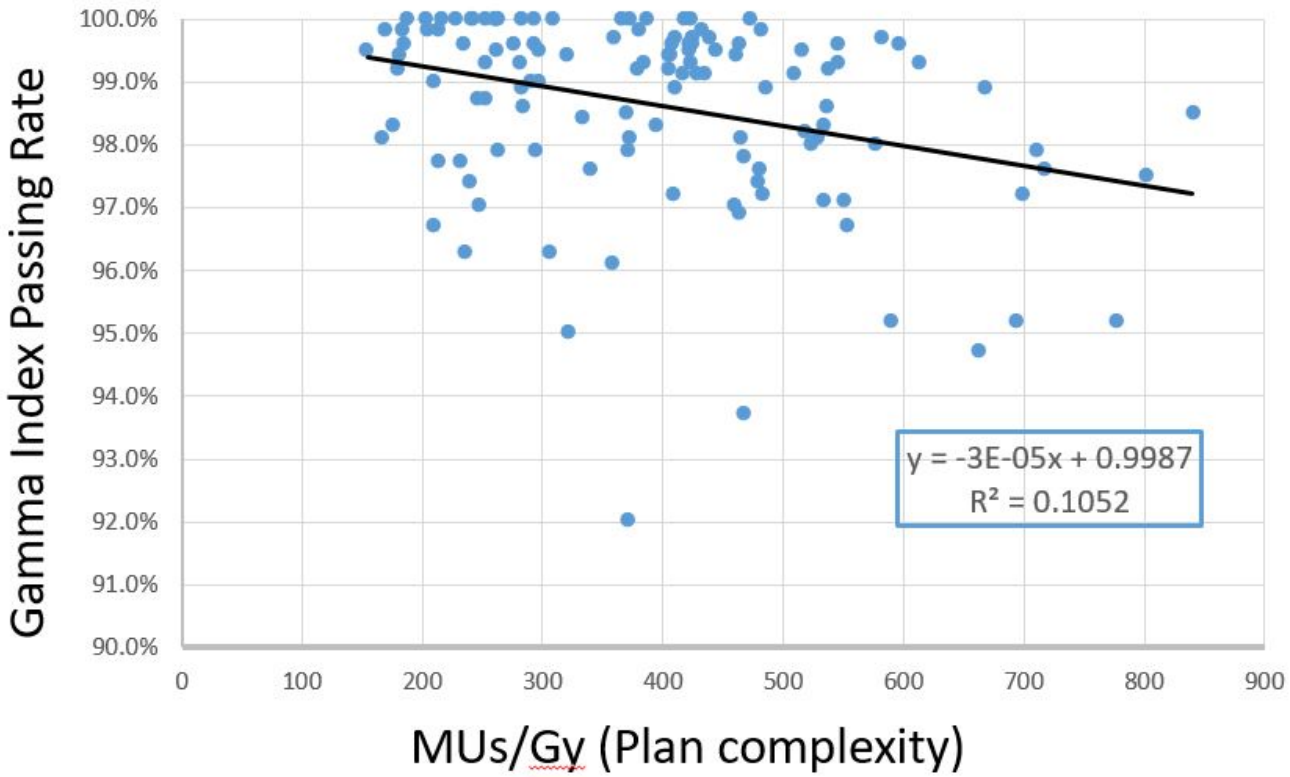
Gamma Index Passing Rate
100.0%
99.0%
98.0%
97.0%
96.0%
95.0%
94.0%
93.0%
92.0%
91.0%
90.0%
0
100
200
300
400
500
600
700
800
900
y = -3E-05x + 0.9987
R² = 0.1052
MUs/Gy (Plan complexity)

74

Clinical commissioning from bulk density synthetic CT to compressed-sensing-accelerated continuous Hounsfield unit synthetic CT for MR-only treatment planning in prostate: an institutional experience

Victoria Yu PhD, David Aramburu Núñez PhD, Laura Happersett MS, Can Wu PhD, Neelam Tyagi PhD, Laura Cervino PhD, Antonio Damato PhD
Memorial Sloan Kettering Cancer Center, New York, NY, USA

Abstract

Purpose: To clinically validate a commercial implementation of a continuous Hounsfield unit synthetic CT with additional compressed-sensing acceleration (cHU-CS), compared to our prior clinical standard consisting of bulk density (BD) synthetic CT for MR-only treatment planning in prostate radiation therapy.

Methods: BD and cHU-CS synthetic CT images (Figure 1 & Table 1) were acquired on 2 Philips 3T MR-RT simulators for 10 patients receiving MR-only prostate radiotherapy and one healthy volunteer. Average HU values within bone and soft tissue were evaluated in the volunteer subject for BD and cHU-CS between the two scanners to evaluate scanner HU value consistency. Using associated CT as ground truth in one patient, the HU accuracy was evaluated by comparing average HU values in thirteen anatomical regions of interest and calculating the mean absolute error (MAE) to CT in the bone for both cHU-CS and BD scans. In dosimetric evaluations, a vendor recommended electron density (ED) calibration curve was compared against the institutional calibration curve for 6MV and 15MV energies. The CT was deformed to synthetic CT source MRI scans to account for anatomical changes in between the CT and the MRI scans. Dosimetric comparisons were performed comparing cHU-CS and BD to the deformed CT in one patient, and cHU-CS vs BD in 10 patients. Treatment plans were optimized for 6MV and 15MV on the original planning CT and then recalculated on BD and deformed CT with the institutional ED curve, and cHU-CS scan with both institutional and vendor ED curves.

Results: In the volunteer HU consistency test, the difference in average HU values within bone and soft tissue from the cHU-CS scans from the two scanners were 9.53 and 3.07 HU, respectively. For HU accuracy evaluations, the MAE to CT in the bone contour for cHU-CS and BD were 131.91HU and 160.54HU. In anatomical ROI comparisons, cHU-CS average HU were in closer agreement to CT when compared with BD in 9/13 of the compared ROIs. All evaluated plan dosimetry parameters on BD or cHU-CS scans were within +/- 1% from that of the deformed CT, regardless of beam energy (Figure 2a,b). Calculations using the institutional ED curve trended closer to the CT as compared with vendor ED curve, suggesting a unified institutional ED curve is suitable for clinical use on the cHU-CS synCT. All evaluated parameters on cHU-CS plans had average difference of less than 1% from that of BD (Figure 2c,d). In terms of target coverage parameters, percent differences trended slightly negative on cHU-CS as compared with BD by <0.5%, indicating that eventual dose could be higher by <0.5% as compared with the routine BD implementation. Significant image quality improvements for fiducial seed and soft tissue visualizations, and bony anatomy reconstructions were seen in cHU-CS.

Conclusion: cHU-CS synthetic CT achieved highly consistent and accurate HU estimations for general pelvis treatment planning applications. Minimal dosimetric differences in prostate radiotherapy plans were observed compared to a routinely utilized BD version. The improvements in image quality will improve routine on-treatment image guidance.

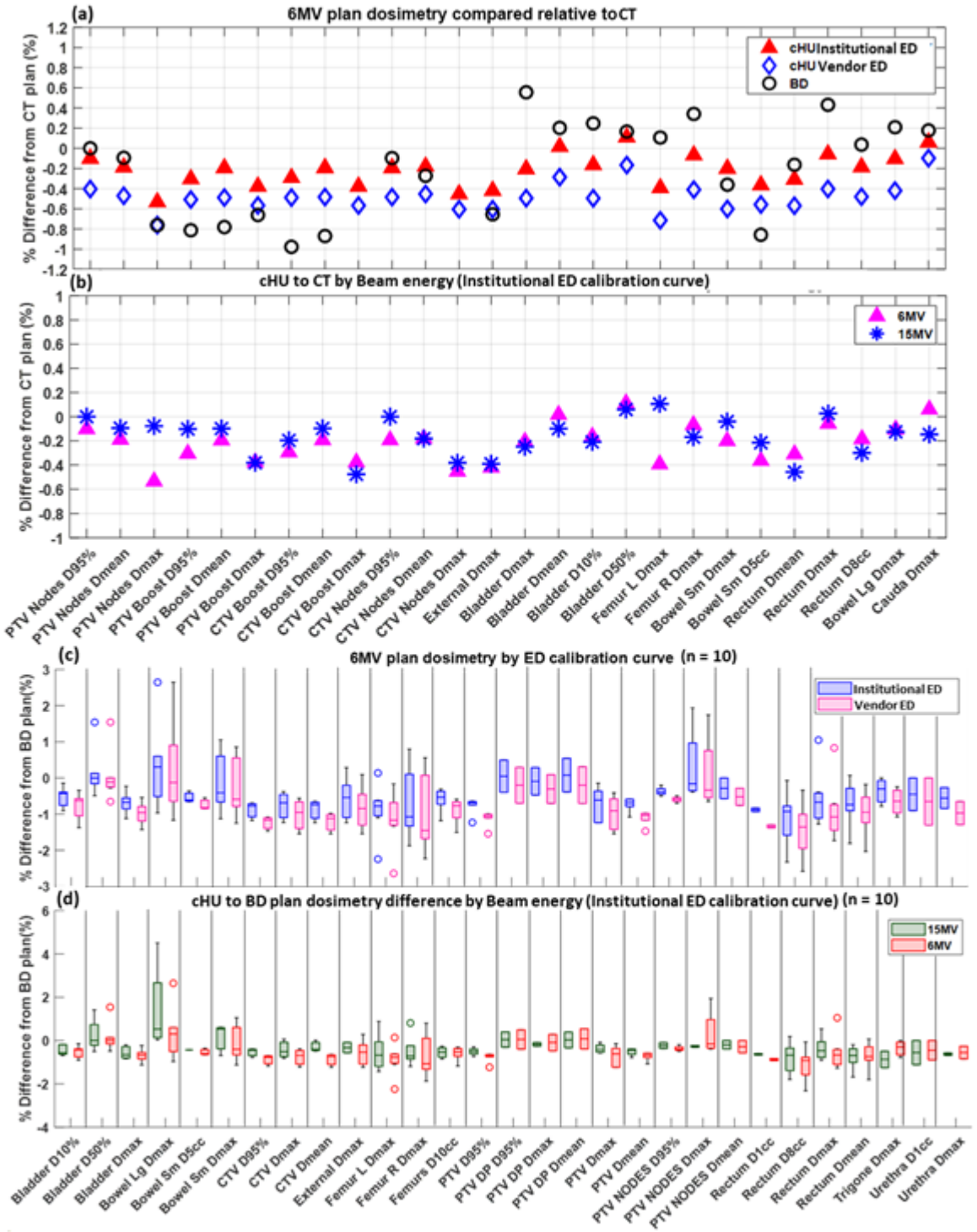

Figure 2: (a) 6 MV Plan dosimetry parameters percent difference to deformed CT. BD, cHU-CS with 2 different ED to HU calibrations. (b) 6MV and 15MV percent differences to deformed CT with institutional ED calibration. (c) 6MV cHU-CS percent dose parameter difference to BD by calibration curve. Each box and whisker includes all % difference values from the evaluated plans for that specific Target or OAR dose metric. (d) : 6 MV vs 15MV cHU-CS percent dose parameter difference to BD side by side. Plan calculated with the institutional standard ED to HU calibration curve.

75

Assessment of differences between treatment using the Australian MRI-linac and standard of care for the MAnTRA clinical trial

Mr Jarrad Begg Masters[1,2,3], Mr Bin Dong[2], Mrs Esther Wong[2], Dr Shivani Kumar PhD[2], Dr Trang Pham PhD[1,2,3], Mr Justin Spicer[1], Mrs Daniela Miller[1], Mr Andrew Wallis[1], Mrs Doaa Elwadia[1,4], Mrs Zoe Moutrie[1], Mr Tony Young[1], A/Prof Gary Liney[1,2,3,5], Dr Paul Liu[6,2], Prof Paul Keall[6,2]

[1]Liverpool and Macarthur Cancer Therapy Centre, Liverpool, NSW, Australia. [2]Ingham Institute for Applied Medical Research, Liverpool, NSW, Australia. [3]South Western Sydney Clinical School, University of New South Wales, Liverpool, NSW, Australia. [4]Discipline of Medical Imaging Science, Faculty of Medicine and Health, The University of Sydney, Sydney, NSW, Australia. [5]Centre for Medical Radiation Physics, University of Wollongong, Wollongong, NSW, Australia. [6]ACRF Image X institute, University of Sydney Central Clinical School, Sydney, NSW, Australia

Abstract

Purpose

The Australian MRI-linac is a bespoke 1 T magnet coupled with a radiation source in parallel. The Mri-linAc Treatments for Radiotherapy Patients (MAnTRA) trial is a phase I Pilot Study on the use of the Australian MRI-Linac to treat patients. The Australian MRI-linac team developed a whole brain treatment procedure using a combined supine and prone set-up. This work assessed the patient set-up reproducibility, dose delivery accuracy and variation in dose distribution relative to standard treatment.

Methods

A whole brain palliative treatment was selected as the first treatment site. Due to the static gantry angle, the right lateral field is treated using a head-first supine set-up and the left lateral field using a head-first prone set-up. Prescribed dose is set at the mid-point. Simulation MRI-linac scans were acquired in the supine and prone set-ups with markers placed on the MRI isocentre for each scan. Both MR scans are then fused onto a supine CT. The supine and prone isocentre positions were used for the respective beam isocentre placement. Reproducibility of the supine and prone positioning was evaluated using a head phantom and 10 repeat set-ups to isocentre. Angular rotations of up to 5° were simulated in the planning system to determine the impact of set-up rotations on whole brain coverage and lens dose. Additional dose to the patient with respect to the clinical procedure was evaluated in order to demonstrate the equivalence of the technique. Due to electron focusing that occurs in parallel MRI-linacs, skin dose was evaluated using GafChromic EBT3 film during an end-to-end test (Figure 1).

Results

Planning using a supine and prone set-up showed equivalence to clinical plans. Reproducibility of phantom rotational and translational positioning was within ± 1° and ± 0.5 mm respectively. Rotations up to 5° in all directions in the planning system did not show significant impacts on the whole brain coverage or lens dose. Summed effective dose to OARs outside the treatment field was 18.4 mSv which represents a worst-case scenario. End-to-end tests of skin dose showed the skin dose was between 90 – 115 % of the prescribed dose expect at the vertex of the head where 121 % was recorded (Table 1).

Figure 1: Films placed inside the insert, on the forehead and on the lens to evaluate dose.

Table 1: Dose received to phantom location at different points.

Placement of film	Per Fraction (cGy)	Full treatment (cGy) (5 Fractions)
Patient's right isocentre	410	2050
Patient's left isocentre	400	2000
Insert (Brain)	410	2050
Patient's right eye	40	200
Patient's left eye	50	250
Vertex of head	485	2425
Back of head	440	2200
Back of neck	445	2225
Forehead	440	2200

Conclusion

A whole brain treatment technique was developed to treat patients on the Australian MRI-linac. Patient set-up was found to be reproducible. In-vivo skin dose results showed agreement with expected dose. The overall results demonstrate the opening of the MAnTRA clinical trial to patient recruitment for treatment using the Australian MRI-linac was safe. The trial was officially opened to recruitment in late 2022.

76

Clinical Use of an MR-based Motion Map to Determine Patient-specific Volumetric Margins in Proton Therapy for Prostate Cancer

Jiyeon Park Ph.D[1,2], Soon Huh Ph.D[1,2]

[1]University of Florida College of Medicine, Gainesville, FL, USA. [2]University of Florida Health Proton Therapy Institute, Jacksonville, FL, USA

Abstract

Purpose: To determine patient-specific margins for planning target volume and organs-at-risk (OAR) in prostate radiation therapy using proton beams, we devised an MR-based three-dimensional motion map for practical clinical application. Individual patients' target and organ motions were assessed with dynamic MR imaging, and the dosimetric effects by the margins were investigated for optimized and robust proton therapy.

Methods: The organ motions were evaluated for 30 intact prostate patients with three fiducial markers implanted at the prostate (base, right apex, and left mid gland) and rectal spacer. Three orthogonal MRIs using balanced fast field echo (b-FFE) sequences were acquired in dynamic mode (dMRI) to evaluate organ motions. The parameters of the b-FFE were adjusted to use a flip angle of 6 degrees and repetition time and echo time of 22 secs and 11 secs, respectively. In addition, T2-weighted turbo spin-echo images (TSE) were scanned for structure delineation. The TSE and the dMRI were fused with CT images to delineate structures with appropriate margins. The MR-based motion map was created from maximum and minimum intensity maps of the dMRI and the subtracted images between the two to determine and judge the margin appropriateness in three orthogonal directions. The target and OAR defined with the patient-specific margins were used in the prostate robustness plan using proton beams. The dosimetric effects of the patient-specific margins were evaluated compared to the dose with regular margins.

Results: The MR-based motion map led to apply image-based margins for target and OAR motions that were monitored longer than proton beam delivery time. The appropriateness of the margins was reviewed in the b-FFE images using the dynamic mode. The motion map also enabled using a patient-specific volumetric margin rather than one fixed value for each three-orthogonal direction. The reliability of the fiducial markers, rectal spacer, and rectal and large bowel gases was evaluated with non-invasive monitoring. The motion maps acquired during multiple days presented inter- and intra-fraction motions. Moreover, proper bladder filling could be guided for patients not tolerant well to the full urinary bladder and pelvic floor muscle tightness for better bladder filling reproducibility during a radiation treatment course. The patient-specific margins from the motion map could reduce unnecessary rectal and bladder doses with image-based motion evaluation.

Conclusion: Using the MR-motion map was efficient and straightforward to apply to the planning procedure to add appropriate margins assessed with non-invasive image-based motion monitoring. Especially for proton therapy that needs precise but robust treatment considering proton beam properties and patient motion uncertainties, the MR motion map can guide the image-based patient-specific margins to save OAR doses.

77

MR Imaging of Free Radical Production during Radiation Chemistry Interactions

Noah Warner[1,2], Joshua Wancura[3,2], Veena Venkatachalam[2,4], Erno Sajo[5], Atchar Sudhyadhom[2]

[1]Harvard-MIT Health Sciences and Technology, Cambridge, MA, USA. [2]Brigham and Women's Hospital, Dana-Farber Cancer Institute and Harvard Medical School, Boston, MA, USA. [3]University of Rochester, Rochester, NY, USA. [4]Blavatnik Institute at Harvard Medical School, Boston, MA, USA. [5]University of Massachusetts Lowell, Lowell, MA, USA

Abstract

Purpose: Production of free radicals in radiation therapy is the mechanism for a significant fraction of indirect DNA damage. Previously, real-time MR images of a radiation beam have been described where the observed contributions were attributed mainly to an oxygen depletion mechanism. This effect was observed following several minutes of irradiation. We hypothesized that T1 signal changes should differ within 60 seconds of irradiation due to rapid free radical production, when oxygen depletion is less of a driving force. The purpose of this study is to understand MR signal change due to radiation chemistry interactions in this < 60 second time regime.

Methods: Radiochemistry simulations were matched to MR imaging experiments of distilled water and 10 mM coumarin (a hydroxyl specific radical scavenger) solution. MR images of each phantom were acquired on a 0.35 T MR-linac during phantom irradiation. A 2D MP-RAGE scan was acquired every 2 seconds for approximately 1 minute during beam-on, and was repeated 64 times to obtain sufficient SNR. The series of 64 scans were averaged at each of the 30 time points. Simulations modeled radiation chemistry product concentrations over a minute of irradiation and were converted to T1 values.

Results: Simulation predictions and experimental observations are consistent, resulting in the first known direct observation of MR signal changes due to free radical production in an MR-linac. Radiation chemistry simulations in both distilled water and coumarin solution suggests that oxygen concentration will linearly decrease over time resulting in a positive linearly increasing contribution to T1 change over time (Figure 1A). Simultaneously, free radical concentrations rapidly grow at the onset of irradiation then grow less rapidly at later times resulting in a sharp decrease in T1 that plateaus to a more constant negative T1 contribution at longer time scales (Figure 1B). When combining the contributions of these two effects, total T1 change initially decreases quickly followed by a linear increase over longer time scales (Figure 1C). This was observed experimentally as shown by the MR signal of both ultrapure distilled water and coumarin solutions. In particular, we found that water signal change over time stays approximately constant (Figure 2A), with slight decrease near the 1-minute time point. This differs from that of the coumarin solution where the signal change initially increases, then decreases at later times (Figure 2B).

Conclusion: MR signal changes produced during short time scale radiation chemistry interactions are observed and presented for the first time. It is shown that short time scale radiation chemistry MR imaging is correlated with factors that influence radiation chemistry, such as the introduction of a hydroxyl scavenger. This suggests that the radiation chemistry interactions in a < 60 second time regime influence x-ray induced MR signal changes. Further work to improve signal to noise ratio (SNR) will be necessary to translate this work into clinical studies.

Figure 1:

Figure 2:

78

Low-field MR Multitasking for an integrated abdominal MRgRT imaging framework

Junzhou Chen MS[1,2], Ye Tian PhD[1], Namgyun Lee[1], Mingsong Cao PhD[2], Wensha Yang PhD[1], Sophia Cui PhD[3], Krishna Nayak PhD[1], Debiao Li PhD[4], Anthony Christodoulou PhD[4], Zhaoyang Fan[1]

[1]University of Southern California, Los Angeles, CA, USA. [2]University of California, Los Angeles, Los Angeles, CA, USA. [3]Siemens Medical Solutions, Los Angeles, CA, USA. [4]Cedars-Sinai Medical Center, Los Angeles, CA, USA

Abstract

Introduction

MRgRT holds great potential for personalized, biologically adaptive radiotherapy. However, critical challenges related to onboard image acquisitions remain in the current abdominal MRgRT workflow. First, in the pre-beam phase, no respiration correlated (i.e., 4D-MR) are available to reassess breathing patterns. Several novel 4D-MR sequences under research are all single-contrast weighted and thus potentially limited in target/OARs delineation. Second, in the beam-on phase, real-time tracking is focused only on the tumor target using a 2D sequence. Although reasonable spatiotemporal resolution can be achieved, this strategy can easily miss valuable 3D information. A few 3D real-time imaging methods have recently been proposed. In addition to certain drawbacks in spatiotemporal resolution or latency, these methods suffer from the same single-contrast-weighting problem. Addressing these issues are perhaps even more critical for relatively low field MR-Linacs (e.g., 0.35T, 0.55T, or 1T) as the research of the MR imaging community has long been focused on ≥1.5T. To fill the technological gap, our study aims to develop a novel low-field MR Multitasking (MR-MT) sequence and demonstrated its feasibility in fulfilling key imaging tasks of abdominal MRgRT.

Methods

Sequence and reconstruction design:

A hybrid GRE-TSE sequence was developed. As shown in Fig. 1A, each repetition time (TR) of our MR-MT sequence starts with a saturation recovery (SR) pulse followed by a group of GRE readouts for T1-weighted acquisitions and then low-flip-angle GRE readouts for proton density-weighted acquisitions. A TSE echo train is appended after the GRE modules to generate T2 weighting. K-space is sampled with a Cartesian spiral-in pattern (Fig. 1B) with 10 lines in each spiral arm and the 10th line at the k-space center being the navigator. The MR-MT sequence can be used for free-breathing multi-dimensional imaging in both pre-beam and beam-on phases. For the pre-beam scan, multi-contrast 4D-MR images can be reconstructed using the MR-MT low-rank model (Fig. 1C). For the beam-on real-time scan, the low-rank parameters from the pre-beam (or "prep") scan can enable multi-contrast real-time display using our recently proposed SPIDERM algorithm (Fig. 2A).

Imaging Parameters:

FOV = 256(SI) x 358(LR) x 256(AP) mm^3. Resolution = 1.6 x 1.6 x 3.2mm^3. TR/TE = 6.0/3.0 ms. Flip Angles: 5/1(GRE), 180(TSE refocusing). Segment lengths: 150/150/100.

Study Details:

3 volunteers were scanned on a whole body 0.55T system (prototype Magnetom Aera, Siemens Healthineers, Erlangen, Germany) equipped with high-performance shielded gradients (45 mT/m amplitude, 200 T/m/s slew rate).

Results

Figure 1.D shows the motion-resolved, multi-contrast, volumetric images for adaptive planning. Figure 2.B demonstrate from the prep scan, we can enable real-time simultaneous volumetric tracking during treatment.

Discussion

In this study, we developed a novel MR-MT sequence that has showed great potential to support major imaging tasks in a typical low-field MRgRT workflow. An integrated MRgRT imaging framework based on this sequence may bring image consistency throughout the daily treatment course, and can be even expanded by including MR simulation, thus helping streamline the entire MR-based RT workflow and improve the overall accuracy and outcome.

Figure1:

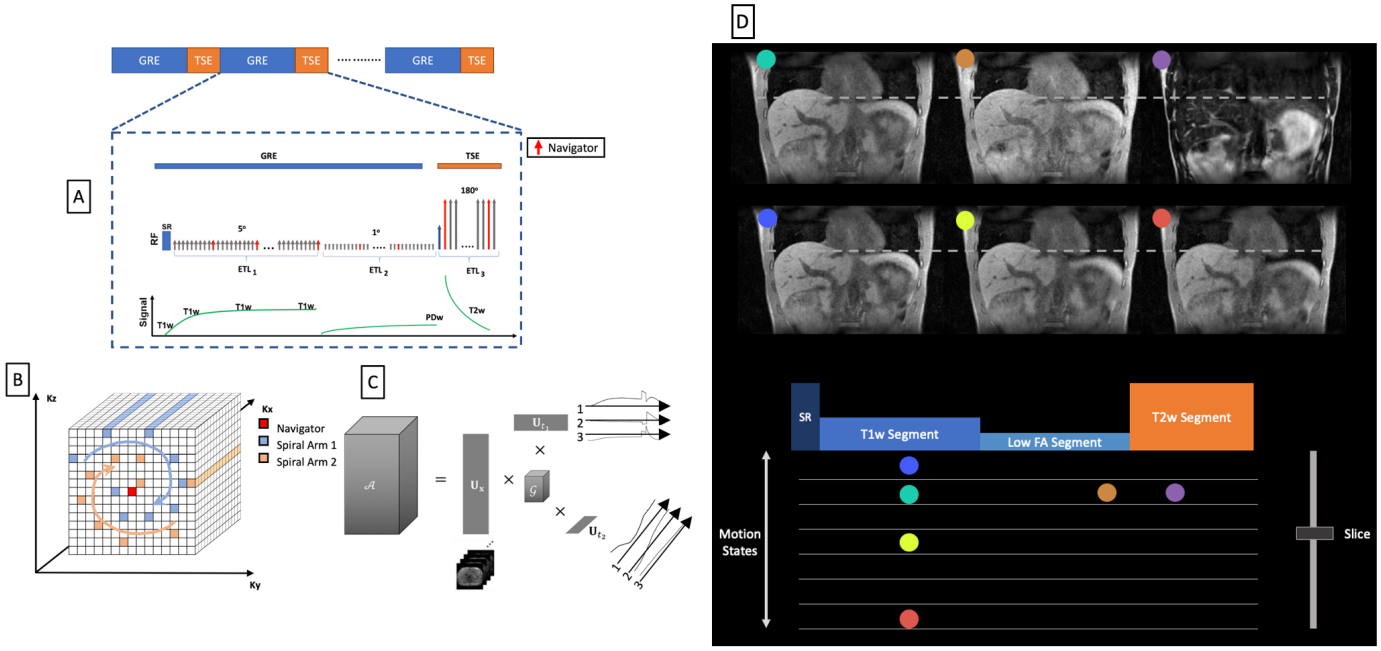

Figure2:

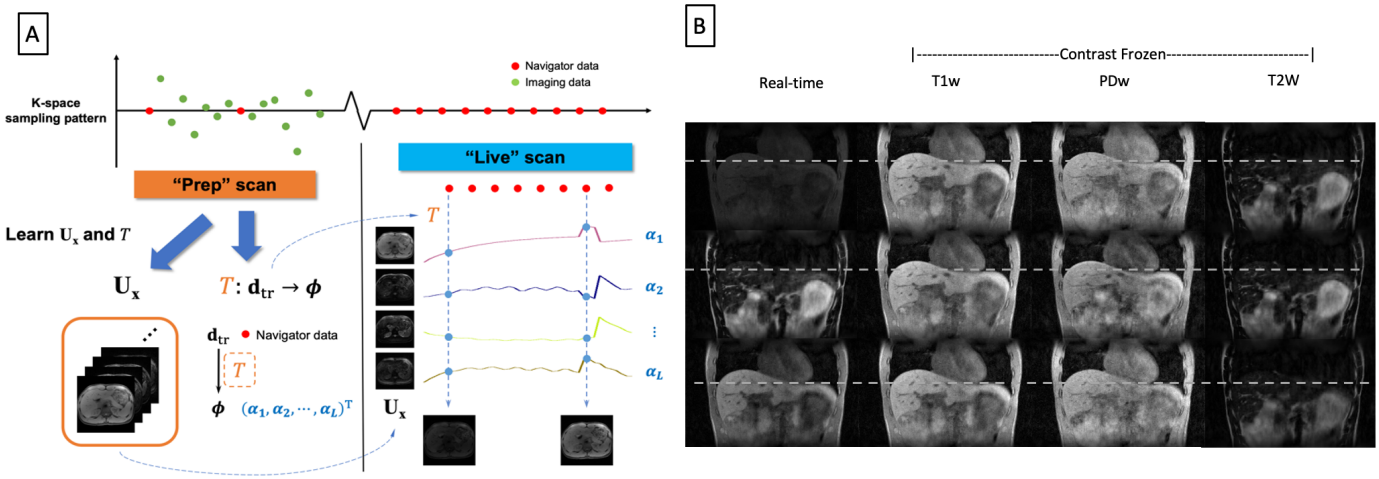
A
K-space sampling pattern
Navigator data
Imaging data
"Prep" scan
"Live" scan
Learn $\mathbf{U}_x$ and T
$\mathbf{U}_x$
T: $\mathbf{d}_{tr} \rightarrow \boldsymbol{\phi}$
$\mathbf{d}_{tr}$
Navigator data
T
$\boldsymbol{\phi}$ $(\alpha_1, \alpha_2, \cdots, \alpha_L)^T$
$\mathbf{U}_x$
α_1
α_2
α_L
B
Contrast Frozen
Real-time
T1w
PDw
T2W

79

Treatment delivery gating of MRI-guided stereotactic radiotherapy for prostate cancer: An exploratory analysis of a Phase III Randomized Trial of CT-vs. MR-guided radiotherapy (MIRAGE)

Dr. Jack Neylon PhD, Dr. Ting Martin Ma MD, PhD, Dr. Daniel Low PhD, Dr. Michael Steinberg MD, Dr. Amar Kishan MD, Dr. Minsong Cao PhD
University of California, Los Angeles, Los Angeles, CA, USA

Abstract

Introduction and Objective:

MRI-guided radiotherapy (MRgRT) allows aggressive margin reduction, in large part due to real-time intrafraction cine tracking and gating. Compared with CT-guided radiotherapy, MRgRT has been shown to reduce acute physician-scored and patient-reported gastrointestinal and genitourinary toxicities associated with prostate stereotactic body radiotherapy (SBRT) in the MIRAGE randomized trial (NCT04384770). The purpose of the present study is to quantify treatment delivery gating in patients receiving MRgRT on the MIRAGE trial.

Methods and Materials:

79 patients received MRgRT on the MIRAGE trial. For all patients, a planning margin of 2mm was placed around the prostate and proximal seminal vesicles and this volume was treated to 40 Gy in five fractions on a MR-Linac (MRIdian, ViewRay Inc). Cine imaging was acquired during treatment at 4 frames/second in the sagittal plane. If >10% of the prostate volume was detected moving outside a 3 mm gating boundary placed around the clinical target volume (CTV), an automatic beam hold would be initiated. An in-house tool was developed to extract treatment time and beam gating status based on treatment logs and real-time cine images. The ratio of the time that the CTV was within the gating window versus the total combined time of target inside or outside the gating boundary was calculated and defined as the duty cycle (Supplementary Figure 1). Cine images with duty cycle less than 0.9 were visually inspected.

Results:

Median treatment time per fraction including image guidance procedure and beam delivery was 1459.3 seconds (IQR: 1331-1660 seconds). The median time for image guidance including acquisition, review and adjustment was 323 seconds (IQR: 251.8-404.6 seconds). A total of 391 treatment fractions were analyzed and the median duty cycle per fraction was 0.972 (IQR: 0.930 -0.976), indicating overall stable positioning of prostate during treatment. However, there were 35 (9.0%) fractions having duty cycles <80% (Figure 1); this corresponded to 24/79 (30.4%) of patients having at least one fraction with a duty cycle <80%. The minimum duty cycle was lower among patients with grade ≥2 GU toxicity compared to those with grade 0-1 GU toxicity (mean 79.8% vs. 85.9%, p=0.07, Figure 2). The proportion of patients with grade ≥2 GU toxicity was greater in patients with a minimum gating cycle <80% (37.5% vs. 18.2%, p=0.06). Visual inspection of the cine image revealed distinct motion patterns including gradual drifting due to bladder/rectum filling and sporadic bulk motions.

Conclusions:

Relatively stable intra-fractional target position was observed during MR-guided prostate SBRT treatment. However, a large fraction (30%) of patients had at least of one treatment fraction with duty cycle less than 80%, underscoring the unpredictable nature of prostate motion and the necessity for real-time motion management.

Figures

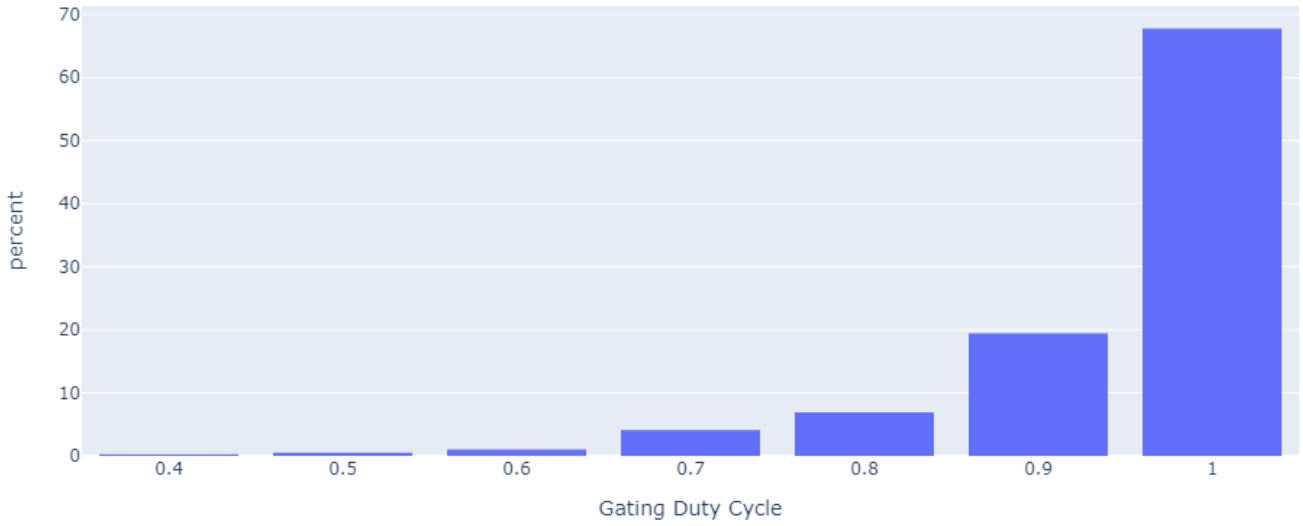

Figure 1. Histogram of gating duty cycle per fraction of all 391 treatment fractions.

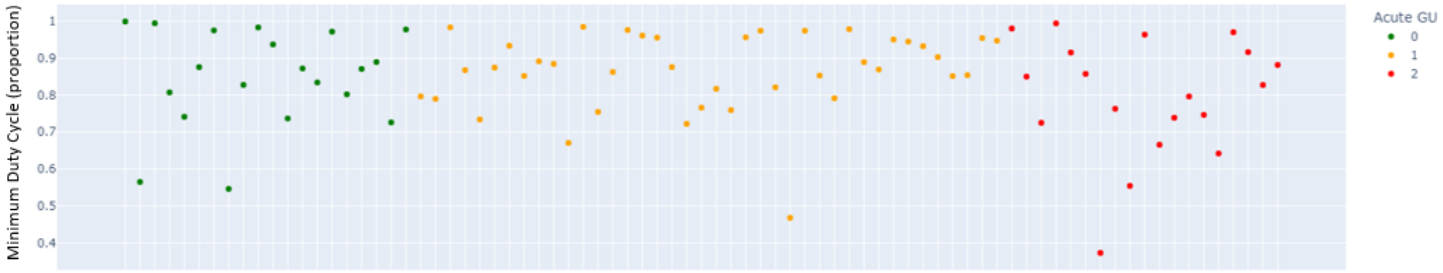

Figure 2. Scatter plot of minimum duty cycle per patient trichotomized by grade of genitourinary toxicity. Each dot corresponds to a patient and color-coded by acute GU toxicity.

80

Simulation-free adaptive radiosurgery for Malignant Spinal Cord Compression Syndrome using MR-LINAC

Assistant Professor Tsuicheng Chiu Ph.D., Associate Professor Strahinja Stojadinovic Ph.D., Assistant Professor You Zhang Ph.D., Assistant Professor Viktor Iakovenko Ph.D., Associate Professor Arnold Pompos Ph.D., Assistant Professor Thomas Banks Ph.D., Assistant Professor Tu Dan M.D.
UT Southwestern Medical Center, Dallas, TX, USA

Abstract

Purpose: To utilize MR-LINAC's adapting ability to achieve simulation-free emergency treatment for spinal cord compression syndrome.

Method: The proposed workflow for the simulation-free treatment includes patient setup, creating an adapted plan from a generic reference plan, and treatment delivery. A prerequisite for fast treatment plan turnaround, while the patient is set up on the treatment couch, is a previously created generic treatment plan ready for patient-specific adaptation. By our approach, trifurcated optimization zones are used to control the dose fall-off, depending on which organs-at-risk (OARs) are in the vicinity of each zone. The trifurcated optimization zones enclose the spinal cord and are illustrated as the upper left (90-degree), upper right (90-degree), and posterior regions (180-degree) in Figure 1. The arrangement is designed to control the dose spillage into surrounding OARs including lungs, heart, esophagus, bronchus, liver, and kidneys. The generic plan has these zones as structures. Once the target is defined based on online MRI, the constraint structures for optimization are created by the auto-margin function while major OARs generated by deformable registration. The idea of using optimization zones for planning instead of using OARs as constraints is lowering the optimization dependent to the OARs. In the emergency treatment, with quick contour deformable registrations or even without OAR contouring, a clinical acceptable plan still can be generated. A post-delivery contouring can be implemented for further dose assessment. Relative electron densities for the heart, esophagus, liver, and kidneys were set to 1 while lungs and bronchus were set to 0.3. Bony structures including targets were set to 1.15. A clinical plan from a C-arm LINAC for spinal metastasis (Rx of 20Gy in 5 fractions) was replanned on MR-LINAC based on the developed workflow. Three comparisons were created: one based on the C-arm planning CT, and two plans based on simplified bulky electron density (ED) overrides, with (first) and without (second) bony structure overrides, to simulate online MRI-CT conversion.

Result: The dosimetric comparisons under the equivalent target coverage are listed in Table 1. The major difference between the original C-arm plan and the MR-LINAC plans is on the hot spot (21.4 Gy vs 23.2 Gy) which is intrinsically linked to the absence of MR-LINAC collimator rotation. The plan quality, however, is clinically acceptable for the emergency treatments. In conclusion, regional control of the dose fall-off produces clinical-quality plans similar to conventional planning. The treatment timeline details are shown in Table 2.

Conclusion: For an emergency cord compression treatment, a simple AP/PA treatment is commonly administered while an IMRT plan is created later. By utilizing a generic pre-plan and MR-LINAC's adaptive treatment capability for such emergency treatments, a higher quality plan can be achieved in a fairly short time frame without patient-specific simulation. The created plan can be further used for treating remaining fractions with efficient MR-LINAC plan adaptation.

Table 2. Treatment time breakdown	
Action Item	Minutes
Patient setup	5
Scan Time	3

Fusion	2
Contour	5-10
Optimization	5
Plan review	-
Beam on time	10-15
Appr. Total Time	30-60

81

Examining Gadolinium-Based Nanoparticle Uptake in Brain Metastases as Quantified by T1 Mapping

Stephanie Bennett PhD[1], Camille Verry MD[2], Evangelia Kaza PhD[1], Xin Miao PhD[3], Ross Berbeco PhD[1], Atchar Sudhyadhom PhD[1]

[1]Brigham and Womens Hospital, Boston, MA, USA. [2]Grenoble Alpes University Hospital, Grenoble, France. [3]Siemens Medical Solutions Usa Inc, Boston, MA, USA

Abstract

Purpose: Radiation therapy currently faces a number of challenges, particularly when delivering radiation to tumors close to organs at risk (OARs), are difficult to visualize (even with image guidance) or are radioresistant. A recently developed, gadolinium-based, theranostic agent shows immense promise in the treatment of previously elusive tumors. Preclinical studies demonstrated its safety, its efficacy as an MRI contrast agent and radiosensitizer during irradiation as well as physiological elimination rates comparable to common contrast agents. These promising pre-clinical results necessitated human trials; several ground-breaking clinical trials are underway examining the theranostic effects of these nanoparticles. Here, we use a method developed to quantify nanoparticle uptake based on quantitative MRI T1 mapping to examine the uptake in brain metastases.

Methods: Data were collected from 14 patients with brain metastases at a higher risk of local recurrence with radiation alone. In this double blinded trial, patients received either an intravenous nanoparticle infusion (100 mg/kg) or placebo (saline) 2-5 days prior to their first SRS treatment. A 3T MAGNETOM Vida (Siemens Healthcare) scanner and head coil were used to image patients, where patients were scanned with a Magnetization Prepared 2 Rapid Acquisition Gradient Echoes (MP2RAGE) T1 mapping sequence prior to nanoparticle infusion as well as 2 hours post infusion. Nanoparticle uptake in individual metastases (delineated by a physician in patient planning scans) was calculated using a known relationship between the change in T1 value resulting from tumor uptake, and nanoparticle concentration. Uptake was examined for patterns; specifically, mean uptake and uptake distribution were examined for each GTV and compared amongst patients

Results: Of 14 patients, 10 appeared to have received nanoparticles. Figure 1 depicts aggregate results for these 10 patients, where each data point represents an individual brain metastasis, and each patient has multiple metastases. The figure presents mean nanoparticle concentration (colored star) and average upper quartile concentration (black star) per GTV. Average uptake was slightly lower than was observed in a prior brain metastases study which used a different scanner and a VFA T1 mapping sequence to quantify nanoparticle uptake. Previous work suggests the MP2RAGE sequence yields more accurate T1 values than VFA. T1 map GTVs were acquired through registration and were therefore susceptible to delineation error at tumor edges; for that reason, the average of upper quartiles better represents the higher concentrations found within GTVs. Figure 2A depicts an observed relationship between tumor diameter and average uptake; data appears to suggest a logarithmic relationship between tumor uptake and tumor size. The distribution of uptake was examined by considering the concentration at the center as compared to the concentration at the surface of each tumor. Figure 2B depicts an observed relationship between the surface to center concentration ratio, and tumor diameter as well as some illustrative tumor cross sections.

Conclusion: We have demonstrated quantifiable uptake of gadolinium-based nanoparticles in patients with multiple brain metastases. We have further demonstrated observed relationships between tumor uptake and tumor size. Further patterns of uptake and distribution will be examined as the trial progresses.

82

Optimizing Pre-processing Workflow to Improve Radiomics Robustness for Longitudinal Abdominal MRIs Acquired with Low Field-Strength MR-linac Systems

Jia Wei[1], Alexia Jones[2], Chipo Raranje[3], Yao Hao Ph.D.[3], Taeho Kim Ph.D.[3], Alex Price M.S.[3], Lauren Henke M.D.[3], Hyun Kim M.D.[3], Borna Maraghechi Ph.D.[3], Eric Laugeman M.S.[3], Michael Gach Ph.D.[3], Jon Hansen Ph.D.[3], Geoffrey Hugo Ph.D.[3], Tong Zhu Ph.D.[3]

[1]Union College, Schenectady, NY, USA. [2]Rockhurst University, Kansas City, MO, USA. [3]Washington University in St Louis, St Louis, MO, USA

Abstract

Purpose: Several studies demonstrated feasibility of daily ViewRay MRI radiomics for response evaluation of pancreatic and rectal cancer. While promising, a fundamental concern has not yet been evaluated systematically: whether pre-processing workflow is optimized to minimize uncertainties with a low field-strength MRI-linac. Using repeated measurements of a large torso phantom, this study quantified SNR, detail preservation, spatial/longitudinal homogeneity under different pre-processing steps and therefore proposed an optimized workflow to improve radiomics repeatability for abdominal MRI.

Methods: Eight datasets of a QUASAR^{TM} Insight phantom (radius=42.6cm/thickness=5.8cm) were acquired in 6 days using the same sequence for daily planning MRI of pancreatic cancer (trueFISP in 17 seconds, FOV=45cmx45cmx24cm, resolution=1.63x1.63mm). *(1) Workflow:* An optimized workflow should include de-noising (intrinsic low SNR), de-biasing (spatial inhomogeneity) and intensity normalization (longitudinal inhomogeneity) to reduce uncertainties while largely preserving details. *(2). Image Quality Measures:* For each dataset, MRIs with flexible coils (FC) and with whole-body coils (BC) were acquired with the same resolution. More average was used for MRIs of BC so that they could be used as the reference to compare those of FC. Built-in phantom inserts (**Fig.1**) were used to calculate the following quality measures of FC data after each pre-processing step. 2.a. SNR improvement: SNR was calculated from Uniform_ROIs and SNR improvement (SNR%) was then quantified as the ratio to the original MRI with FC. 2.b. Detail preservation: was calculated as the structural similarity index (SSIM) of Resolution_ROIs between MRIs of FC and BC within the same scan section. 2.c. Spatial and longitudinal image homogeneity: was quantified as the coefficient-of-variation among intensity of six Uniform_ROIs within each scan (CoV_Spatial) and of mean intensity of Uniform_ROIs across 8 longitudinal scans (CoV_Longitudinal). 2.d. Radiomics repeatability: was quantified as the coefficient-of-variations of a radiomics parameter (CoV_Radiomics) across longitudinal scans. <5%/[5%,10%]/>10% indicate excellent/good/poor repeatability accordingly. *(3). Different algorithms for pre-processing steps:* Pre-processing algorithms (**Tab.1**) were implemented with Slicer Software (V.5.0.2).

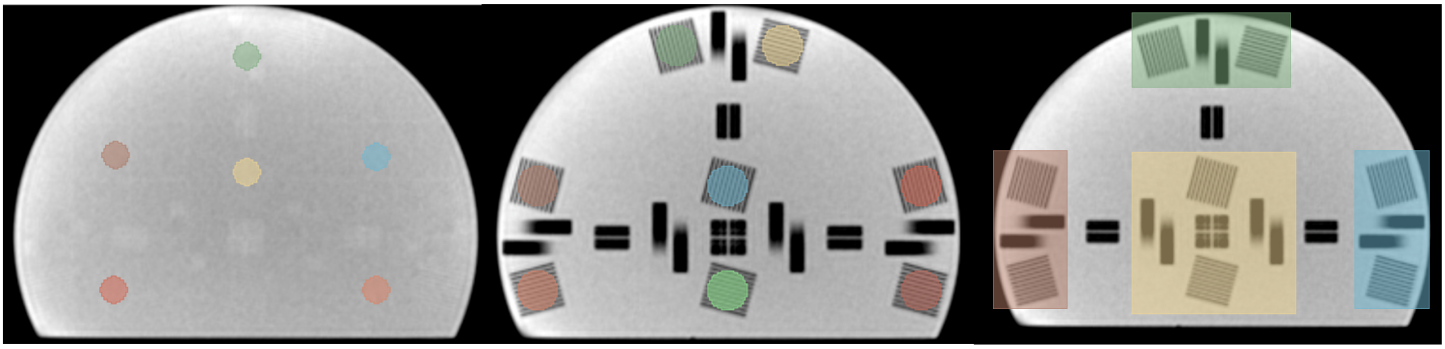

Fig. 1: Region-of-interests inside the Insight Phantom for quantifying image quality (**Left**) Six **Uniform_ROIs** in the uniform insert to evaluate the SNR and spatial and longitudinal image homogeneity, (**Middle**) Eight **Resolution_ROIs** in the resolution/slice thickness insert to evaluate the preservation of image details, (**Right**) Four **Radiomics_ROIs** in the resolution/slice thickness insert to evaluate of overall radiomics repeatability.

PRE-PROCESSING STEPS	ALGORITHMS AND CONFIGURATIONS	QUALITY MEASURES
DE-NOISING	Median filter (two levels of neighborhood size), Gaussian filter (3 Sigma levels), Curvature anisotropic diffusion and Gradient anisotropic diffusion (three conductance and three iteration levels)	**SNR%, SSIM**
DE-BIASING	N4ITK (Four FWHM and four iteration levels)	**CoV_Spatial**
INTENSITY-NORMALIZATION	Min-max, Z-transformation, Histogram-matching (three numbers of histogram levels and three numbers of matching points)	**CoV_Longitudinal**
RADIOMICS CALCULATION	Fixed bin width (three levels)	**CoV_Radiomics**

Tab.1: Different algorithms evaluated in this study and the corresponding image quality measures used for quantitative comparisons among algorithms

Results: Pre-processing significantly affected ViewRay abdominal MRI quality. Both gradient and curvature anisotropic diffusion improved SNR more than 50% with only 20% loss of image details. A N4ITK bias-field correction with a FWHM=0.25 and at least four layers of iterations reduced spatial inhomogeneity from >20% to <2% among Uniform_ROIs. The order of de-noising/de-biasing also matters: when de-biasing first followed by de-noising, it improved spatial homogeneity 1.5 times better than those if the reversed order was applied. Both Z-transformation and histogram-matching improved radiomics repeatability significantly: 63 or 52 out of 93 radiomics parameters had excellent repeatability (CoV_Radiomics<5%) after Z-transformation or histogram-matching compared to 18 from without normalization. In addition, only 33 radiomics parameters always have at least good repeatability (<10%) independent of pre-processing methods (**Fig.2**), indicating challenges of multi-center studies and the necessity of standardized/optimized pre-processing workflows.

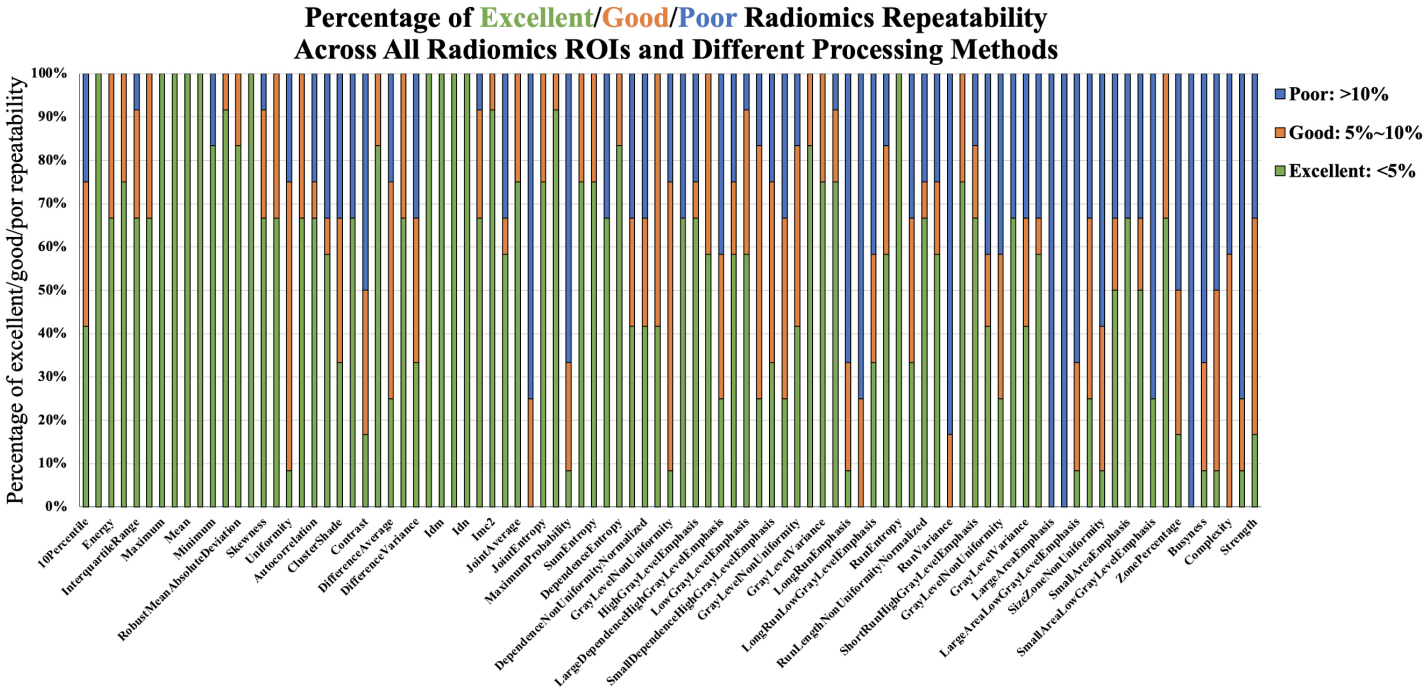

Fig.2. For each radiomics parameter (X-axis), the dependency of its repeatability on different intensity normalization methods is illustrated as the stack-plot of the percentage of **excellent (green)**/**good (orange)**/**poor (blue)** repeatability among all four Radiomics_ROIs. Only 33 out of 93 radiomics parameters have at least good repeatability no matter which processing methods were used, indicating the necessity of having optimized pre-processing workflows.

Conclusion: An optimized pre-processing workflow is proposed, containing three consecutive steps of de-biasing with the N4ITK bias-correction, denoising with gradient anisotropic diffusion and intensity normalization with Z-transformation. This workflow improved radiomics repeatability of ViewRay abdominal MRI and can potentially be used for multi-center clinical studies.

83

A simulation and phantom study to evaluate the accuracy of T1 measurements and contrast agent concentration conversion for dynamic contrast-enhanced MRI protocol optimization

Dr. Yen-Peng Liao Ph.D., Dr. Jie Deng Ph.D.
UT Southwestern Medical Center, Dallas, Texas, USA

Abstract

Purpose

DCE-MRI is a quantitative imaging method to evaluate tumor angiogenesis. T1 measurements are essential for converting the signal-time curve to gadolinium concentration-time curve after contrast agent injection. Variable flip angle (VFA) is a practical approach for T1 quantification. Generally, major parameters, such as TR, TE, and FA in the SPGR sequence, are the same in both T1 mapping and DCE acquisition. A shorter TR benefits higher temporal resolution, which, however, may affect the accuracy of T1 measurements and contrast concentration conversion. The purpose of this study was to investigate the effect of TR on the accuracy of VFA T1 measurements and concentration conversion in DCE-MRI.

Methods

The Essential System Phantom for Relaxometry (CaliberMRI) consisting of fourteen vials filled with different concentrations of $NiCl_2$ solution (C = 0.29, 0.60, 1.04, 1.64, 2.52, 3.68, 5.43, 7.74, 11.3, 16.5, 23.3, 32.7, 46.0, 65.3 mM), with the relaxivity (r_1) of 0.619 $mM^{-1}s^{-1}$ at 20°C was used to measure different T1 values and simulate tissue concentration changes in DCE. The phantom was scanned on a 1.5T MRI. 3D SPGR images were acquired using seven flip angles of 2°, 5°, 10°, 15°, 20°, 25°, and 30°. We tested five image sets acquired with different TR of 3.6, 5, 7, 10, and 20 ms. For the simulation part, the relaxation rate (i.e., 1/T1) of each vial was simulated by the linear model: $R1(C)=r1\bullet C+R1_{water}$, where $R1_{water}$ is 0.367 s^{-1}. The simulated SPGR signal in each vial is $S(R1)=M0\bullet\sin\alpha\bullet(1-e^{-TR\bullet R1})/(1-\cos\alpha\bullet e^{-TR\bullet R1})$, where α is the flip angle (30° in this study). The simulated SPGR signals across all vials were then converted to tissue contrast concentration changes by $C=\{-\ln[(1-K)/(1-K\bullet\cos\alpha)]/TR-R1_{water}\}/r1$, where $K=S/S_0\bullet(1-e^{-TR\bullet R10})/[(1-\cos\alpha\bullet e^{-TR\bullet R10})]$.

Results

Figure 1 demonstrated the simulated SPGR signal in each vial (**A**) and the linear regression of the relaxation rate difference (ΔR1) vs. the concentration [NiCl2] (**B**). The simulated data suggested that [NiCl2] estimation was independent of TR. Figure 2 showed the linear regression of ΔR1 from the phantom signals of 14 vials vs. [NiCl2] by using the T10 measured in the VFA dataset with TR = 3.6 ms (**A**) and using the 'gold standard' $T1_0$ provided by NIST (**B**). The relaxivity calculated using the VFA $T1_0$ was close to the true r_1 of 0.619 $mM^{-1}s^{-1}$. Further, the measured T1 and calculated r_1 varied with TR (Table 1).

Discussion

The accuracy of the T1 measurements depended on the TR of the SPGR scan. The linearity between the estimated ΔR1 and contrast agent concentration can be distorted using a $T1_0$ estimated from a T1 mapping sequence acquired with different TR. To minimize this effect, T1 mapping should use the same TR as in the DCE sequence.

Figure 1.

Figure 2.

Table 1

TR (ms)	Measured T_{10} (s)	r_1, measured T10 ($mM^{-1}s^{-1}$)	r_1, NIST T10 ($mM^{-1}s^{-1}$)
3.6	0.623	0.628	0.139
5	0.878	0.587	0.186
7	1.262	0.473	0.254
10	1.665	0.383	0.351
20	2.09	0.335	0.951

84

Dosimetric Gains of Plan Adaptation with MR guided RT for Pancreas Patients

Professor ANIL SETHI PhD, Ms Emily Ness BS, Dr Brian Lee PhD, Professor John Roeske PhD, Professor William Small MD, Professor Tamer Refaat MD
Stritch School of Medicine, Loyola University Chicago, Maywood, IL, USA

Abstract

Purpose/Objectives:

We aim to document dosimetric gains associated with MR guided adaptive radiation therapy (MRgART) for pancreas stereotactic body radiotherapy (SBRT) patients.

Materials/Methods:

This IRB approved study evaluated SBRT plans of 23 pancreas cancer patients treated with MRgART on a 0.35T MR linac in our department between 2018 and 2022. Prescription treatment dose was 40Gy to PTV and 50Gy to GTV in five fractions with 6MV FFF X-rays. For each fraction, a reference treatment plan was computed on the daily MR image for dose prediction. If OARs exceeded dose tolerance, the treatment plan was re-optimized and adapted in an iso-toxicity approach. The decision to adapt was driven by OAR dose tolerance V36 ≤ 0.5cc for stomach, duodenum, small and large bowel (SB, LB). This retrospective review assessed adapted plan specifications, reasons for adaptation, and dosimetric gains achieved with adaptive RT for each OAR (Dmean, Dmax and V36Gy) and PTV coverage (V40Gy) by comparing predicted vs. re-optimized plans.

Results:

Of the 112 completed SBRT fractions, 63(56.3%) were adapted. Due to their proximal anatomic location, stomach, duodenum and small bowel were the most likely determinant of plan adaptation (33.3%, 30.2% and 27% fractions respectively). Excess dose to large bowel was the least likely cause of adaptive RT (9.5%). For 14.3% of fractions, GTV/PTV coverage was the decisive factor. For adapted fractions, average improvements (decrease) in V36Gy (cc) for stomach, duodenum, SB, and LB were (mean ± s.d.) 1.7±1.2, 2.1±1.3, 1.1±0.9, and 4.0±3.2 cc respectively. The corresponding dose reductions in average Dmax for Stomach, Duodenum, SB, LB were 18.5±6.4%, 16.1±10.3%, 15.6±10.2%, and 22.8±22.7% respectively. Plan adaptation also resulted in average dose drops in OAR Dmean of 3±4.8%, 6.7±4%, 6±5.8%, 2.2±9.6% respectively. For adaptive RT driven by target coverage, V40Gy for PTV improved on average by 16.0%.

Conclusion:

Large inter and intra-fractional changes resulting from soft-tissue deformation, weight loss, peristalsis, and/or respiratory/cardiac motion may occur in pancreas SBRT patients. These anatomical changes lead to sub-optimal PTV/OAR

doses that may be effectively mitigated with MRI guided adaptive radiation therapy.

86

R2*-MRI with super-paramagnetic iron oxide nanoparticles (SPION) to auto-contour voxel-wise functional liver parenchyma volume for primary and metastatic liver cancers

Dr Danny Lee Ph.D.
Allegheny Health Network, Pittsburgh, PA, USA. Drexel University College of Medicine, Philadelphia, PA, USA

Abstract

Purpose: Super-paramagnetic iron oxide nanoparticles (SPION) are phagocytized by the hepatic Kupffer cells (KC) in the liver and shorten MRI signals within the volume of functional liver parenchyma (FLP) where KCs are found. However, malignant tumors lacking KCs exhibit minimal signal change, resulting in increasing liver heterogeneity. SPIONs as an MRI contrast agent (SPION-CA) can safely label hepatic macrophages and be localized within hepatic parenchyma for T2*- and R2*-MRI of the liver. To date, no study has utilized the R2*-MRI with SPIONs for quantifying liver heterogeneity to characterize the volume of FLP (FLPV) in the R2* liver map.

Methods: This study investigates whether SPIONs enhances liver heterogeneity for an auto-contouring tool to identify voxel-wise FLPV. This study was comprised of 6 steps. First, T2* image sets, a 3D T2*-MRI with 3 echoes sequences in conjunction with an exhalation breath hold (Ex-BH) for motion management, were acquired before and after the intravenous SPION-CA injection using a 1.5T Elekta Unity MR-Linac (Elekta; Stockholm, Sweden). The two sets of pre- and post-SPION T2* image sets were transferred to MiM software (v7.0.6, MIM Software Inc, Cleveland, OH). The liver and tumor contours, manually delineated by a physician for radiation treatment planning, were then copied to both pre- and post-SPION T2* image sets in the MiM. Then, both liver contours of the pre- and post-SPION T2* image sets were extracted by binary masking for the voxel-wise 3D liver volumes. Next, we calculated R2* relaxation rates for R2* liver maps and auto-contoured FLPV. Finally, the FLPV was overlaid on the liver image. This allowed us to evaluate the efficiency of an in-house auto-contouring tool to improve conformal avoidance for further uses of FLPV during radiation treatment planning.

Results: This was the first study to directly evaluate the impact of SPIONs on FLPV in R2*-MRI for 12 liver cancer patients. By using SPIONs, liver heterogeneity was improved across pre- and post-SPION MRI sessions. On average, 60% of the liver [range 40%−78%] was identified as FLPV in our auto-contouring tool with a pre-determined threshold of the mean R2* of tumor and liver. This method performed well in 10 out of 12 liver cancer patients; the remaining 2 needed a longer echo time or more SPIONs for darker background in FLPV. Using FLPV, we demonstrated the efficiency of our auto-contouring tool to identify FLPV while overlaying FLPV on a liver image to visually inspect the tumor and FLPV.

Conclusions: This was the first study to directly evaluate the impact of SPIONs on functioning liver parenchyma with T2*- and R2*-MRI in patients with primary and metastatic liver cancers on Elekta Unity MR-Linac. By using SPIONs, liver heterogeneity was improved across pre- and post-SPION MRI sessions. Our auto-contouring tool identified an average of 60% of the liver as a FLPV and performed well in 10 out of 12 liver cancer patients. These results demonstrate that our auto-contouring tool with SPIONs can facilitate the heterogeneous R2* of liver, which is a desirable technique for achieving accurate liver SBRT planning.

87

Radioimmunomodulating Properties of Super-Paramagnetic Iron Oxide Nanoparticles (SPION) in vitro used as Alternative Contrast Agent for MRI-Guided Liver Stereotactic Body Radiotherapy (SBRT)

MD, Ph.D Alexander Kirichenko MD, PH.D[1], Michael Shurin MD, Ph.D[2], Galina Shurin PH.D[2], Aishvarya Godla[3]

[1]Allegheny Health Network Cancer Institute, Pittsburgh, PA, USA. [2]University of Pittsburgh Medical Center, Pittsburgh, PA, USA. [3]University of Pennsylvania, Philadelphia, PA, USA

Abstract

Background

Ferumoxytol® (Feraheme, AMAG Pharmaceuticals, Waltham, MA) is a SPION agent that is increasingly utilized off-label as hepatic MRI contrast. This agent has the advantage of providing a functional assessment of the liver based upon its uptake by hepatic Kupffer cells proportionate to vascular perfusion, resulting in strong T1, T2 and T2* relaxation effects and enhanced contrast of malignant tumors, which lack Kupffer cells. The latter characteristic has been recently utilized for online radiotherapy treatment plan adaptation and more accurate MR-guided liver SBRT. However potential radiotoxicity of SPION has never been addressed for its safe use as an alternative contrast agent during MRI-guided liver SBRT on MR-Linac. The purpose of this study was to determine radiosensitivity of human macrophages loaded with SPIONs in vitro.

Methods

Human monocyte and macrophages cell line in cultures were loaded with clinically relevant concentration of Ferumoxytol (30μg/ml) for 2 and 24 h and irradiated to 3Gy, 5Gy and 10Gy. Cells were washed and cultured for additional 24 and 48 h prior to assessing their phenotypic activation by flow cytometry and function, including viability (Annexin V/PI assay), proliferation (MTT assay) and cytokine expression (Luminex assay).

Results

Our results demonstrate that SPION affected both human monocytes and macrophages in vitro. Specifically, iron oxide nanoparticles decreased radiation-induced apoptosis and prevented radiation-induced inhibition of human monocyte proliferative activity. Furthermore, Ferumoxytol protected monocytes from radiation-induced modulation of phenotype. For instance, while irradiation decreased polarization of monocytes to CD11b+CD14+ and CD11bnegCD14neg phenotype, Ferumoxytol prevented these effects. In macrophages, Ferumoxytol counteracted the ability of radiation to up-regulate cell polarization to CD11b+CD14+ phenotype, and prevented radiation-induced down-regulation of expression of HLA-DR and CD86 molecules. Finally, Ferumoxytol uptake by human monocytes down-regulated expression of pro-inflammatory chemokines MIP-1α (Macrophage inflammatory protein 1α), MIP-1β (CCL4) and RANTES (CCL5). In macrophages, Ferumoxytol reversed the effect of radiation on the expression of IL-1RA, IL-8, IP-10 (CXCL10) and TNF-α, and up-regulates expression of MCP-1 (CCL2) and MIP-1α.

Conclusion

SPION agent Ferumoxytol increases resistance of human monocytes to radiation-induced cell death in vitro and supports anti-inflammatory phenotype of human macrophages under radiation. The effect is radiation dose-dependent and depends on the duration of Feraheme uptake.